Gas in Void Galaxies

Kathryn Kreckel

Submitted in partial fulfillment of the
requirements for the degree
of Doctor of Philosophy
in the Graduate School of Arts and Sciences

COLUMBIA UNIVERSITY

2012

ABSTRACT

Gas in Void Galaxies

Kathryn Kreckel

Void galaxies, residing within the deepest underdensities of the Cosmic Web, present an ideal population for the study of galaxy formation and evolution in an environment undisturbed by the complex processes modifying galaxies in clusters and groups, and provide an observational test for theories of cosmological structure formation. We investigate the neutral hydrogen properties (i.e. content, morphology, kinematics) of void galaxies, both individually and systematically, using a combination of observations and simulations, to form a more complete understanding of the nature of these systems.

We investigate in detail the H I morphology and kinematics of two void galaxies. One is an isolated polar disk galaxy in a diffuse cosmological wall situated between two voids. The considerable gas mass and apparent lack of stars in the polar disk, coupled with the general underdensity of the environment, supports recent theories of cold flow accretion as an alternate formation mechanism for polar disk galaxies. We also examine KK 246, the only confirmed galaxy located within the nearby Tully Void. It is a dwarf galaxy with an extremely extended H I disk and signs of an H I cloud with anomalous velocity. It also exhibits clear misalignment between the kinematical major and minor axes, and a general misalignment between the H I and optical major axes. The relative isolation and extreme underdense environment make these both very interesting cases for examining the role of gas accretion in galaxy evolution.

To study void galaxies as a population, we have carefully selected a sample of 60 galaxies that reside in the deepest underdensities of geometrically identified voids within the SDSS. We have imaged this new Void Galaxy Survey in H I at the Westerbork Synthesis Radio Telescope with a typical resolution of 8 kpc, probing a volume of 1.2 Mpc and 12,000 km s^{-1} surrounding each galaxy. We reach H I mass limits of 2×10^8 $M_\odot$ and column density

sensitivities of 5×10^{19} cm^{-2}. We find that the void galaxies are generally gas rich, low luminosity, blue disk galaxies, but identify three as early type galaxies. The void galaxy optical and H I properties are not unusual for their luminosity and morphology. The small scale clustering in the void is similar to that in higher density regions, and we identify 18 H I rich neighboring galaxies in the voids. Two of these are systems of three galaxies linearly aligned and joined by a H I bridge, suggestive of filamentary formation within the void. We find no population of H I rich low luminosity galaxies within the observed voids that are not close companions of the targeted sample.

Finally, to put these observations in a theoretical context, we analyze a $(120\ h^{-1}$ Mpc$)^3$ adaptive mesh refinement hydrodynamic simulation that contains a high resolution subvolume centered on a $\sim$30 Mpc diameter void. We construct mock observations with $\sim$1 kpc resolution of the stellar and gas properties of these systems which reproduce the range of colors and luminosities observed in the SDSS for nearby galaxies, however we find no strong trends with density. We also make predictions for a significant population of low luminosity (M_r = -14) dwarf galaxies that is preferentially located in low density regions and specifically in the void center.

Table of Contents

List of Figures

List of Tables

Acknowledgments

There are many people without whom I would never have completed this thesis. First and foremost is my advisor, Jacqueline, who so generously allowed me to continue as her student when life and love led me to move away from NYC. Her scientific passion and curiosity have greatly inspired me, and her enthusiasm is a constant reminder of how fun research can (and should) be.

I am deeply indebted to the astronomy department at the University of Illinois at Urbana-Champaign, who were so welcoming to me as a rogue grad student. I am especially grateful to Tony Wong, who found me a desk and always found the time to meet with me to talk about papers and proposals. I really enjoyed my time at UIUC, and know that my knowledge of astronomy is much broader for it.

Many, many thanks to all the grad students at Columbia who so generously let me stay on their couches, as well as to all those who offered but I never burdened. You are all most welcome to come visit and stay on my couch any time. Thanks to all my office-mates, for your help and your distractions. Thanks especially to Emily, Cameron, Kyle, Maria and Andy for your friendship and nerdy jokes.

Much of my thesis work relied on observations, and I am deeply indebted to Gyula Jozsa at WSRT and Bob Barr at MDM for their technical support. I am also grateful to my thesis committee for their continued advice and support. The department secretaries, Millie and Ayoune at Columbia and Mary Margaret and Jeri at UIUC, have been fantastic, working tirelessly to solve bureaucratic problems so I don't have to.

Finally, thank you to my family, for all your love and support. To my parents, who have always encouraged my academic interests, and to my husband, who is always there for me.

Chapter 1

Introduction

In an effort to test our current theories of cosmology and galaxy evolution, it is instructive to consider galaxies in extreme environments. Just as studies of clusters and cluster galaxies have helped us understand the role interactions play in driving transformations in galaxies, and set one scale size by which we can test predictions of ΛCDM, voids and void galaxies also provide key insights into galaxy formation and evolution in a similarly extreme environment. Located within large scale underdense regions, void galaxies are in many ways very similar to galaxies in 'average' environments, but in a few keys ways are very distinct. This allows us to examine our understanding of the different role internal and external processes play to evolve systems with simplified external effects. In addition, their unique cosmological location is ideal to test predictions from cosmology by examining the ways in which galaxies populate the voids.

1.1 Voids in Large-Scale Structure

While much of astronomy focuses on studying observable matter, the majority of the universe appears to be empty. Large scale structure in the universe was recognized to exist even in the earliest nebulae surveys of William and John Herschel and of Shapley & Ames (1932), where an excess of galaxies in the northern hemisphere due to the Virgo cluster is apparent. However the eventual identification of the Local Supercluster by de Vaucouleurs (1953, 1958) was only the beginning of our understanding of large scale structure. The Cos-

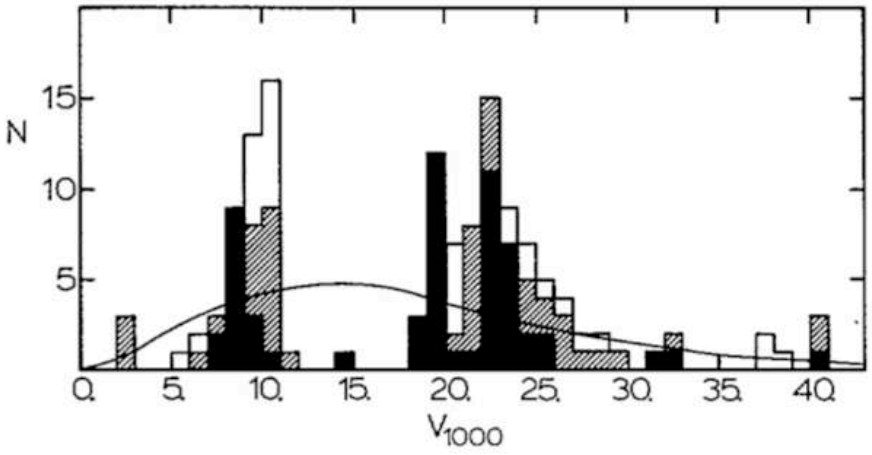

Figure 1.1: Distribution of galaxies in redshift space along three different sightlines in the Boötes void (light, dark, and shaded histograms), as compared with the predicted uniform distribution (curve). Even in this first detection of a void, a void galaxy is evident at $V_{1000} = 15$. From Kirshner et al. (1981).

mic Web that is now understood to permeate the universe is outlined by the arrangement of galaxies into filaments, walls and clusters (Zel'Dovich 1970; Klypin & Shandarin 1983; de Lapparent et al. 1986; Bond et al. 1996), but the majority of the volume of space exists between these structures, in the underdense voids (Pan et al. 2011).

1.1.1 Observational Discovery

Regions nearly devoid of galaxies were apparent in the earliest investigations of galaxy distributions in redshift space (Gregory & Thompson 1978; Einasto et al. 1980). This was solidified by observations of three sightlines through the Boötes void, all of which showed a strong deviation from a uniform distribution of galaxies, and together outlined a million cubic megaparsec void (Figure 1.1, Kirshner et al. 1981) . Since then, numerous galaxy redshift surveys have mapped ever deeper and wider areas (CfA, Huchra et al. 1983; Las Campanas, Shectman et al. 1996; 2dF, Colless et al. 2001; 2MASS Redshift Survey, Huchra et al. 2005; 6dF, Jones et al. 2009). The recently completed SDSS redshift survey (Abazajian et al. 2009), which includes nearly a million galaxies over a quarter of the sky out to redshifts of $z \sim 0.2$, clearly outlines these large scale features (Figure 1.2). Blind H I surveys are also underway which counterbalance the optically selected surveys, with similar

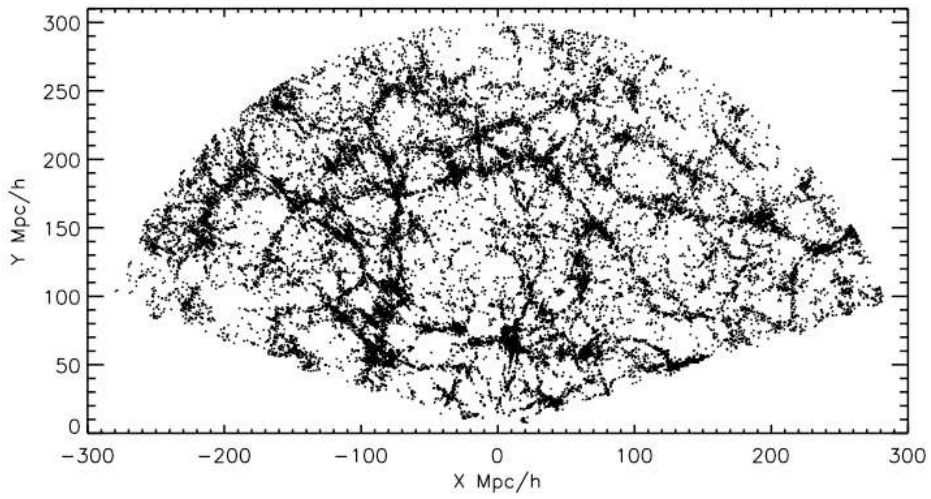

Figure 1.2: Distribution of galaxies in the SDSS DR7 redshift survey. Slice is taken from the 5° surrounding a declination of 20°, out to a distance of 300 h^{-1} Mpc. The clusters and connecting filaments and walls bound very clearly defined, low density voids.

results (HIPASS, Meyer et al. 2004; ALFALFA, Saintonge et al. 2008).

Voids range in size but can be quite large, with diameters of 20-60 h^{-1} Mpc, and a median size of 34 h^{-1} Mpc (Pan et al. 2011). When considering only the most luminous galaxies, $M_r < -20.0$, voids are slightly larger, however the fainter galaxies generally seem to respect the voids defined by the brightest galaxies (Peebles 2001; von Benda-Beckmann & Müller 2008). Beyond scale sizes of ∼100 Mpc we seem to reach an end of greatness, and observe homogeneity (Kirshner 2002), though observations of deviations from this may be cosmologically significant (see Section 1.4).

The density profile within voids appears somewhat bucket-shaped (Figure 1.3, left) and quite robust at different void sizes, with relatively uniform interiors and sharply defined walls (Ceccarelli et al. 2006; Pan et al. 2011). Void centers are quite empty, typically with density contrast $\delta \equiv \Delta\rho/\rho \sim -0.9$, and the few galaxies interior to the voids tend to lie near the void walls (Hoyle & Vogeley 2004).

1.1.2 Theoretical Understanding

Dark matter only ΛCDM numerical simulations are able to generally reproduce the observed features of the Cosmic Web (see for example the Millennium Simulation, Springel et al. 2005; Little & Weinberg 1994). Initial perturbations in a Gaussian primordial density field

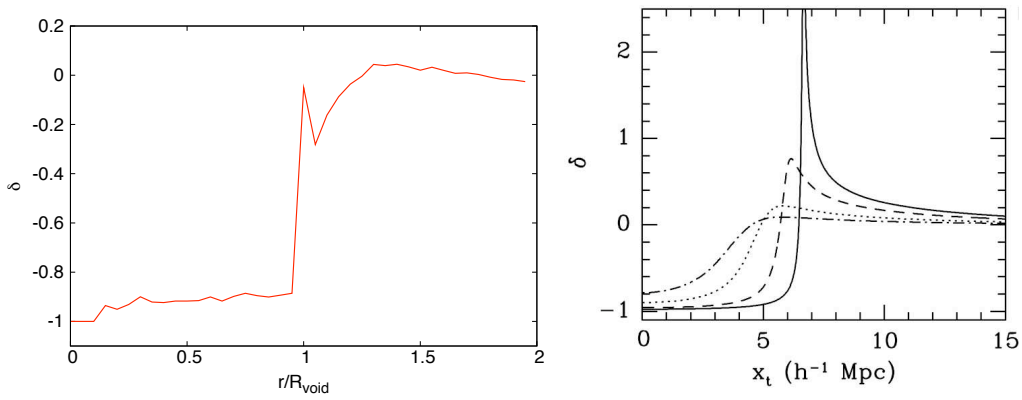

Figure 1.3: Average radial density profile of voids, as observed in the SDSS DR7 redshift survey (left, from Pan et al. (2011)) and as predicted by linear gravitation theory (right, from Sheth & van de Weygaert (2004)). Each point is measured for a spherical shell at that radius. The extremely low central underdensity, steep edge and spike in density at the void boundary is well matched by theory.

grow, with overdense regions collapsing and underdense regions effectively expanding. The resulting voids, as defined by the dark matter distribution, are fairly spherical, and contain within them a hierarchy of smaller voids which merge over time (van de Weygaert & van Kampen 1993). The shape of the void radial density profile is fairly well explained by linear gravitation theory (Sheth & van de Weygaert 2004), where shells of material within the voids experience a gradient from the center to the edge that result in relatively faster motions of material at the void center resulting in accumulation of material at the void boundary (Figure 1.3, right).

The dilution of intervening material results in a web of void substructure in the dark matter, where void galaxies are assumed to be situated. The majority of cosmological simulations focus on the evolution of dark matter, as that dominates gravitationally on these larger scales. While galaxies are presumed to fairly sample the underlying dark matter density field, there are certainly environmental effects that strongly influence the formation and growth of galaxies (see Section 1.3), and in fact there are discrepancies between the predicted dark matter halo population within voids and the observed galaxies (see Section 1.4).

1.2 Void Galaxies

While it is clear that these void regions are extremely underdense, they are not entirely empty. However to define a void galaxy population, one first needs a method to identify the boundaries of the void.

1.2.1 Identification and Selection

A variety of different techniques have been used in the literature to observationally identify voids and void galaxies, each with different advantages and drawbacks. Colberg et al. (2008) provides an interesting comparison of the results of different void-finding algorithms for the same data set.

Early surveys were limited by fairly incomplete galaxy sampling, making it difficult to trace exactly the void boundaries, and void galaxies were identified solely by a threshold in the local density. Grogin & Geller (1999) calculated the 5 h^{-1} Mpc smoothed galaxy number density, weighted against the magnitude-limited sample within the CfA2 survey, and selected galaxies at less than half the mean to be a 'lowest density' void sample. Rojas et al. (2004) identified voids galaxies as having the three nearest neighbors beyond 7 h^{-1} Mpc in a volume limited sample of the SDSS DR1. Techniques such as these are very successful at identifying isolated galaxies, however omit any true considerations of the surrounding large scale structure and may be contaminated by isolated objects in diffuse walls and filaments.

With larger, more complete redshift surveys it is possible to identify voids first by locating the void centers, typically at isolated galaxies or local minimums, and then growing maximally empty spherical voids within a set of galaxies above some luminosity threshold (Patiri et al. 2006b; Hoyle & Vogeley 2004; Pan et al. 2011). One then identifies void galaxies as residing within the spherical regions. This technique is significantly more robust, however as void shapes are not precisely spherical and void galaxies tend to be located at the outskirts of voids (see Section 1.1.2), they may miss some fraction of the void galaxy population.

A third class of void-finding algorithm makes no assumption about the size or shape of the voids, but attempts to outline them organically. This can be done by identifying void centers of a gridded (von Benda-Beckmann & Müller 2008) or tessellated (Kreckel et al. 2011) volume and including only those neighboring areas that are below a density threshold

as belonging to the void. These irregularly shaped voids contain more of the void galaxy population, but are more dependent on the assumption that the galaxy distribution serves as a fair tracer of the underlying dark matter distribution.

1.2.2 Properties

Despite the differences in identifying void galaxy populations, observationally void galaxies are consistently found to be fainter, bluer, later type, with higher specific star formation rates (star formation rate per unit stellar mass) than galaxies in average density environments (Grogin & Geller 1999, 2000; Rojas et al. 2004, 2005). While their gas content has been less studied, Szomoru et al. (1996) found that galaxies in the Boötes void are generally gas rich and disk-like, and Huchtmeier et al. (1997) found dwarf galaxies in voids to have a higher $M_{H\ I}/L_B$ ratio the deeper within the underdensity they resided. It should be noted that while in some respects void galaxies are statistically distinct, in other ways they are typical for their fixed galaxy type. In their mean colors of red and blue galaxies, measured separately, they are similar to galaxies in average density environments (Balogh et al. 2004; Patiri et al. 2006b). There is some evidence to suggest that at fixed luminosity the blue galaxies in voids are slightly bluer (von Benda-Beckmann & Müller 2008), however Park et al. (2007) argue that it is only the morphology and luminosity of void galaxies which is dependent on environment, with all other statistical correlations stemming from these two factors. Extremely low metallicity galaxies have been discovered in voids (Corbin et al. 2005; Pustilnik et al. 2006), suggesting that in general voids are a promising location for the study of unevolved dwarf galaxies (Pustilnik & Tepliakova 2011).

1.3 Role of Environment on Galaxy Evolution

It has been well established that elliptical and S0 galaxies are more abundant than spiral galaxies within clusters (Dressler 1980; Postman & Geller 1984), and the extension of this morphology-density relation to average density regions suggests that the physical mechanism behind this transformation requires a denser environment (Goto et al. 2003). The ram pressure stripping and harassment experienced in clusters, and to a lesser extent the tidal interactions that dominate in galaxy groups, are specific only to those high density environments where these forces can act to transform spiral disk galaxies. There is some

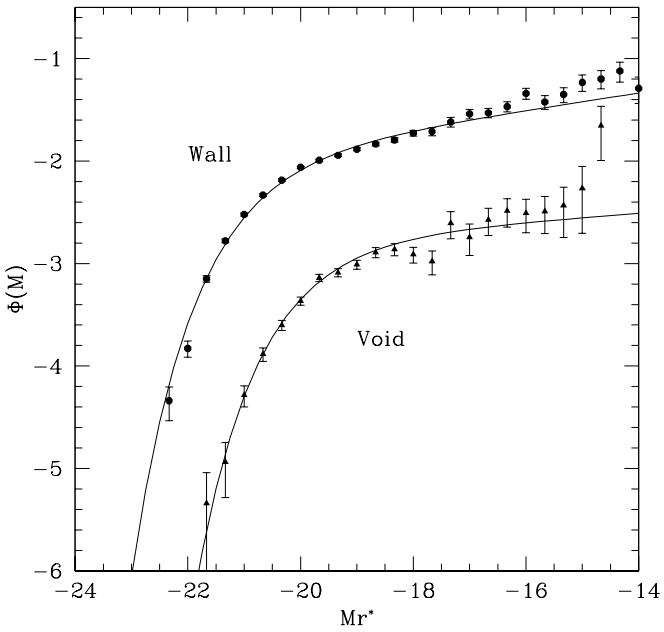

Figure 1.4: Luminosity functions of galaxies in low density regions ('Void') and all galaxies in higher density regions ('Wall'). The solid lines show the best Schechter function fit to each. The 'Void' sample is shifted to contain relatively fewer bright galaxies. From Hoyle et al. (2005).

suggestion that this relation extends to voids, as void galaxies are found to be more disk-like than 'average' galaxies (Rojas et al. 2004), and, though the statistics are limited, they may have a lower fraction of early-type galaxies (Park et al. 2007).

While those mechanisms that rely on high density gas environments will not be at play in voids, void galaxies are not necessarily isolated and may be subject to interactions. Somewhat counterintuitively, the clustering of galaxies in voids is not found to be very different than for galaxies in 'average' environments (Szomoru et al. 1996). Predictions from the evolution of a primordial Gaussian distribution in the density field find that galaxy clustering is not monotonic, and galaxies in moderate underdensities are less clustered than galaxies in moderate overdensities, but galaxies in the least dense regions are more clustered than galaxies in moderate underdensities (Abbas & Sheth 2007). Thus while void galaxies may be described as isolated on large scales, they are not necessarily alone. Elliptical galaxies, generally thought to have been formed by galaxy mergers, are found in voids, as are red galaxies with minimal recent star formation (Rojas et al. 2004, 2005). Croton

& Farrar (2008) argue that these 'red and dead' systems can theoretically also be formed by purely secular evolution, with internally driven radio-mode AGN able to quench star formation.

Evolution of the void environment progresses as a low Ω_m universe, and as such the evolution of galaxies should proceed relatively normally but at a slower pace (Goldberg & Vogeley 2004). Thus a density contrast of $\delta = -0.9$ is comparable to treating the void interior as a $\Omega_M = 0.021$, $\Omega_\Lambda = 0.48$, $h = 0.84$ universe, resulting in suppression of growth within the void relative to the surrounding standard cosmology. Indeed, void galaxies are systematically fainter, with a luminosity function that is shifted and has fewer of the brightest galaxies compared to denser regions (Figure 1.4, Hoyle et al. 2005). Void galaxies are also observed to have elevated star formation rates (see Section 1.2.2), and as it has been observed that the star formation rate has been decreasing over cosmic time (Madau et al. 1998; Steidel et al. 1999), perhaps they may be considered as simply younger and in an earlier stage of their evolution.

Fresh gas accretion is necessary for galaxies to maintain the star formation rates seen today without depleting their observed gas mass in less than a Hubble time (Larson 1972). And in fact, to the highest redshifts we are able to probe, the size and shape of H I disks of galaxies seems fairly robust (Prochaska & Wolfe 2009). Some amount of gas recycling is possible in a "galactic fountain" resulting from supernovae within the disk, however careful kinematic studies of rotation in gas disks in nearby galaxies suggests that at least 10% externally accreted gas is needed (Fraternali & Binney 2008).

Historically, this gas was assumed to condense out of reservoirs of hot gas existing in halos around galaxies (Rees & Ostriker 1977; Silk 1977; White & Rees 1978; White & Frenk 1991), however recent simulations have renewed interest in an alternative method involving the slow accretion of cold gas along filaments (Binney 1977; Kereš et al. 2005; Dekel & Birnboim 2006; Dekel et al. 2009). Observational evidence of this cold mode of accretion is growing (Sancisi et al. 2008), and simulations suggest that in low mass dark matter halos, prevalent during the earlier stages of galaxy growth at high redshifts and at $z = 0$ in low density regions, that cold mode accretion dominates (Figure 1.5, Kereš et al. 2009). Thus void galaxies are both lower mass and earlier in their evolution, this mechanism may be relatively more important in providing cold gas readily available for star formation to void galaxies. Detailed kinematic studies of the gas content of void galaxies provides a unique

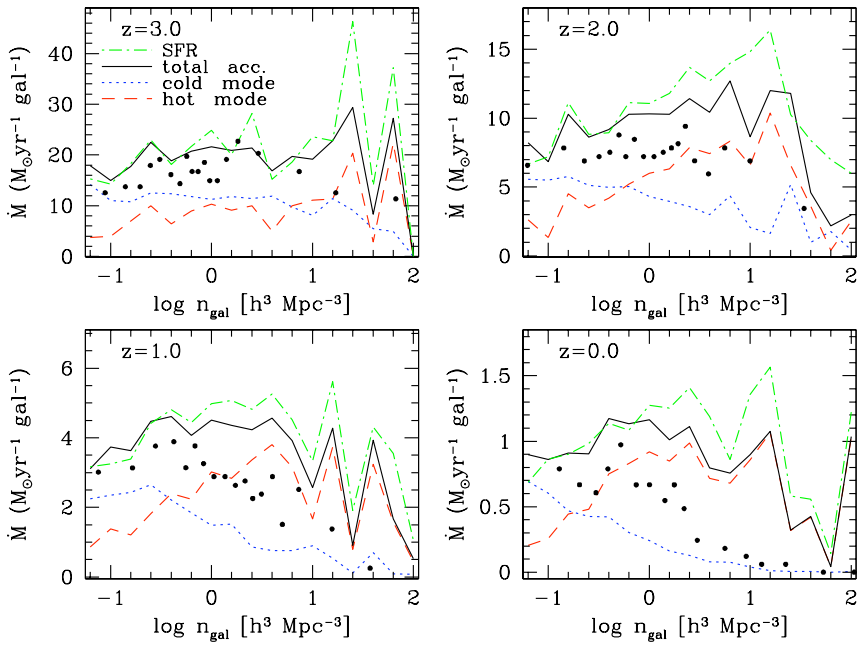

Figure 1.5: The simulated gas accretion rate due to hot (red dashed) and cold (blue dotted) modes of gas accretion, as a function of galaxy number density at different redshifts. Cold mode accretion is found to dominate at higher redshifts and lower galaxy densities compared to hot mode accretion. The SFR (green dash-dot) and total accretion rate (black solid) are also shown. Points show the median value for bins with equal numbers of galaxies. From Kereš et al. (2005)

sample of younger, star forming galaxies where their inherent isolation may allow us to distinguish the effects of close encounters and galaxy mergers from other mechanisms of gas accretion.

1.4 Void Galaxy Constraints on Cosmology

As voids constitute a fundamental feature in the cosmic web, they and the galaxies within them can provide key constraints on cosmology. These constraints are quite varied but must necessarily be met for theory to conform completely with observations.

One of the most discussed cosmological tests basted on void galaxies comes from the observation that low mass and low luminosity galaxies seem to respect the voids defined by larger galaxies (Weinberg et al. 1991; Popescu et al. 1997). This void phenomenon is in contradiction with expectations from CDM simulations, which predict that the voids

should be filled with low mass halos (Peebles 2001). While it has been confirmed that there is not enough suppression of galaxy formation in voids to cause this effect (Hoeft et al. 2006), many argue that with more detailed CDM and ΛCDM simulations the emptiness of voids is a natural product of cosmology theory (Mathis & White 2002; Furlanetto & Piran 2006; von Benda-Beckmann & Müller 2008). It has additionally been argued that a sufficiently tailored halo occupation distribution function is sufficient to match simulations with observations, with no dependence on the halo environment (Tinker & Conroy 2009). However within the Local Volume, where we are most sensitive to detecting low luminosity and low surface brightness galaxies, a discrepancy persists, and we observe only a tenth as many dwarf galaxies as are expected (Tikhonov & Klypin 2009). As this controversy arises from attempts to compare observed galaxies with simulated dark matter halos, full baryonic cosmological simulations, including a complete treatment of galaxy and star formation, are needed to accurately understand the ΛCDM predictions.

The scale sizes of voids within the cosmologically local ($z < 1$) universe can also provide constraints on cosmology. The WMAP cold spot, if due to the late integrated Sachs-Wolfe effect, would imply the presence of a ∼140 Mpc diameter supervoid, which is unlikely to have developed naturally through ΛCDM (Rudnick et al. 2007). Such a supervoid, if discovered in upcoming deeper redshift surveys such as the SDSS-III Baryon Oscillation Spectroscopic Survey of Luminous Red Galaxies, will have far reaching implications for the concordance ΛCDM model and may place constrains on dark energy (Granett et al. 2008). Void shapes can also place a potential constraint on theories of dark energy. As the voids behave as expanding bubbles over time, their ellipticity provides a sensitive probe of the underlying dark energy equation of state (Park & Lee 2007; Lee & Park 2009; Biswas et al. 2010), though it remains to be seen if the sparse sampling of the cosmic web by galaxies and the complications of tidal effects on void boundaries allow a sensitive enough measurement (Lavaux & Wandelt 2010).

Voids can also provide a unique environment to constrain alternate theories of gravity. The chameleon mechanism (Khoury & Weltman 2004) proposes the addition of a scalar gravitational field that is tied to the local gravitational potential. This field would provide anomalous acceleration that could have effects on a cosmological scale, such as quintessence, but would be shielded locally by the gravitational potential of the Sun, the Milky Way and the Local Group. One test of this theory is to observe the internal kinematics of isolated,

low mass galaxies in void environments (Hui et al. 2009). If the galaxy as a whole is not self-shielding, then the motions of internal material that is not self-shielded (i.e. gas, dust) should be different than that of objects that are self-shielded (i.e. stars). Such constraints would be up to two orders of magnitude more sensitive than what is available from our Milky Way Galaxy.

1.5 This Thesis

In this thesis we present the results of both new observations and new simulations, focusing on detailed examination of the neutral gas in void galaxies. We observe individually interesting systems (Section I), and examine in detail the gas morphology and kinematics to elucidate the role gas accretion and the void environment has played in the evolution of these galaxies. We also pursue a more systematic approach through the careful selection and H I imaging of 60 galaxies in a new Void Galaxy Survey (VGS, Section II). This sample allows us to statistically examine a robustly defined population of void galaxies, and directly address cosmological predictions. Finally, we also present the results of a new hydrodynamic cosmological simulation (Section III), which we use to compare with our observations and make predictions for the lowest luminosity void galaxy population. This multi-faceted approach to studying void galaxies individually in detail, statistically as a population, and theoretically in simulations, allows us to form a complete picture of how void galaxies can provide key insights into previously introduced questions of galaxy evolution and provide a unique test of cosmology.

Chapter 2 discusses the serendipitous discovery within the VGS of a small disk galaxy that has an extremely extended H I disk oriented perpendicular to the stellar disk. This polar disk galaxy has acquired a significant mass of H I without disturbing the central rotational support of the stellar disk. We discuss the implications of this discovery in the context of cosmological cold flows, and argue that this system provides strong evidence that these flows play an ongoing role in galaxy evolution.

Chapter 3 presents high resolution H I observations of KK 246, one of the few galaxies confirmed to reside within the Local Void. The proximity of this extremely faint void galaxy provides a unique opportunity to study in detail stellar and gas features. This dwarf galaxy also presents an extremely extended, slightly misaligned gas disk, as well as additional signs

of ongoing gas accretion and gas inflow.

Chapter 4 introduces the Void Galaxy Survey (VGS), a sample of 60 galaxies selected purely by their geometry to be centrally located within voids identified in the SDSS. This chapter presents a pilot study of H I imaging for 15 galaxies in the sample, and finds that they represent a very interesting collection of gas rich systems, many of which have small companions or signs of interaction. In addition to the gas content we discuss the integrated SDSS optical properties and derived star formation rates.

Chapter 5 analyzes results from the complete VGS study of 60 void galaxies, 55 with H I imaging. We examine the gas morphology and kinematics for the sample, and make statistical comparisons of the H I and optical properties with galaxies in average density environments. We find that void galaxies do represent a systematically different galaxy population, and speculate as to how this relates to their evolutionary history and large scale environment. In addition, we address the phenomenon of 'missing' void galaxies and find no evidence for H I rich galaxies missed by optical surveys.

Chapter 6 presents results from a new cosmological hydrodynamic simulation that is centered on a large void. High resolution allows us to construct mock observations of the galaxies residing in and around voids, which we compare directly with observations. We also compare galaxies within the simulation as a detailed function of their position within and around the void. Finally, we examine the population of low luminosity galaxies which persist in overpopulating the voids.

Chapter 7 concludes by summarizing our results and discussing the ongoing questions and future work to be pursued in this field.

Part I

Individually Interesting Objects

Chapter 2

Polar disk galaxy found in wall between voids

The following text has been published in the Astronomical Journal. The full reference for the published work is Stanonik, K., Platen, E., Aragón-Calvo, M. A., van Gorkom, J. H., van de Weygaert, R., van der Hulst, J. M., & Peebles, P. J. E. 2009, ApJL, 696, L6.

We have found an isolated polar disk galaxy in what appears to be a cosmological wall situated between two voids. This void galaxy is unique as its polar disk was discovered serendipitously in an H I survey of SDSS void galaxies, with no optical counterpart to the H I polar disk. Yet the H I mass in the disk is comparable to the stellar mass in the galaxy. This suggests slow accretion of the H I material at a relatively recent time. There is also a hint of a warp in the outer parts of the H I disk. The central, stellar disk appears relatively blue, with faint near UV emission, and is oriented (roughly) parallel to the surrounding wall, implying gas accretion from out of the voids. The considerable gas mass and apparent lack of stars in the polar disk, coupled with the general underdensity of the environment, supports recent theories of cold flow accretion as an alternate formation mechanism for polar disk galaxies.

2.1 Introduction

Polar ring galaxies are peculiar galaxies encircled by a ring of stars, gas and dust with perpendicular spin (Rubin 1994). These distinct kinematic components are confirmed by observations of their H I distribution (Schechter et al. 1984; van Gorkom et al. 1987; Arn-

aboldi et al. 1997), which generally exhibit extended emission throughout the polar ring with a central gap. Kinematically, we see that some of these structures are more disk-like than ring-like (Iodice et al. 2006), are massive enough to be self gravitating (Arnaboldi & Sparke 1994), and have the suggestion of spiral arms (Arnaboldi et al. 1997). The central galaxy is generally a rotationally supported S0 or elliptical galaxy and shares a common geometric center with the polar disk, however is relatively gas poor. Polar disk galaxies are relatively rare, with only a few percent of S0s that have now or have had a polar ring (Whitmore et al. 1990). They are particularly useful and interesting as their perpendicular dynamics allow a three dimensional probe of the dark matter potential (Schweizer et al. 1983; Sackett et al. 1994; Combes & Arnaboldi 1996).

The formation mechanism for polar disks is not entirely clear, but presumably requires a second formation event to form the perpendicular spin components. Originally, a major merger or close encounter was assumed necessary (Schweizer et al. 1983), however neither theory resolves the problem of the central disk retaining its rotational support in systems with significantly massive polar disks, as with NGC 4650A (Bournaud & Combes 2003; Bournaud et al. 2005; Iodice et al. 2006). The issue is also confused by indeterminate ages of observed polar disks, which are partly dependent on the stability of polar oriented structures (Sparke 2004). More recent theories and simulations suggest cold accretion along cosmological filaments may form and continue to feed these polar disks (Macciò et al. 2006).

We have found a polar disk galaxy in relatively isolated, void-like conditions, situated in a tenuous sheet-like configuration between two voids. It was found as part of an H I survey of 15 void galaxies selected using an early version of the Watershed Void Finder (Platen et al. 2007) and the Sloan Digital Sky Survey (SDSS, Adelman-McCarthy et al. 2008), with each galaxy in a different void. It has no optical polar ring visible in the SDSS imaging but a massive, extended H I polar disk. This suggests cold flow accretion as the most likely formation mechanism, and sheds a new and surprising light on the nature of galaxies populating the most desolate areas in the Universe (cf e.g. Peebles 2001). Observations are described in Section 2.2, shown in Section 2.3, and comparisons with theory made in Section 2.4.

2.2 Observations

SDSS J102819.24+623502.6 is part of a pilot for a larger study of galaxy formation in underdense regions of the SDSS redshift survey (Chapters 4 & 5 of this thesis). Our lonely galaxy is situated at a RA & Dec (J2000) of 10:28:19.02 +62:35:02.0 and a redshift of $z = 0.0178446$. It is fairly blue, with a g-band magnitude of 17.67 and r-band magnitude of 17.41 as reported in the sixth data release from the SDSS. Note that these images reach to magnitudes of g $\sim$ 23, as the drift-scan mode employed by the SDSS results in an effective exposure time in each band of 54.1 s (York et al. 2000). A distance of 76 Mpc is calculated assuming $H_o = 70$ km s^{-1} Mpc^{-1}, which gives a scale of $1'' = 370$ pc.

The 21 cm line of our target was observed for 12 hours at Westerbork Synthesis Radio Telescope(WSRT) in Maxi-short configuration, which optimizes imaging of very extended sources in a single track observation with shortest baselines of 36, 54, 72 and 90 meters. We observed in 4 IFs each with 512 channels, a 10 MHz bandwidth, and 2 polarizations. The target redshift corresponds to an optical heliocentric velocity of 5302 km s^{-1}, so channel increments of 19.5 kHz give a velocity resolution of 4.27 km s^{-1}.

All calibration was done using standard AIPS procedures. Continuum emission was subtracted from the UV data by linear interpolation from the line free channels. Image cubes were created with a CLEAN box around the H I emission that cleaned down to 2 mJy beam^{-1} (4 σ). Images were created with uniform weighting and robust 1 to give a balance of high resolution, a beam size of $22''.1 \times 19''.5$, with low noise, a rms of 0.5 mJy beam^{-1}. This corresponds to a 3σ detection limit in column density of 6.2×10^{18} cm^{-2} and in mass of 2.0×10^8 M$_\odot$ for a galaxy with velocity width 100 km s^{-1}. 0^{th} and 1^{st} moment maps were made, with 1.5σ clipping applied to a mask that is Hanning and Gaussian smoothed over 3 cells, both in velocity and spatially, respectively.

2.3 Results

2.3.1 Galaxy Parameters

The total H I image and intensity weighted velocity field are shown in Figure 2.1. We calculate a total H I mass of $M_{H\,I} = (3.0 \pm 0.5) \times 10^9$ M$_\odot$. There is an angle of 90° between the central stellar disk and the polar H I disk, which warps at 20 kpc to 77°.

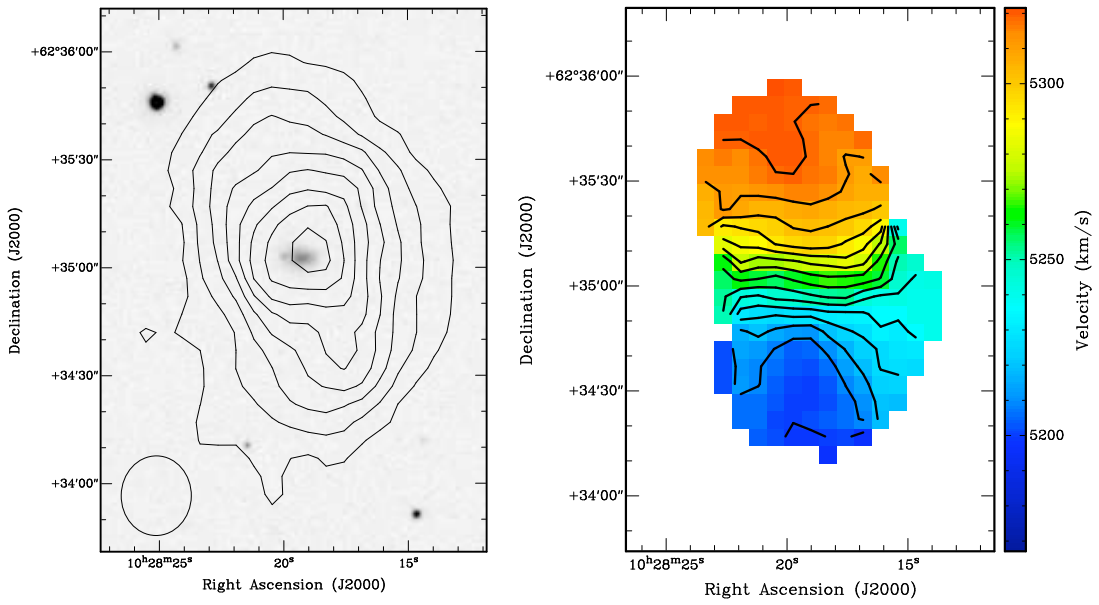

Figure 2.1: SDSS J102819.24+623502.6. On the left, the g-band image overlaid with H I contours. The column density contours are 0.76 (1.9σ), 2.0, 3.3, 4.5, 5.9, 7.0, 8.4, 9.6 x 10^{20} cm^{-2}. On the right, the intensity weighted velocity field overlaid with 8.5 km s^{-1} contours.

A comparison of slices through the data cube in position-velocity along the major axis of the H I disk compared to the major axis of the central stellar disk (Figure 2.2) clearly demonstrate that the regular rotation within this misaligned gas disk is completely decoupled from the stellar component. The major axis slice (left panel, Figure 2.2) confirms the notion from the velocity field that the H I is a disk and not a ring. The rotation curve increases non-linearly with increasing radius and appears to flatten out at a radius of about 30″, or 11 kpc. The rotation at the last measured point (about 22 kpc) is 100 km s^{-1} (assuming an inclination of 40° derived from a best fit of the velocity field). This implies a dynamical mass of 5 x 10^{10} $M_\odot$ within 22 kpc. The SDSS r_{90} value of 6.6″ gives a radius of 2.4 kpc, so the extent of the H I gas is about 9 times the extent of the perpendicular stellar disk. The inverse concentration index for SDSS galaxies, taken from the ratio of r_{50} to r_{90}, correlates tightly with morphological type (Shimasaku et al. 2001), and in our central, stellar galaxy is consistent with an exponential, rotationally supported disk.

Analysis of the optical spectra available from SDSS allows an approximate measure of the stellar mass in the central galaxy. The parameters are calculated by Yip et al. (2009,

in preparation) who utilizes the spectrum services provided by Dobos et al. (2006), and the stellar population model by Bruzual & Charlot (2003) to find a mass of 1.6 $\times$ 10^9 $M_\odot$ for the part of our galaxy falling within the 3″ fiber. This provides a lower limit for the stellar mass of the entire galaxy. Since this area is roughly half the optical extent of our tiny galaxy, we expect the total stellar mass to be twice that, roughly equal to the H I mass in the polar disk. This is similar to the polar disk simulated by Macciò et al. (2006) which had a baryonic mass in the polar ring of only a third the mass of the central S0 galaxy, and NGC 4650A which has twice the mass in gas and stars in its polar disk as in the central host galaxy (Iodice et al. 2002).

Our target was also observed by GALEX as part of its All Sky Survey (AIS), and serendipitously in the field of a guest observer 1619 s NUV exposure. Figure 2.3 overplots H I contours over the deep NUV image. The 19th magnitude UV emission follows the disk of the central optical galaxy, with no detection along the polar disk.

2.3.2 Large Scale Environment

Cosmologically, the galaxy is relatively isolated within a wall between two voids (Figure 2.4). A cursory look at 18 other polar ring galaxies taken from Whitmore et al. (1990) which are contained within the SDSS redshift survey finds them in average or slightly overdense environments (Platen, private communication). This is consistent with a photometric statistical study by Brocca et al. (1997) of the visible environments of 56 polar ring galaxies,

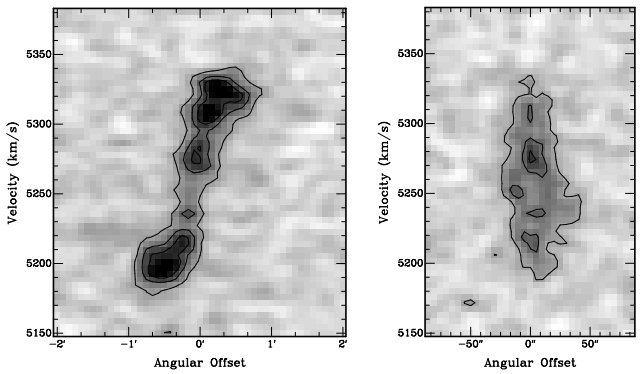

Figure 2.2: PV diagrams aligned with the polar disk (left) and central stellar disk (right). Note the central hole in the gas distribution in both slices. Contours in both images are at increments of 1.5 mJy beam^{-1} (3σ).

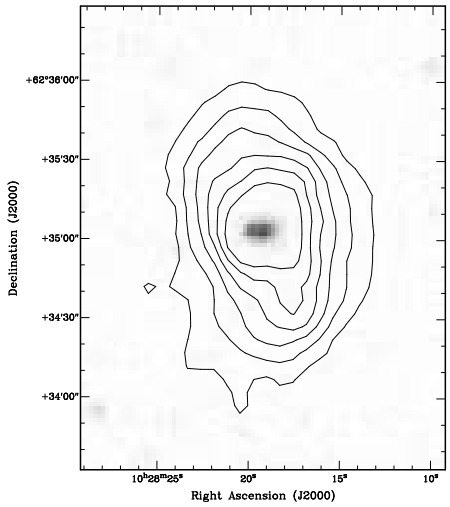

Figure 2.3: SDSS J102819.24+623502.6, galex NUV image overlaid with H I contours. H I contours are incremented as in Figure 2.1, NUV detection is 19.0 magnitude after 1619 second exposure.

which found them to be similar to normal galaxies.

The two voids and their dividing wall were identified with the closely related Watershed Void Finder (WVF, Platen et al. 2007) and Cosmic Spine formalism (Aragón-Calvo et al. 2010). The starting point is the Delaunay tessellation field estimator reconstructed density field inferred from the local SDSS galaxy distribution (Schaap & van de Weygaert 2000). The WVF identifies the voids and traces their spatial outline, the Cosmic Spine formalism recovers the wall forming the boundary between the two voids.

Following its identification, we determine the geometry, shape and orientation of the wall. These are inferred from the principal components of the covariance matrix $\mathcal{C}_{ij} = \mathrm{Var}(r_i r_j)$, computed on the basis of the 34 SDSS galaxies within a distance of 8.5 Mpc around the void galaxy. The wall's flattening is estimated from the ratio of its smallest eigenvalue, e_3, over the other two eigenvalues e_1 and e_2. The obtained thickness of the wall, ~ 1.3 Mpc, corresponds to a flattening of $\sim 96\%$.

Figure 2.4 shows the spatial distribution of the galaxies in and around the wall, with the nearest neighbor 4.7 Mpc away, and the boundary voids roughly 25 Mpc in radius. The size of the upper void is a lower limit as it continues past the edge of the SDSS survey area. These maps are created using galaxy redshifts from SDSS DR6, which is limited to

galaxies with $r < 17.77$ magnitudes and $55''$ separation from any neighbors. The polar disk is at an angle of $\sim 25°$ from the normal of the wall, and the central stellar disk is similarly misaligned $\sim 25°$ away from the plane of the wall. Roughly, however, the polar disk appears more perpendicular to the wall than aligned.

2.4 Discussion

With our data we can probe in H I an area of 650 kpc $\times$ 650 kpc on the plane of the sky surrounding SDSS J102819.24+623502.6, with a velocity range from 4232 km s^{-1} to 6196 km s^{-1}. Despite the significant volume probed, no companions are detected above the 2.0 $\times$ 10^8 M$_\odot$ limit in H I. Down to the SDSS limits, the neighborhood surrounding our lonely galaxy is empty within 3.5 Mpc. This environmental isolation makes it unlikely that the substantial 3 $\times$ 10^9 M$_\odot$ of neutral hydrogen we detect was accreted through a merger or close encounter, and we propose cold accretion as the most likely mechanism (Binney

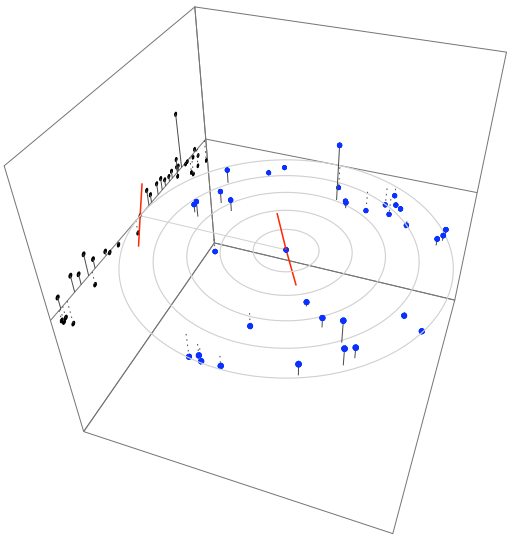

Figure 2.4: The location and orientation of the polar disk within the wall, between the two voids. The full volume of the sphere with galaxies brighter than $m_g = 17.76$ out to 10 Mpc has been plotted, with concentric circles every 2 Mpc in the plane of the wall. This demonstrates the loneliness of our galaxy and the emptiness of the bounding voids. An edge-on view is projected on the left, showing the thinness of the wall. The red line indicates the position and orientation of the projected major axis of the H I disk.

1977; Kereš et al. 2005; Dekel & Birnboim 2006).

Furthermore, satellite mergers are generally accompanied by a burst of star formation and the addition of existing stars to the system, neither of which are seen. We do see NUV emission in the stellar disk (Figure 2.3), indicating star formation occurred there within the recent past, however the lack of UV or optical emission in the polar disk is convincing. Perhaps we are observing this system in the earliest stage of its development, where the slowly accreted gas has not yet cooled sufficiently to begin forming stars. The measured column density never passes above the 10^{21} cm^{-2} surface density threshold proposed by Skillman (1987) even without correcting for inclination, leading us to expect little to no star formation in our extended disk.

Slow accretion has been proposed as a formation mechanism for the optically discovered, H I rich polar disk galaxy NGC 4650A (Iodice et al. 2006). While tidal accretion simulations by Bournaud & Combes (2003) can reproduce massive, gas-rich and star-poor polar rings, Bournaud et al. (2005) note that such a encounters would convert the central galaxy into an elliptical remnant, and not the rotationally supported disk found in NGC 4650A and suggested in our system. Cold flow accretion as a formation mechanism of polar disks has also been "observed" serendipitously in two simulations. Macciò et al. (2006) discovered a polar disk galaxy that formed in their simulation area through the infall of cold gas along a 1 Mpc long filament. Brook et al. (2008) found that their cosmological simulation contained a polar disk galaxy that was stable over timescales of 3-5 Gyr. In both cases, comparisons of the simulated galaxies with observations produce amazing optical and dynamical similarities.

The orientation of the central stellar disk $\sim 25^\circ$ from the wall is surprising. Recent observational and simulation results (Trujillo et al. 2006; Brunino et al. 2007; Aragón-Calvo et al. 2007; Hahn et al. 2007) show that disk galaxies statistically align their spin axis to lie within the wall they are embedded in. Such an alignment would then naturally lend itself to accretion of material within the plane of the wall, forming a polar disk. This, however, is not what we see, and instead the accreted material appears to be falling in out of the voids.

What we may witness reflects the process of a hierarchically evolving void population (Sheth & van de Weygaert 2004). As voids expand and evacuate matter from their interior, they tend to merge with neighboring voids into ever larger underdensities. The heuris-

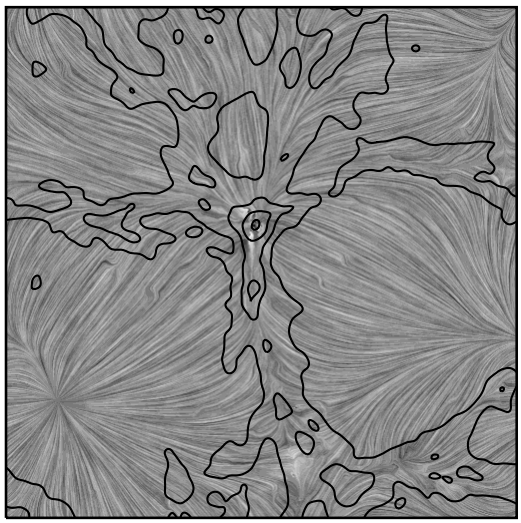

Figure 2.5: N-body simulation showing the flow lines of the cosmic velocity field, with density contours superimposed. Clearly visible is the flow out of the minima onto the wall-like boundaries, and then along these structures towards the high-density peaks.

tic simulation of Dubinski et al. (1993) illustrates how a group of spherical voids, embedded within a larger underdense area, expand until they meet. Once they touch, matter at the sheetlike boundaries of the voids starts to stream along these interstices towards the emerging higher density boundary surrounding the entire complex of merging voids (see Figure 2.5). As a result we observe the thinning and dissolution of the intervoid walls while they get gradually integrated in the emerging larger-scale void and remain visible as its tenuous interior substructure. The position of our galaxy within its wall is reminiscent of this situation, supporting the idea that the polar gas is not falling in from the wall, as that material is instead streaming away, but out of the bounding voids.

We have discovered completely by chance, as in simulations, a key example of polar disk formation in which accretion of cold gas is the most likely formation scenario.

Chapter 3

KK 246, a dwarf galaxy with extended H I disk in the local void

The following text will appear in the Astronomical Journal. The full reference for the published work is Kreckel, K., Peebles, P. J. E., van Gorkom, J. H., van de Weygaert, R., & van der Hulst, J. M. 2011.

We have found that KK 246, the only confirmed galaxy located within the nearby Tully Void, is a dwarf galaxy with an extremely extended H I disk and signs of an H I cloud with anomalous velocity. It also exhibits clear misalignment between the kinematical major and minor axes, indicative of an oval distortion, and a general misalignment between the H I and optical major axes. We measure a H I mass of $(1.05 \pm 0.08) \times 10^8$ $M_\odot$, and a H I extent 5 times that of the stellar disk, one of the most extended H I disks known. We estimate a dynamical mass of 4.1×10^9 $M_\odot$, making this also one of the darkest galaxies known, with a mass-to-light ratio of 89. The relative isolation and extreme underdense environment make this an interesting case for examining the role of gas accretion in galaxy evolution.

3.1 Introduction

The lowest-density environments, voids (Einasto et al. 1980; Kirshner et al. 1981), provide an interesting location to study the gas content and accretion history of galaxies (van de Weygaert & Platen 2009). Despite their underdense environment, galaxies in voids are

bluer with more ongoing star formation than field galaxies (Rojas et al. 2004, 2005; Park et al. 2007; von Benda-Beckmann & Müller 2008). In H I, they are typically late type and gas rich (Szomoru et al. 1996, Chapters 4 & 5 of this thesis). As they appear to reside in a generally more youthful state, diffuse gas accretion may still be a dominant process affecting void galaxies in low mass halos. Kereš et al. (2005) specifically predict cold mode accretion to dominate in low-density environments.

KK 246, also referred to as ESO 461-036, is a dwarf irregular galaxy residing a few Mpc within the Tully Void, an extremely large void at least 23 Mpc in radius (Tully et al. 2008). It is extremely isolated, with no companion galaxies discovered within 3 Mpc either optically (Karachentsev et al. 2004) or in neutral hydrogen (HIPASS, Wong et al. 2006). Its $M_{H\ I}/L_B$ ratio does not distinguish it from other dwarf irregular galaxies (Karachentsev et al. 2006). It is the only confirmed galaxy to reside in the Local Void, and one of only 16 galaxies tentatively identified to reside in this enormous volume (Nasonova & Karachentsev 2011), presenting a challenge to ΛCDM, which overpopulates the voids (Peebles 2001; Tinker & Conroy 2009; Tikhonov & Klypin 2009).

This galaxy was targeted as part of the Faint Irregular Galaxies GMRT Survey (FIGGS, Begum et al. 2008), where GMRT H I imaging shows disk-like rotation and the suggestion of a huge warp at the faintest contours. However, as the galaxy fell at the edge of the observing band, imaging did not include the full velocity range of this galaxy. We have imaged KK 246 at the VLA and EVLA with high sensitivity and discovered it to have an extremely extended H I disk as well as possible signs of ongoing gas accretion. In Section 3.2 we describe the observations and in Section 3.3 we discuss the results. In Section 3.4 we discuss the implications and in Section 3.5 we present our conclusions.

3.2 Observations

As our target is at low declination, it was first observed at the VLA in CnB array during spring 2009. These observations were centered at slightly higher frequencies to avoid the effects of aliasing in the lower 0.5 MHz of the bandpass by the VLA correlator on the EVLA antennas, and our target is well contained within the remaining unaffected 2.625 MHz bandwidth. A correlator problem with antenna 12, which was needed for the shortest baseline, led to extended and irregular sidelobes and poor sensitivity to extended emission.

We supplemented these data in summer 2010 with EVLA observations in D array. Observing parameters for both array configurations are listed in Table 3.1. The D array observations were made at a lower velocity resolution, but the data were resampled to match the velocity distribution of the CnB observations so the two data sets could be combined in the UV plane. Continuum emission was removed by interpolating from the line free channels in the UV plane. Images were made with natural weighting and a 30 arcsecond UV taper to achieve the highest sensitivity. After Hanning smoothing we have a velocity resolution of 10.3 km s^{-1}; the spatial resolution is $47'' \times 33''$. Using the Clean algorithm, we constructed an image cube where we cleaned down to 0.4 mJy $beam^{-1}$ (1σ) using a clean box around the emission in each channel. Total intensity and intensity weighted velocity field maps were constructed with a smoothing mask of 30 km s^{-1}, $60''$, and a 2.5σ cutoff. The calibration of the VLA data was done in AIPS, and the calibration of the EVLA data was done in CASA. Both data sets were combined, cleaned and imaged in CASA.

Table 3.1: Parameters of the VLA, EVLA and combined observations

Quantity	**VLA**	**EVLA**	**Combined**
Configuration	CnB	D	...
Date	May/June 2009	July 2010	...
No. telescopes	25	19	...
Exposure time (h)	18	2.5	...
Total bandwidth (MHz)	3.1	4	3.1
Channel width (kHz)	24.4	15.6	24.4
No. channels	128	256	128
Shortest spacing (m)	35	35	35
Longest spacing (km)	$\sim$10	1	10
FWHP primary beam (arcmin)	$\sim$32	$\sim$32	$\sim$32
Synthesized beam (arcsec $\times$ arcsec)	16 $\times$ 14	131 $\times$ 43	47 $\times$ 33
Noise per channel (mJy $beam^{-1}$)	0.5	1.7	0.4

3.3 Results

H I contours overlaid on the Second Palomar Observatory Sky Survey Digitized Sky Survey B-band image, the corresponding velocity field, and the velocity field overlaid on the HST ACS F606W image from the Hubble Legacy Archive are shown in Figure 3.1. Most apparent is the misalignment between the major axes of the H I and optical disks. This alignment is not quite a polar disk, exhibiting an angle of about 20° in the center and almost 55° at the largest extent of the H I disk.

We measure a total H I mass of $(1.05 \pm 0.08) \times 10^8$ $M_\odot$, assuming a distance of 7.83 Mpc (Karachentsev et al. 2004), and a total flux of 7.3 Jy km s^{-1} (Table 3.2). This is consistent with the HIPASS observations of 7.5 Jy km s^{-1} (Doyle et al. 2005). Karachentsev et al. (2004) measured an absolute B-band magnitude of -12.96 assuming a distance of 5.6 Mpc, however with a revised distance measured using the tip of the red giant branch of 7.83 Mpc (Karachentsev et al. 2006) this becomes -13.69 magnitudes, and gives a H I mass to light ratio of $M_{H\ I}/L_B = 2.32$.

The H I velocity field exhibits a noticeable misalignment of the kinematic major and minor axes (Figure 3.1, right panel). This signature could be caused by departure from

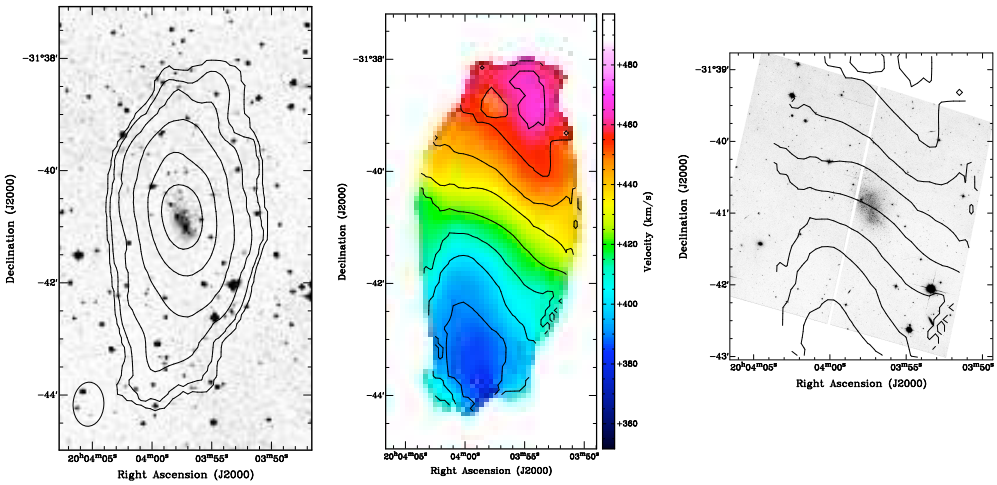

Figure 3.1: Left: KK 246, B-band Second Palomar Observatory Sky Survey Digitized Sky Survey image, overlaid with H I contours. The column density contours are $2(1.8\sigma), 4, 8, 16, 32 \times 10^{19}$ cm^{-2}. Center: the velocity field, with increments of 10.3 km s^{-1} marked. Right: HST ACS F606W image from the Hubble Legacy Archive overlaid with the velocity field.

axisymmetry in the mass distribution, such as an oval distortion and is indicative of a bar instability that may drive gas inflow (Bosma 1981). A position velocity slice along the kinematic disk major axis (position angle $-10°$ degrees) shows regular disk rotation with a flat rotation curve (Figure 3.2, top panel). Apparent in the velocity field is a spot on the northeast edge of the disk with an anomalously low velocity compared with regular disk rotation. A position velocity slice from the disk center through this position (Figure 3.2, bottom panel) shows a faint, 2.5 σ feature that is extended in both position and velocity. Careful examination of the H I channel maps (Figure 3.3) reveals that the emission (indicated in red) persists over 20 km s^{-1} in three separate channels. Any emission in channels at higher velocities is masked by emission from the bulk of the disk gas.

The H I disk at its lowest column density contours is quite irregular and somewhat asymmetric. A tilted ring fit was made to the velocity field using the GIPSY task ROTCUR.

Table 3.2: Optical and H I Parameters

Parameter	**Value**	**Reference**
R.A. (J2000)	20 03 57.4	Lauberts (1982)
Dec (J2000)	-31 40 53	Lauberts (1982)
Dist (Mpc)	7.83	Karachentsev et al. (2006)
R_{Ho} (arcmin)	0.6	Karachentsev et al. (2004)
m_B (mag)	17.06	Lauberts & Valentijn (1989)
B-band extinction (mag)	1.28	Karachentsev et al. (2004)
M_B (mag)	-13.69	...
L_B ($L_\odot$)	4.6×10^7	...
Total H I flux (Jy km s^{-1})	7.3	this work
Total H I mass ($M_\odot$)	$(1.05 \pm 0.08) \times 10^8$	this work
$R_{H\ I}$ (arcmin)	3	this work
W_{20} (km s^{-1})	93	this work
M_{dyn} ($M_\odot$)	4.1×10^9	this work
$M_{H\ I}/L_B$	2.3	this work
$R_{H\ I}/R_{Ho}$	5	this work
M_{dyn}/L_B	89	this work

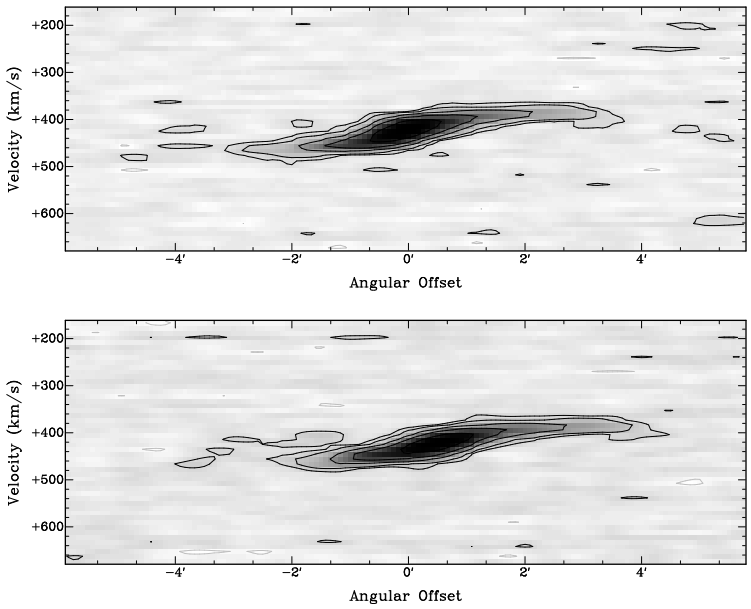

Figure 3.2: Position-velocity diagrams, aligned with the major axis (top) and anomalous gas (bottom). Contours are at -1, 1 (2.5σ), 2, 5, 10, and 20 mJy beam^{-1}.

Resulting fit parameters are shown in Figure 3.4, however because of the signs of radial streaming motions within the disk the physical implications of the derived position angles and inclinations are unclear. If we allow for radial motions within the rings, they are best fit by including inward velocities of $\sim$5 - 10 km s^{-1}, consistent with streaming motions seen in other disk galaxies (Gentile et al. 2007). From the global velocity profile, we measure a 20% H I line width of $W_{20} = 93$ km s^{-1}. Correcting for inclination, at an average inclination angle of 65°, we find a half-line width $W_{20,i}/2 = 51$ km s^{-1}. The orientation parameters from the rotation curve analysis were then applied to the total intensity map to calculate the H I surface density profile, corrected to face-on, which is perfectly exponential in the central disk but somewhat shallower at the furthest extent (Figure 3.5). H I can be reliably detected to a radius of 3′ (6.8 kpc at the assumed distance), where the H I face-on column density corresponds to $2 \times 10^{19}\ cm^{-2}$. Enclosed within this radius we measure a total dynamical mass of 4.1×10^9 M$_\odot$. Using the Holmberg diameter $D_{Ho} = 1.2'$(Karachentsev et al. 2004) we find a H I to optical diameter of $D_{H\ I}/D_{Ho} = 5$. Careful inspection of the data suggests that low column density gas continues to extend to the north, and no sharp edge is seen in a slice in the intensity map profile (Figure 3.6). This emission is not at the position of the anomalous gas cloud, but is on the same northern side of the disk.

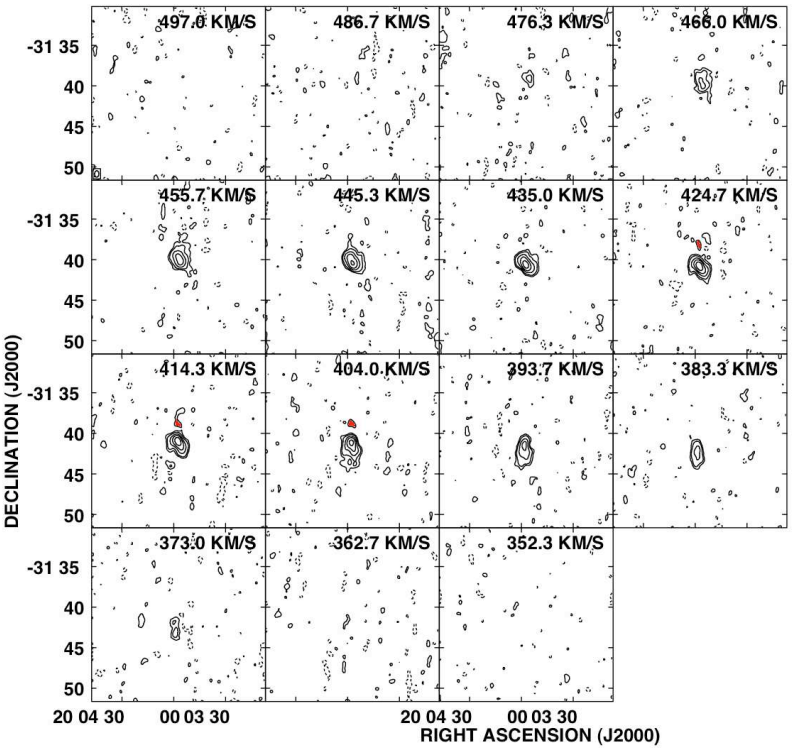

Figure 3.3: H I channel maps. Contours are -1, 1 (2.5σ), 2, 5, 10, and 20 mJy beam^{-1}. The synthesized beam is in the lower left corner of the top left image. The anomalous gas clump can be seen in three channels and is shaded in red.

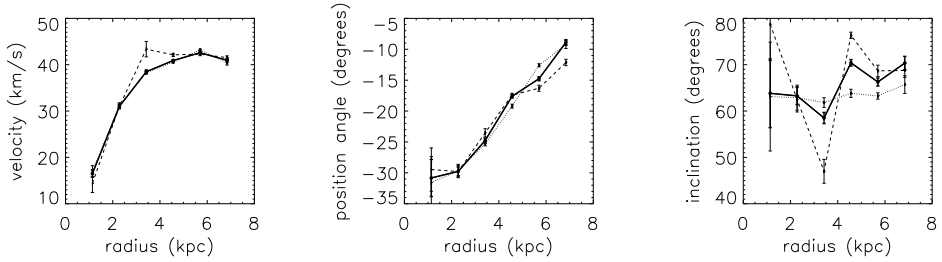

Figure 3.4: Tilted ring fit parameters, calculated using ROTCUR, for the velocity (left), position angle (center) and inclination (right) as a function of radius. Values calculated for the whole disk are shown with a solid line. The approaching side (dotted line) and the receding side (dashed line) calculated separately are also shown.

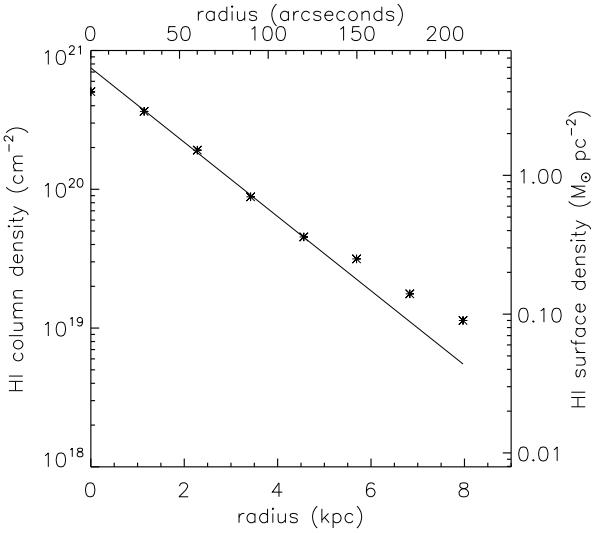

Figure 3.5: Surface density profile using output from ROTCUR in ELLINT. Values are corrected for face-on, and the last point is fairly low confidence. The line shows an exponential fit to the inner disk surface density.

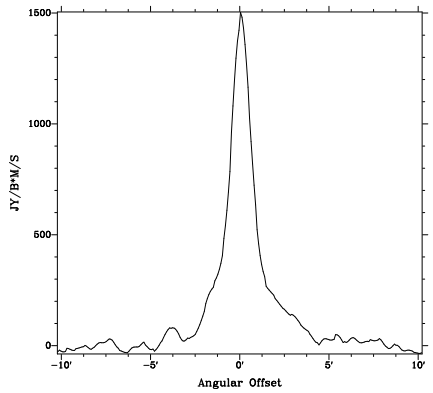

Figure 3.6: Intensity map profile along a position angle of -10°, roughly the H I major axis at the furthest extent of the disk. There is no sharp edge to the disk to the north (right) like we see to the south (left). Compare with Carignan & Purton 1998 Figure 4.

3.4 Discussion

KK 246 is not overly H I rich for its luminosity when compared with the other dwarf galaxies, but its H I disk is quite extended (Figure 3.7). It is similar in extent to other extremely extended H I disk galaxies in the literature (NGC 2915, Meurer et al. 1996; DDO 154, Carignan & Purton 1998; ESO 215-G?009, Warren et al. 2004), and the most extended H I

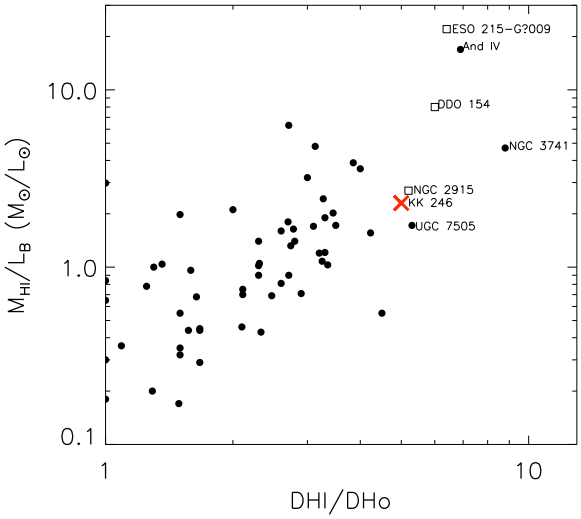

Figure 3.7: H I mass to B-band Luminosity as a function of the H I to optical diameter for the FIGGS sample (dots). KK 246 is marked by a cross, and it and other extended disks from the FIGGS sample are labeled. Also included are extended H I disks from the literature ESO 215-G?009 (Warren et al. 2004), DDO 154 (Carignan & Purton 1998), and NGC 2915 (Meurer et al. 1996).

disks in the FIGGS sample (And IV; NGC 3741, Begum et al. 2005; UGC 7505). From Figure 3.7 it is clear that while there is a general trend for more gas rich disks to be more extended compared to their stellar disk, as found by Begum et al. (2008) and van Zee et al. (1995), it is not necessary that extended H I disks be overly H I rich, or vice-versa. This suggests that some of these gas disks, like KK 246 and NGC 2915, may be somewhat more diffuse despite their relative size.

Most of these other extended H I galaxies are described as 'isolated' by the literature, and for comparison we look in detail at the environments of these galaxies within the Local Volume and around the Local Void (Figure 3.8). Karachentsev et al. (2004) has a catalog of local galaxies that is ∼80% complete to a limiting apparent magnitude of $m_b = 17.5$, roughly an absolute magnitude of -12 a distance of 8 Mpc, with the majority of the distances determined by Hubble flow-independent measures. We also take into account improved distances to some of the sample (Karachentsev et al. 2006). Except for UGC 7505, which is at 12 Mpc, and KK246, which is nearly at 8 Mpc but is well established to be within the Local Void (Tully et al. 2008), all are well within the boundaries of this catalog. The mean

nearest neighbor distance is about 400 kpc, and by this measure all of these galaxies are relatively isolated, none having a neighbor within 500 kpc. Here we include all neighbors that are brighter than a limiting magnitude of $m_B = 17.5$, approximately $M_B = -14.5$ at 8 Mpc. This is true for all galaxies, except NGC 3741, even when considering the distance to the sixth nearest neighbor. This suggests that a galaxy must be relatively undisturbed to develop and sustain such an extended H I disk. However there is no clear correlation with underdensity, as our void galaxy does not have the most extended disk. The polar disk galaxy recently discovered within a void is also found to have a strikingly extended H I disk, and in that case the lack of stars and substantial mass in the perpendicular component suggest that cold accretion is the most likely source of the polar gas disk (Chapter 2 of this thesis).

It is difficult to make direct comparisons between KK 246 and other void galaxies as its proximity makes it uniquely well resolved. KK 246 is significantly fainter than other void galaxies imaged in H I (Szomoru et al. 1996, Chapter 4 & 5 of this thesis), however it is roughly comparable to the 6 H I detected companion void galaxies in Chapter 5 of this thesis, which range from $-11 > M_r > -16$ and have H I masses of (5 - 30) $\times 10^7$ $M_\odot$. KK 246 is not particularly blue in color when compared with low luminosity SDSS galaxies, having

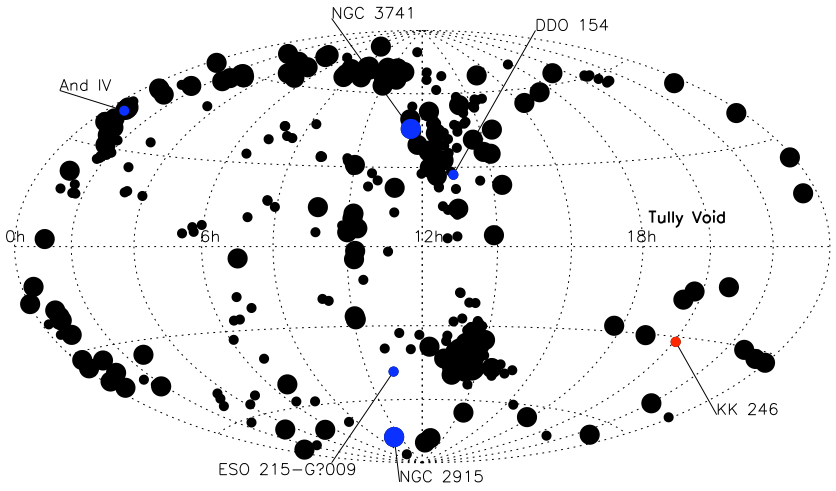

Figure 3.8: All-sky distribution of those galaxies brighter than m_B=17.5 within 4 Mpc (larger dots) and within 8 Mpc (smaller dots). The extended H I disk galaxies discussed in the text, as well as the Local Void, are marked accordingly.

B - R $\sim$ 1 (Lauberts & Valentijn 1989), but it is significantly redder than the companion void galaxies, which have $B - R \sim 0.6$. While these galaxies also do not have particularly extreme H I mass to light ratios, their H I extents and kinematics are largely unresolved and present an interesting population for higher resolution imaging.

Because the disk of KK 246 is so large, we are able to trace the flat rotation curve out to fairly large radii, and observe no decline at the outmost extent. Thus we measure a fairly high lower-limit for the total dynamical mass, and relatively large mass-to-light ratio of 89, making this one of the darker galaxies known (other examples are NGC 2915 and NGC 3741 with mass-to-light ratios of 76 and 107 respectively). An H-band study of local galaxies (Kirby et al. 2008) estimated a stellar mass of 5×10^7 $M_\odot$, approximately half the H I mass we report. Assuming a total gas mass of 1.4 times the H I mass, we find an upper limit on the baryon fraction of 5%, substantially lower than the expected cosmic baryon fraction of 17%, but in agreement with the finding that the lowest mass halos are 'missing' relatively more of their baryons (McGaugh et al. 2010). Simulations of dwarf galaxies in voids and filaments find strong suppression of star formation through photoheating by the UV background as a function of halo mass and independent of the galaxy environment (Hoeft et al. 2006; Hoeft & Gottlöber 2010), though for the inclination-corrected half-line width $W_{20,i}/2 = 51$ km s^{-1} we find that KK 246 is still relatively baryon poor compared to these predictions although in good agreement with the baryonic Tully-Fisher relation as extended to low-mass dwarf galaxies by Trachternach et al. (2009). Hoeft & Gottlöber (2010) in particular suggest that galaxies at the outskirts of voids, as KK 246 is, may be subject to additional photo-heating from nearby higher density regions and thus be relatively darker than galaxies in the void centers.

It is possible we are missing a diffuse, extended stellar component in the galaxy. High resolution ACS imaging shows KK 246 to be optically quite irregular, with no clear nucleus or disk structure (Figure 3.1, right panel). Perhaps the main stellar component we see is a bar for an extremely low surface brightness stellar disk. This would explain some of the anomalous disk kinematics we see, particularly the misalignment between the major and minor kinematic axes, which can be driven by a bar instability and is typically a sign of gas inflow or outflow. However, the H I is inclined to nearly edge-on and we see no diffuse stellar features along the H I disk (Figure 3.1, left), and the galaxy is not particularly underluminous for the H I we observe (Figure 3.7). This suggests that the kinematic misalignment

may be a result of gas inflow without, necessarily, a driving bar. With such a small, dark matter dominated galaxy it is possible that the rotation of a triaxial dark matter halo could drive the irregular kinematics and large extent, similar to what is seen in NGC 2915 (Bureau et al. 1999), and sustain a long-lived sloshing of the neutral hydrogen disk that prevents settling to form stars in the disk outskirts.

In general, there is an apparent misalignment between the major axis of the H I and stellar disks, so perhaps the irregular gas disk kinematics is indicative of a large scale warp. Roškar et al. (2010) simulated a persistent extended warp in a disk galaxy, and found that a relatively minor merger was able to misalign the stellar disk from the extended hot gas halo, but any subsequently accreted cold gas was torqued into alignment with the original orientation, along the hot halo. They find their warps are destroyed when the influx of fresh gas is cut off, or when the central stellar disk grows to occupy the region of the warp. The void environment may be ideal for retarding both these mechanisms, thus allowing the persistence of large extended warped disks.

The anomalous H I cloud we observe is similar to, but less significant than, the H I 'beard' observed in NGC 2403, which is believed to result from H I gas located above the plane of the galaxy that is rotating more slowly (Fraternali et al. 2002). In KK 246, the anomalous gas is at 'forbidden' velocities, inconsistent with the full disk rotation. We estimate an upper limit on the H I mass of 2×10^6 $M_\odot$. This is consistent with the mass estimate for high velocity clouds around the Milky Way Galaxy (van Woerden et al. 1999), and presents a similar situation to the high velocity clouds found around NGC 2403 and M33 that provide the best observational evidence of ongoing gas accretion onto galaxies (Sancisi et al. 2008). As the cloud in KK 246 is clearly far removed from the small stellar component at the center of the galaxy, it seems that its origin from galactic fountain effects is unlikely. In addition, the inner disk is perfectly exponential, but the decrease in surface density at the edge is not as sharp (Figure 3.5), which combined with the trailing faint H I emission to the north of the galaxy (Figure 3.6) is suggestive of additional ongoing gas accretion.

3.5 Conclusions

We have observed in detail the H I disk of KK 246, the only confirmed galaxy in the Local Void, and found that it is extremely extended and shows signs of an anomalous gas cloud within the disk. In addition, there is a clear misalignment between the major axis of the H I and stellar disks, and there are kinematic signs of an oval distortion in the H I disk, suggestive of gas inflow in the central region. We measure a total H I mass of $(1.05 \pm 0.08) \times 10^8$ $M_\odot$, and a H I extent of 5 times the optical Holmberg diameter, one of the most extended H I disks known. The rotation curve is flat to the edge of the H I disk, and we calculate a dynamical mass of 4.1×10^9 $M_\odot$. Thus it is also one of the darkest galaxies known, with a mass-to-light ratio of 89.

When compared with other galaxies with extended H I disks, we find that relative isolation is a necessary, but not sufficient, condition for their existence. Alternatively, we find that these extended H I disks are not necessarily overly H I rich for their luminosity, as in the case of KK 246. This suggests that these systems are able to convert their gas into stars in a fairly typical manner, while retaining an extended diffuse gas disk. The anomalous kinematics of a small, $< 10^6$ $M_\odot$, component of the disk suggest that perhaps ongoing gas accretion is playing a role in maintaining this extended disk.

Part II

The Void Galaxy Survey

Chapter 4

Only the Lonely: H I Imaging of Void Galaxies

The following text has been published in the Astronomical Journal. The full reference for the published work is Kreckel, K., Platen, E., Aragón-Calvo, M. A., van Gorkom, J. H., van de Weygaert, R., van der Hulst, Kovac, K., Yip, C.-W., J. M., & Peebles, P. J. E. 2011, AJ, 141, 4.

Void galaxies, residing within the deepest underdensities of the Cosmic Web, present an ideal population for the study of galaxy formation and evolution in an environment undisturbed by the complex processes modifying galaxies in clusters and groups, as well as provide an observational test for theories of cosmological structure formation. We have completed a pilot survey for the H I imaging aspects of a new Void Galaxy Survey (VGS), imaging 15 void galaxies in H I in local ($d < 100$ Mpc) voids. H I masses range from 3.5×10^8 to 3.8×10^9 $M_\odot$, with one nondetection with an upper limit of 2.1×10^8 $M_\odot$. Our galaxies were selected using a structural and geometric technique to produce a sample that is purely environmentally selected and uniformly represents the void galaxy population. In addition, we use a powerful new backend of the Westerbork Synthesis Radio Telescope that allows us to probe a large volume around each targeted galaxy, simultaneously providing an environmentally constrained sample of fore- and background control sample of galaxies while still resolving individual galaxy kinematics and detecting faint companions in H I. This small sample makes up a surprisingly interesting collection of perturbed and inter-

acting galaxies, all with small stellar disks. Four galaxies have significantly perturbed H I disks, five have previously unidentified companions at distances ranging from 50 to 200 kpc, two are in interacting systems, and one was found to have a polar H I disk. Our initial findings suggest void galaxies are a gas-rich, dynamic population which present evidence of ongoing gas accretion, major and minor interactions, and filamentary alignment despite the surrounding underdense environment.

4.1 Introduction

With the prevalence of ever wider and deeper redshift surveys, from the second Center for Astrophysics Redshift Survey (Huchra et al. 1983) to the Sloan Digital Sky Survey (SDSS, York et al. 2000), we have refined our ability to identify the elongated filaments, sheetlike walls and dense compact clusters that compose the Cosmic Web (Zel'Dovich 1970; Klypin & Shandarin 1983; de Lapparent et al. 1986; Bond et al. 1996; van de Weygaert & Bond 2008). These structures surround voids, enormous regions $10-30h^{-1}$ Mpc in diameter that are largely devoid of galaxies and occupy most of the volume of the Universe (Gregory & Thompson 1978; Einasto et al. 1980; Kirshner et al. 1981; de Lapparent et al. 1986; Hoyle & Vogeley 2004; for a recent review see van de Weygaert & Platen 2009). Within these underdense – but not empty – regions, large galaxy redshift surveys have allowed us to distinguish an environmentally defined population of void galaxies residing in regions up to 10 times less dense than the cosmic mean. Largely unaffected by the complexities and processes modifying galaxies in high-density environments, these isolated void regions are expected to hold important clues to understanding the environmental influences on galaxy formation and evolution (Szomoru et al. 1996; Grogin & Geller 2000; Corbin et al. 2005; Patiri et al. 2006b; Pustilnik et al. 2006; Wegner & Grogin 2008, Chapter 2 of this thesis). Additionally, the apparent underabundance of galaxies in the void regions may present a challenge for currently favored galaxy formation theories (Peebles 2001; Mathis & White 2002; Gottlöber et al. 2003; Furlanetto & Piran 2006; Tinker & Conroy 2009), while their distribution is expected to trace substructure within voids, tenuous features which are fossil remnants of the hierarchical buildup of the Cosmic Web (Dubinski et al. 1993; van de Weygaert & van Kampen 1993; Popescu et al. 1997; Sheth & van de Weygaert 2004; Patiri et al. 2006a; Tikhonov & Karachentsev 2006).

Void galaxies appear to have a more youthful state of star formation. As a population, void galaxies are statistically bluer, have a later morphological type, and have higher specific star formation rates than galaxies in average density environments (Grogin & Geller 1999, 2000; Rojas et al. 2004, 2005). Whether void galaxies are intrinsically different or whether their characteristics are simply due to the low mass bias of the galaxy luminosity function in low density regions is still an issue of discussion. Overall, the mean colors of the red and blue void galaxy populations, taken separately, are comparable to galaxies in average density environments at the same luminosity, though an excess of blue galaxies is apparent (Balogh et al. 2004; Patiri et al. 2006b). This suggests that in some respects the general underdensity of the environment has had little to no impact on their development, raising the question of to what extent the global (∼20 Mpc) as opposed to local (∼1 Mpc) environment shapes the formation and evolution of galaxies. Park et al. (2007) suggest that it is only the morphology and luminosity of void galaxies which is dependent on their environment, with all other statistical correlations stemming from these two key parameters. Interestingly, they and others find contradictory indications of a slight blueward shift of the blue cloud in voids at fixed luminosity (Blanton et al. 2005; von Benda-Beckmann & Müller 2008). No such shift has been found for the red sequence of early type galaxies.

Less is known about the gas content of void galaxies. Szomoru et al. (1996) surveyed galaxies within the Boötes void with pointed observations of 24 *IRAS* selected galaxies, of which 16 were detected. Most of these galaxies are found to be gas-rich and disk-like, with many gas-rich companions, however more complete redshift surveys show that many of the targeted galaxies reside in the outer realms of the void and with some reason might be identified with the moderate density environment of walls (Platen 2009, also see Section 4.5). Huchtmeier et al. (1997) find that dwarf galaxies in voids have a higher $M_{H\ I}/L_B$ ratio the deeper within the underdensity they reside. Because of the active star-forming nature of void galaxies, detailed H I observations are key to understanding the environmental differences observed.

The unique nature of void galaxies provides an ideal chance to distinguish the role of environment in gas accretion and galaxy evolution on an individual basis. Fresh gas accretion is necessary for galaxies to maintain star formation rates seen today without depleting their observed gas mass in less than a Hubble time (Larson 1972). Historically, this gas was assumed to condense out of reservoirs of hot gas existing in halos around

galaxies (Rees & Ostriker 1977; Silk 1977; White & Rees 1978; White & Frenk 1991), with some amount of gas recycling via galactic fountains (Fraternali & Binney 2008). However, recent simulations have renewed interest in the slow accretion of cold gas along filaments (Binney 1977; Kereš et al. 2005; Gao et al. 2005; Dekel & Birnboim 2006; Dekel et al. 2009). Void galaxies provide a unique sample of younger, star forming galaxies where their inherent isolation may allow us to distinguish the effects of close encounters and galaxy mergers from other mechanisms of gas accretion, and their constrained environment allows a search for systematic trends in neutral gas content and distribution with cosmological density.

Despite the remarkable success of ΛCDM cosmology in explaining the general cosmic matter distribution there are a few telling discrepancies, the most prominent of which concerns the over-prediction of low-mass halos within voids (Mathis & White 2002; Gottlöber et al. 2003; Furlanetto & Piran 2006; Peebles & Nusser 2010). The observed density of faint ($-18 < M_B < -12$) galaxies in voids is only 1/100th that of the mean (Kuhn et al. 1997; Karachentsev et al. 2004), in contrast to the predictions of high-resolution ΛCDM simulations that the density of low mass halos ($10^9 M_\odot < M < 10^{11} M_\odot$) should be 1/10th that of the cosmic mean (Warren et al. 2006; Hoeft et al. 2006). In addition, simulations predict that these low mass halos will trail into the voids, while in deep optical surveys we see that dwarf galaxies avoid the empty regions defined by the more luminous galaxies (Kuhn et al. 1997). This phenomenon has also been noted in blind H I surveys (Saintonge et al. 2008) and deep surveys of the local volume (Tikhonov & Klypin 2009), where in general most void galaxies are found at the edges of voids. Peebles (2001) has strongly emphasized that this dearth of dwarf and/or low surface brightness galaxies in voids cannot be straightforwardly understood in our standard view of galaxy formation.

There have been many solutions proposed which aim to limit galaxy formation within the least massive halos (Furlanetto & Piran 2006; Hoeft et al. 2006). Tinker & Conroy (2009) suggest that the void phenomenon might be understood if the properties of galaxies are solely dependent on the mass of the dark halos in which they live, independent of their environment, assuming a sufficiently tailored halo occupation distribution. However, it remains difficult to explain how the implied severe degrees of bias between high- and low-luminosity galaxies at the void boundaries can be reconciled with the observations of nearby voids: there are no indications for the predicted segregation of fainter galaxies being found further into the void interior (Vogeley, private communication). It is also revealing that

predictions for the galaxy distribution in void regions by different semi-analytical galaxy formation schemes, in the context of the Millennium simulation or other simulations (Mathis & White 2002; De Lucia et al. 2006; Bower et al. 2006), disagree with each other at a remarkably fundamental level (see e.g. Platen 2009). Ultimately, we will need a better understanding of the various gas, radiation and feedback processes, such as investigated by Hoeft et al. (2006). The issue remains far from solved, and progress will largely depend on new observations.

Within the context of hierarchical cosmological structure formation scenarios, voids are expected to exhibit a rich dark matter substructure which is a remnant of the hierarchical buildup of voids and provides additional constraints on theories of cosmological evolution (Regős & Geller 1991; van de Weygaert & van Kampen 1993; Sheth & van de Weygaert 2004; Colberg et al. 2005; Ceccarelli et al. 2006; Aragon-Calvo et al. 2010). The merging of expanding voids dilutes the intervening substructure to cause a cosmic flow away from the void centers and along walls and filaments (Dubinski et al. 1993; Sheth & van de Weygaert 2004). The extent to which the tenuous void substructure may also be recognized in the galaxy distribution is not yet fully settled, however there may be a link between the star formation activity of void galaxies and the influx of (coldly) accreting matter transported along dark matter filaments (Zitrin et al. 2009; Park & Lee 2009b, a). Some observational studies claim to recognize patterns in the void galaxy distribution (Popescu et al. 1997; Szomoru et al. 1996; Platen 2009). Moreover, there are indications that the clustering of galaxies in voids appears to be of comparable strength to that of galaxies in average density environments (Szomoru et al. 1996), possibly related to the strong clustering of voids and their primordial precursors (Abbas & Sheth 2007).

We have undertaken a new multi-wavelength Void Galaxy Survey (VGS) of $\sim$60 geometrically selected void galaxies. In this project we intend to study in detail the gas content, star formation history and stellar content, as well as the kinematics and dynamics of void galaxies and their companions in a broad sample of void environments. Each of the galaxies has been selected from the deepest interior regions of identified voids in the SDSS redshift survey on the basis of a unique geometric technique, described in Section 4.2, with no a priori selection on intrinsic properties of the void galaxies (ie. luminosity or color).

We present here the results of a pilot study, observing 15 void galaxies in H I at the Westerbork Synthesis Radio Telescope (WSRT). Our selection procedure for this pilot sample

and for the full VGS are explained in Section 4.2. Our observations, detailed in Section 4.3, have sufficient sensitivity and resolution to allow us to map the gas distribution and kinematics for each of our target galaxies. In addition, the large field of view and wide redshift range allows a simultaneous detection of faint nearby companions, as well as background galaxies residing in higher density regions. This allows a very accurate determination of the local environment and direct evidence of gas interactions. A detailed presentation of the results is given in Section 4.4. An extensive analysis of the void galaxy properties is the subject of Section 4.5. A discussion of our preliminary findings and speculations as to their implications are to be found in Section 4.6, with conclusions presented in Section 4.7. Throughout the paper we have assumed $H_o = 70\ \mathrm{km\,s^{-1}\ Mpc^{-1}}$, except where noted.

4.2 Sample Selection

Voids are the (mostly) empty regions between the filaments, walls and clusters in the Cosmic Web. While these large underdense regions represent one of the most prominent aspects of the cosmic matter distribution, there is no unanimity with respect to their definition. Unlike e.g. clusters of galaxies, voids are not well-defined physical objects. Instead, they are the regions surrounding the minima in the cosmic matter and galaxy distribution. Different opinions exist on their extent and boundary, the medium with respect to which they should be identified, and the practical implementation of such definitions to the galaxy distribution. As a result, there is a large variety of void finding formalisms. Some refer to the galaxy distribution, while others use the dark matter density field. Some identify isolated spherical voids, while others attempt to reconstruct the nontrivial void shapes and geometries by means of overlapping spheres or cubes. While all methods can generally identify an underdense volume, they differ significantly in identifying the location of the edge of the void. A telling illustration of this can be found in the overview and quantitative comparison of various void finding algorithms by Colberg et al. (2008).

The challenge for studies of voids is therefore to identify them in an unbiased and cleanly defined manner. For our purpose it is of key importance that we make no a priori assumptions about the scale and shape of voids, and that we find voids entirely independent of the intrinsic properties of galaxies. To this end, we invoke a unique geometric void finding algorithm. It is purely based on the local spatial structure of the galaxy distribution and

guarantees the definition of an unbiased sample of void galaxies.

4.2.1 Geometric Void Identification

Our galaxy sample is defined on the basis of the optical SDSS redshift survey, which covers over 10,000 square degrees and catalogs redshifts for over 900,000 galaxies brighter than 17.77 Petrosian magnitudes in the r-band and more than $55''$ away from any other cataloged galaxy. The pilot program void galaxies were selected from the SDSS Data Release 3 (DR3), while the full Void Galaxy Survey uses the complete DR7.

The first step in detecting void galaxies is outlining the voids in the survey volume. It is important for our purpose that we follow a strictly geometric procedure. This involves the reconstruction of the density field from the spatial galaxy distribution, followed by the identification of void regions within the spatial density field. Finally, we search for the SDSS galaxies which lie within the interior of the identified voids.

4.2.1.1 The DTFE density field

For the density field reconstruction we use the DTFE procedure, the Delaunay Tessellation Field Estimator (Schaap & van de Weygaert 2000; Schaap 2007; van de Weygaert & Schaap 2009). This technique translates the spatial distribution of the galaxies in the SDSS, in a volume from $z = 0.003$ to $z = 0.03$, into a continuous density field. In addition to the computational efficiency of the procedure, the density maps produced by DTFE have the virtue of retaining the anisotropic and hierarchical structures which are so characteristic of the Cosmic Web (Schaap 2007; van de Weygaert & Schaap 2009). The recent in-depth analysis by Platen et al. (2010) has shown that for very large point samples, the DTFE even outperforms more elaborate high-order methods with respect to quantitative and statistical evaluations of the density field. As a result, the DTFE density field is highly suited for objectively tracing structural features such as walls, filaments and voids.

The DTFE procedure involves four steps. The first step is the definition of the galaxy sample and corresponding survey volume. The subsequent step consists of the computation of the Delaunay tessellation defined by the spatial galaxy distribution. DTFE exploits the adaptivity of this tessellation to the local density and geometry of the generating spatial point process. The third step involves the local density estimate at each of the sample galaxies' positions. This is based on the volume of the contiguous Voronoi cell, the volume

defined by all Delaunay tetrahedra to which a given sample galaxy belongs. In the final step, these local density values form the basis for a piecewise linear interpolation within the volume of each Delaunay tetrahedron. In this, the Delaunay Tessellation Field Estimator is the multidimensional equivalent of simple piecewise one-dimensional linear interpolation from an irregularly distributed set of points which uses the Delaunay triangulation as an adaptive and irregular interpolation grid.

The resulting product of the DTFE procedure is a volume-covering continuous density field. For a an extensive description of the full DTFE procedure we refer to van de Weygaert & Schaap (2009). Below we shortly describe the key steps of the DTFE machinery.

SDSS DR3 sample

The SDSS DR3 galaxy sample is a *magnitude* limited sample, consisting of galaxies brighter than $m_r = 17.77$. For our density field determination we take all sampled information, which makes it necessary to correct for the inhomogeneous selection process. By default, we assume that all galaxies - independent of their luminosity - are a fair tracer of the underlying galaxy density field.

Following this assumption, we correct for the dilution as a function of survey depth by weighing each sample galaxy by the reciprocal $w(z)$ of the radial selection function $\psi(z)$ at the distance of the galaxy. For the SDSS, the selection function $\psi(z)$ as a function of redshift z is well fitted by the expression forwarded by Efstathiou & Moody (2001)

$$\psi(z) \,=\, \exp\left\{-\left(\frac{z}{z_r}\right)^{\beta}\right\}\,, \tag{4.1}$$

where z_r is the characteristic redshift of the distribution and β specifies the steepness of the curve.

Delaunay Tessellation

The **Delaunay Tessellation** of the galaxy distribution divides up the sample volume in a unique volume-covering tiling of tetrahedra. Each of these Delaunay tetrahedra is defined by a set of four galaxies in such a way that their circumscribing spheres does not contain any of the other galaxies of the generating galaxy sample (Delaunay 1934). For practical purposes, we assume *vacuum boundary conditions*: outside the SDSS galaxy sample volume we take the minimal assumption of having no galaxies. For its efficient computation we use

the CGAL library [1].

DTFE Density Estimate

The DTFE density value estimate at the location of each galaxy is taken to be inversely proportional to the volume of the *contiguous Voronoi cell*, i.e. the region defined by all Delaunay tetrahedra of which a given galaxy is a vertex. For a sample galaxy i, we identify all N_i neighboring Delaunay tetrahedra $\mathcal{T}_j$, which together constitute the contiguous Voronoi cell $\mathcal{W}_i \cup_j \mathcal{T}_j$. Summation of the individual tetrahedral volumes $V(\mathcal{T}_j)$ yields the volume of the contiguous Voronoi cell,

$$V(\mathcal{W}_i) \,=\, \sum_{j=1}^{N_i} V(\mathcal{T}_j)\,. \tag{4.2}$$

The resulting DTFE estimate $\widehat{f}_i$ of the density field at sample point i is

$$\widehat{f}_i \,=\, \frac{4\,w(z_i)}{V(\mathcal{W}_i)}\,. \tag{4.3}$$

where the weight $w(z_i)$ is the sample selection weight at the galaxies' redshift z_i. Note that the factor of four takes account of the fact that in three dimensions each sample point belongs to four tetrahedra. In practice, the density of all galaxies is calculated by looping in sequence over all Delaunay tetrahedra.

DTFE Density Field Interpolation

DTFE uses the adaptive and minimum triangulation properties of Delaunay tessellations to use the tessellations as adaptive spatial interpolation intervals for irregular point distributions (Bernardeau & van de Weygaert 1996). By doing so, the DTFE generalizes the concept of a natural interpolation interval to any dimension D.

Once the Delaunay tessellation has been constructed, and the densities at each sample point determined, the DTFE determines the density gradient within each Delaunay tetrahedron $\mathcal{T}_j$. The gradient can be directly inferred from the density values at its four vertices, i.e. at the location of the four sample galaxies defining the tetrahedron.

Following the determination of the density gradients in all Delaunay tetrahedra, the DTFE density value at any point $\widehat{\mathbf{r}}$ within the sample volume can be calculated by determining in which tetrahedron it is located and subsequently computing its density estimate from the simple linear interpolation equation. To obtain an image of the density field, the density is calculated at each of the voxel locations of the image grid.

[1] CGAL is a `C++` library of algorithms and data structures for Computational Geometry, see `www.cgal.org`

4.2.1.2 The Watershed Void Finder

The Watershed Void Finder (WVF, Platen et al. 2007) is applied to the DTFE density field for identifying its underdense void basins. The WVF is an implementation of the *Watershed Transform* for segmentation of images of the galaxy and matter distribution into distinct regions and objects and the subsequent identification of voids.

The basic idea behind the watershed transform finds its origin in geophysics. It delineates the boundaries of the separate domains, the *basins*, into which yields of e.g. rainfall will collect. The analogy with the cosmological context is straightforward. By equating the cosmic density field to a landscape, the WVF identifies the valleys with *cosmic voids*. They are separated from each other by boundaries consisting of the *walls* and *filaments* in the Cosmic Web. These are identified with the related Spine formalism (Aragón-Calvo et al. 2010).

The WVF consists of eight steps, which are extensively outlined in Platen et al. (2007). For the success of the WVF it is of the utmost importance that the density field retains its topology. To this end, the two essential first steps relate directly to DTFE, which guarantees the correct representation of the hierarchical nature, the weblike morphology dominated by filaments and walls, and the presence of voids (van de Weygaert & Schaap 2009). Because in and around low-density void regions the raw density field is characterized by a relatively high level of noise, a second essential step suppresses the noise using a $\mathrm{R}_f = 1\ h^{-1}$ Mpc Gaussian filter. The subsequent central step of the WVF formalism consists of the application of the discrete watershed transform on this filtered density field. Thus providing us with a set of voids. Analysis of mock catalogs show that a choice of $\mathrm{R}_f = 1\ h^{-1}$ Mpc recovers the majority of small scale voids, and within distances of $100\ h^{-1}$ Mpc errors are dominated by the inherent limitations of the observational redshift survey (Platen 2009).

Unlike most void finders, the WVF has the advantage of having no a priori assumptions about scale and shape of voids (see Colberg et al. 2008, for a comparison of different algorithms). Instead, these are completely determined by the topological structure of the cosmic density field. Because it identifies a void segment on the basis of the crests in a density field surrounding a density minimum, it is able to trace the void boundary even though it has a distorted and twisted shape. Also, because the contours around well chosen minima are by definition closed, the transform is not sensitive to local protrusions between

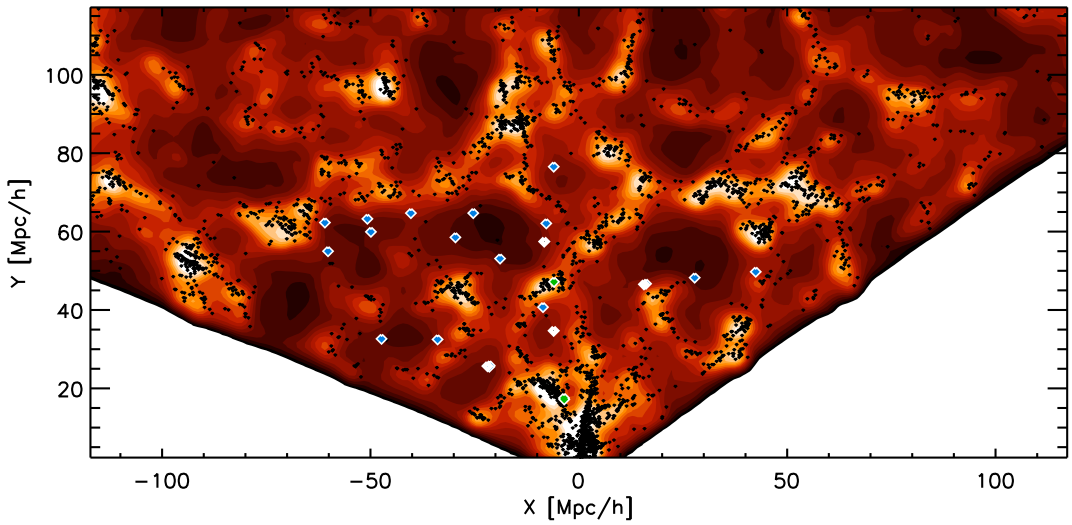

Figure 4.1: SDSS density map and galaxies in the SDSS galaxy redshift survey region from which we selected the galaxies in the Void Galaxy Survey, in a slice of thickness $4h^{-1}$Mpc. The DTFE computed galaxy density map, Gaussian smoothed on a scale of $R_f = 1h^{-1}$Mpc, is represented by the colorscale map. The map runs from dark red, at lowest void densities, to beige, the average cosmic galaxy density. The SDSS galaxies are superimposed as dark dots. The pilot sample void galaxies are represented by white diamonds, while the blue diamonds indicate the position of void galaxies from the full Void Galaxy Survey. The green diamonds are control sample galaxies (see Section 4.4.5).

two adjacent voids.

A representative DTFE density map in a slice through the SDSS galaxy distribution is shown in Figure 4.1, with superimposed symbols indicating the original spatial distribution of galaxies and subsequently determined void galaxies.

4.2.2 Void Galaxy Selection

Upon having obtained the complete list of voids in the SDSS survey volume, and the spectroscopically targeted void galaxies within their realm, we evaluate for each of the galaxies whether it conforms to a set of additional criteria. The galaxy should be

- located in the interior central region of clearly defined voids, if possible near the center, and be as far removed from the boundary of the voids as possible.

- removed from the edge of the SDSS survey volume, as we do not wish to have galaxies in voids which extend past the edge of the SDSS coverage.
- not within ≈ 750km s^{-1} from a foreground or background cluster. This assures that the presence in a void of a galaxy can not be attributed to the Finger of God effect.
- preferably within a redshift $0.01 < z < 0.02$, allowing sufficient sensitivity and resolution in our observations of the gas structure and kinematics in the galaxies.

Other than the SDSS redshift survey limit of

$$M_r \;=\; 17.77 - 5\log_{10}\frac{cz}{H_o\ 10pc} \tag{4.4}$$

there is no selection on luminosity or color of the void galaxies in our sample, the selection is purely dictated by the local geometric structure of the Cosmic Web.

The spectroscopic selection criteria of the SDSS do exclude bright, nearby galaxies and omit some galaxies in particularly crowded fields, however these effects are not relevant to our sample. There is also a poorly constrained surface brightness selection in the SDSS main galaxy sample.

Apart from avoiding the Finger of God effect, note that redshift distortions due to cosmic large scale flows, and as a result of cluster infall, are not affecting our selection. These tend to amplify the density and contrast of filaments, sheets and cluster outskirts in redshift space, while leading to emptier voids: void galaxies detected in redshift space are therefore highly likely to also live in physical voids (cf. Kaiser 1987; Praton et al. 1997; Shandarin 2009).

Figure 4.2 illustrates our selection procedure for two cases. The locations of the void galaxy in the SDSS footprint (heavy dot, top right) are removed from the survey edge and each other. The DTFE density map in two mutually perpendicular slices intersecting at the galaxy location, along the line pointing radially towards the observer (bottom left and center), show their position centrally located in the deepest underdensities. To accentuate this, the images also contain a map of the spinal/watershed contours of the density field overlaid on top of the distance field in order to give an idea of the spatial structure of the surrounding large scale structure (top left). The distance field shows the minimum distance from the void edge, and is maximized at the void center. The locations of the SDSS DR3 galaxies within these thin slices are indicated by the diamond shaped points, while the

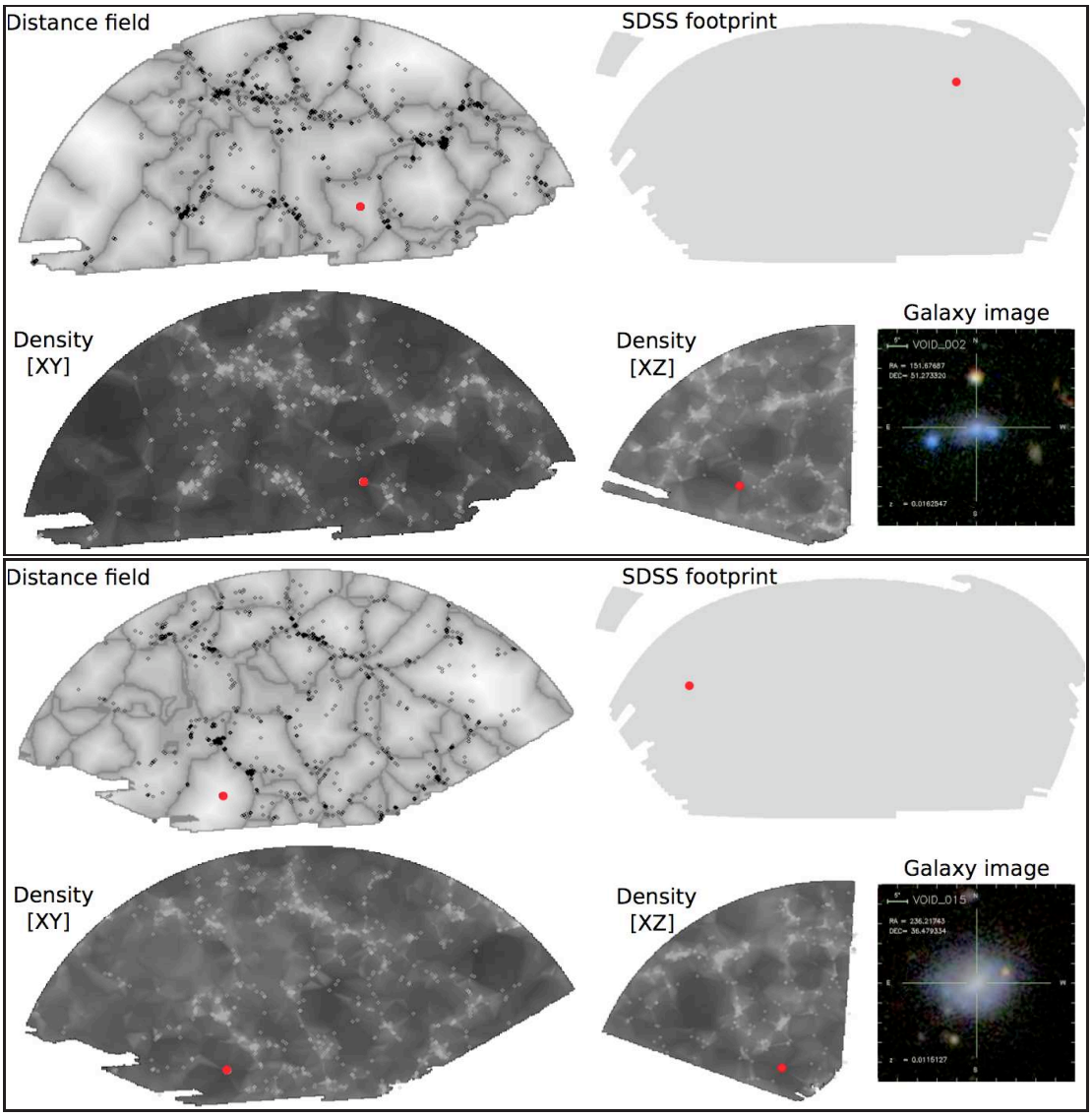

Figure 4.2: Two examples of selecting our galaxies by geometry from the SDSS using different visualizations of the density field. Top right panel: SDSS DR7 sky map footprint, with the void galaxy indicated by a heavy red dot, to show it is positioned away from the survey edge. Bottom right: galaxy image from SDSS database. Bottom left and center: DTFE density greyscale maps in two mutually perpendicular slices intersecting at the galaxy location. Top left: The SpineWeb/watershed contours of the density field are shown in dark gray on top of the distance field (described in Section 4.2.2) in gray scale. The locations of the SDSS DR3 galaxies within the thin density field and distance field slices are indicated by the diamond shaped points, while the heavy red dot represents the target galaxy located away from any walls or filaments and deep within the underdensity.

heavy dot represents the target galaxy. A small galaxy image from the SDSS database (bottom right) shows the optical appearance of our geometrically selected void galaxy.

4.2.3 Resulting Sample

In Figure 4.3 we present the SDSS color images of our 15 selected void galaxies, taken from the SDSS online Finding Chart tool (DR7, Abazajian et al. 2009). The images have been scaled to the same physical scale. The parameters for the target galaxies, extracted from the SDSS catalog, are given in Table 4.1 along with the program and SDSS names. In the remainder, we will mainly use the program name "VGS_α", unless otherwise stated. Likewise, the companion galaxies found in our program will receive a program name "VGS_αa", "VGS_αb", etc., where α is the number for the parent void galaxy.

To obtain an impression of the true thee-dimensional environment of the selected void galaxies, we have included a set of 3-D galaxy distribution visualizations around void galaxies VGS_12 (Figure 4.4) and VGS_58 (Figure 4.5). In a box of size 24 h^{-1} Mpc centered around each of these void galaxies, the structure of the surrounding galaxy distribution is depicted from the three different perspectives. In these panels, bright galaxies have large

Table 4.1: Parameters of selected void galaxies taken from the SDSS catalog. Units of right ascension are hours, minutes, and seconds, and units of declination are degrees, arcminutes, and arcseconds. z is the spectroscopic redshift. g and r list the apparent model magnitudes available in the SDSS DR7 catalog. Absolute magnitudes have been corrected for Galactic extinction.

Name	SDSS ID	ra (J2000.0)	dec (J2000.0)	z	g	r	$g-r$	M_r
VGS_01	SDSS J083707.48+323340.8	08 37 07.5	+32 33 41	0.018531	17.67	17.17	0.49	-17.4
VGS_07	SDSS J100642.44+511623.9	10 06 42.5	+51 16 24	0.016261	17.36	17.30	0.06	-16.9
VGS_09	SDSS J102250.68+561932.1	10 22 50.7	+56 19 32	0.012995	17.78	17.52	0.26	-16.2
VGS_12	SDSS J102819.23+623502.6	10 28 19.2	+62 35 03	0.017804	17.67	17.41	0.26	-17.0
VGS_14	SDSS J103506.46+550847.5	10 35 06.5	+55 08 48	0.013154	16.99	16.72	0.28	-17.1
VGS_30	SDSS J130526.08+544551.9	13 05 26.1	+54 45 52	0.019435	18.27	18.05	0.22	-16.6
VGS_32	SDSS J132232.48+544905.5	13 22 32.5	+54 49 06	0.011835	14.70	14.17	0.53	-19.4
VGS_34	SDSS J132718.56+593010.2	13 27 18.6	+59 30 10	0.016539	16.09	15.22	0.87	-19.1
VGS_35	SDSS J135113.62+453509.2	13 51 13.6	+45 35 09	0.017299	16.77	16.36	0.41	-18.0
VGS_36	SDSS J135535.46+593041.3	13 55 35.5	+59 30 41	0.022398	16.81	16.46	0.36	-18.5
VGS_38	SDSS J140034.49+551515.1	14 00 34.5	+55 15 15	0.013820	17.30	16.95	0.35	-16.9
VGS_42	SDSS J142416.41+523208.3	14 24 16.4	+52 32 08	0.018762	16.49	15.88	0.61	-18.7
VGS_44	SDSS J143052.33+551440.0	14 30 52.3	+55 14 40	0.017656	15.38	14.92	0.46	-19.5
VGS_45	SDSS J143553.77+524400.6	14 35 53.8	+52 44 01	0.014553	17.60	17.33	0.26	-16.7
VGS_58	SDSS J154452.18+362845.6	15 44 52.2	+36 28 46	0.011522	16.05	15.70	0.35	-17.8

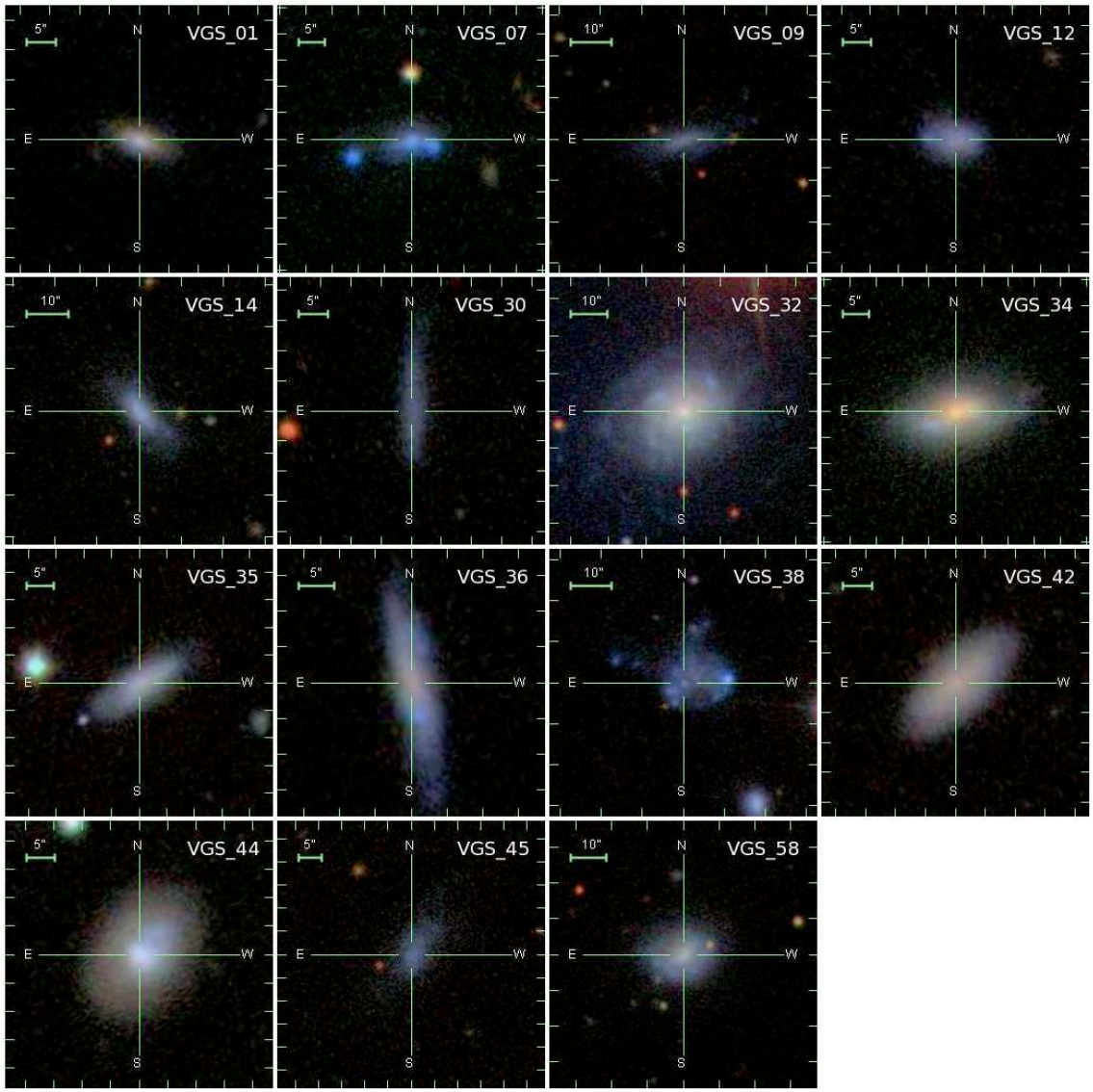

Figure 4.3: Our sample of void galaxies, scaled to the same physical size. Composite color images are taken from the online SDSS Finding Chart tool.

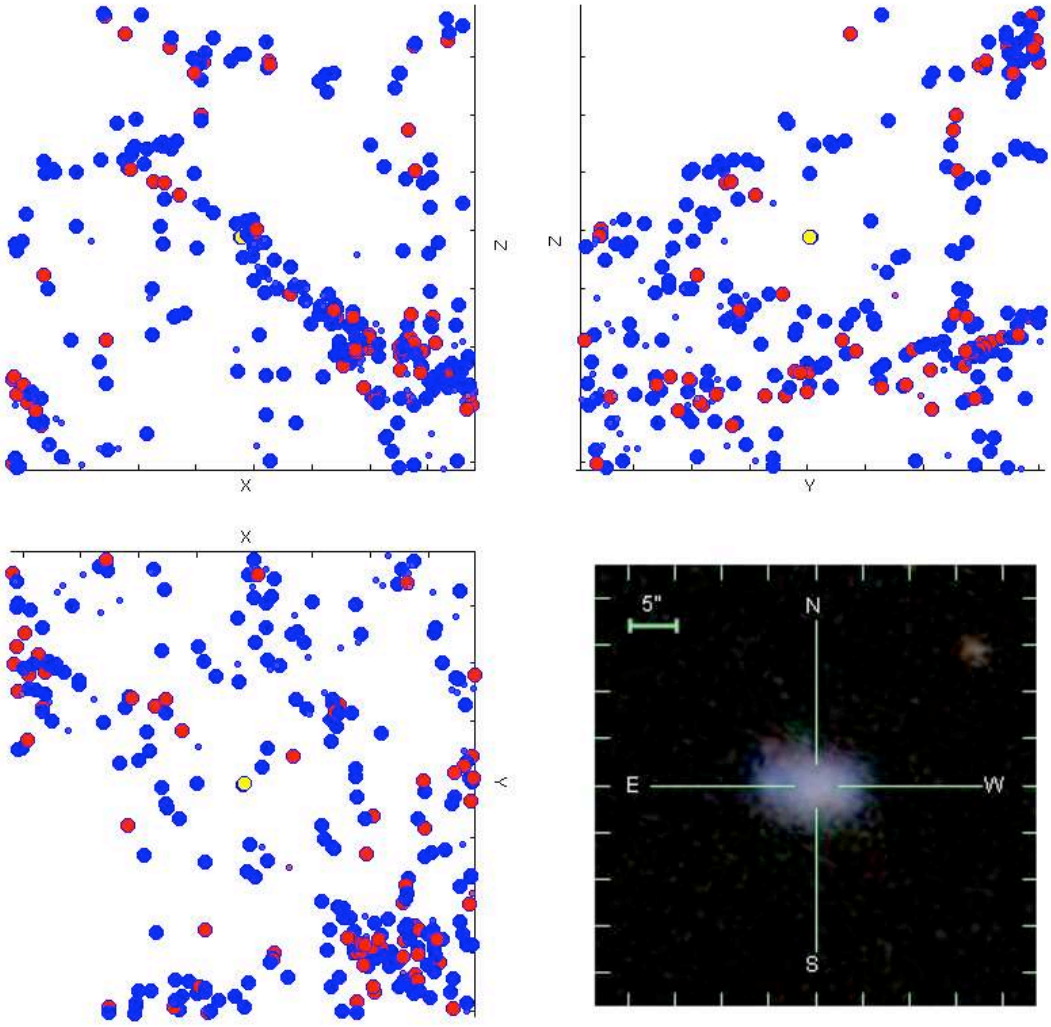

Figure 4.4: The SDSS galaxy distribution in and around the void in which galaxy VGS_12 of our void galaxy sample is located, seen from three different perspectives. The galaxies are located within a box of size 24 h^{-1} Mpc centered on VGS_12 (in yellow). Bright galaxies have large dots (B < -16), fainter ones are depicted by smaller dots. Redder galaxies, with $g - r > 0.6$ are indicated by red dots. Bluer galaxies, with $g - r \leq 0.6$, are indicated by blue dots. The SDSS image of the galaxy is shown in the bottom right panel.

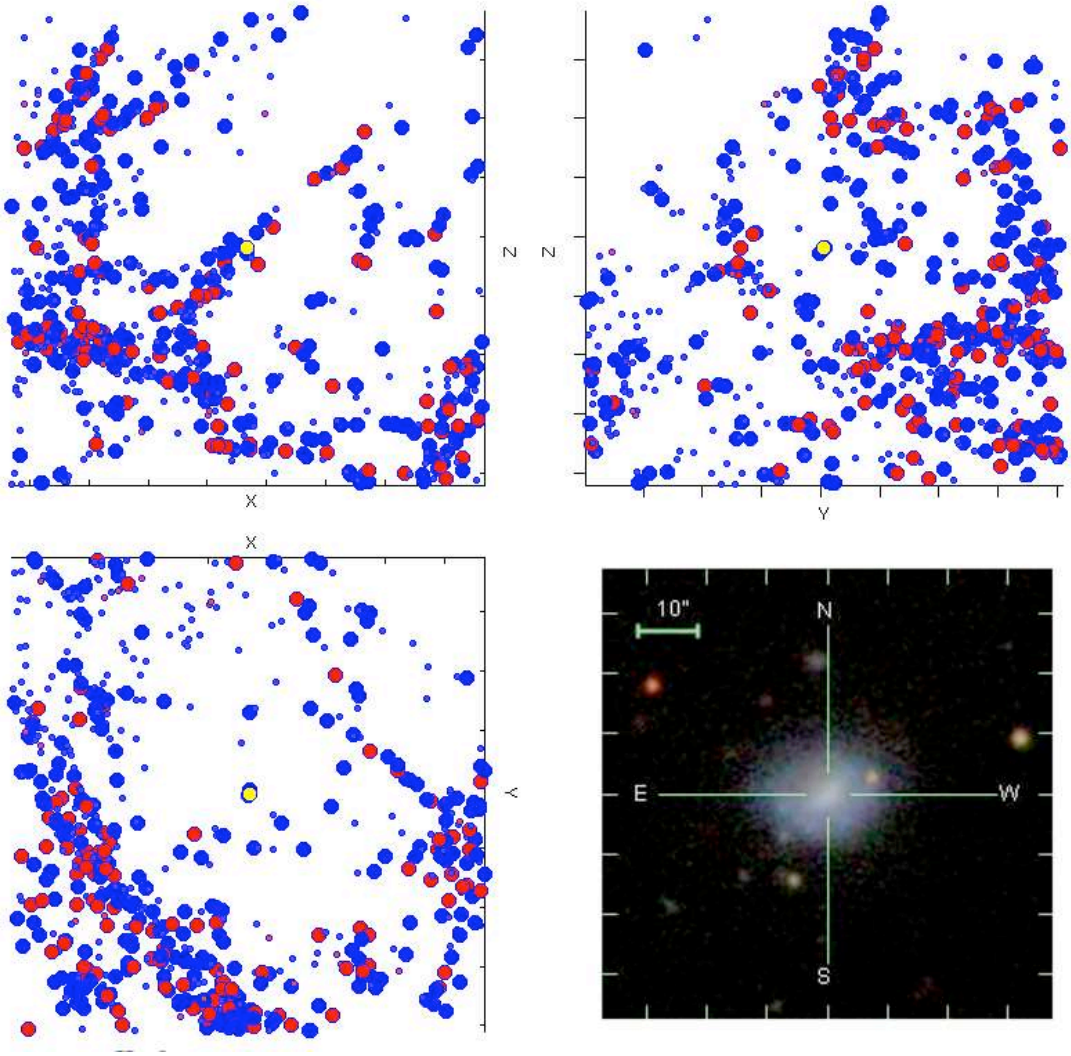

Figure 4.5: The SDSS galaxy distribution in and around the void in which galaxy VGS_58 of our void galaxy sample is located, seen from three different perspectives. The galaxies are located within a box of size 24 h^{-1} Mpc centered on VGS_58 (in yellow). Bright galaxies have large dots (B < -16), fainter ones are depicted by smaller dots. Redder galaxies, with $g - r > 0.6$ are indicated by red dots. Bluer galaxies, with $g - r \leq 0.6$, are indicated by blue dots. The SDSS image of the galaxy is shown in the bottom right panel.

dots (B < -16), while fainter ones are depicted by smaller dots. Redder galaxies, with $g-r > 0.6$ are indicated by red dots, and bluer galaxies, with $g-r \leq 0.6$, are indicated by blue dots.

Void 14 lies well within the interior of a huge void, surrounded by filamentary structures. On one side these are embedded within a massive wall-like complex. The geometry of the spatial galaxy distribution around the polar ring galaxy VGS_12 has been discussed at length in Chapter 2 of this thesis: the galaxy lies within a tenuous wall in between two voids. This is perhaps most evident in the top left panel, where we see a planar concentration forming the division between a large void (to the top of the box) and a smaller void (to the bottom of the box). A comparison between the spatial distribution of red and blue dots reveals a strong segregation in the low-density regions. In particular the VGS_58 maps illustrate the avoidance by red galaxies of underdense areas. A similar distinction in spatial distribution between faint and bright galaxies is far harder to notice, if at all.

The nature of our galaxies can be immediately appreciated from the color-magnitude diagram in Figure 4.6. For comparison we include a volume-limited sample of galaxies in underdense regions defined by our void-finding algorithm from the SDSS DR7, including all galaxies brighter than $M_r = -16.9$ within a redshift range $z < 0.02$. Most of our galaxies are in the blue cloud and at the faint end of the galaxy luminosity function, where the

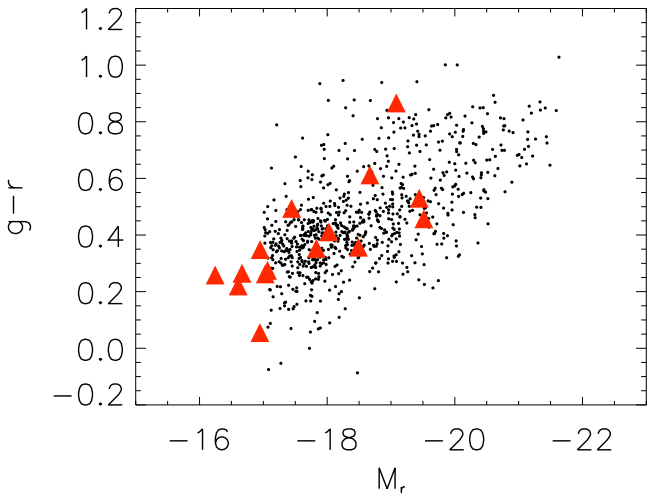

Figure 4.6: Color-magnitude diagram for our void galaxy sample (triangles), compared with a volume limited ($z < 0.02$, $M_r < -16.9$) sample of void galaxies from the SDSS.

bulk of SDSS void galaxies reside. See Section 4.5 for a detailed discussion of how our void galaxy sample compares with other void galaxies samples.

Table 4.2 contains parameters for the voids surrounding each target galaxy, taken from our void finding algorithm applied to the SDSS reconstructed density field. For the galaxies that seem to reside in between two voids we have quoted two values, for the two nearest voids.

Column (1) lists the program name.

Column (2) lists the (equivalent) void radius R_{void},

$$R_{void} \equiv \left(\frac{3\,V_{void}}{4\pi} \right)^{1/3} , \tag{4.5}$$

where V_{void} is the volume of the void. It corresponds to the radius the void would have if it were spherical.

Column (3) gives $D_{gal,void}$, the distance of the galaxy from the void center.

Column (4) gives the the ratio of void center distance to void radius,

$$DR \equiv \frac{D_{gal,void}}{R_{void}}. \tag{4.6}$$

Note that nearly all detected voids are elongated, so that galaxies located within the voids' interior may still have $DR > 1$.

Column (5) provides the filtered density contrast of the void,

$$\delta \equiv \frac{\rho_{void}}{\rho_u} - 1 , \tag{4.7}$$

at a filtering scale $\mathrm{R}_f = 1\mathrm{h}^{-1}\mathrm{Mpc}$. Here, ρ_u is the mean density, estimated by the average point intensity from the SDSS volume (see Platen 2009).

Column (6) lists the distance to the nearest neighbor.

Column (7) lists the average distance of the six nearest neighbors.

Column (8) gives the void name, taken from Fairall (1998) and Hoyle & Vogeley (2002).

Table 4.2: Parameters of the voids surrounding the target void galaxies. Listed are: name of the target void galaxy (1), (equivalent) void radius R_{void} (2), the distance $D_{gal,void}$ of the galaxy from the void center (3), ratio of void center distance to void radius (4), the filtered density contrast δ at $R_f = 1h^{-1}$Mpc (5), the distance to the nearest neighbor (6), the average distance of the six nearest neighbors (7) and the void name taken from Fairall (1998) and Hoyle & Vogeley (2002) (8). See Section 4.2.3 for further specification.

Name	R_{void} (Mpc)	$D_{gal,void}$ (Mpc)	DR	δ	Nearest nbr	Nearest nbr6	Void Name
(1)	(2)	(3)	(4)	(5)	(6)	(7)	(8)
VGS_01	16.72	18.48	1.11	-0.68	1.92	2.77	UrsaMajor
VGS_07	16.72	13.39	0.80	-0.82	3.97	4.67	UrsaMajor
VGS_09	16.50	19.77	1.20	-0.67	1.52(4)	4.09	Leo(Top)
VGS_12	18.64/16.72	17.22/17.68	0.92/1.06	-0.78	3.51	4.01	UrsaMinorII/UrsaMajor
VGS_14	16.50	18.37	1.11	-0.68	1.52(2)	4.18	Leo(Top)
VGS_30	16.25	12.69	0.78	-0.85	3.31	5.16	UrsaMinorII
VGS_32	18.64	17.26	0.93	-0.74	3.69	4.65	UrsaMinorI
VGS_34	18.64	9.65	0.52	-0.66	3.39	4.19	UrsaMinorI
VGS_35	16.25	12.71	0.78	-0.57	2.82	4.07	UrsaMinorII
VGS_36	16.25/18.64	15.66/22.03	0.96/1.18	-0.74	2.86	3.67	UrsaMinorII(Top)/UrsaMinorI
VGS_38	18.64	14.98	0.80	-0.58	1.61	3.50	UrsaMinorI
VGS_42	18.64/16.25	19.25/12.79	1.03/0.79	-0.66	1.87	3.80	UrsaMinorI/UrsaMinorII
VGS_44	18.64	15.70	0.52	-0.83	2.99	4.13	UrsaMinorI
VGS_45	18.64	16.50	0.88	-0.38	3.10	3.44	UrsaMinorI
VGS_58	14.57	12.59	0.86	-0.88	0.34	5.26	CoronaBorealisII

While all targets were ideally chosen for their isolation and central location within the void, our pilot sample selection was limited to the galaxy redshift survey data available with the incomplete DR3. As the catalog has been completed since then some of these targets have proven to be in slightly less centrally located, though still underdense, environments. This, and the fact that most voids have rather elongated shapes, explains why several of the sample galaxies have a distance R_{void} to the void center which is in the order of the (equivalent) void scale R_{void}. Galaxies VGS_07, VGS_34, VGS_44, and VGS_58 are the best in terms of location near the center of the void and not near a wall-like configuration.

4.3 Observations

Our targets were observed 2006-2007 with the Westerbork Synthesis Radio Telescope (WSRT) in Maxi-short configuration. The shortest baselines of 36, 54, 72 and 90 meters optimize surface brightness sensitivity in a single 12 hour observation. Its longest spacing of 2754 meters results in an angular resolution of approximately $20''$. Observing parameters are detailed in Table 4.3. We observed using 512 channels per 10 MHz bandwidth, at four si-

Table 4.3: Parameters of the WSRT observations

Configuration	Maxi-short
Date	2006, 2007
No. telescopes	13
Exposure time	12 h
Total bandwidth	40 MHz
No. channels	512
Shortest spacing	36 m
Longest spacing	2754 m
FWHM primary beam	$36'$
Synthesized beam	$19'' \times 19''/\sin(\delta)$
rms	0.4 mJy Beam^{-1}
velocity resolution	8.6 km s^{-1}

multaneously observed frequencies, each with two polarizations. Along with the observation centered at the target galaxy, three other simultaneous observations were made centered at frequencies 8.3 MHz, -8.3 MHz and -16.6 MHz removed from the target galaxy, resulting in a velocity coverage of nearly 10,000 km s^{-1} with each telescope pointing. Target redshifts ranged from 0.012 to 0.022, so channel increments of 19.5312 kHz give a typical velocity resolution of 4.25 km s^{-1} using the heliocentric optical velocity definition. After applying Hanning smoothing this is reduced to 8.6 km s^{-1}. The full width at half maximum of the primary beam is $36'$, which at a redshift of 0.015 is a 700 kpc $\times$ 700 kpc area on the sky.

Each observation consisted of a 12 hour target exposure, calibrated by two 15 min snapshots, one observed before and one observed after, using two of 3C48, 3C286, 3C147 and CTD93. Due to the location's impressive phase stability, our calibration observations once every 12 hours are sufficient for phase calibration. The absolute flux scale is determined using the flux scale of Baars et al. (1977) in the AIPS task SETJY. At a first channel frequency of 1406.9212 MHz, a corresponding flux of 14.79 Jy, 16.00 Jy, and 22.10 Jy are used for 3C286, 3C48, and 3C147, respectively. For the non-standard calibrator CTD93 we use the 20 cm flux of 4.83 Jy, as listed in the VLA calibrator manual. All calibration is done using standard AIPS procedures.

Continuum emission is subtracted from the UV data by interpolation from the line free channels. Image cubes are created with a CLEAN box around the H I emission that cleans down to 0.5 mJy beam^{-1} (1 σ). Images are created with a robust parameter of 1 (Briggs

1995) and corrected for the primary beam. Data cubes are then Hanning smoothed to achieve a sensitivity of 0.4 mJy beam^{-1}. Zeroth and first moment maps are made over a narrow velocity range encompassing the detection, with Hanning and Gaussian smoothing over 25 km s^{-1} and 30″ and 1.5σ clipping. For galaxies removed from the beam center the cutoff value is scaled to correct for the primary beam.

The continuum baseline fit from the line free channels, which is used to determine the continuum subtraction in the UV data, is also used to create a 1.4 GHz continuum image. Images are created with a robust parameter of 1 and CLEANed down to 0.2 mJy beam^{-1} (1.5 σ).

The separation between a void galaxy and the edge of the neighboring velocity range is about 5 MHz once edge channels are excluded, which at the average distance of 70 Mpc corresponds to a cosmological distance of ∼15 Mpc. This is large enough to distinguish these neighboring velocity ranges as removed from the target void, which maximally extend to about 15 Mpc in radius (Table 4.2). For blind H I detections throughout the neighboring velocity range, excluding the target galaxy, data cubes are smoothed to 20 km s^{-1} with a 6 kilowavelength taper, producing a 40″ beam and 1σ sensitivity of 0.25 mJy beam^{-1}. Zeroth moment maps are made with Hanning and Gaussian smoothing and 5σ clipping before correcting for the primary beam to provide a simple blind detection algorithm. We then selected by eye the regions with HI emission that are extended both spatially and in velocity and call this our control sample.

4.4 Results

In our sample of 15 void galaxies (Table 4.1 and Figure 4.7) we have one non-detection, and discovered one previously known and five previously unknown companions (Table 4.4 and Figure 4.8). Of the five void galaxies with companions, two are interacting in H I. All H I-detected companions have optical counterparts within the SDSS. Of the nine isolated void galaxies, two exhibit clear irregularities in the kinematics of their gas disks. Target galaxies have a range of H I masses from 3.5 $\times$ 10^8 M$_\odot$ to 3.8 $\times$ 10^9 M$_\odot$ and one non-detection with a 3σ upper limit of 2.1 $\times$ 10^8 M$_\odot$, assuming a 150 km s^{-1} velocity width. Companion galaxies have masses ranging from 5.0 $\times$ 10^7 M$_\odot$ to 4.5 $\times$ 10^8 M$_\odot$. H I properties of the target and companion galaxies are given in Table 4.5.

Table 4.4: Companion galaxies parameters taken from the SDSS catalog. Units of right ascension are hours, minutes, and seconds, and units of declination are degrees, arcminutes, and arcseconds. g and r list the apparent model magnitudes as measured by the SDSS DR7. Absolute magnitudes have been corrected for galactic extinction. $\Delta\theta$, Δd and Δv list the displacement from the beam center, projected sky separation, and velocity separation, respectively, between the target and companion galaxy.

name	SDSS ID	ra (J2000.0)	dec (J2000.0)	g	r	$g-r$	M_r	$\Delta\theta$ ($'$)	Δd (kpc)	Δ v (km s^{-1})
VGS_07a	SDSS J100519.69+511038.3	10 05 19.7	+51 10 38	20.15	20.12	0.03	-14.1	14.2	288	-21
VGS_09a	SDSS J102241.41+561208.5	10 22 41.4	+56 12 09	22.29	22.26	0.02	-11.4	7.5	121	-85
VGS_30a	SDSS J130531.13+544553.8	13 05 31.1	+54 45 54	18.67	18.39	0.29	-16.2	0.7	17	-74
VGS_34a	SDSS J132640.92+593202.5	13 26 40.9	+59 32 03	20.41	20.31	0.10	-14.0	5.1	104	42
VGS_38a	SDSS J140032.44+551445.9	14 00 32.4	+55 14 46	17.74	17.59	0.15	-16.1	0.6	9	-21
VGS_38b	SDSS J140025.68+551318.5	14 00 25.7	+55 13 19	19.02	18.82	0.20	-14.9	2.3	37	10

Table 4.5: H I properties of targeted void galaxies and companions. Non-detections list the 3σ upper limit on the H I mass. V_{sys} is the systemic H I velocity, using the optical definition. D is the distance to the target galaxy. r_{90} and $r_{H\,I}$ list the optical and H I radius, respectively. When possible, poorly resolved systems list the upper limit for $r_{H\,I}$ and M_{dyn}. W_{50} and W_{20} are the 50% and 20% H I line widths, respectively, corrected for instrumental broadening. The inclination, i, is calculated such that 90° is edge-on.

Name	$M_{H\,I}$ ($10^8 M_\odot$)	V_{sys} (km s^{-1})	D (Mpc)	r_{90} (kpc)	$r_{H\,I}$ (kpc)	W_{50} (km s^{-1})	W_{20} (km s^{-1})	i (°)	M_{dyn} ($10^{10} M_\odot$)	$M_{H\,I}/L_r$
VGS_01	< 2.1	-	-	2.4	-	-	-	60	-	-
VGS_07	8.6 ± 0.8	4901	70	2.6	9.2	119	144	50	1.28	1.9
VGS_07a	3.23 ± 0.65	4880	69	3.5	-	41	49	-	-	9.7
VGS_09	10.3 ± 1.0	3881	55	3.1	9.1	110	126	68	0.74	4.4
VGS_09a	0.57 ± 0.14	3796	54	1.5	-	41	49	-	-	20.2
VGS_12	29.9 ± 4.2	5316	76	2.4	18.0	154	179	29	10.55	6.2
VGS_14	6.4 ± 1.0	3933	56	3.3	8.7	110	134	67	0.72	1.3
VGS_30	5.5 ± 1.0	5666	81	3.7	< 7.5	50	93	77	< 0.12	1.7
VGS_30a	4.52 ± 0.79	5592	79	2.1	-	24	41	-	-	2.1
VGS_32	38.0 ± 4.5	3522	50	4.1	19.0	171	187	46	6.29	0.9
VGS_34	23.9 ± 2.9	4917	70	3.6	10.2	231	299	50	5.34	0.7
VGS_34a	0.50 ± 0.16	4959	70	1.1	-	33	58	-	-	1.7
VGS_35	10.7 ± 1.3	5191	74	3.0	10.8	145	187	65	1.61	0.9
VGS_36	19.8 ± 2.7	6684	95	5.0	13.0	190	224	79	2.82	1.1
VGS_38	9.1 ± 0.7	3853	55	2.8	6.9	50	92	39	0.26	2.0
VGS_38a	0.86 ± 0.14	3832	54	1.3	-	67	75	-	-	0.4
VGS_38b	1.39 ± 0.22	3863	55	1.4	-	41	66	-	-	2.0
VGS_42	4.0 ± 1.5	5601	80	3.5	< 8.1	128	171	58	< 1.08	0.2
VGS_44	4.9 ± 1.1	5295	76	3.6	< 7.0	76	110	31	< 0.90	0.1
VGS_45	3.5 ± 1.3	4316	62	4.0	< 6.9	68	102	66	< 0.22	1.0
VGS_58	7.0 ± 0.6	3351	48	2.6	7.4	143	151	38	2.39	0.7

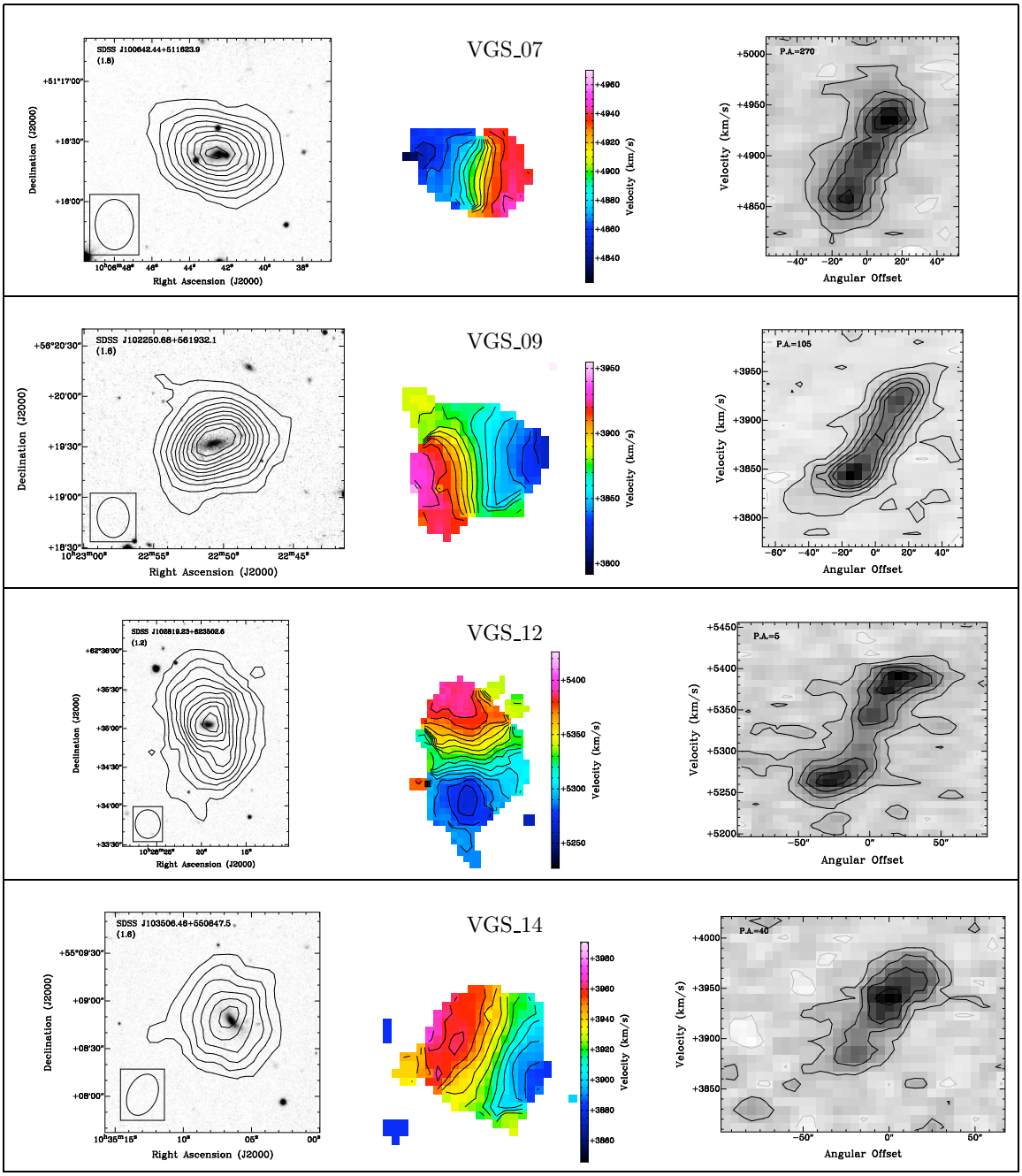
VGS_07
SDSS J100642.44+511623.9
(1.8)
Declination (J2000)
Right Ascension (J2000)
Velocity (km/s)
P.A.=270
Angular Offset
VGS_09
SDSS J102250.68+561932.1
(1.6)
P.A.=105
VGS_12
SDSS J103819.23+523502.6
(1.2)
P.A.=5
VGS_14
SDSS J103506.46+550847.5
(1.6)
P.A.=40

Figure 4.7

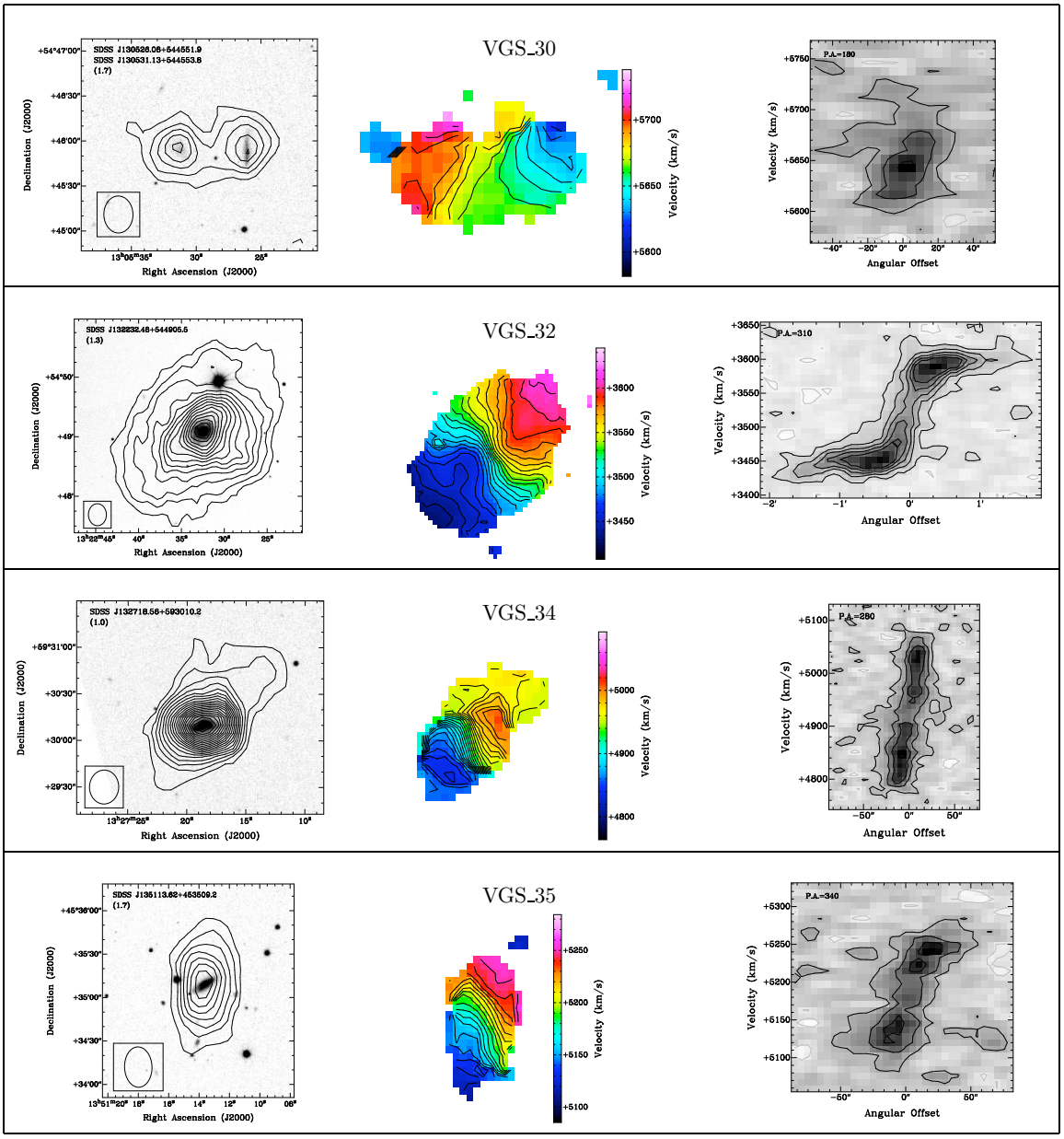
VGS_30
SDSS J130526.08+544551.9
SDSS J130531.13+544553.8
(1.7)
Declination (J2000)
Right Ascension (J2000)
Velocity (km/s)
P.A.=180
Angular Offset
VGS_32
SDSS J132232.46+544905.5
(1.3)
P.A.=310
VGS_34
SDSS J132718.56+593010.2
(1.0)
P.A.=280
VGS_35
SDSS J135113.62+453509.2
(1.7)
P.A.=340

Figure 4.7

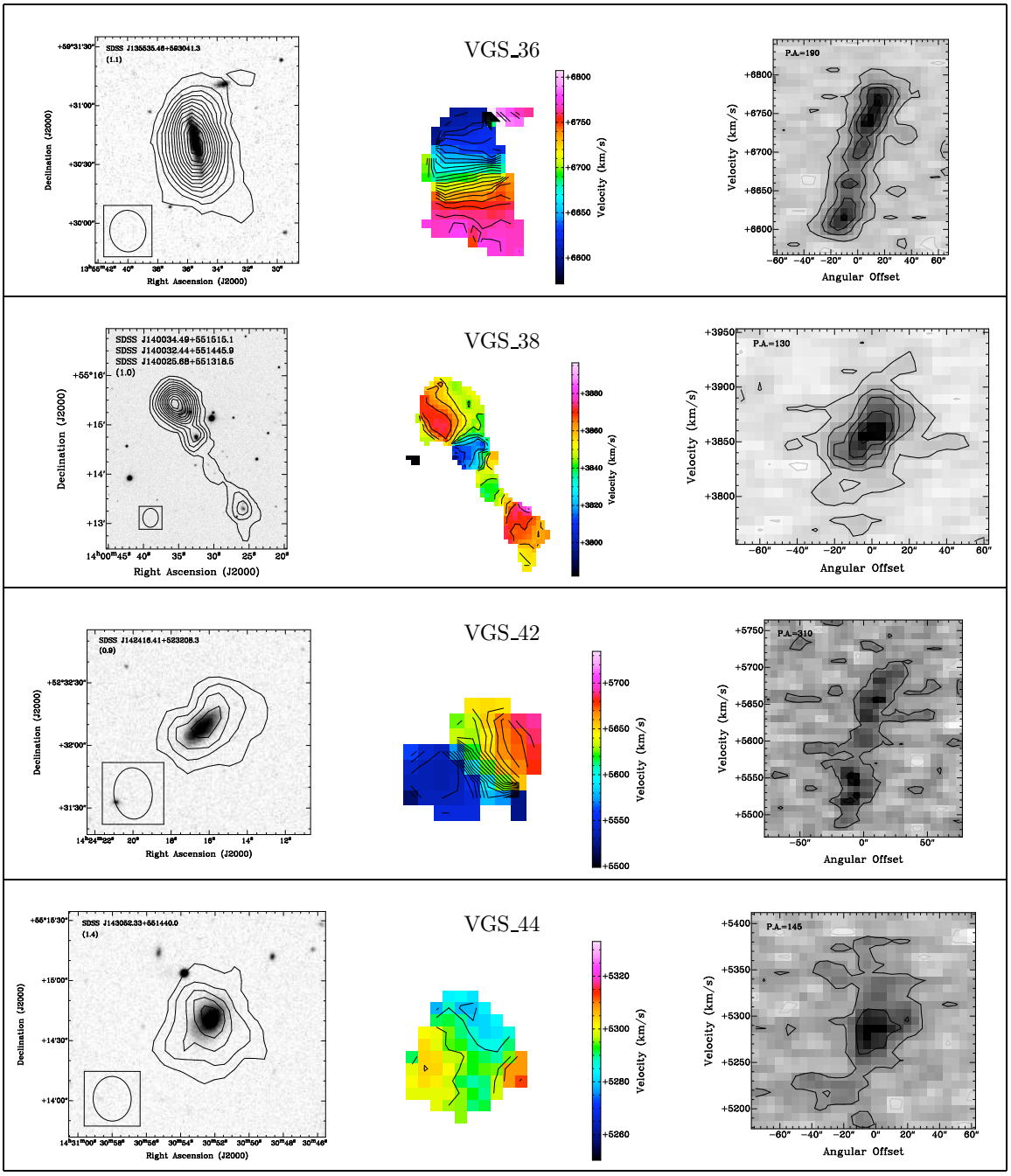
VGS_36
SDSS J135535.48+583041.3
(1.1)
Declination (J2000)
Right Ascension (J2000)
Velocity (km/s)
P.A.=190
Velocity (km/s)
Angular Offset
VGS_38
SDSS J140034.49+551515.1
SDSS J140032.44+551445.9
SDSS J140025.68+551318.5
(1.0)
Declination (J2000)
Right Ascension (J2000)
Velocity (km/s)
P.A.=130
Velocity (km/s)
Angular Offset
VGS_42
SDSS J142416.41+523208.3
(0.9)
Declination (J2000)
Right Ascension (J2000)
Velocity (km/s)
P.A.=310
Velocity (km/s)
Angular Offset
VGS_44
SDSS J143052.33+561440.0
(1.4)
Declination (J2000)
Right Ascension (J2000)
Velocity (km/s)
P.A.=145
Velocity (km/s)
Angular Offset

Figure 4.7

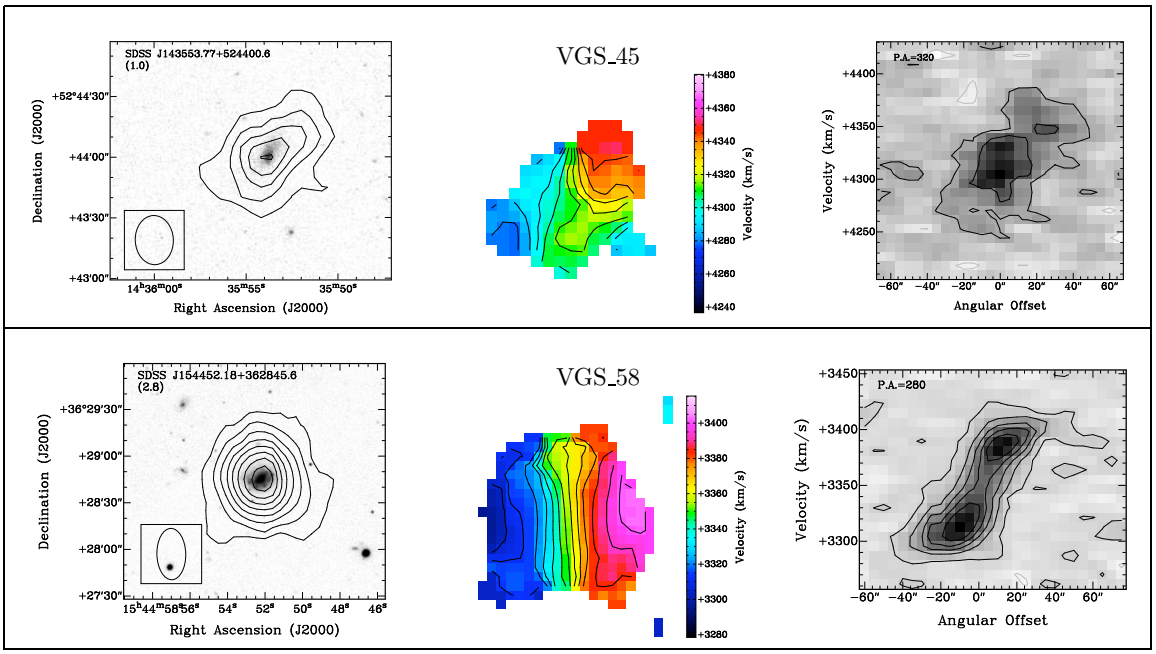

Figure 4.7: Targeted void galaxies. Contours in the total intensity maps (left) are at $5 \times 10^{19}\ cm^{-2}$ plus increments of $10^{20}\ cm^{-2}$. Confidence level (σ) of the lowest contour is given in the top left corner of each image. Lines in the velocity field images (center) indicate increments of 8 km s^{-1}. Position-Velocity diagrams (right) are along the kinematic major axis, contours are at increments of -1.5 (grey), 1.5 (black) + increments of 3σ .

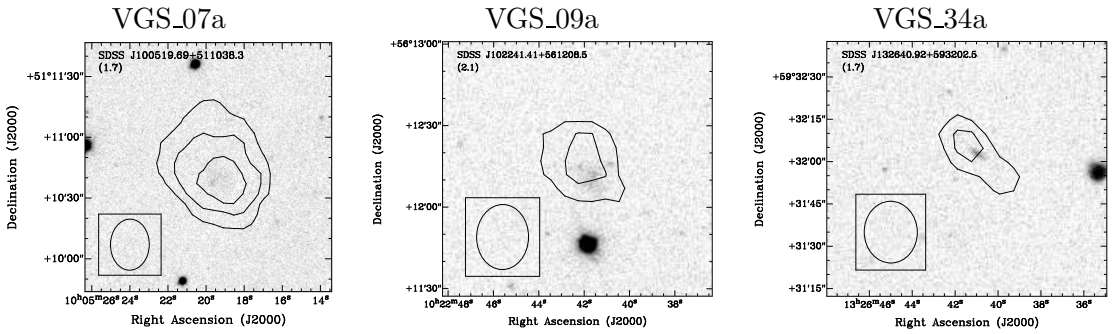

Figure 4.8: Companions. Note that VGS_30a, VGS_38a and VGS_38b are shown in Figure 4.7 along with the targeted void galaxy. Contours in the total intensity maps are at $5 \times 10^{19}\ cm^{-2}$ plus increments of $10^{20}\ cm^{-2}$. Confidence level (σ) of the lowest contour is given in the top left corner of each image.

4.4.1 HI Data

H I mass is calculated using the standard formula, $M_{H\,I} = 2.356 \times 10^5\, d^2 \int S\, dv\ M_\odot$, where d is the distance in Mpc, S is in Jy and dv is in km s^{-1}. The integrated flux is taken from the total intensity maps described in Section 4.3. A rough global profile is constructed by summing the flux in a tight box surrounding the target. The 50% H I line width (W_{50}) and 20% H I line width (W_{20}) are corrected for instrumental broadening following Verheijen & Sancisi (2001), and broadening due to random motions is neglected. Errors of 15 km s^{-1} reflect uncertainties of one channel on either side. Systemic velocities are estimated from tilted ring fits of the velocity field, with typical errors of 5 km s^{-1}.

Because the majority of the void galaxies are not well enough resolved to reliably fit tilted rings to the kinematics of the gas disk, we measure the radial surface density profile following the iterative deconvolution method described by Lucy (1974) as implemented by Warmels (1988). This technique projects the two dimensional surface brightness map along the disk minor axis to create a one dimensional strip distribution which shows projected surface brightness as a function of position along the disk major axis. Assuming an azimuthally symmetric and circular disk, this strip distribution is then iteratively modeled to reconstruct the radial surface density profile (Figure 4.9). As discussed by Swaters et al. (2002), this iterative deconvolution method is known to restore too much flux to the disk center, so while the iterative fit was stopped at 10 iterations to prevent this, we may systematically be slightly underestimating our radii and significantly overestimating our central surface densities. Position angles are determined by considering both the g-band optical as well as the H I kinematic major axes. The H I radius, $R_{H\,I}$, is taken as that point where the surface density drops below 1 $M_\odot$ pc^{-2}. Upper limits are listed for those galaxies with an H I extent smaller than the synthesized beam size. Typical uncertainty in the radius is 5″, about 1.5 - 2 kpc for our void sample. This is much larger than the typical 0.5″ (150 - 200 pc) errors in the optical r_{90} radius, containing 90% of the Petrosian flux.

As all detected target galaxies exhibit disklike rotation, the inclination corrected circular velocity is used to estimate a dynamical mass, M_{dyn}, for the volume interior to $R_{H\,I}$ as

$$M_{dyn}(r < R) \;=\; \frac{W_{50}^2 R_{H\,I}}{\sin^2 i\ G}\ M_\odot. \tag{4.8}$$

Inclinations, i are calculated from SDSS r-band isophotal major and minor axes. Following the assumption that disks be intrinsically oblate and axisymmetric, with a three dimensional

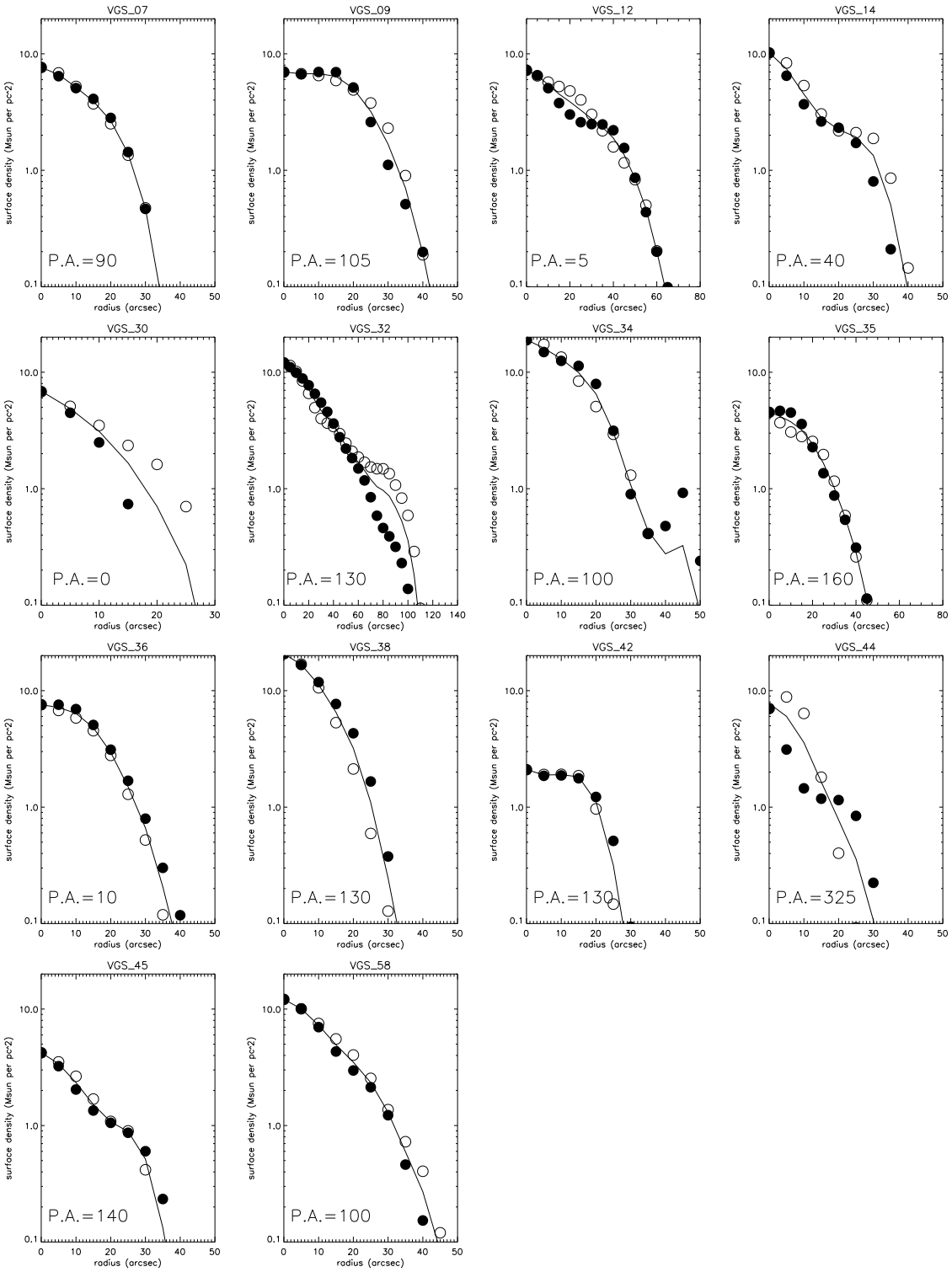

Figure 4.9: Radial surface density profiles for the east (open circles) and west (filled circles) sides of each disk, with the average overdrawn.

axis ratio of $q_o = 0.19$ (Geha et al. 2006), we use

$$\sin i \;=\; \sqrt{\frac{1-(b/a)^2}{1-q_o^2}}. \tag{4.9}$$

A choice of $q_o = 0.3$ changes the resulting inclinations by less than 10%. For targets which have no cataloged r-band major and minor axes, we use u-band values. The r-band and u-band inclinations are generally in agreement to within 10%. Due to these uncertainties in the inclination and in the H I radius we expect our dynamical masses to be accurate within roughly a factor of two.

4.4.2 Radio Continuum Data

Continuum images, with a typical sensitivity of 0.12 mJy beam^{-1}, are used to calculate at 1.4 GHz star formation rate following Yun et al. (2001), as

$$SFR_{1.4GHz} \;=\; \frac{L_{1.4}(ergs\ s^{-1}\ Hz^{-1})}{1.7\ \times\ 10^{28}} M_\odot\ year^{-1}. \tag{4.10}$$

Continuum emission is detected in only four void galaxies, and only two are extended enough (VGS_07 and VGS_32) to rule out confusion with possible active galactic nucleus (AGN) emission, however all radio luminosities are low enough that the net AGN contribution should be small. For those galaxies without emission we calculate a 3σ upper limit (Table 4.6), which we find to be in general agreement with the Hα star formation rate (described below).

4.4.3 Optical Data

To determine the stellar mass of the galaxies from the SDSS optical spectra, each spectrum is pre-corrected for dust extinction due to the Milky Way using the map by Schlegel et al. (1998). Adopting the approach used by various authors (e.g., Gwyn & Hartwick 2005; Salim et al. 2007), the stellar mass is determined by fitting to the full galaxy spectra (3800–9200 Å in the observed frame) from the SDSS DR6 (Adelman-McCarthy et al. 2008) the dust-attenuated Bruzual & Charlot (2003) stellar population model spectra, where the dust model of Calzetti et al. (2000) is used to correct for intrinsic dust extinction. The overall model is composed of simple stellar populations with stellar age ranges from 5 Myr to 11 Gyr and stellar metallicity ranges from 0.004 to 0.05. The dust extinction is a free parameter which is determined simultaneously through the best-fit stellar continuum. Using a galaxy

Table 4.6: Stellar and star formation parameters for void galaxies. Targets not detected in the 1.4 GHz continuum list the 3σ upper limit on the $\mathrm{SFR}_{1.4GHz}$.

Name	$\mathbf{M_*}$ ($10^8\mathbf{M_\odot}$)	$\mathbf{SFR}_{H\alpha}$ ($\mathbf{M_\odot\ yr^{-1}}$)	$\mathbf{SFR}_{1.4GHz}$ ($\mathbf{M_\odot\ yr^{-1}}$)	**EW(Hα)** (**Å**)	$\mathbf{SFR}_{H\alpha}/M_*$ ($10^{-11}\ \mathbf{yr^{-1}}$)	$\mathbf{SFR}_{H\alpha}/M_{\mathbf{H\ I}}$ ($10^{-11}\ \mathbf{yr^{-1}}$)
VGS_01	6.8	1.43	< 0.16	55.3	211.5	-
VGS_07	0.4	0.25	0.20	202.9	604.4	28.6
VGS_09	0.4	0.00	< 0.08	16.7	0.0	0.0
VGS_12	10.5	0.05	< 0.15	22.4	5.2	1.8
VGS_14	2.0	0.14	< 0.08	53.4	70.7	21.7
VGS_30	0.7	0.17	< 0.17	11.3	241.8	31.5
VGS_32	68.6	-	0.57	15.1	0.0	0.0
VGS_34	75.4	0.95	2.97	32.2	12.6	39.7
VGS_35	12.8	0.07	< 0.14	19.7	5.6	6.7
VGS_36	19.4	0.17	< 0.23	17.0	8.7	8.5
VGS_38	0.5	0.00	< 0.08	-0.3	0.0	0.0
VGS_42	38.9	0.11	< 0.16	9.5	2.9	28.3
VGS_44	21.1	1.47	0.95	85.9	69.8	302.4
VGS_45	0.6	0.00	< 0.10	11.4	0.0	0.0
VGS_58	10.0	0.11	< 0.06	10.9	11.3	16.1

sample that is all galaxies included in both the SDSS DR4 and the SDSS DR6 data, the agreement between our dust-free stellar mass estimates and those from the line-indices approach performed upon the SDSS DR4 galaxies (Kauffmann et al. 2003c) is on average $\sim$0.25 dex (Yip et al. 2010 in prep.).

As the SDSS spectroscopy samples the light of each galaxy in the central $3''$-diameter area, an aperture correction is applied in deriving the stellar mass of the whole galaxy. The correction is taken to be the ratio between the flux within the Petrosian radius (which encompasses more than $\sim$90% of a galaxy regardless of the light profile, Strauss et al. 2002) to that within the central $3''$ diameter of each galaxy, as such $\mathrm{m}_*^{petro} = \mathrm{m}_*^{fiber}\, 10^{-0.4\,(m^{petro}-m^{fiber})}$, where m_* and m denote the stellar mass and the observed frame magnitude of the galaxy, respectively. Stellar masses and Hα star formation rates, as determined by the Hα luminosity of the optical spectra with an aperture correction applied, are given in Table 4.6.

Even though we are considering a galaxy population which may be systematically different, our stellar mass estimates are accurate within the tolerances of the method, and are relatively insensitive to the assumed parameters for stellar age and metallicity. Our void galaxy sample shows an agreement of $\sim$0.25 dex between our stellar mass estimates and

those in the MPA-JHU DR7 catalog [1] which is based on fits to the photometry through an approach similar to Kauffmann et al. (2003c) and Salim et al. (2007). Our choice of the modeled stellar age lower bound, 5 Myr, ensures that the massive stars ($\sim$ 100 $M_\odot$) are included in the model. On the choice of the modeled stellar metallicities: the stellar masses are expected to be fairly insensitive to the modeled stellar metallicities, because they are derived from the stellar continuum luminosity, whereas the stellar metallicity of the galaxies affects primarily the absorption line strengths. On the other hand, the stellar mix does determine the amplitude of the underlying stellar absorption in the Hα line. The average Hα stellar absorption in the SDSS galaxies is 1.3 Å (Hopkins et al. 2003; Miller et al. 2003) determined through an approach which is independent of stellar population model, and is small compared with the average restframe Hα emission equivalent width of our galaxies, calculated to be about 50 Å.

4.4.4 Notes on Individual Void Galaxies

Many of our void galaxies appear morphologically and dynamically quite unexceptional. VGS_09, VGS_14, VGS_36, VGS_42, VGS_45, and VGS_58 all appear to exhibit regular disk-like rotation in their H I contours, and a fairly smooth, disk-like stellar component. At 3σ contour levels their H I appears uniform and axisymmetric within resolution limits. However, our small sample does include a number of notable individual galaxies.

VGS_07 has a faint companion which does not appear to be interacting. It exhibits a clumpy, knotty, blue morphology similar to that seen in chain-galaxies forming at high redshift, or like edge-on, low surface-brightness galaxies. It has an enormous 200 Å Hα equivalent width, suggesting a high star formation rate per unit stellar mass, and possible starburst. We see fairly regular disk-like kinematics within the gas distribution. It sits near the center of the void and not near a wall-like configuration.

VGS_12 is a polar ring galaxy, and is discussed in detail in Chapter 2 of this thesis. It is one of the most massive of our sample, in both its H I ($3.0 \pm 0.5 \times 10^9$ $M_\odot$) and dynamical (1.5×10^{11} $M_\odot$) mass, and is substantially more massive in H I than stellar mass (1.05×10^9 $M_\odot$). In addition, its H I disk is extremely extended compared to the optical, yet free of stars down to the SDSS surface brightness limits, ruling out most merger scenarios.

[1] The MPA-JHU catalog is publicly available and may be downloaded at http://www.mpa-garching.mpg.de/SDSS/DR7/

Simulations can reproduce such gas-rich, star-poor rings through tidal encounters, however at equal mass ratios they destroy the rotational support of the central galaxy, resulting in the formation of an elliptical remnant (Bournaud et al. 2005). The low concentration index, r_{90}/r_{50}, of 2.25 implies the central stellar disk is late type (Shen et al. 2003) and thus rotationally supported, suggesting an alternative formation mechanism such as slow accretion of cold gas is necessary (Iodice et al. 2006). In addition, VGS_12 is situated in a thin wall between two voids, and aligned such that this gas would have been accreted out of the voids.

VGS_30 is accompanied by a similar sized H I rich companion. The two are seen to be embedded in a common H I envelope, and due to the thinness of the target galaxy disk, presumably they are interacting for the first time. They are cosmologically situated in a void wall between two large voids.

VGS_32 is particularly close by, and thus significantly better resolved in optical and H I imaging. It displays a quite beautiful flocculent spiral pattern, and a textbook flattened rotation curve. It sits nicely isolated in the middle of a void.

VGS_34 has a very faint, kinematically distinct protuberance in H I. The disturbed optical morphology also suggests that the target is undergoing some sort of interaction, as the bulge appears extremely red while the farther reaches of the disk appear relatively blue and distorted. The H I extension does align with a small, distant H I detected companion. VGS_34 also has a very large rotational velocity. Like VGS_07, it sits near the center of the void and not near a wall-like configuration. Because the SDSS fiber only contains light from the central red bulge, stellar mass and star formation rate parameters derived for this galaxy may not accurately represent the galaxy as a whole.

VGS_35 presents a fairly regular appearance in H I, except in its orientation. We see it exhibiting a strong warp, or perhaps a mis-aligned H I disk as we see in VGS_12. This is complicated by the elongated beam, which is suspiciously aligned with the H I in the disk. Possibly the elongation of the beam is exaggerating a slight warp in the H I disk, as the velocity contours in the center appear aligned with the optical disk, and bend away only in the outer parts. It is located near the transition of a small void into a larger one.

VGS_38 has the most optically disturbed appearance, and it was also the only selected void galaxy to have a known companion, VGS_38a, which is only 12 kpc away on the sky and at nearly overlapping velocity. The surprising discovery of a third galaxy, VGS_38b, aligned

with the first two, all three of which are connected by a faint 1σ H I bridge, results in a system that stretches nearly 50 kpc across the sky. VGS_38, despite its chaotic appearance, exhibits relatively smooth rotation in the direction perpendicular to the line of galaxies. It is difficult to understand how this system could have undergone a major, disruptive interaction while leaving the gas disk unperturbed. It is located at the edge of its void.

4.4.5 Control Sample

From projection of each observation's primary beam through the SDSS redshift catalog we find that there are 22 SDSS galaxies in the neighboring velocity ranges of our data set. From our H I blind search for control sample galaxies (described in Section 4.3), we detect 11 of the known SDSS galaxies and have upper limits for another seven, with mass limit $M_{H\,I} = 2.9 \times 10^4\ d^2\ M_\odot$, d in Mpc and assuming a velocity width of 100 km s^{-1}. The data on the remaining four galaxies were badly affected by man made interference and could not be used. We also include with this control sample five galaxies detected in H I which are not in the SDSS redshift survey, all with optical counterparts. This brings the control sample to a total of 23 galaxies. We calculate the environmentally filtered density contrast (see Section 4.2) for each control sample galaxy, and find almost all of them are in average or overdense environments. The *g*-band images with H I contours of all H I detected control galaxies are presented in Figure 4.10, and color images of all control galaxies are presented in Figure 4.11.

To ensure confidence in our detections we only consider galaxies within $25'$ of the beam center, which corresponds to a factor of five reduced sensitivity. The combination of larger distances and displacement from the beam center produces fairly low S/N detections, resulting in larger mass uncertainties than for our targeted void galaxies. The lowest H I contour levels for our control sample (Figure 4.10) correspond to roughly twice the column density as the H I contours for our void galaxies (Figure 4.7). The H I mass detection of NGC 5422 is actually less than the estimated error, however kinematics and spatial coincidence with the optical galaxy allow us to identify this as a real detection. Parameters for all detected and nondetected control galaxies are listed in Tables 4.7, 4.8 and 4.9.

Table 4.7: Control sample galaxy parameters taken from the SDSS catalog. To be compared with Table 4.1. Units of right ascension are hours, minutes, and seconds, and units of declination are degrees, arcminutes, and arcseconds. z is the spectroscopic redshift. g and r list the apparent magnitudes as measured by the SDSS DR7. Absolute magnitudes have been corrected for galactic extinction. δ indicates the filtered density contrast, described in Section 4.2.3. $\Delta\theta$ lists the angular displacement from the beam center. Control galaxies # 4, 9, 19, 20 and 21 are not spectroscopically targeted by the SDSS.

#	SDSS ID	ra (J2000.0)	dec (J2000.0)	z	g	r	$g-r$	M_r	δ	$\Delta\theta$ ($'$)
1	SDSS J083649.77+325109.3	08 36 49.8	+32 51 09	0.025672	16.26	15.90	0.36	-19.4	0.28	17.9
2	SDSS J102002.03+562423.8	10 20 02.0	+56 24 24	0.024881	17.53	17.22	0.31	-18.0	7.81	23.8
3	SDSS J102257.38+555449.3	10 22 57.4	+55 54 50	0.025082	15.63	15.08	0.55	-20.1	7.81	24.7
4	SDSS J102316.27+562656.2	10 23 16.3	+56 26 56	-	18.57	18.50	0.07	-16.6	6.84	8.2
5	SDSS J102653.21+622011.4	10 26 53.2	+62 20 12	0.031975	15.41	14.78	0.64	-20.9	-0.44	17.9
6	SDSS J102823.88+623706.6	10 28 23.9	+62 37 07	0.030462	16.39	15.60	0.78	-20.0	1.84	2.2
7	SDSS J102942.07+624826.2	10 29 42.1	+62 48 27	0.023326	16.64	16.24	0.40	-18.8	1.63	16.5
8	SDSS J103105.76+623531.5	10 31 05.8	+62 35 32	0.030938	18.09	17.73	0.36	-17.9	3.65	19.2
9	SDSS J130418.89+544209.9	13 04 18.9	+54 42 10	-	18.81	18.50	0.30	-15.7	3.23	10.4
10	SDSS J132433.97+592018.6	13 24 34.0	+59 20 19	0.028574	15.29	14.38	0.91	-21.1	0.04	23.1
11	SDSS J132523.37+593643.1	13 25 23.4	+59 36 43	0.026625	15.10	14.65	0.46	-20.7	-0.13	16.0
12	SDSS J132630.72+594313.7	13 26 30.7	+59 43 14	0.029162	15.30	14.48	0.83	-21.1	0.21	14.4
13	SDSS J132722.97+592537.8	13 27 23.0	+59 25 38	0.028064	16.96	16.80	0.16	-18.7	0.31	4.6
14	SDSS J135839.08+552910.3	13 58 39.1	+55 29 10	0.027418	18.06	17.86	0.20	-17.5	-0.70	21.5
15	NGC 5422	14 00 42.0	+55 09 52	0.006071	12.93	12.06	0.87	-20.1	24.71	5.5
16	SDSS J140058.24+553405.1	14 00 58.2	+55 34 05	0.006174	16.37	15.90	0.47	-16.2	24.71	19.1
17	SDSS J140101.95+545555.2	14 01 02.0	+54 55 55	0.005950	17.31	16.69	0.61	-15.4	17.97	19.7
18	SDSS J142515.68+522128.9	14 25 15.7	+52 21 29	0.031980	17.84	17.56	0.29	-18.2	-0.32	14.0
19	SDSS J143422.81+522839.0	14 34 22.8	+52 28 39	-	16.51	16.26	0.25	-17.2	1.48	20.6
20	SDSS J143441.11+523935.1	14 34 41.1	+52 39 35	-	18.32	18.14	0.18	-15.3	1.48	11.8
21	SDSS J143519.21+522745.0	14 35 19.2	+52 27 45	-	18.32	18.02	0.29	-15.4	1.48	17.0
22	SDSS J143744.16+524331.2	14 37 44.2	+52 43 32	0.011288	15.87	15.69	0.18	-17.8	1.48	16.8
23	SDSS J143835.24+524223.1	14 38 35.2	+52 42 23	0.011301	15.63	15.15	0.48	-18.3	1.48	24.5

Table 4.8: H I properties of control sample galaxies. To be compared with Table 4.5. Non-detections list the 3σ upper limit on the H I mass. V_{sys} is the systemic H I velocity, using the optical definition. D is the distance to the target galaxy. r_{90} and $r_{H\,I}$ list the optical and H I radius, respectively. When possible, poorly resolved systems list the upper limit for $r_{H\,I}$ and M_{dyn}. W_{50} and W_{20} are the 50% and 20% H I line widths, respectively, corrected for instrumental broadening. The inclination, i, is calculated such that 90° is edge-on.

#	$M_{H\,I}$ ($10^8 M_\odot$)	V_{sys} (km s^{-1})	D (Mpc)	r_{90} (kpc)	$r_{H\,I}$ (kpc)	W_{50} (km s^{-1})	W_{20} (km s^{-1})	i (°)	M_{dyn} ($10^{10} M_\odot$)	$M_{H\,I}/L_r$
1	43.0 ± 7.7	7702	110	6.4	19.7	194	229	70	4.89	1.0
2	18.6 ± 10.8	7464	107	5.8	< 9.8	59	119	26	< 1.05	1.6
3	24.2 ± 16.3	7525	107	10.1	-	213	260	61	-	0.3
4	5.8 ± 3.4	7350	105	3.6	-	39	51	74	-	1.7
5	137.6 ± 79.0	9593	137	8.5	37.9	187	148	30	30.02	0.8
6	< 7.3	-	131	3.9	-	-	-	70	-	-
7	20.4 ± 7.6	6998	100	3.2	15.0	50	202	46	0.43	0.8
8	< 18.1	-	133	5.2	-	-	-	78	-	-
9	2.3 ± 1.2	4765	68	2.4	< 4.3	105	114	72	< 0.31	1.6
10	< 24.0	-	122	9.5	-	-	-	68	-	-
11	105.0 ± 21.6	7987	114	6.3	22.7	73	150	43	1.50	0.8
12	< 10.8	-	125	9.4	-	-	-	58	-	-
13	36.5 ± 6.3	8419	120	6.8	15.7	95	160	50	1.42	1.7
14	13.3 ± 9.0	8225	118	4.3	-	134	155	63	-	1.8
15	0.6 ± 0.9	1821	26	3.8	-	-	-	57	-	0.0
16	< 0.7	-	26	1.9	-	-	-	60	-	-
17	< 0.7	-	25	1.1	-	-	-	25	-	-
18	35.0 ± 19.7	9594	137	2.9	20.6	206	214	65	6.21	2.6
19	21.1 ± 6.8	3386	48	3.8	11.5	96	117	30	2.54	3.8
20	3.2 ± 1.5	3386	48	1.5	-	96	108	63	-	3.2
21	2.5 ± 0.8	3386	48	2.6	-	58	71	60	-	2.2
22	15.6 ± 5.6	3386	48	3.0	10.1	54	87	51	0.29	1.6
23	< 4.5	-	48	3.0	-	-	-	66	-	-

Table 4.9: Stellar and star formation parameters for control sample galaxies. To be compared with Table 4.6. Targets not detected in the 1.4 GHz continuum list the 3σ upper limit on the $\mathrm{SFR}_{1.4GHz}$.

#	$\mathbf{M_*}$ ($10^8\mathbf{M_\odot}$)	$\mathbf{SFR}_{H\alpha}$ ($\mathbf{M_\odot\ yr^{-1}}$)	$\mathbf{SFR}_{1.4GHz}$ ($\mathbf{M_\odot\ yr^{-1}}$)	$\mathbf{EW(H\alpha)}$ (Å)	$\mathbf{SFR}_{H\alpha}/M_*$ ($10^{-11}\ \mathbf{yr^{-1}}$)	$\mathbf{SFR}_{H\alpha}/\mathbf{M_{H\ I}}$ ($10^{-11}\ \mathbf{yr^{-1}}$)
1	55.0	0.36	< 0.67	16.9	6.6	8.4
2	8.5	0.28	< 1.19	35.1	32.4	14.8
3	302.0	0.21	< 1.37	2.6	0.7	8.8
4	-	-	< 0.33	-	-	-
5	407.4	0.70	1.32	3.2	1.7	5.1
6	354.8	0.00	< 0.85	-1.2	0.0	-
7	20.0	0.27	< 0.49	24.8	13.8	13.5
8	-	-	< 2.10	12.4	-	-
9	-	-	< 0.15	-	-	-
10	-	-	< 2.78	0.1	-	-
11	-	-	12.29	-	-	-
12	691.8	7.14	9.33	46.2	10.3	-
13	4.5	0.38	< 0.39	44.1	84.6	10.3
14	-	-	< 1.10	40.1	-	-
15	-	-	< 0.02	-	-	-
16	3.2	0.00	< 0.08	2.4	0.0	-
17	2.8	0.00	< 0.08	-1.1	0.0	-
18	20.0	0.70	< 0.76	134.7	34.9	19.9
19	-	-	< 0.17	-	-	-
20	-	-	< 0.08	-	-	-
21	-	-	< 0.12	-	-	-
22	0.2	0.10	< 0.12	120.5	641.4	6.5
23	-	-	< 0.52	5.2	-	-

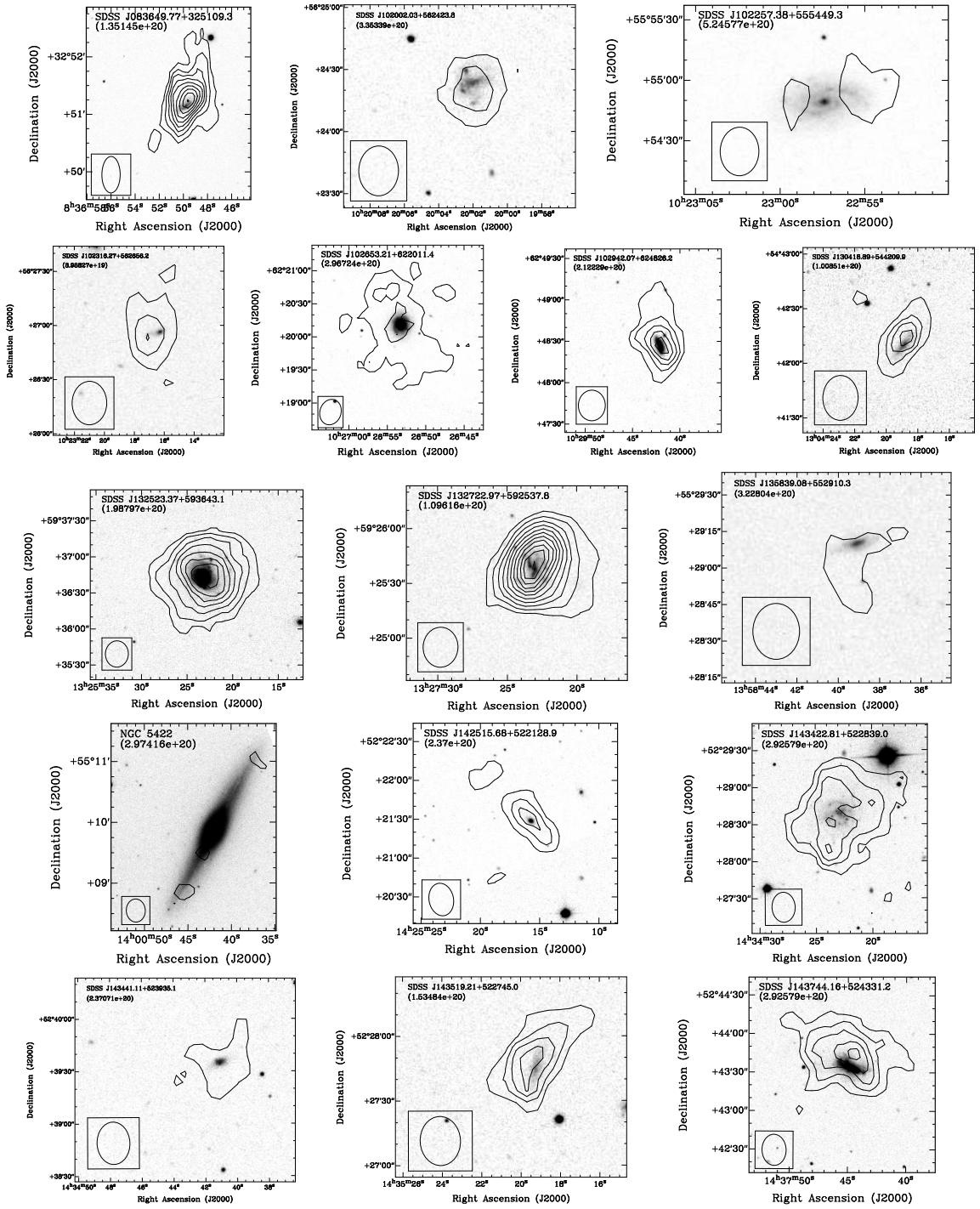

Figure 4.10: Control sample. Contours in the total intensity maps are at intervals of 2σ, with the corresponding column density value (in units of cm^{-2}) given in the top left corner of each image. Note that low signal to noise results in relatively high 2σ column densities of $\sim 2 \times 10^{20}\ cm^{-2}$. Contours for NGC 5422 represent a 1σ detection.

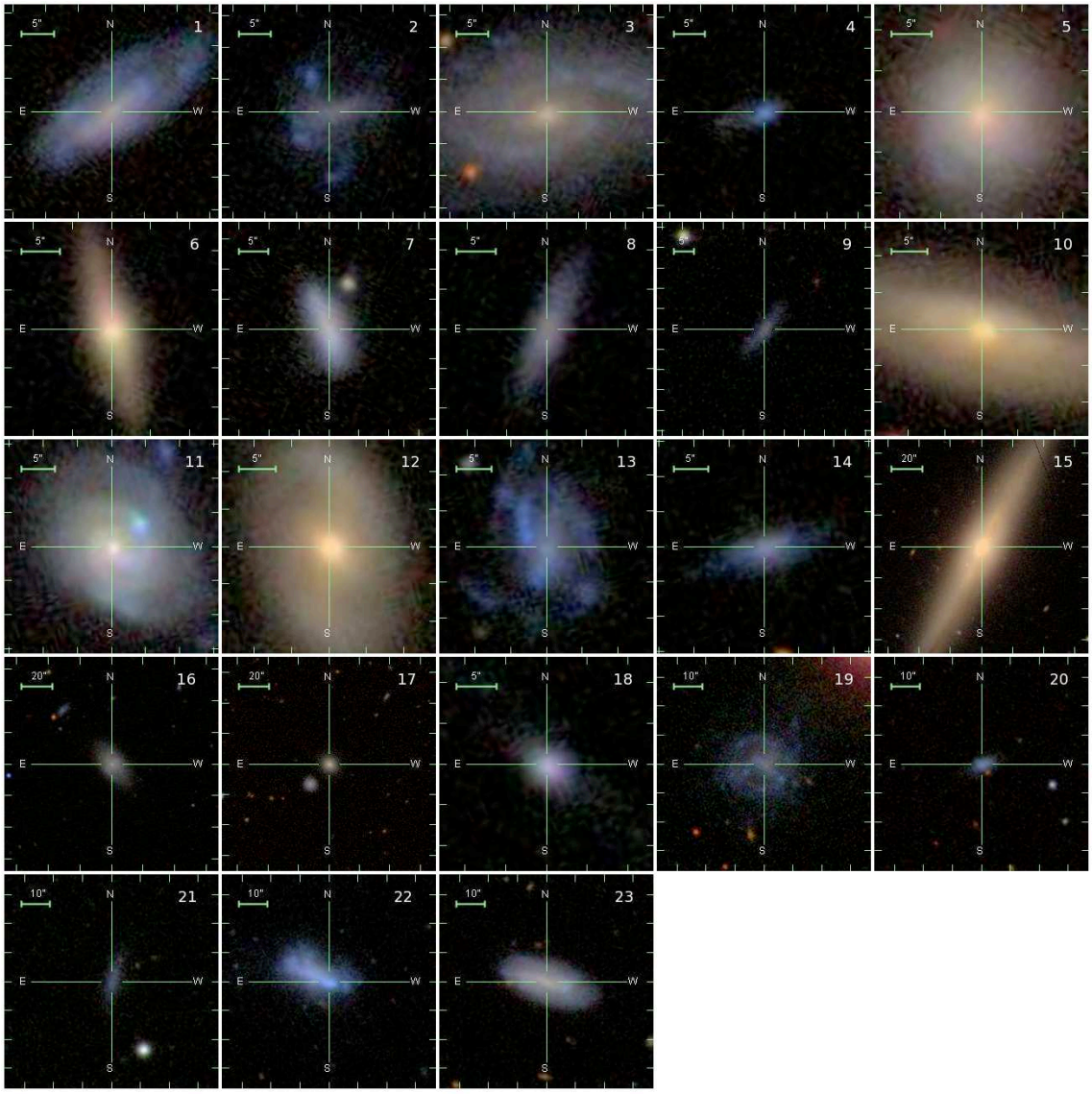

Figure 4.11: Our control sample galaxies, scaled to the same physical size as the void galaxy sample in Figure 4.3. Composite color images are taken from the online SDSS Finding Chart tool.

4.5 Analysis

Our void galaxy sample is carefully selected to represent the galaxies populating the deepest underdensities (Figure 4.4, 4.5). For comparison we constructed a volume-limited ($z < 0.02$, $M_r < -16.9$) comparison sample of SDSS galaxies, and use our DTFE procedure to calculate the density field (see Section 4.2). Eleven of our 15 void galaxies fall within these volume-limited criteria. In Figure 4.12, we compare the properties of the volume-limited sample as a function of density with our void sample, the *IRAS* selected Boötes void galaxy sample of Szomoru et al. (1996), and the second Center for Astrophysics redshift survey (CfA2) lowest density void galaxy subsample of Grogin & Geller (1999). Due to the incompleteness of past redshift surveys and brighter magnitude limits, the densities of the Boötes void galaxies and the CfA2 void galaxies have been recalculated based on their inclusion in the SDSS following our method described in Section 4.2, which results in the identification of many of these galaxies as being in average or even overdense environments. In this respect we emphasize the advantage of using the localized and better defined density values of the DTFE method, defined by the spatial galaxy distribution itself, as opposed to more conventional artificially filtered density values. As a result, our geometric selection criterion manages to probe a galaxy population which is truly representative of the extremely underdense and desolate void interiors, instead of the more conventional techniques probing the galaxies near the void boundaries.

The main photometric and spectroscopic comparison sample of void galaxies against which we measure our pilot sample of geometrically selected void galaxies is that used by Rojas et al. (2004) and Rojas et al. (2005). Their sample of 1010 void galaxies out to z = 0.089 was compiled from the first SDSS data release, where they define a void galaxy as having the third nearest neighbor be at a distance greater than 10 Mpc. All other galaxies are placed into a wall galaxy sample. Within these samples they constructed a bright ($M_r \leq -17$) and nearby (d < 103 Mpc) subsample of 76 void galaxies and 1071 wall galaxies. Although our geometric method is very different, ten of our void galaxies satisfy these luminosity and distance criteria.

As has been noted by e.g. Rojas et al. (2004), more luminous galaxies prefer denser environments, and our void galaxy sample is able to probe specifically those low luminosity galaxies which make up the bulk of the void galaxy population that were previously

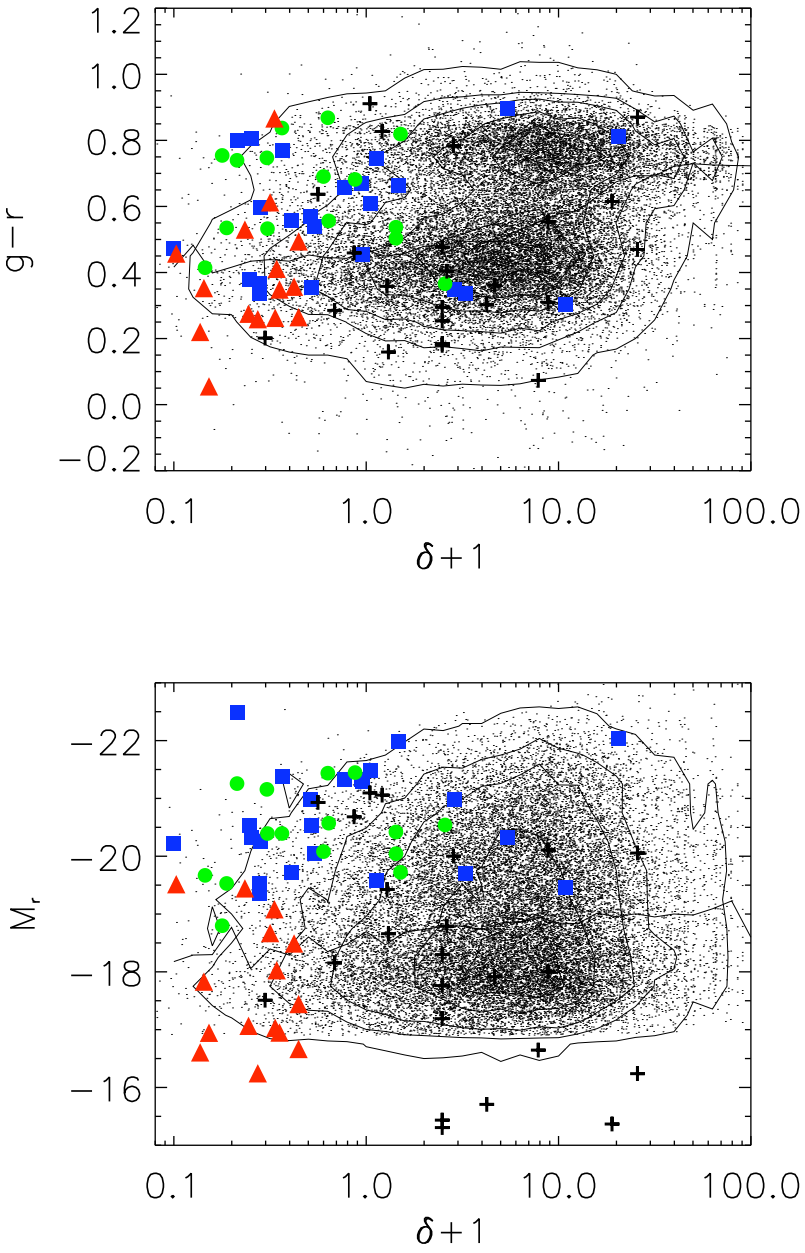

Figure 4.12: Distribution of $g-r$ colors and r-band absolute magnitudes for our void galaxy sample (triangles), our control galaxy sample (crosses), the Boötes void galaxy sample of Szomoru et al. (1996) (squares) and the CfA void galaxy sample of Grogin & Geller (1999) (circles) as a function of density, compared with a volume limited ($z < 0.02$, $M_r < -16.9$) sample of SDSS galaxies (points, with contours to guide the eye). The line represents the median of the SDSS sample.

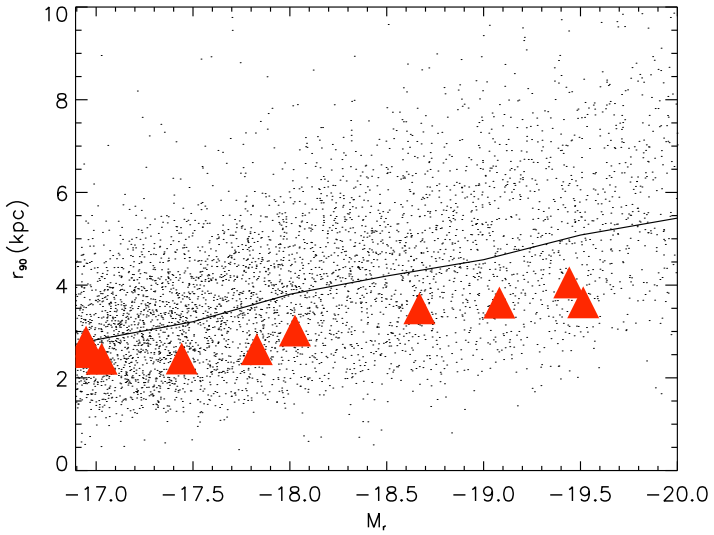

Figure 4.13: The r-band r_{90} radii of the stellar disk. Our late-type void galaxies (triangles) fall systematically below the median (line) of a volume limited SDSS sample of late-type galaxies (dots).

inaccessible. Also apparent in Figure 4.12 is the dominance of blue galaxies at the deepest underdensities, where we again are more accurately sampling the void galaxy population. For our 10 bright, nearby void galaxies, we find a median r-band luminosity of -18.3 $\pm$ 0.3, and median $g-r$ color of 0.46 $\pm$ 0.06, which is in good agreement with the bright, nearby void galaxy sample of Rojas et al. (2004). We also note that our control sample is fairly representative of the range of absolute magnitudes, colors, and densities contained within the SDSS.

While we have selected void galaxies with a representative distribution of absolute magnitudes, we find that our void galaxies have stellar disks that are smaller than average. Compared with the volume limited SDSS sample, we find the r-band r_{90} radius of our late type void galaxies is systematically lower than the median for late type galaxies (Figure 4.13), where galaxies with a concentration index $r_{90}/r_{50} < 2.86$ are taken to be late type following Shen et al. (2003).

While our targeted void galaxies are small, they would generally not be classified as dwarf galaxies. All have $M_r <$ -16 and exhibit moderate circular velocities, typically 50-100 km s^{-1}. All galaxies exhibit signs of rotation in H I, though limiting resolution and lower sensitivity at the disk outskirts means we do not always see a flattening of the rotation

Table 4.10: Stellar and star formation properties as compared with Rojas et al. (2005)

Property	Our void sample ($\mu \pm \sigma_\mu$)	Rojas void sample ($\mu \pm \sigma_\mu$)	Rojas wall sample ($\mu \pm \sigma_\mu$)
EW(Hα)(Å)	32.143 ± 7.90	33.316 ± 3.74	21.91 ± 0.809
$\log_{10}(M_*/M_\odot)$	9.217 ± 0.152	9.333 ± 0.066	9.390 ± 0.018
SFR(Hα)($M_\odot$ yr^{-1})	0.451 ± 0.188	0.323 ± 0.048	0.194 ± 0.011
S-SFR(Hα)(yr^{-1})	(39.81 ± 20.9) $\times 10^{-11}$	(17.57 ± 3.222) $\times 10^{-11}$	(12.57 ± 0.958) $\times 10^{-11}$

curve. M_{dyn} is typically 10^9 to 10^{10} $M_\odot$. The companion galaxies detected are mostly dwarf galaxies, however our small number statistics for this pilot sample limit us from extending these few detections to draw conclusions on the missing dwarf galaxy population pointed out by Peebles (2001).

The stellar and star formation properties of our nearby, bright sample measured from the SDSS spectra are in general agreement with the values found for the nearby, bright void galaxy sample of Rojas et al. (2005), and show our pilot sample to be a good representation of the actively star-forming galaxies typically found in voids (Table 4.10). Even our small sample exhibits the same trend for increased Hα equivalent width, star formation rate (SFR) and specific SFR (star formation rate per stellar mass, S-SFR) in low density environments when compared with the wall sample of Rojas et al. (2005). Despite these average increases, we do not see a clear trend of S-SFR with density, but we do see a hint of a trend for increased SFR per H I mass at the lowest densities (Figure 4.14). The mean S-SFR for our full void sample is (88 ± 45) × 10^{-11} year^{-1} and for our control sample is (82 ± 63) × 10^{-11} year^{-1}.

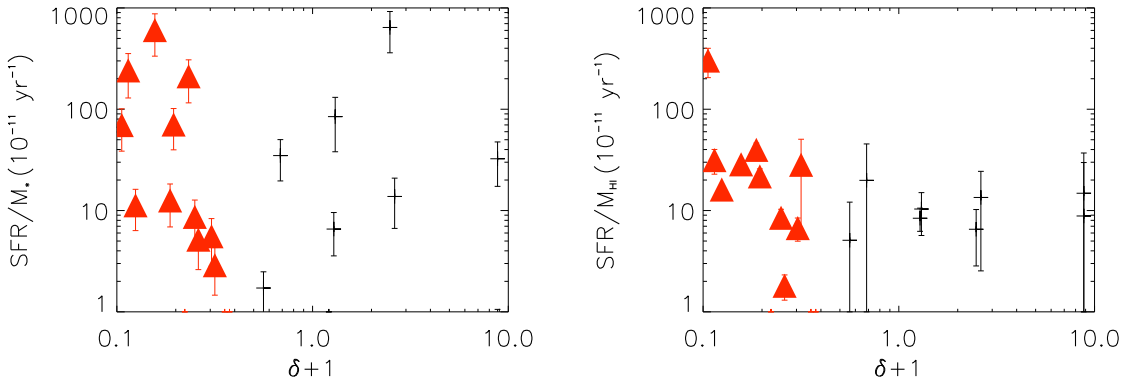

Figure 4.14: S-SFR (left) and SFR/H I mass (right) as a function of density for our void galaxies (triangles) and our control sample (crosses).

The mean SFR per H I mass is $(37 \pm 22) \times 10^{-11}$ year^{-1} for our void sample and $(11 \pm 2) \times 10^{-11}$ year^{-1} for our control sample. Our complete sample of 60 void galaxies will be more suitable for the identification of possible trends with density.

Because our control sample for this pilot study is not very large, we have drawn from the literature two additional comparison samples with which to compare H I properties. The first is a sample of 113 late-type dwarf and irregular galaxies from the WHISP project (Westerbork observations of neutral Hydrogen in Irregular and SPiral galaxies, van der Hulst et al. 2001) observed with the WSRT, selected to have Hubble type later than Sd or magnitude fainter than $M_B = -17$ (Swaters et al. 2002, S02). These galaxies were not selected in any way for environment, and in general their cosmological environments are unknown. In an attempt to control for environment, we also compare with the H I imaging survey of 43 Ursa Major galaxies brighter than -16.8 and more inclined than 45° with the WSRT (Verheijen & Sancisi 2001, VS01). Because of their shared membership in the Ursa Minor poor cluster, we assume some uniformity of environment within this comparison sample.

While optically our sample is blue with higher star formation rates than galaxies in average density environments, the H I content appears to be more typical. As in Geha et al. (2006), we find that the smallest galaxies are the most gas-rich. Figure 4.15 shows that the ratio of $M_{H\,I}/L_r$ increases with decreasing luminosity similar to S02 and VS01. This trend seems to persist over a wide range of luminosities and environments. Huchtmeier et al. (1997) measured that $M_{H\,I}/L_B$ increases with decreasing density. We do not see such a trend with density within our small sample of void galaxies (Figure 4.16), nor do we see a significant difference between our void sample and control sample, or compared to the higher density comparison samples of S02 or VS01 (Figure 4.15).

Our void galaxies follow the tight relation between H I mass and H I diameter demonstrated by S02 and VS01 (Figure 4.17, right). The agreement of our underdense sample with both comparison samples shows that the mean H I surface density is quite robust, regardless of environment. Galaxy samples also show a correlation between H I mass and optical diameter (e.g. Verheijen & Sancisi (2001)). The range of optical diameters of our void galaxies is too small to look for a trend, but the measured values seem reasonable (Figure 4.17, left). Our control sample does appear to lie on the correlation. We also note that while the resolution is not optimal, our H I disks typically appear roughly exponential

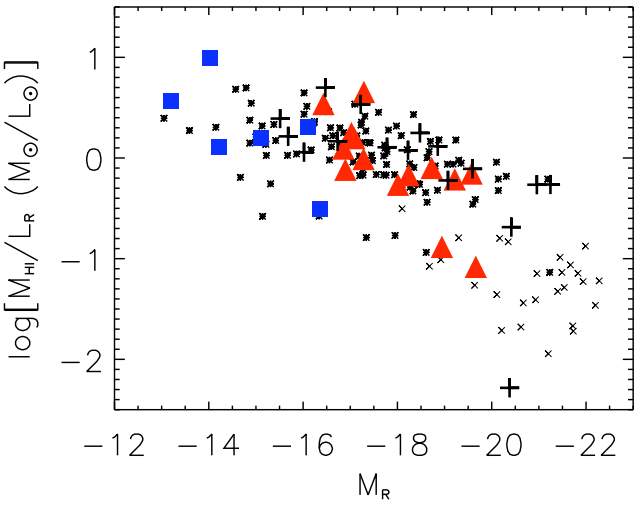

Figure 4.15: H I mass to light ratio for our targeted void galaxies (triangles), companion galaxies (squares), and our control galaxies (crosses). For additional comparison, late-type disk galaxies from Swaters et al. (2002) (stars) and Ursa Major galaxies from Verheijen & Sancisi (2001) (X's) are included.

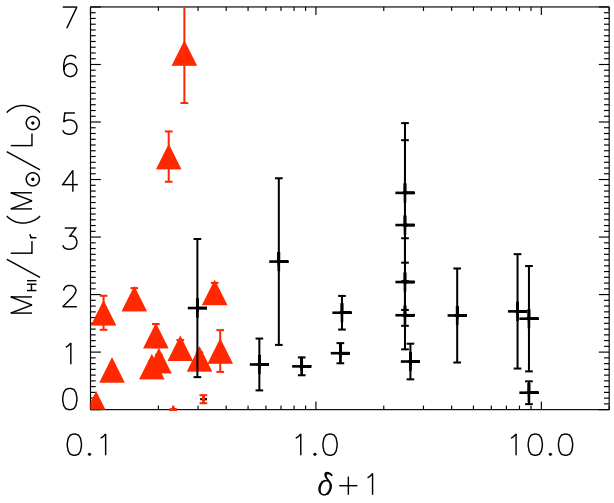

Figure 4.16: H I mass to light ratio as a function of density for our void galaxies (triangles) and our control sample (crosses).

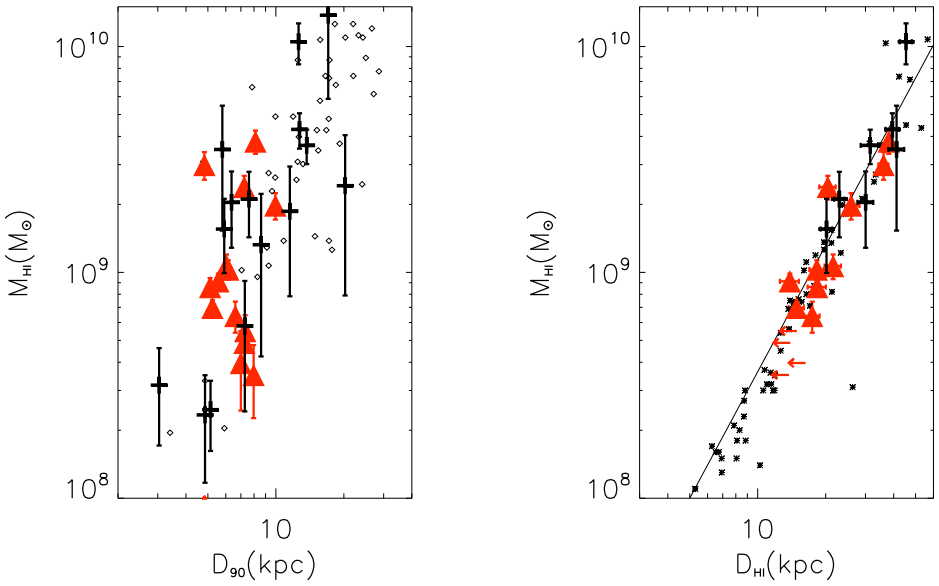

Figure 4.17: H I mass versus optical diameter on the left, and versus H I diameter on the right. Our target galaxies (triangles) and control sample (crosses) are compared with the sample of late-type galaxies by Swaters et al. (2002) at right (stars) and a cross-match of ALFALFA galaxies (Giovanelli et al. 2007) with the SDSS catalog at left (diamonds). Overplotted on the right is the fit from Verheijen & Sancisi (2001) for their sample of Ursa Major galaxies. Red arrows mark the upper limit on the diameter for those void systems which are poorly resolved in H I.

in shape at their outer extent (Figure 4.9), as was found by S02 for their late type disk galaxies.

Hoeft et al. (2006) predict the effects of UV background ionization will suppress star formation and lead to a reduced baryon fraction in small, $M_{tot} \sim 10^9$ $M_\odot$ halos. Our halos are just on the verge of this boundary, with $M_{dyn} > 2 \times 10^9$ $M_\odot$, however we see no deviation from the baryonic Tully-Fisher relationship (Figure 4.18). W_{20} values have been corrected for turbulent velocity broadening and inclination angle. Error bars reflect a 10% uncertainty in inclination. Baryonic masses have been calculated from the sum of the stellar mass and 1.4 times the H I mass to estimate the total gas component from our H I measurement. In some of our systems (open triangles) we do not observe a flattening of the rotation curve due to poor resolution or truncated H I disks. As expected, better

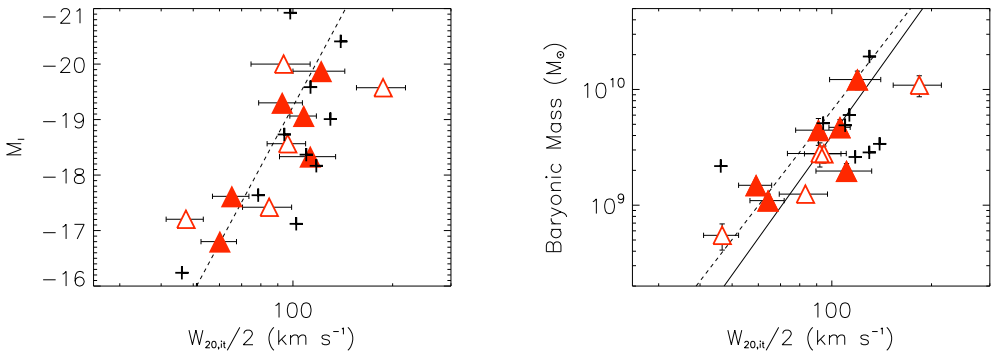

Figure 4.18: Void galaxies following the I-band (left) and baryonic (right) Tully-Fisher relationship, where the filled symbols are galaxies for which we observe a flattened rotation curve and the open symbols are systems where the rotational velocity continues to rise at the furthest radii. Crosses indicate our control sample galaxies. The dashed lines were taken from Geha et al. (2006) which were fit to over three orders of magnitude mass range. The solid line shows the fit taken from McGaugh et al. (2000).

determined systems (filled triangles) show a tighter correlation and are more consistent in their scatter about the Tully-Fisher relationship, as derived in environmentally insensitive samples (McGaugh et al. 2000; Geha et al. 2006).

4.6 Speculation

With such a small sample, it is difficult to discuss the statistical properties of our void galaxy sample. It is tempting, instead, to consider the situation of individual galaxies in our sample and the way they might illustrate the larger picture of galaxy evolution in voids which we are interested in investigating.

In some respects we expect to find galaxy evolution progressing within voids somewhat independent of their large scale environment. Simulations show that halos in underdense regions at fixed halo mass have assembled at later times (Gao et al. 2005), so we would expect that the galaxies we find there to simply be in a slightly earlier stage of their development. This is reflected in the increased number of blue, star forming galaxies found in voids (Rojas et al. 2004, 2005). However the formation of red elliptical galaxies by mergers is not excluded, and in fact the galaxies in the very deepest underdensities cluster

more strongly than those in more moderately underdense regions, though less strongly than in average density regions (Abbas & Sheth 2007). This is similar to the conclusions of Szomoru et al. (1996), who found a similar number of H I companions for void and cluster galaxies. The clustering of dwarf companions appears somewhat consistent, regardless of environment (Weinberg et al. 1991). Our sample probes to lower H I limits than Szomoru et al. (1996), though they covered a much larger volume, and already we find a third of our void galaxies have previously unidentified companions, two of which share a common H I envelope with the targeted void galaxy.

We may expect environment will play some role. Cold mode accretion dominates in low mass halos and at earlier times (Kereš et al. 2009), so we expect to see evidence of this ongoing slow accretion, though it may be difficult to distinguish from the effects of minor mergers. As void galaxies are statistically bluer at fixed luminosity than galaxies at higher densities (Park et al. 2007; von Benda-Beckmann & Müller 2008), perhaps this is evidence of different mechanisms of gas accretion at play. VGS_12, our void galaxy with a polar disk of H I gas, might provide direct evidence that these processes do occur within voids, as it is difficult to amass such a substantial amount of H I without disrupting the rotational support of the central stellar disk (Bournaud et al. 2005, Chapter 2 of this thesis). We also note that the properties which do not seem to be sensitive to the low density environment ($M_{H\ I}/L_r$, the ratio of H I mass to H I diameter, the Tully-Fisher relation) are more indicative of the internal effects within the galaxies. The SFR, which we find is tentatively higher in voids, is instead indicative of an external effect, such as higher gas inflow.

Additional evidence of environmental effects should be evident. Hierarchical merging through the expansion of voids and thinning of void walls results in the formation of substructure within voids. Filaments in dark matter which are quite distinct in simulations are tenuously traced by dark matter halos, but depending on the halo occupation distribution may not be apparent in the galaxy distribution, particularly when limited to the distribution of bright galaxies. These alignments may be more apparent in H I as with VGS_38, where the linear alignment of all three galaxies, including the H I bridge between them, may already be sufficient to identify a filament within the void that is not apparent in the SDSS redshift survey.

Filaments which are too low density to be traced by galaxies may still be traced by low column density H I or warm ionized gas (McLin et al. 2002; Manning 2002; Stocke et al.

2007). The intervening regions between the aligned components we detect near our void galaxies are ideal locations to use background quasars as probes and search for absorption due to underlying filamentary structure.

4.7 Conclusion

We have completed a pilot study imaging in H I 15 void galaxies selected from the SDSS and located in d $<$ 100 Mpc voids. Galaxies were selected purely by their environment to be located in areas less than half the cosmic density. We detected 14 of our target galaxies with masses from 3.5 $\times$ 10^8 to 3.8 $\times$ 10^9 $M_\odot$, and had one nondetection with a 3σ upper limit of 2.1 $\times$ 10^8 $M_\odot$. In addition we detected six companion galaxies in H I, two of which appear to be interacting with the targeted void galaxy.

We also constructed a control sample from the SDSS redshift survey galaxies and H I detected galaxies in the ∼10,000 km s^{-1} velocity range simultaneously imaged by the WSRT behind and in front of the target galaxy with each pointing. Of 18 detectable SDSS cataloged galaxies contained within the volume, we detected 11 in H I with masses 6.0 $\times$ 10^7 $M_\odot$ to 1.4 $\times$ 10^{10} $M_\odot$. In addition, we include five galaxies detected in H I which were not contained in the SDSS redshift catalog. Because of their location within the SDSS footprint we were able to environmentally locate these systems as almost all being in regions at or above the cosmic mean. Due to the small size of this control sample, when comparing specific H I properties of our void galaxies we also looked to comparison samples of well studied galaxies taken from the literature with similar size and luminosity constraints, though their environments are not known.

Provisionally, we find that our void galaxies have small optical stellar disks, typical H I masses for their luminosity, and generally follow the Tully-Fisher relation. Consistent with previous surveys, they have increased rates of star formation, with the suggestion of a trend for increased star formation at lowest density. While this pilot sample is too small for any statistical findings, we did discover many of our targets to be individually interesting dynamically and kinematically in their H I distributions. In particular, one shows possible evidence of ongoing cold mode accretion.

Ultimately, we aim to compile a sample of ∼60 void galaxies which will comprise a new Void Galaxy Survey (VGS). This sample size will be comparable to the H I sample of 24

void galaxies and 18 H I detected companion galaxies in Boötes by Szomoru et al. (1996), but more representative of the faint void galaxy population in a more distributed collection of voids. Our sample will also provide a good compliment to the sample of 76 SDSS void galaxies examined photometrically and spectroscopically by Rojas et al. (2004) in similarly nearby voids, and will be ideal for a careful investigation of the questions surrounding how void galaxies get their gas, form substructures and generally populate the most underdense regions of the universe.

Chapter 5

The Void Galaxy Survey: I. Optical Properties and H I Morphology and Kinematics

The following text will be submitted to the Astronomical Journal. The full reference for this work is Kreckel, K., Platen, E., Aragón-Calvo, M. A. , van Gorkom, J. H., van de Weygaert, R., van der Hulst, J. M., Beygu, B. 2011, in prep.

We have carefully selected a sample of 60 galaxies that reside in the deepest underdensities of geometrically identified voids within the SDSS. H I imaging of 55 galaxies with the WSRT reveals morphological and kinematic signatures of ongoing interactions and gas accretion. We probe a total volume of 485 Mpc^3 within the voids, with an angular resolution of 8 kpc at an average distance of 85 Mpc. We reach column density sensitivities of 5×10^{19} cm^{-2}, corresponding to an H I mass limit of 3×10^8 $M_\odot$. We detect H I in 41 galaxies, with total masses ranging from 1.7×10^8 to 5.5×10^9 $M_\odot$. The upper limits on the 14 non-detections are not inconsistent with their expected H I mass to light ratios. We find that the void galaxies are generally gas rich, low luminosity, blue disk galaxies, with optical and H I properties that are not unusual for their luminosity and morphology. The sample spans a range of absolute magnitudes (-16.1 > M_r > -20.4) and colors ($0.06 < g - r < 0.87$), and includes disk and irregular galaxies. We also identify three as

early type galaxies, all of which are not detected in H I. All galaxies have stellar masses less than 3 $\times$ 10^{10} $M_{\odot}$, suggesting the void galaxy population may still be in the process of assembling. The small scale clustering in the void, within 600 kpc and 200 km s^{-1}, is similar to that in higher density regions, and we identify 18 H I rich neighboring galaxies in the voids. Most are within 100 kpc and 100 km s^{-1} of the targeted galaxy, and we find no significant population of H I rich low luminosity galaxies filling the voids as predicted by simulations.

5.1 Introduction

Voids represent a unique environment for the study of galaxy evolution (van de Weygaert & Platen 2009). The lower density environment, equivalent to a lower Ω_m universe (Goldberg & Vogeley 2004), should result in shorter merger histories and slower evolution of galaxies. As different mechanisms of gas accretion are believed to dominate in low mass halos, voids present a unique environment in which to search for signs of ongoing cold mode accretion (Kereš et al. 2005). The nature of these void galaxies also provides a test of cold dark matter (CDM) cosmology theory, which predicts that these underdense regions should be filled with low mass dark matter halos that are not observed as low luminosity galaxies (Peebles 2001). This may have implications for galaxy formation through the suppression of star formation in the lowest mass halos (Hoeft et al. 2006), and may provide general insights into how galaxies populate dark matter halos (Tinker & Conroy 2009)

Observations of void galaxies selected by different methods consistently show that they are typically low luminosity and late type disk galaxies (Grogin & Geller 1999; Rojas et al. 2004). They are blue with elevated specific star formation rates (Grogin & Geller 2000; Rojas et al. 2005), though it is not clear if these characteristics are different from low luminosity disk galaxies in the field (Patiri et al. 2006b; Park et al. 2007). As the observed shift in the luminosity function results naturally from CDM cosmology (Hoyle et al. 2005; Aragón-Calvo 2007, Chapter 6 of this thesis), it is possible that the large scale underdensity surrounding void galaxies has little effect on the evolution of these systems.

We are undertaking a multi-wavelength study of 60 void galaxies as part of a new Void Galaxy Survey (VGS, see Chapter 4 of this thesis). A variety of different techniques have been developed to identify voids and void galaxies within galaxy redshift surveys. Colberg

et al. (2008) provides an interesting comparison of the results of different void-finding algorithms applied to a single set of simulation data. These techniques generally agree in locating large scale underdensities, however the extent and shape of the identified voids differ dramatically. We employ a powerful geometric method that makes no assumption about the size or shape of the voids within a galaxy distribution. This unique approach allows us to robustly identify a void galaxy population suitable for systematic study.

The earliest void galaxy surveys were severely biased by the selection methods, targeting only emission-line (Kirshner et al. 1981; Lee et al. 2000) or IRAS bright (Szomoru et al. 1996) galaxies. Subsequent void galaxy studies were based on more uniformly selected redshift surveys with denser coverage were also biased by the shallow depth available and select only the more luminous void galaxies (Grogin & Geller 1999), which do not represent the bulk of the low luminosity void galaxy population. We use the Sloan Digital Sky Survey (SDSS) Data Release 7 (DR7), which contains uniform photometry and spectroscopic distances to all galaxies over a quarter of the sky that are brighter than 17.77 r-band magnitudes, and focus on relatively nearby galaxies (D $<$ 100 Mpc) allowing us to probe void galaxies to M_r = -17. In this paper we discuss the SDSS optical properties of 60 void galaxies, carefully selected by their geometry to be centrally located within the deepest underdensities, and we image the neutral gas content in 55 of these systems with the Westerbork Synthesis Radio Telescope (WSRT).

The WSRT employs a new backend that enables us to simultaneously image a wide velocity range encompassing the full radial extent of the void with high sensitivity, and good velocity and spatial resolution to trace gas morphology and kinematics of both the target and any neighboring galaxies within the void. Systematic H I imaging of void galaxies has been undertaken by Szomoru et al. (1996), who identified 24 IRAS selected galaxies within the Boötes void. Their targets were generally gas rich and late type, with H I morphologies consistent with similar galaxies in the field, though their sample suffers from contamination by galaxies in higher density substructures within the void (Chapter 4 of this thesis). Single dish observations of dwarf galaxies identify targets in the void as having slightly higher H I mass to light ratio (Huchtmeier et al. 1997; Pustilnik et al. 2002), though the sample size is small and targets are typically unresolved and may be confused within the H I beam. H I blind observations of voids have not revealed a large number of uncataloged detections (Weinberg et al. 1991, Saintonge et al. 2008).

In Section 5.2 we describe our methods for identifying voids and void galaxies. Section 5.3 outlines the H I observations undertaken at the WSRT, and Section 5.4 details our results. We discuss the significance and implications of this work in Section 5.5, and include a full catalog of the H I and SDSS optical data for the sample in Appendix 5.A. Except in Section 5.2, we assume $H_0 = 70$ km s^{-1} Mpc^{-1}.

5.2 Sample selection

A complete description of our void finding method and void galaxy selection criteria are presented in the pilot study for this project (Chapter 4 of this thesis). We summarize here the main points of our technique and refer the reader to the more detailed description previously published and references therein.

We apply the Delaunay Tessellation Field Estimator (DTFE[1]; Schaap & van de Weygaert 2000; Schaap 2007; van de Weygaert & Schaap 2009) to the SDSS redshift survey. We use these galaxies, independent of their luminosity, as tracers to recover the underlying dark matter density field within the local universe. Using redshift as a proxy for distance, we construct contiguous Voronoi tessellations within the three dimensional galaxy distribution, and consider the piecewise linear extrapolation of these cells over the whole sample volume by means of the corresponding dual Delaunay tessalation. The result is a tessellation of the whole volume where the area of each cell is inversely related to the galaxy density at that position. After weighting the resulting density field for the decrease in luminosity sensitivity as a function of redshift, we apply a 1 h^{-1} Mpc Gaussian smoothing filter to the reconstructed dark matter density field.

The void identification proceeds by treating the reconstructed density field as a landscape of hills and valleys that is slowly flooded. As neighboring valleys fill and intervening hills are submerged we identify void substructure and boundaries at these higher density regions. In this way we organically outline the void shapes, without imposing requirements of spherical voids or selection of a local minimum, and are able to unambiguously identify galaxies that reside within the voids. This watershed transform results in basins that are identified as voids by the Watershed Voidfinder algorithm (Platen et al. 2007), and the cor-

[1]Public software available at http://www.astro.rug.nl/∼voronoi/DTFE/dtfe.html (Cautun & van de Weygaert 2011)

responding boundaries are subsequently identified as walls and filaments using the Cosmic Spine formalism (Aragón-Calvo et al. 2010).

We have selected a sample of 60 galaxies located in the local universe using voids identified within the SDSS DR7. A redshift limit of $z < 0.025$ is imposed to maximize the H I sensitivity and spatial resolution considering the $\sim 20''$ resolution of the WSRT. We also exclude any galaxies within ∼750 km s^{-1} of the line of sight of a cluster to avoid contamination by redshift distortions, such as the finger of god effect. An initial sample of galaxies is selected to have a density contrast, $\delta \equiv \rho/\rho_u - 1$, of less than -0.5, where ρ_u is the mean density estimated for the SDSS. We then choose only those galaxies most centrally located within their void and away from the SDSS boundaries so the surrounding void is well contained within the redshift survey. All galaxies were selected purely by their environmental geometry, with no bias for morphology, luminosity or color outside of the inherent SDSS redshift survey limitations. This is clear when observing the range of galaxy type in the SDSS color images as scaled to the same physical size (see Figure 5.A-1). The SDSS positions of all 60 galaxies are shown in Figure 5.1.

5.3 Observations

We list the properties measured from the SDSS in Table 5.1. We observed a total of 55 of the 60 VGS galaxies at the WSRT between 2006-2010, with the instrumental parameters given in Table 5.2. All targets were observed in maxi-short configuration, with shortest baselines of 36, 54, 72 and 90 meters to maximize surface brightness sensitivity and a longest baseline of 2754 meters to achieve angular resolutions of $19'' \times 19''/cos(\delta)$ using an optimal u,v taper for the detection of low surface brightness emission. This corresponds to spatial scales of ∼8 kpc at 85 Mpc, the average distance for our sample. As the WSRT is an east-west array, we scheduled full 12 hour track observations to achieve complete UV coverage of each target, however a number of our observations were interrupted by priority target of opportunity observations. Some, but not all, of our incomplete observations were completed at later times. The final total integration time for all galaxies not detected in H I is at least 10.5 hours. The final total integration time for detected galaxies is at least 8 hours, with only VGS_18 having just 5 hours. Total integration times for each target are included in Table 5.4.

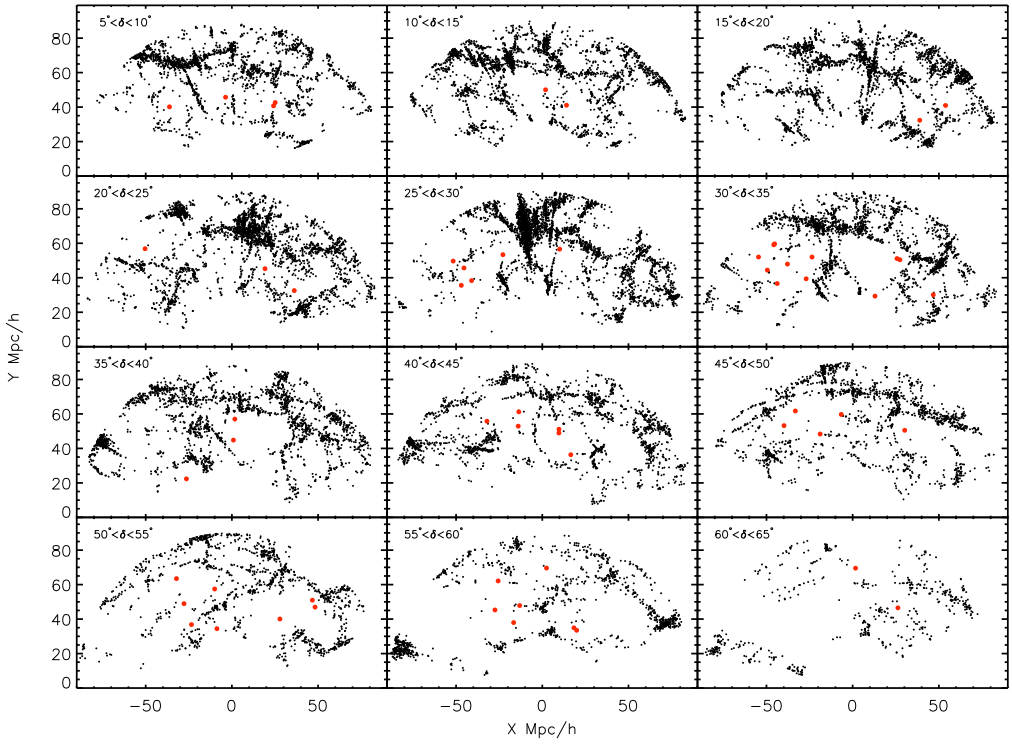

Figure 5.1: The position of the VGS galaxies (red) within the SDSS galaxy distribution (black). Each panel shown a slice in declination of 5°, with the specific range plotted given in the upper left corner.

Target observations were done with two polarizations and 512 channels of 19.5 kHz each, for a total bandwidth of 10 MHz. All data reductions were done using AIPS. The absolute flux scale was determined using Baars et al. (1977) and corrected to the observing frequency. Two of the flux calibrators 3C48, 3C286, 3C147 and CTD93 were observed with 15 minute snapshots, one before and one after the target observation, which were also used for phase and bandpass calibration. The non-standard calibrator CTD93 was calibrated assuming a 20 cm flux of 4.83 Jy, as given in the VLA calibrator manual.

Continuum emission is subtracted in the UV plane using the emission free channels of each cube. Image cubes with a robust parameter of 1 were CLEANed down to 0.5 mJy beam^{-1} ($\sim$1 σ) based on a box around the emission region of each cube, and were Hanning smoothed to a typical velocity resolution of 8.6 km s^{-1}. Zeroth and first moment maps were made using masking by a data cube Hanning and Gaussian smoothed to 25 km s^{-1} and 30″, respectively, and 1.5σ clipping. We reach typical column density sensitivities of 5 $\times$ 10^{19} cm^{-2}.

Table 5.1: Parameters of selected void galaxies taken from the SDSS catalog. Units of right ascension are hours, minutes, and seconds, and units of declination are degrees, arcminutes, and arcseconds. g and $g-r$ are drawn from the apparent model magnitudes as measured by the SDSS DR7. Absolute magnitudes have been corrected for galactic extinction. δ gives the filtered density contrast at $R_f = 1\ h^{-1}$ Mpc.

Name	SDSS ID	ra (J2000)	dec (J2000)	z	r	$g-r$	M_r	δ
VGS_01	J083707.48+323340.8	08 37 07.5	+32 33 41	0.018531	17.17	0.49	-17.4	-0.77
VGS_02	J085453.60+181924.6	08 54 53.6	+18 19 25	0.022558	17.39	0.40	-17.6	-0.83
VGS_03	J090500.99+183128.4	09 05 01.0	+18 31 28	0.016868	17.51	0.46	-16.9	-0.80
VGS_04	J091355.47+244552.3	09 13 55.5	+24 45 52	0.016228	16.55	0.53	-17.8	-0.75
VGS_05	J092252.91+513243.7	09 22 52.9	+51 32 44	0.022437	15.03	0.76	-19.9	-0.93
VGS_06	J093602.69+515638.6	09 36 02.7	+51 56 39	0.023032	17.40	0.31	-17.6	-0.85
VGS_07	J100642.44+511623.9	10 06 42.5	+51 16 24	0.016261	17.30	0.06	-16.9	-0.84
VGS_08	J102235.27+453821.2	10 22 35.3	+45 38 21	0.019613	17.72	0.33	-16.9	-0.82
VGS_09	J102250.68+561932.1	10 22 50.7	+56 19 32	0.012995	17.52	0.26	-16.2	-0.78
VGS_10	J102316.63+091330.1	10 23 16.6	+09 13 30	0.015781	16.86	0.34	-17.4	-0.84
VGS_11	J102351.86+095914.8	10 23 51.9	+09 59 15	0.016486	16.05	0.51	-18.3	-0.61
VGS_12	J102819.23+623502.6	10 28 19.2	+62 35 03	0.017804	17.41	0.26	-17.0	-0.74
VGS_13	J103152.68+315034.6	10 31 52.7	+31 50 35	0.019126	16.35	0.48	-18.3	-0.71
VGS_14	J103506.46+550847.5	10 35 06.5	+55 08 48	0.013154	16.72	0.28	-17.1	-0.81
VGS_15	J103913.14+310650.4	10 39 13.1	+31 06 50	0.019071	15.40	0.56	-19.2	-0.76
VGS_16	J104807.05+430525.4	10 48 07.1	+43 05 25	0.013308	17.57	0.28	-16.2	-0.88
VGS_17	J105042.23+315119.5	10 50 42.2	+31 51 20	0.010695	16.95	0.18	-16.4	-0.77
VGS_18	J105352.26+214549.6	10 53 52.3	+21 45 50	0.016383	17.47	0.39	-16.8	-0.78
VGS_19	J111029.61+134558.1	11 10 29.6	+13 45 58	0.014467	16.52	0.39	-17.5	-0.52
VGS_20	J114124.92+415221.9	11 41 24.9	+41 52 22	0.016630	18.04	0.17	-16.3	-0.92
VGS_21	J114303.00+404939.1	11 43 03.0	+40 49 39	0.017344	15.02	0.83	-19.4	-0.87
VGS_22	J114535.20+270742.5	11 45 35.2	+27 07 43	0.019162	17.57	0.37	-17.1	-0.44
VGS_23	J121716.54+124742.8	12 17 16.5	+12 47 43	0.016688	15.24	0.41	-19.1	-0.82
VGS_24	J121754.98+583935.6	12 17 55.0	+58 39 36	0.023207	14.90	0.55	-20.1	-0.80
VGS_25	J121908.24+372644.1	12 19 08.2	+37 26 44	0.019014	17.64	0.26	-17.0	-0.86
VGS_26	J122032.40+604958.4	12 20 32.4	+60 49 58	0.023186	16.38	0.46	-18.7	-0.84
VGS_27	J122123.12+393659.4	12 21 23.1	+39 36 59	0.014941	17.77	0.35	-16.3	-0.71
VGS_28	J124420.87+082412.5	12 44 20.9	+08 24 13	0.015286	17.61	0.69	-16.5	-0.82
VGS_29	J125119.35+480144.3	12 51 19.4	+48 01 44	0.020022	16.28	0.36	-18.4	-0.65
VGS_30	J130526.08+544551.9	13 05 26.1	+54 45 52	0.019435	18.05	0.22	-16.6	-0.89
VGS_31	J131606.19+413004.2	13 16 06.2	+41 30 04	0.020903	14.75	0.32	-20.1	-0.64
VGS_32	J132232.48+544905.5	13 22 32.5	+54 49 06	0.011835	14.17	0.53	-19.4	-0.80
VGS_33	J132505.06+430405.9	13 25 05.1	+43 04 06	0.018236	17.61	0.45	-16.9	-0.82
VGS_34	J132718.56+593010.2	13 27 18.6	+59 30 10	0.016539	15.22	0.87	-19.1	-0.81
VGS_35	J135113.62+453509.2	13 51 13.6	+45 35 09	0.017299	16.36	0.41	-18.0	-0.70
VGS_36	J135535.46+593041.3	13 55 35.5	+59 30 41	0.022398	16.46	0.36	-18.5	-0.75
VGS_37	J135836.29+292121.4	13 58 36.3	+29 21 21	0.019354	17.06	0.35	-17.6	-0.87
VGS_38	J140034.49+551515.1	14 00 34.5	+55 15 15	0.013820	16.95	0.35	-16.9	-0.64
VGS_39	J140328.54+324151.7	14 03 28.5	+32 41 52	0.019037	15.25	0.81	-19.4	-0.74
VGS_40	J141326.46+503841.6	14 13 26.5	+50 38 42	0.023717	16.90	0.50	-18.2	-0.89
VGS_41	J141916.95+472839.1	14 19 17.0	+47 28 39	0.023371	17.21	0.43	-17.8	-0.92
VGS_42	J142416.41+523208.3	14 24 16.4	+52 32 08	0.018762	15.88	0.61	-18.7	-0.68
VGS_43	J142540.61+443835.2	14 25 40.6	+44 38 35	0.021455	17.85	0.36	-17.0	-0.86
VGS_44	J143052.33+551440.0	14 30 52.3	+55 14 40	0.017656	14.92	0.46	-19.5	-0.89
VGS_45	J143553.77+524400.6	14 35 53.8	+52 44 01	0.014553	17.33	0.26	-16.7	-0.62
VGS_46	J144338.46+322002.7	14 43 38.5	+32 20 03	0.015915	16.80	0.35	-17.4	-0.63
VGS_47	J145314.59+462910.8	14 53 14.6	+46 29 11	0.022155	14.56	0.75	-20.4	-0.89
VGS_48	J145450.57+305729.0	14 54 50.6	+30 57 29	0.024966	17.13	0.64	-18.1	-0.88

Continued on next page

Table 5.2: Parameters of the WSRT observations

Configuration	Maxi-short
Date	2006-2010
No. telescopes	13
Total bandwidth	40 MHz
No. channels	4×512
Shortest spacing	36 m
Longest spacing	2754 m
FWHM primary beam	$36'$
Synthesized beam	$19'' \times 19''/\sin(\delta)$
rms (robust = 1)	0.4 mJy Beam^{-1}
velocity resolution	8.6 km s^{-1}

Table 5.1 – Continued

Name	SDSS ID	ra (J2000)	dec (J2000)	z	r	$g-r$	M_r	δ
VGS_49	J145659.94+313308.5	14 56 59.9	+31 33 09	0.024920	15.51	0.41	-19.7	-0.85
VGS_50	J145909.32+324756.3	14 59 09.3	+32 47 56	0.020358	15.35	0.72	-19.4	-0.85
VGS_51	J151211.61+243344.1	15 12 11.6	+24 33 44	0.025307	17.02	0.23	-18.3	-0.93
VGS_52	J151410.95+064449.0	15 14 11.0	+06 44 49	0.018018	17.61	0.27	-16.9	-0.90
VGS_53	J152523.40+291018.8	15 25 23.4	+29 10 19	0.021473	15.65	0.54	-19.2	-0.79
VGS_54	J153035.83+264408.5	15 30 35.8	+26 44 09	0.023895	16.28	0.70	-18.9	-0.68
VGS_55	J153132.44+343055.8	15 31 32.4	+34 30 56	0.025146	16.27	0.46	-19.0	-0.94
VGS_56	J153341.47+280843.5	15 33 41.5	+28 08 44	0.018715	15.79	0.74	-18.8	-0.82
VGS_57	J153821.22+331105.1	15 38 21.2	+33 11 05	0.022171	14.59	0.53	-20.4	-0.69
VGS_58	J154452.18+362845.6	15 44 52.2	+36 28 46	0.011522	15.70	0.35	-17.8	-0.88
VGS_59	J154615.07+332017.8	15 46 15.1	+33 20 18	0.019028	17.81	0.39	-16.8	-0.67
VGS_60	J155721.55+254718.9	15 57 21.6	+25 47 19	0.019646	15.85	0.81	-19.0	-0.78

Given the $36'$ full width half maximum of the WSRT primary beam and the 10 MHz bandwidth, with each observation we probe a total area covering $\sim$1.2 Mpc and $\sim$1,200 km s^{-1} at 85 Mpc, the average distance of our sample. Blind H I detections were identified using data cubes smoothed to 20 km s^{-1} and a 6 kilowavelength taper, increasing the 1σ sensitivity to $\sim$0.25 mJy beam^{-1}, and 5σ clipping in forming a zeroth moment map. We consider only detections within $25'$ of the beam center, which corresponds to a factor of five reduced sensitivity. Candidate objects were then confirmed by eye to be extended both spatially and in velocity, and those confirmed to be environmentally located within the void are included here as companion void galaxies (Table 5.3).

Table 5.3: Companion galaxy parameters taken from the SDSS catalog. Units of right ascension are hours, minutes, and seconds, and units of declination are degrees, arcminutes, and arcseconds. g and $g-r$ are drawn from the apparent model magnitudes as measured by the SDSS DR7. Absolute magnitudes have been corrected for galactic extinction. $\Delta\theta$, Δd and Δv list the displacement from the beam center, projected sky separation, and velocity separation, respectively, between the target and companion galaxy. δ gives the filtered density contrast at $R_f = 1$ h^{-1} Mpc.

name	SDSS ID	ra (J2000.0)	dec (J2000.0)	r	$g-r$	M_r	$\Delta\theta$ ($'$)	Δd (kpc)	Δ v (km s^{-1})	δ
VGS_07a	J100519.69+511038.3	10 05 19.7	+51 10 38	20.12	0.03	-14.1	14.2	288	-21	-0.84
VGS_09a	J102241.41+561208.5	10 22 41.4	+56 12 09	22.26	0.02	-11.4	7.5	121	-85	-0.78
VGS_10a	J102308.72+085847.1	10 23 08.7	+08 58 47	16.31	0.31	-17.9	14.8	292	20	-0.84
VGS_26a	J122105.48+610514.2	12 21 05.5	+61 05 14	13.79	0.52	-21.0	15.8	455	-856	-0.55
VGS_30a	J130531.13+544553.8	13 05 31.1	+54 45 54	18.39	0.29	-16.2	0.7	17	-74	-0.89
VGS_31a	J131614.69+412940.0	13 16 14.7	+41 29 40	14.38	0.50	-20.4	1.6	42	-10	-0.64
VGS_31b	J131559.18+412955.9	13 15 59.2	+41 29 56	16.78	0.21	-18.0	1.3	34	50	-0.64
VGS_34a	J132640.92+593202.5	13 26 40.9	+59 32 03	20.31	0.10	-14.0	5.1	104	42	-0.81
VGS_36a	J135533.54+593110.7	13 55 33.5	+59 31 11	19.10	0.14	-15.8	0.6	17	0	-0.75
VGS_37a	J135836.06+292321.3	13 58 36.1	+29 23 21	16.26	0.36	-18.3	2.0	48	-114	-0.82
VGS_38a	J140032.44+551445.9	14 00 32.4	+55 14 46	17.59	0.15	-16.1	0.6	9	-21	-0.64
VGS_38b	J140025.68+551318.5	14 00 25.7	+55 13 19	18.82	0.20	-14.9	2.3	37	10	-0.64
VGS_39a	J140321.80+324530.3	14 03 21.8	+32 45 30	19.48	-0.04	-15.2	3.9	92	73	-0.74
VGS_51a	J151230.45+243352.1	15 12 30.4	+24 33 52	20.66	0.05	-14.6	4.3	133	19	-0.85
VGS_53a	J152641.63+292359.8	15 26 41.6	+29 24 00	16.78	0.24	-18.1	21.9	586	-26	-0.79
VGS_54a	J153035.99+264446.1	15 30 36.0	+26 44 46	19.05	0.42	-16.1	0.6	18	-98	-0.65
VGS_56a	J153443.07+281309.6	15 34 43.1	+28 13 10	18.91	0.29	-15.7	14.3	333	47	-0.83
VGS_57a	J153836.08+331637.6	15 38 36.1	+33 16 38	17.83	0.13	-17.1	6.4	175	-72	-0.61

5.3.1 HI properties

H I parameters of these galaxies are calculated following the methods described in the pilot study (Chapter 4 of this thesis). H I properties for all target and companion galaxies are listed in Table 5.4. H I mass is calculated as $M_{H\,I} = 2.36 \times 10^5\ d^2 \int S\ dv\ M_\odot$, where d is distance in Mpc, S is flux density in Jy and dv is in km s^{-1}. For targets at an average distance of 85 Mpc and assumed velocity width of 100 km s^{-1} the 3σ upper limit on detections is $\sim 3 \times 10^8\ M_\odot$. We measure the 20% and 50% H I line width, W_{20} and W_{50}, of each galaxy by constructing a global H I profile, summing the flux in each channel for a boxed area around the galaxy. 15 km s^{-1} errors reflect uncertainties of one channel on either side.

As in our pilot study, the majority of the targets are incompletely resolved by the WSRT, many extending no more than 2 or 3 times the H I beam. To estimate the radial extent of the H I we apply the iterative deconvolution method described by Lucy (1974), which sums

the H I total intensity along the disk minor axis to create a one dimensional strip profile of the disk. This profile is then iteratively fit assuming an axisymmetric disk to recover the face-on H I radial surface density profile (see Figure 5.A-3). We measure the H I radius, $r_{H\,I}$, as that position where the surface density falls below 1 $M_\odot$ pc^{-2}, and quote an upper limit where we are resolution limited, with typical errors of $\sim$2 kpc.

Inclinations are calculated from SDSS r-band isophotal radii under the assumption that galaxy disks are intrinsically oblate and axisymmetric with a three dimensional axis ratio of $q_o = 0.19$ (Geha et al. 2006), with estimated errors of 10%. Position angles are determined by considering both the r-band optical and H I kinematic major axes. In cases where they disagree significantly (VGS_12) we choose the orientation of the H I disk.

5.3.2 SDSS optical parameters

As part of the SDSS survey, optical spectra were obtained for each galaxy using a 3″ fiber, which in addition to being used to determine redshift, may be used to estimate other stellar properties. We use the publicly available MPA-JHU catalog for SDSS DR7 [2] to obtain estimates of the star formation rate (SFR) and stellar mass in all void and control galaxies (Table 5.5). Star formation rates are calculated from the emission line features and aperture corrected to estimate the total SFR for the galaxy, using the method developed by Brinchmann et al. (2004). Stellar masses are obtained using fits to the *ugriz* photometry following the philosophy of Kauffmann et al. (2003c) and Salim et al. (2007), and correcting for the contribution by emission lines to the broadband magnitudes using the fiber spectra. Errors in the SFR are relatively large, roughly a factor of two. Errors on the stellar mass estimate are typically $\sim$0.1 dex, with significantly larger scatter for the lowest ($M_* \sim 10^8$ $M_\odot$) stellar masses.

[2] http://www.mpa-garching.mpg.de/SDSS/DR7/

Table 5.4: H I properties of targeted void galaxies and companions. Non-detections list the 3σ upper limit on the H I mass. t lists the total integration time for each object. V_{sys} is the systemic H I velocity, using the optical definition. D is the distance to the target galaxy. r_{90} and $r_{H\,I}$ list the optical and H I radius, respectively. When possible, poorly resolved systems list the upper limit for $r_{H\,I}$ and M_{dyn}. W_{50} and W_{20} are the 50% and 20% H I line widths, respectively, corrected for instrumental broadening. The inclination, i, is calculated such that 90° is edge-on.

Name	**t**	$M_{\mathbf{H\,I}}$	V_{sys}	**D**	$\mathbf{r_{90}}$	$\mathbf{r_{H\,I}}$	W_{50}	W_{20}	**i**	**P.A.**	$\mathbf{M_{dyn}}$	$\mathbf{M_{H\,I}/L_r}$
	(hr)	(10^8 $M_\odot$)	(km s^{-1})	**(Mpc)**	**(kpc)**	**(kpc)**	(km s^{-1})	(km s^{-1})	(°)	(°)	(10^{10} $M_\odot$)	
VGS_01	12.0	< 2.1	-	-	2.4	-	-	-	60	-	-	-
VGS_02	12.0	6.49 ± 1.85	6637	95	3.4	< 7.6	111	136	47	80	< 1.00	0.80
VGS_03	12.0	< 1.85	-	-	1.8	-	-	-	55	-	-	-
VGS_04	12.0	< 1.71	-	-	1.5	-	-	-	46	-	-	-
VGS_05	12.0	< 3.27	-	-	6.1	-	-	-	37	-	-	-
VGS_06	12.0	15.63 ± 2.52	6883	98	3.9	12.9	180	187	71	282	2.71	1.90
VGS_07	12.0	8.6 ± 0.8	4901	70	2.6	9.2	119	144	50	270	1.28	1.9
VGS_07a	12.0	3.23 ± 0.65	4880	69	3.5	-	41	49	-	-	-	9.7
VGS_08	12.0	3.95 ± 1.51	5853	84	4.4	< 5.7	84	126	51	12	< 0.39	0.89
VGS_09	12.0	10.3 ± 1.0	3881	55	3.1	9.1	110	126	68	105	0.74	4.4
VGS_09a	12.0	0.57 ± 0.14	3796	54	1.5	-	41	49	-	-	-	20.2
VGS_10	12.0	15.01 ± 2.00	4737	68	5.4	10.2	152	176	87	310	1.36	2.21
VGS_10a	12.0	16.73 ± 1.91	6637	95	6.5	-	177	193	-	-	-	1.5
VGS_11	12.0	21.73 ± 2.11	4907	70	4.2	17.0	75	100	18	5	6.16	1.38
VGS_12	12.0	29.9 ± 4.2	5316	76	2.4	18.0	154	179	29	5	10.55	6.2
VGS_13	12.0	12.35 ± 2.45	5691	81	3.5	12.8	213	229	68	275	3.89	0.82
VGS_14	12.0	6.4 ± 1.0	3933	56	3.3	8.7	110	134	67	40	0.72	1.3
VGS_15	0.0	-	-	-	7.6	-	-	-	53	-	-	-
VGS_16	12.0	< 1.16	-	-	1.7	-	-	-	60	-	-	-

Continued on next page

Table 5.4 – Continued

Name	t	$M_{\mathrm{H\ I}}$	V_{sys}	D	r_{90}	$r_{\mathrm{H\ I}}$	W_{50}	W_{20}	i	P.A.	M_{dyn}	$M_{\mathrm{H\ I}}/L_r$
	(hr)	(10^8 $M_\odot$)	(km s^{-1})	(Mpc)	(kpc)	(kpc)	(km s^{-1})	(km s^{-1})	(°)	(°)	(10^{10} $M_\odot$)	$M_\odot/L_\odot$
VGS_17	0.0	-	-	-	3.4	-	-	-	79	-	-	-
VGS_18	5.0	3.91 ± 1.17	4850	69	3.5	< 7.1	118	134	82	312	< 0.58	0.99
VGS_19	12.0	3.16 ± 0.76	4318	62	1.7	< 1.5	32	125	60	230	< 0.01	0.43
VGS_20	0.0	-	-	-	1.1	-	-	-	43	-	-	-
VGS_21	8.0	21.45 ± 3.58	5171	74	8.8	15.8	314	330	79	288	9.38	0.51
VGS_22	12.0	< 2.62	-	-	1.6	-	-	-	63	-	-	-
VGS_23	8.5	38.52 ± 4.57	4990	71	4.5	16.9	203	236	49	75	7.11	1.16
VGS_24	12.0	< 3.35	-	-	4.6	-	-	-	35	-	-	-
VGS_25	12.0	1.69 ± 0.64	5680	81	2.3	< 2.0	135	135	43	325	< 0.46	0.37
VGS_26	10.5	14.90 ± 3.23	6942	99	5.8	12.5	206	231	69	75	3.55	0.69
VGS_26a	10.5	100.25 ± 18.28	4907	70	6.8	-	171	257	-	-	-	0.6
VGS_27	12.0	3.32 ± 0.75	4421	63	1.7	< 3.7	41	91	55	55	< 0.05	1.31
VGS_28	12.0	< 1.67	-	-	4.2	-	-	-	54	-	-	-
VGS_29	0.0	-	-	-	3.8	-	-	-	65	-	-	-
VGS_30	12.0	5.5 ± 1.0	5666	81	3.7	< 7.5	50	93	77	180	< 0.12	1.7
VGS_30a	12.0	4.52 ± 0.79	5592	79	2.1	-	24	41	-	-	-	2.1
VGS_31	12.0	19.89 ± 2.90	6247	89	4.0	< 10.4	153	178	52	155	< 2.31	0.25
VGS_31a	12.0	14.63 ± 1.97	5691	81	6.5	-	196	298	-	-	-	0.1
VGS_31b	12.0	1.66 ± 0.95	4850	69	2.1	-	110	170	-	-	-	0.1
VGS_32	12.0	38.0 ± 4.5	3522	50	4.1	19.0	171	187	46	310	6.29	0.9
VGS_33	12.0	8.39 ± 1.81	5443	78	2.0	< 8.3	110	117	60	285	< 0.77	1.97
VGS_34	12.0	23.9 ± 2.9	4917	70	3.6	10.2	231	299	50	280	5.34	0.7
VGS_34a	12.0	0.50 ± 0.16	4959	70	1.1	-	33	58	-	-	-	1.7
VGS_35	12.0	10.7 ± 1.3	5191	74	3.0	10.8	145	187	65	340	1.61	0.9
VGS_36	12.0	19.8 ± 2.7	6684	95	5.0	13.0	190	224	79	190	2.82	1.1
VGS_36a	12.0	-	6684	95	1.6	-	-	-	-	-	-	-

Continued on next page

Table 5.4 – Continued

Name	t	$M_{\mathrm{H\ I}}$	V_{sys}	D	r_{90}	$r_{\mathrm{H\ I}}$	W_{50}	W_{20}	i	P.A.	M_{dyn}	$M_{\mathrm{H\ I}}/L_r$
	(hr)	(10^8 $M_\odot$)	(km s^{-1})	(Mpc)	(kpc)	(kpc)	(km s^{-1})	(km s^{-1})	(°)	(°)	(10^{10} $M_\odot$)	$M_\odot/L_\odot$
VGS_37	12.0	13.46 ± 1.89	5787	83	5.6	12.8	153	186	67	195	2.05	1.70
VGS_37a	12.0	8.57 ± 1.67	4318	62	3.1	-	50	92	-	-	-	0.5
VGS_38	12.0	9.1 ± 0.7	3853	55	2.8	6.9	50	92	39	130	0.26	2.0
VGS_38a	12.0	0.86 ± 0.14	3832	54	1.3	-	67	75	-	-	-	0.4
VGS_38b	12.0	1.39 ± 0.22	3863	55	1.4	-	41	66	-	-	-	2.0
VGS_39	11.0	< 2.59	-	-	3.7	-	-	-	66	-	-	-
VGS_39a	11.0	2.56 ± 0.39	5171	74	1.1	-	16	32	-	-	-	3.0
VGS_40	12.0	6.00 ± 1.40	7091	101	2.8	< 4.2	206	231	42	77	< 2.32	0.43
VGS_41	10.5	< 2.86	-	-	1.8	-	-	-	29	-	-	-
VGS_42	12.0	4.0 ± 1.5	5601	80	3.5	< 8.1	128	171	58	310	< 1.08	0.2
VGS_43	14.0	< 2.87	-	-	2.0	-	-	-	30	-	-	-
VGS_44	12.0	4.9 ± 1.1	5295	76	3.6	< 7.0	76	110	31	145	< 0.90	0.1
VGS_45	12.0	3.5 ± 1.3	4316	62	4.0	< 6.9	68	102	66	320	< 0.22	1.0
VGS_46	12.0	5.55 ± 1.66	4751	68	2.9	< 4.9	186	202	71	260	< 1.10	0.80
VGS_47	12.0	13.02 ± 2.71	6630	95	8.0	12.4	317	325	72	340	7.97	0.12
VGS_48	0.0	-	-	-	3.6	-	-	-	68	-	-	-
VGS_49	12.0	< 3.60	-	-	3.9	-	-	-	40	-	-	-
VGS_50	12.0	55.27 ± 7.30	6129	88	3.2	16.1	287	330	83	349	7.85	1.29
VGS_51	12.0	19.01 ± 2.46	7476	107	4.3	< 10.1	172	206	63	285	< 2.18	1.27
VGS_51a	12.0	1.00 ± 0.21	4990	71	1.4	-	68	68	-	-	-	2.0
VGS_52	12.0	9.00 ± 2.25	5426	78	3.8	10.0	118	117	70	275	0.92	2.07
VGS_53	13.0	5.19 ± 1.66	6450	92	5.4	< 2.2	162	178	64	155	< 0.42	0.14
VGS_53a	13.0	4.38 ± 2.16	6942	99	6.2	-	119	119	-	-	-	0.3
VGS_54	9.0	33.18 ± 4.00	7028	100	6.7	16.5	240	265	80	38	5.72	1.21
VGS_54a	9.0	-	4421	63	3.0	-	-	-	-	-	-	-
VGS_55	8.5	17.33 ± 3.56	7485	107	5.7	13.2	154	197	55	145	2.71	0.60

Continued on next page

Table 5.4 – Continued

Name	**t**	$M_{\mathbf{H\ I}}$	V_{sys}	**D**	$\mathbf{r}_{90}$	$\mathbf{r}_{\mathbf{H\ I}}$	W_{50}	W_{20}	**i**	**P.A.**	$\mathbf{M}_{dyn}$	$\mathbf{M_{H\ I}/L}_r$
	(hr)	(10^8 $\mathbf{M}_\odot$)	(km $\mathbf{s}^{-1}$)	**(Mpc)**	**(kpc)**	**(kpc)**	(km $\mathbf{s}^{-1}$)	(km $\mathbf{s}^{-1}$)	(°)	(°)	(10^{10} $\mathbf{M}_\odot$)	$\mathbf{M}_\odot/\mathbf{L}_\odot$
VGS_56	12.0	< 2.67	-	-	3.3	-	-	-	59	-	-	-
VGS_56a	12.0	2.15 ± 0.66	6247	89	2.1	-	101	109	-	-	-	1.5
VGS_57	13.0	6.37 ± 1.48	6630	95	5.7	< 9.0	119	187	30	330	< 3.01	0.06
VGS_57a	13.0	1.72 ± 0.49	5443	78	1.9	-	59	101	-	-	-	0.3
VGS_58	12.0	7.0 ± 0.6	3351	48	2.6	7.4	143	151	38	280	2.39	0.7
VGS_59	12.0	< 2.59	-	-	3.1	-	-	-	67	-	-	-
VGS_60	12.0	2.51 ± 1.61	5890	84	4.9	< 5.7	273	281	81	106	< 2.53	0.09

Table 5.5: Stellar and star formation parameters for void galaxies

Name	M_* ($10^8 M_\odot$)	$\mathbf{SFR}_{H\alpha}$ ($M_\odot$ $\mathbf{yr}^{-1}$)	$\mathbf{SFR}_{H\alpha}/M_*$ (10^{-11} $\mathbf{yr}^{-1}$)	$\mathbf{SFR}_{H\alpha}/M_{\mathbf{H\ I}}$ (10^{-11} $\mathbf{yr}^{-1}$)
VGS_01	4.5	0.08	15.3	-
VGS_02	4.5	0.08	16.2	13.1
VGS_03	2.4	0.04	15.3	-
VGS_04	7.4	0.14	17.0	-
VGS_05	129.1	0.03	0.2	-
VGS_06	2.6	0.17	55.4	10.7
VGS_07	0.5	0.18	278.1	20.5
VGS_08	1.9	0.06	24.8	14.1
VGS_09	0.7	0.04	48.9	3.9
VGS_10	2.2	0.09	36.7	6.1
VGS_11	11.5	0.14	10.9	6.4
VGS_12	1.6	0.08	42.6	2.6
VGS_13	10.6	0.11	9.4	9.2
VGS_14	1.6	0.07	40.1	11.3
VGS_15	26.0	0.04	1.4	-
VGS_16	0.9	0.03	32.6	-
VGS_17	0.2	0.08	277.6	-
VGS_18	2.1	0.04	15.1	9.3
VGS_19	3.7	0.12	28.1	36.9
VGS_20	0.5	0.07	139.8	-
VGS_21	93.6	0.11	1.0	4.9
VGS_22	1.9	0.04	19.8	-
VGS_23	19.3	0.44	19.9	11.3
VGS_24	-	-	-	-
VGS_25	1.4	0.10	61.1	56.5
VGS_26	19.9	0.34	15.6	22.7
VGS_27	1.0	0.03	26.3	8.7
VGS_28	-	-	-	-
VGS_29	8.1	0.21	22.1	-
VGS_30	1.0	0.06	48.0	10.0
VGS_31	35.1	1.42	35.6	71.5
VGS_32	27.9	0.26	8.2	6.9
VGS_33	1.7	0.02	10.8	2.7
VGS_34	75.4	0.87	10.9	36.4

Continued on next page

Table 5.5 – Continued

Name	M_* ($10^8 M_\odot$)	**SFR**$_{H\alpha}$ ($M_\odot$ **yr**$^{-1}$)	**SFR**$_{H\alpha}/M_*$ (10^{-11} **yr**$^{-1}$)	**SFR**$_{H\alpha}/M_{\mathbf{H\ I}}$ (10^{-11} **yr**$^{-1}$)
VGS_35	6.6	0.11	13.8	10.0
VGS_36	8.9	0.26	26.2	13.3
VGS_37	4.1	0.11	24.1	8.3
VGS_38	0.7	0.07	88.2	7.8
VGS_39	102.3	0.20	1.8	-
VGS_40	11.6	0.20	15.1	32.9
VGS_41	6.1	0.10	15.0	-
VGS_42	25.3	0.16	5.7	40.8
VGS_43	1.9	0.05	21.7	-
VGS_44	32.5	0.79	21.9	161.5
VGS_45	1.1	0.05	39.3	13.1
VGS_46	3.3	0.09	24.3	16.5
VGS_47	213.4	0.59	2.5	45.5
VGS_48	19.4	0.12	5.3	-
VGS_49	33.1	0.76	19.8	-
VGS_50	83.5	0.36	4.0	6.5
VGS_51	3.6	0.27	65.7	14.0
VGS_52	1.3	0.06	37.5	6.3
VGS_53	32.0	0.27	7.6	52.7
VGS_54	42.5	0.18	3.8	5.6
VGS_55	15.7	0.17	9.2	9.6
VGS_56	49.0	0.27	4.9	-
VGS_57	113.5	1.73	13.3	271.7
VGS_58	3.9	0.11	25.1	16.1
VGS_59	1.8	0.05	22.4	-
VGS_60	56.5	0.13	2.0	51.0

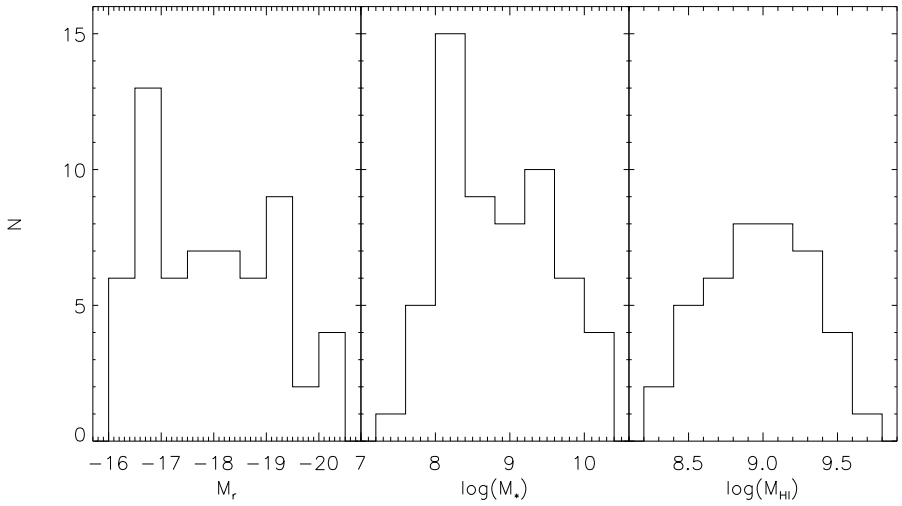

Figure 5.2: Distributions for the absolute magnitude, stellar mass and H I masses in the VGS.

5.4 Results

Despite differing void finding methods, there is general agreement that void galaxies are usually faint, late type, blue disk galaxies, but the details of their properties at fixed luminosity and morphological type are less clear, and may depend on an accurate identification of the void galaxy population (Grogin & Geller 1999, 2000; Rojas et al. 2004, 2005; Patiri et al. 2006b; Park et al. 2007; von Benda-Beckmann & Müller 2008). From our sample of 60 void galaxies, 55 were observed in H I and 14 were not detected. Measurements of the first 15 galaxies are discussed as a pilot study to this project in Chapter 4 of this thesis, and are included again here for completeness. The VGS includes a range of luminosities, from -16.2 > M_r > -20.4, corresponding to a stellar mass range of 2 $\times$ 10^7 $M_\odot$ to 2 $\times$ 10^{10} $M_\odot$. We measure H I masses ranging from 1.7 $\times$ 10^8 $M_\odot$ to 5.5 $\times$ 10^9 $M_\odot$. Distributions for the absolute magnitude, stellar mass and H I masses are shown in Figure 5.2. Along with the selected galaxy sample, we have detected by their H I emission 18 other void galaxies within $\sim$ 800 km s^{-1} and 25′ of the VGS targets (Table 5.3). As these are H I selected they probe to fainter luminosities, as faint as $M_r \sim -14$, with H I masses as low as $\sim 5 \times 10^7$ $M_\odot$.

We find that our sample consists almost exclusively of gas-rich blue disk galaxies, about half of which have strongly irregular or disturbed H I morphologies and kinematics. In the following sections we compare the VGS H I observations at the WSRT with two catalogs

of resolved H I observations in the literature. The first is drawn from the Westerbork observations of neutral Hydrogen in Irregular and SPiral galaxies (WHISP), which presents an atlas of the H I morphology and kinematics for a large number of galaxies. This sample is biased towards gas rich targets but unconstrained environmentally. We use the atlas of 73 galaxies presented in Swaters et al. (2002). In addition, we also compare with an atlas of 43 spiral galaxies in the Ursa Major cluster, also observed with the WSRT (Verheijen & Sancisi 2001). This sample is located within a poor cluster of galaxies, and extends to higher luminosities than Swaters et al. (2002). These two atlases together encompass a large range of galaxy H I morphologies and kinematics, all observed with the same radio interferometer as the VGS.

5.4.1 Optical color and morphology

Though we have selected the VGS purely by the geometric environment, it spans a range of luminosities and colors. In Figure 5.3 we compare the color-magnitude distribution with a magnitude limited ($z < 0.03$, $m_r < 17.77$) sample of SDSS galaxies. Our void galaxies exhibit a wide range of colors, however there are significantly fewer red galaxies and more blue galaxies in the void. Our sample of void galaxies is also shifted towards fainter galaxies, with no galaxies brighter than $M_r = -20.4$. This matches the generally observed shift in the luminosity function found in underdense regions and predictions from CDM cosmology (Hoyle et al. 2005; Aragón-Calvo 2007, Chapter 6 of this thesis). None of the VGS galaxies have a stellar masses above 3×10^{10} $M_\odot$, the observationally identified transition mass below which galaxies are typically younger, and still in the process of assembling (Kauffmann et al. 2003b).

The VGS spans a range of stellar morphologies, however the distance to this sample makes morphological subtypes difficult to distinguish by eye, and we find that it is also very difficult to constrain with simple parameterization. In considering whether any of the VGS are elliptical galaxies, we note that most of the red galaxies with $g - r > 0.6$ appear to be edge on disks or bulge dominated systems. Classification by the galaxy concentration index, defined as the ratio of the Petrosian radius containing 90% of the light to that containing 50% (r_{90}/r_{50}), is also not perfect, as half of those with a high concentration index appear to be bulge dominated disk galaxies. Judging the SDSS images by eye (see Figure 5.A-1), only three might be classified as early type galaxies. VGS_24 and VGS_41 have very smooth

stellar distributions but are blue, while VGS_05 is red but appears to have a bar and may be an SB0 galaxy. All three are not detected in H I. We show these three, as well as examples of bulge free (VGS_10), spiral (VGS_15) and irregular (VGS_17) galaxies in Figure 5.4.

None of the VGS sample shows strong evidence of AGN activity. We detected 1.4 GHz radio continuum emission in 15 VGS galaxies at above ∼1 mJy, which corresponds to luminosities of less than 5×10^{21} W Hz^{-1}, consistent with star formation (Smolčić et al. 2008). This can also be constrained optically following a line index classification scheme using the N II λ6583, O III λ5007, H α and H β emission features (Baldwin et al. 1981) measured in the SDSS spectra (Figure 5.5, left). Using only targets where the signal to noise ratio is greater than three, our galaxies are not classified as AGNs according to the demarcation determined by Kewley et al. (2001). The less strict demarcation determined by Kauffmann et al. (2003a) allows seven of our targets as possible AGNs, two of which (VGS_24 and VGS_54) do fall significantly away from the region containing star-forming

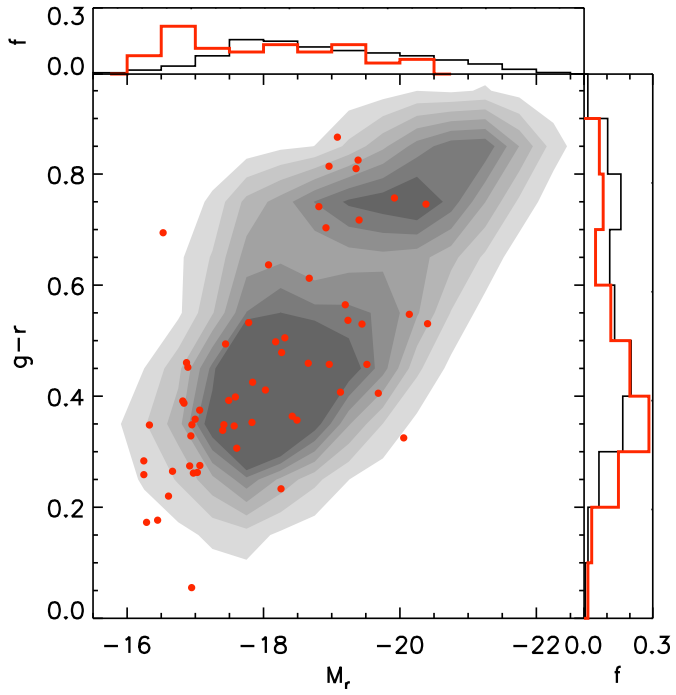

Figure 5.3: Color magnitude diagram of the VGS (red) compared with a magnitude limited sample of galaxies from SDSS selected in a similar redshift range $0.01 < z < 0.03$. Our void galaxies are typically blue and faint, but do span a range of colors and luminosities.

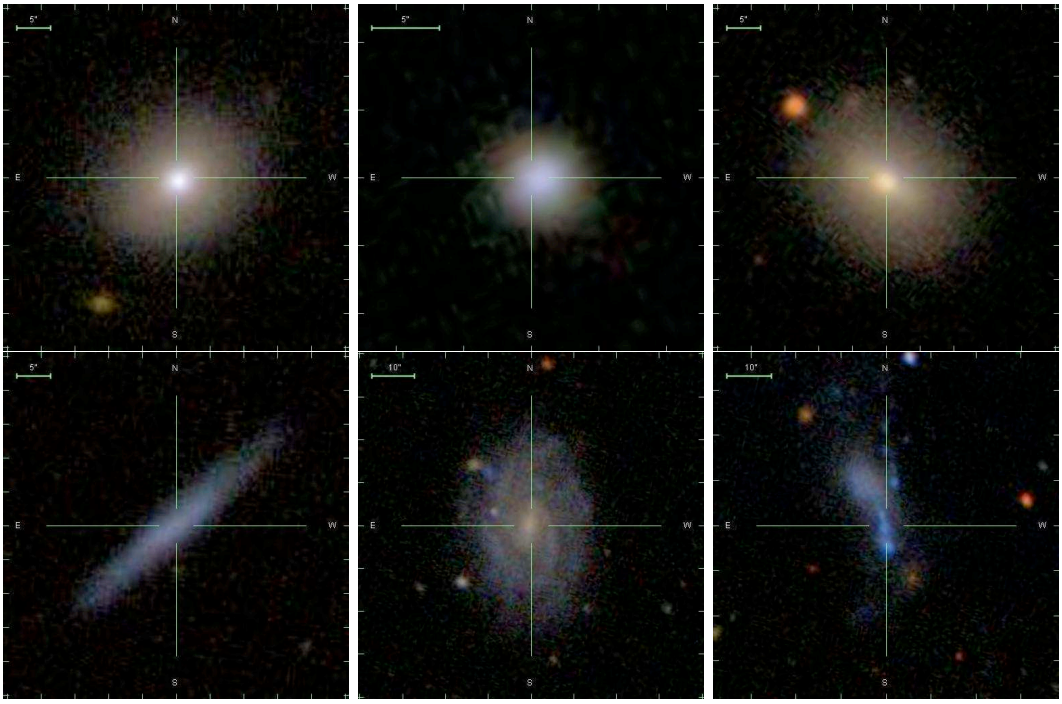

Figure 5.4: The VGS includes a range of stellar morphologies, with elliptical (VGS_24, top left; VGS_41, top center), lenticular (VGS_05, top right), bulge free (VGS_10, bottom left), spiral (VGS_15, bottom center), and irregular (VGS_17, bottom right) galaxies.

galaxies. These seven AGN candidates are among the brighter and redder galaxies in our sample (Figure 5.5, right). VGS_24 is one of three elliptical galaxies in this sample, and none of these or the AGN candidates have strong radio continuum emission at 1.4 GHz.

5.4.2 Size

In our pilot study we reported systematically smaller stellar disks in the galaxies compared with a volume limited sample of SDSS galaxies, however this systematic effect appears to be due largely to small number statistics within the original sample of 15 galaxies. Figure 5.6 shows a preference for smaller stellar disks but no statistically significant difference in the sizes of the VGS galaxies as compared to a magnitude limited sample of SDSS galaxies ($z < 0.025$, $m_r < 17.77$).

The most robust measure of optical galaxy size available from the SDSS pipeline, r_{90} differs significantly from the Holmberg, D25 or exponential disk scale length measures that are typically available in the literature for H I galaxy samples. Using $D_{H\,I}/D_{90}$, the VGS

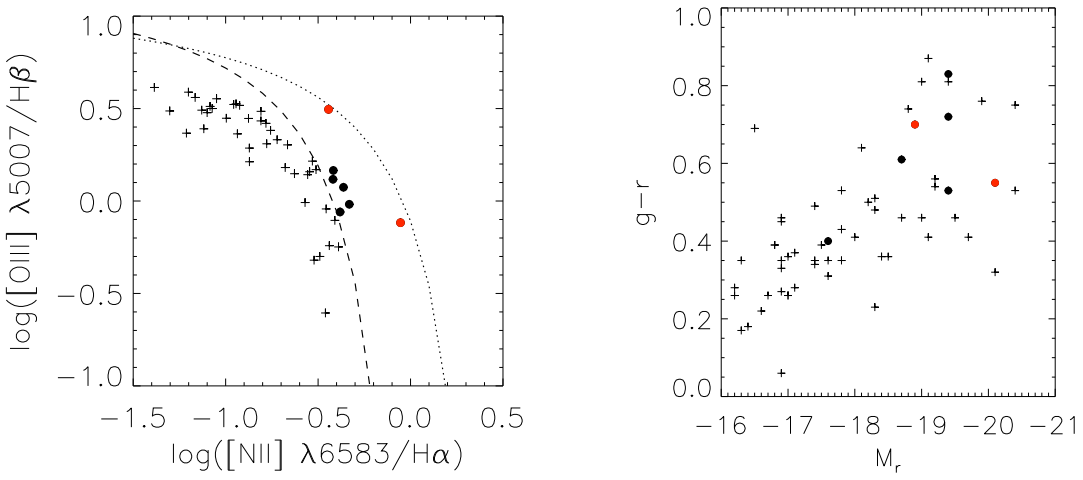

Figure 5.5: Left: The BPT (Baldwin et al. 1981) diagram for the VGS, showing the ratio of emission-line flux in [O III]/H β to [N III]/H α. No galaxies fall above the AGN demarkation determined by Kewley et al. (2001) (dotted line). Seven galaxies (circles; VGS_02, VGS_21, VGS_24, VGS_42, VGS_50, VGS_54) are classified as AGNs by relation in Kauffmann et al. (2003a) (dashed line), with two falling significantly away from the star-forming galaxies (red circles). Right: The location of these seven galaxies within the color magnitude distribution for the VGS. Most of the AGN candidates are among the redder and more massive galaxies in the sample. Colors and symbols are as in the BPT diagram.

spans a reasonable range (Figure 5.7, left), with the H I disks two to three times more extended than the stellar disks. The SDSS pipeline provides an estimate of the exponential disk scale length, which we find in good agreement with the WHISP sample (Figure 5.7, right). By this measure, some of the H I disks are comparable or smaller than the stellar disk, however in these cases the galaxies are edge-on disks and we suspect the SDSS pipeline is unable to accurately measure these scale lengths.

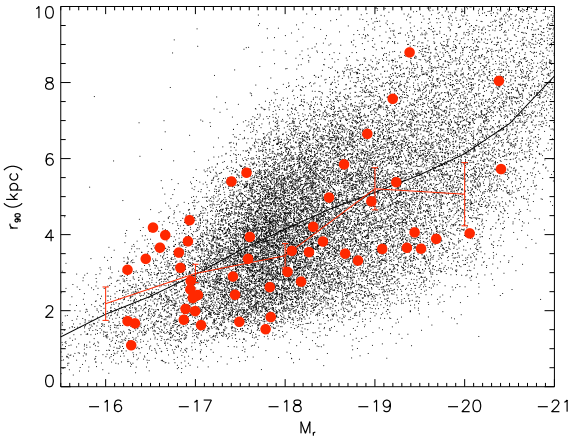

Figure 5.6: Optical size of the late type ($r_{90}/r_{50} < 2.86$) disks of the VGS (circles) and a SDSS sample at $0.01 < z < 0.03$, with the mean values of each overplotted. Unlike in the pilot sample, there is no systematic offset in the sizes of the stellar disks for the VGS galaxies. There is a preference for smaller disks, however the distribution of sizes at fixed luminosity for the full VGS is in agreement with the larger SDSS sample, within the error in the mean and given the relatively small sample size.

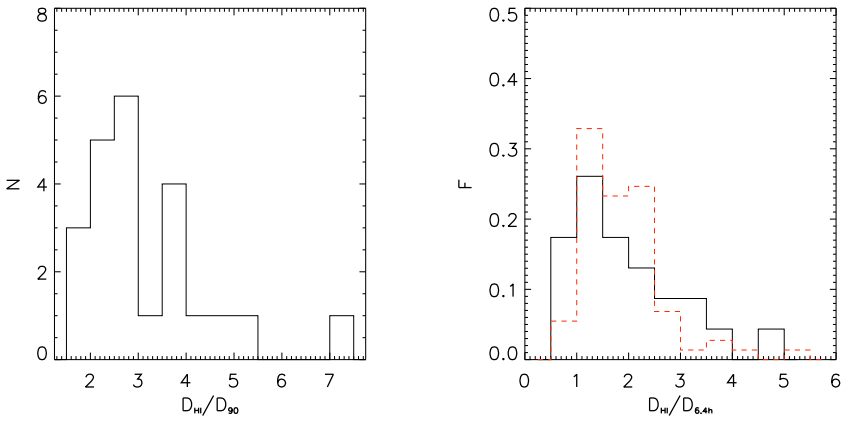

Figure 5.7: Distribution of H I to optical diameter ratios. The r_{90} radius (left) and 6.4 times the exponential disk scale length (right) measure slightly different extents of the stellar component, however the galaxies appear consistent with the late-type galaxies studied by Swaters et al. (2002) (red dashed line).

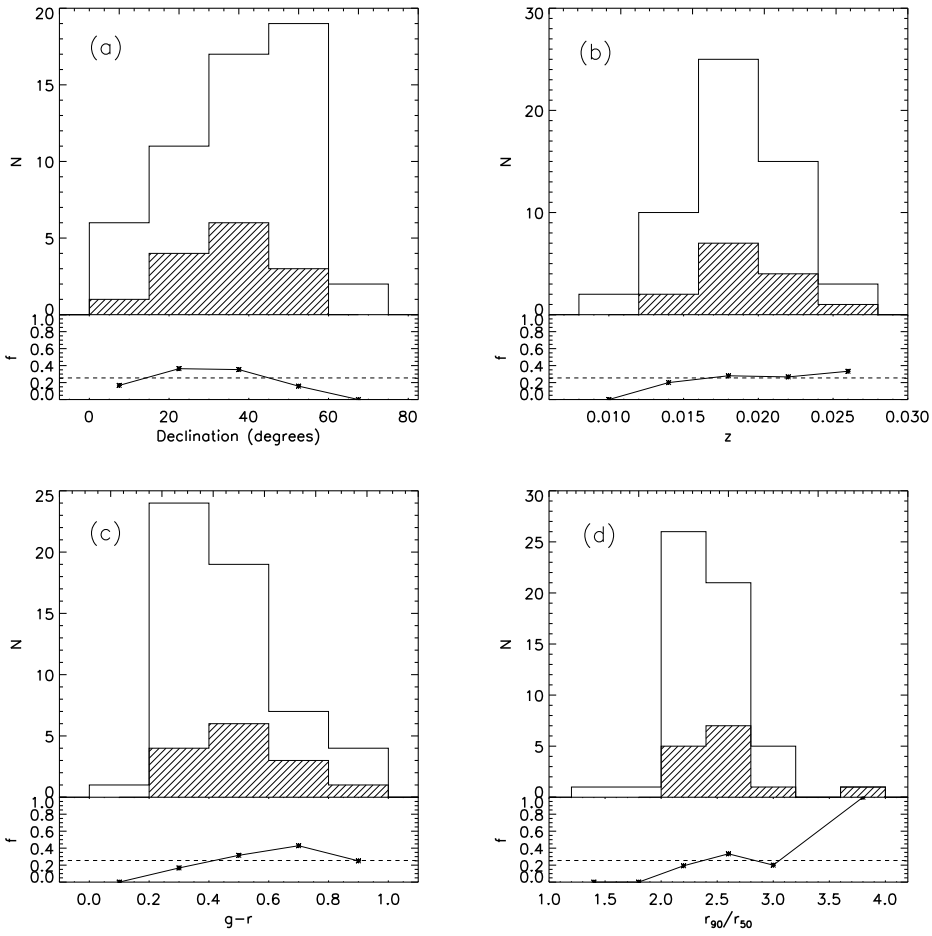

Figure 5.8: Number of galaxies in the in the full VGS (unshaded region) compared to the H I non-detections (shaded region) as a function of (a) declination, (b) redshift, (c) $g-r$ color, and (d) concentration index. The fraction of non-detections is plotted at the bottom of each panel, with the dashed line indicating the overall non-detection fraction. There are very few red galaxies, with $g-r > 0.6$, or elliptical (highly concentrated) galaxies, with $r_{90}/r_{50} > 2.86$. In general, there are no strong correlations, and the red and elliptical galaxies we observe are not found to be preferentially not-detected at a significant level. We also note that we are not biased against detecting targets at low declination or high redshift.

5.4.3 HI non-detections

We detect 41 of the 55 galaxies observed at the WSRT in H I, a 75% detection rate. There is no clear correlation with distance (Figure 5.8a) as might be expected if H I sensitivity

was limiting, or with declination (Figure 5.8b), which can cause extremely elliptical beam shapes for east-west arrays like the WSRT. In general, we find no significant correlations in the non-detections (Figure 5.8). As already mentioned, color and concentration index (r_{90}/r_{50}) are not infallible indicators of optical morphology, which might be expected to correlate with the non-detections. There is a slight correlation with color though the errors are large due to the small sample size. Dividing the sample by color at $g - r = 0.6$, $77 \pm 13\%$ of blue galaxies were detected while only $64 \pm 24\%$ of red galaxies were detected. We do note that the only 3 galaxies that look morphologically like elliptical or S0 galaxies are not detected in H I.

Six of the non-detections (VGS_04, VGS_22, VGS_16, VGS_03, VGS_41, VGS_43) have very similar optical morphologies, with particularly small stellar components ($r_{90} < 2$ kpc) and blue, disk-like morphologies. All are fainter, with $-16 < M_r < -18$, and presumably have an H I content that is slightly below the detection limits. To test this we scaled the intensity of emission in each cube to a common distance and, assuming the spatial and velocity resolution remains roughly equivalent between targets, stacked the emission for these non-detected targets. This increased the sensitivity to ~ 0.24 mJy per beam and resulted in a $(1.2 \pm 0.3) \times 10^8$ $M_\odot$ detection, just below the detection limits for the galaxies individually. Stacking limits from combining the other eight non-detections are considerably lower and not statistically significant, $(4.9 \pm 1.7) \times 10^7$ $M_\odot$. However, we note that the upper limits for the H I content in the non-detected galaxies in general are not inconsistent with the expected H I content based on the galaxy luminosities (see Section 5.4.5).

5.4.4 HI morphology and kinematics

H I imaging of the VGS reveals it to contain a diverse collection of H I rich galaxies, with about half showing signs of strongly disturbed gas morphology or kinematics. Five are clearly interacting with companions, four have some gas that does not follow the regular disk rotation, five are asymmetric at the 3σ H I contours, six have a lopsided H I distribution, eight are kinematically lopsided, and three have warps (see Figure 5.A-2, for the complete atlas). Similar optical inspection of the WHISP galaxies in Swaters et al. (2002) reveal that nearly all their targets have irregularities in the gas morphology or kinematics with similar frequency. This is also found in studies of integrated H I galaxy profiles (Richter & Sancisi 1994). The Ursa Major cluster galaxies reside in a very different environment and appear

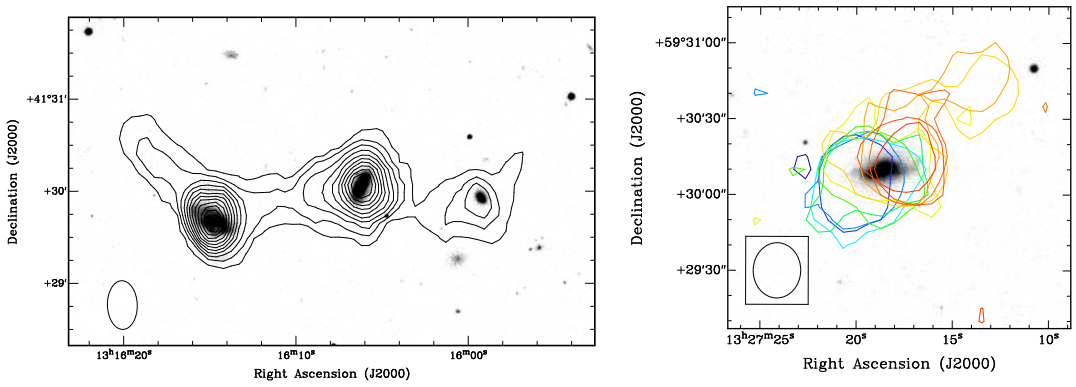

Figure 5.9: Examples of void galaxies with gas outside the disk. VGS_31 (left) shows signs of interaction between three close galaxies connected by a low column density H I bridge. VGS_34 (right) shows disk rotation along the optical disk with a significant amount of H I at velocities inconsistent with regular rotation to the north-west side. VGS_31 is imaged with natural weighting and contours at 5×10^{19} cm^{-2} plus increments of 10^{20} cm^{-2}. VGS_34 shows the g-band image with H I contours overdrawn at 1.2 mJy beam^{-1} (2.5σ) from different channels. The contours from different channels, each 24 km s^{-1} apart, are color coded from blue to red to indicate the shift in velocity of the H I emission.

significantly more regular, with only about a quarter having strong irregularities in the gas, however as they are larger they may also be affected by deeper gravitational potentials. Both the WHISP and Ursa Major cluster galaxies have a significant number of H I rings, which we would be unable to resolve for the majority of the VGS galaxies.

Some of the VGS galaxies are particularly striking. Figure 5.9 shows two examples of galaxies with kinematically irregular gas located outside the disk with no clear optical counterpart. VGS_34 has an H I disk with regular rotation that is centered on the optical galaxy, however in addition it has low column density gas to the north-west that persists over multiple channels in velocity. This gas is inconsistent with the disk rotation and has no clear optical counterpart, however the optical morphology is quite disturbed, suggesting a recent interaction. It also has a small companion galaxy about 100 kpc away at a nearly coincident velocity. VGS_31 is one of two VGS galaxies discovered to have two nearby companions, and in both cases the three galaxies are linearly aligned and joined within a low column density common envelope of H I. Figure 5.10 shows three more examples of gas disks that are morphologically or kinematically lopsided. VGS_14 is kinematically lopsided,

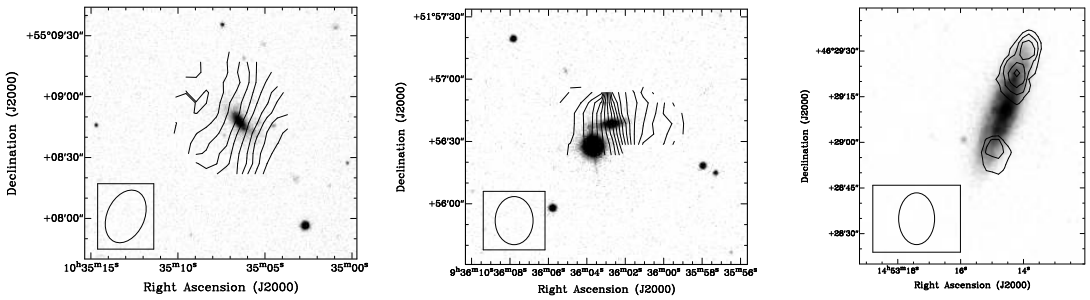

Figure 5.10: Examples of void galaxies with irregular gas disks. VGS_14 (left) is kinematically lopsided, with a shallower velocity gradient on the north-east side of the optical disk. VGS_06 (center) is warped in its outmost extent, with velocity field lines that are perpendicular in the center to the disk major axis but warps strong to the west and more weakly to the east. VGS_47 (right) has a lopsided H I distribution, with significantly more H I to the north-east edge of the disk. Velocity field lines in VGS_14 and VGS_06 are at intervals of 8 km s^{-1}. VGS_47 has been imaged using uniform weighting to increase the resolution, and velocity smoothed to 35 km s^{-1} to improve the sensitivity. Here the H I contours show lopsided distribution of the high column density gas, at 8×10^{20} cm^{-2} (2σ) plus increments of 4×10^{20} cm^{-2}.

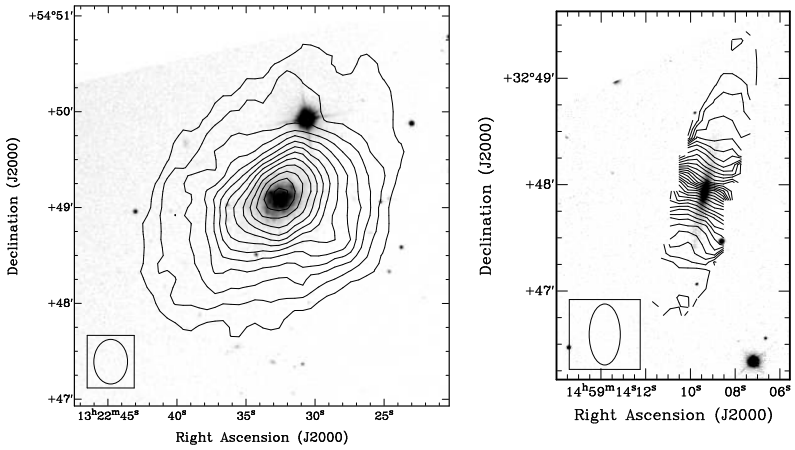

Figure 5.11: Examples of void galaxies with regularly distributed gas disks. VGS_32 (left) has a well resolved, fairly symmetric H I disk. VGS_50 (right) is nearly edge on, and kinematically symmetric with no sign of a warp. H I contours in VGS_32 are at 9×10^{19} cm^{-2} (3σ) plus increments of 10^{20} cm^{-2} for a naturally weighted image. The velocity field in VGS_50 indicates intervals of 8 km s^{-2}.

exhibiting a shallower velocity gradient to the north-east side. VGS_06 is warped in the outer extent, and VGS_47 is very lopsided in the distribution of H I across the disk. We also show for completeness in Figure 5.11 examples of galaxies that are fairly regular in the H I morphology (VGS_32) and kinematics (VGS_50).

The high fraction of strongly irregular H I disks is surprising if we consider void galaxies as evolving in relative isolation, where galaxies are observed to have a smaller fraction of asymmetric H I profiles (Espada et al. 2011). However void galaxies are not by definition isolated. Szomoru et al. (1996) found that on small scales (< 1 Mpc) the number of neighboring galaxies detected around targeted galaxies in the Boötes void is similar to that in average environments, a result supported by the VGS sample (see Section 5.5.4). The strong H I irregularities present clear evidence of ongoing interactions and gas accretion, and is fairly typical for gas rich galaxies.

5.4.5 HI content

The VGS reproduces the trend for fainter galaxies to be relatively more gas rich than brighter galaxies, as is generally observed in disk galaxies. In Figure 5.12 we compare the H I mass to light ratio of the void and companion galaxies with H I imaged galaxies in the WHISP sample (Swaters et al. 2002) and the Ursa Major cluster (Verheijen & Sancisi 2001). Here we have converted the SDSS *ugriz* bands to Johnson-Cousins *R*-band magnitudes following the prescription of Jester et al. (2005). The VGS generally agrees with the two samples within the errors, with the upper limits for the non-detections also falling within the range observed. All three samples achieve similar H I column density sensitivities, though our sample is at significantly larger distances.

Only one galaxy, VGS_12, appears to have an unusually large H I mass to light ratio of 6.2 given its absolute magnitude M_r = -17, and from the misalignment of its H I disk it is clear that the evolution of this system is progressing in an unusual fashion. This galaxy is discussed briefly in Section 5.5.1 and more fully in Chapter 2 of this thesis. We observe no systematic increase in the H I mass to light ratio for the VGS, somewhat in contrast to previous observations and predictions from cosmological simulations. Chapter 6 of this thesis determines that simulated galaxies in the most underdense regions have slightly higher H I mass to light ratios at fixed luminosity. An increased H I mass to light ratio has also been reported in H I studies of dwarf galaxies in voids (Huchtmeier et al. 1997),

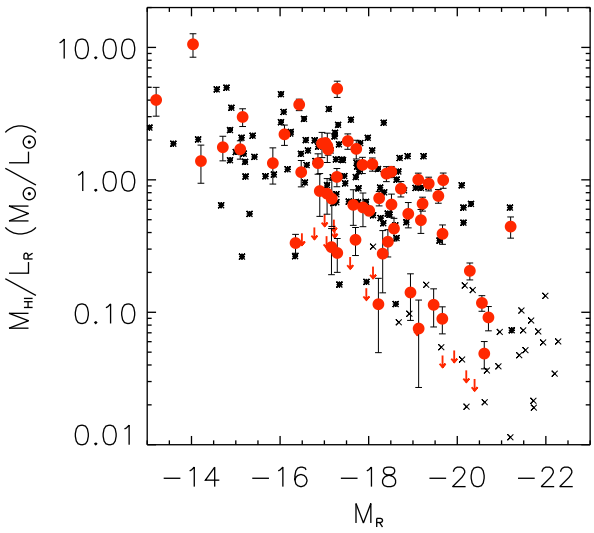

Figure 5.12: H I mass to light ratio as a function of R-band absolute magnitude for the VGS and companion galaxies (circles) compared with WHISP galaxies (stars, Swaters et al. 2002) and Ursa Major cluster galaxies (crosses, Verheijen & Sancisi 2001). Upper limits on the VGS non-detections are also indicated (arrows). Our VGS follows the trend for fainter galaxies to have relatively higher H I mass to light ratios.

and a small sample of void galaxies selected from the Second Byurakan and Case surveys (Pustilnik et al. 2002), though in both studies the targets are typically unresolved and may be confused within the large H I beam. The significantly larger sample size in this study allows more robust comparison with 'average' galaxies, and provides no evidence for an increased H I mass to light ratio.

5.4.6 Star formation

None of the VGS galaxies have SFRs that would suggest they are undergoing a starburst, the highest having $\sim$2 $M_\odot$ yr^{-1} but the majority falling below 1 $M_\odot$ yr^{-1}. As the SFR is typically lower for smaller galaxies, it is useful to normalize the SFR by the stellar mass and consider the specific star formation rate (S-SFR) for these systems. The S-SFR has been found to be enhanced in void galaxies (Rojas et al. 2005; von Benda-Beckmann & Müller 2008), which suggests that as a population they are still in the process of building their stellar disks. However, as this is generally the case for smaller galaxies (Kauffmann

et al. 2003b), it is not clear if these results hold at fixed luminosity and morphological type (Park et al. 2007). Comparing the VGS with a magnitude limited ($z < 0.03$, $m_r < 17.77$) sample of SDSS galaxies we find no trend for higher S-SFR as a function of galaxy stellar mass. This discrepancy with past results may come from the different range of luminosities probed, as our sample consists of relatively faint void galaxies (Figure 5.2), whereas the most significant effect on S-SFR is identified in void galaxies brighter than $M_r \sim -19$ (Rojas et al. 2005; von Benda-Beckmann & Müller 2008).

Recently the star formation efficiency (SFE), measured as the star formation rate normalized by the H I mass, has been considered as a way to judge the general effectiveness of turning gas into stars. The GALEX Aricebo SDSS Survey (GASS) compares the SFE for a large sample of galaxies with stellar masses above 10^{10} $M_\odot$, and find it stays relatively constant at $\log_{10}$(SFE) $\sim$ -9.5 when considered as a function of parameters such as stellar mass, color, and morphology (Schiminovich et al. 2010). Only four galaxies in the VGS have stellar masses within this range, two of which are detected and have $\log_{10}$(SFE) of -8.6 and -9.1, higher than the average and suggestive that void galaxies are somewhat more efficient in their star formation. Two are not detected in H I, with lower limits on the $\log_{10}$(SFE) of -10 and -9.1. We continue our investigation into the efficiency of star formation in void galaxies with lower stellar masses in Section 5.5.2.

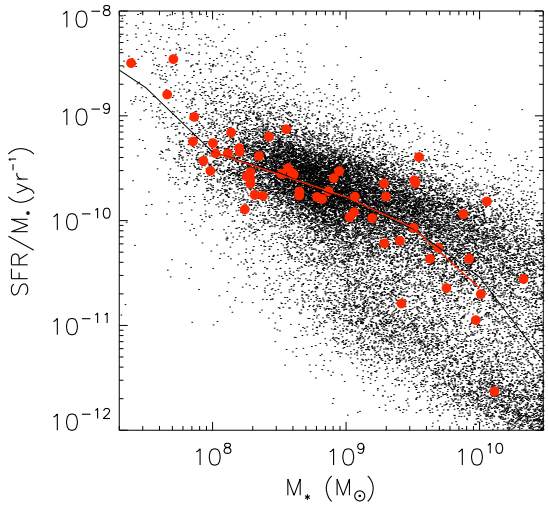

Figure 5.13: SFR normalized by stellar mass as a function of stellar mass for the VGS (red) and a magnitude limited ($z < 0.03$, $m_r < 17.77$) sample of SDSS galaxies (black). The medians of both samples (lines) agree quite well, suggesting that buildup of the stellar disks in the VGS is appropriate to their smaller sizes.

5.5 Discussion

Given the observed H I and optical properties of the VGS, we consider what role the large scale environment might play in the evolution of these systems and the implications for cosmology.

5.5.1 Evidence for ongoing gas accretion

The strong disturbances we observe in the H I morphologies and kinematics (see Section 5.4.4) present convincing evidence for ongoing gas accretion in these systems. None of the galaxies with lopsided H I disks highlighted in Figure 5.10 have companions detected in H I, however these galaxies are small enough, with H I radii of $\sim$10 kpc and rotational velocities of $\sim$150 km s^{-1}, that rotation timescales are only a few hundred million years and without recent gas accretion these disks are expected to settle in much less than a Hubble time (Simonson 1982). However it is difficult to distinguish the effects of different gas accretion mechanisms, such as interactions, internal gas recycling, and cosmological inflow. Simulations suggest that gas accreted from the intergalactic medium can either be shock heated to form a hot halo or can penetrate directly to the halo center as a cold flow, depending on the halo mass. For low mass halos, found predominately at higher redshifts and at $z = 0$ in low density environments, these cold flows may be the dominant mechanism for galaxy growth (Kereš et al. 2005; Dekel et al. 2009; Kereš et al. 2009).

This appears to be the case for VGS_12, which was found to have an extremely extended and massive H I disk oriented perpendicular to the direction of the stellar disk, and is discussed at length in Chapter 2 of this thesis. The polar disk is devoid of stars, and the central stellar disk has retained its rotational support, suggesting a slow accretion of polar material. This mechanism for the formation of polar disks has also been suggested for NGC 4650A (Iodice et al. 2006), and has been reproduced in simulations (Macciò et al. 2006). In the VGS we also find two systems, VGS_38 and VGS_31, with three galaxies linearly aligned and joined by low column density H I, that is very suggestive of filamentary formation. Hierarchical void theory predicts that void galaxies will reside in relatively low density substructure within the void (Dubinski et al. 1993; Sahni et al. 1994; Sheth & van de Weygaert 2004; Furlanetto & Piran 2006; Einasto et al. 2011), which has been observed in simulations (Springel et al. 2005) as well as in nearby voids (Popescu et al. 1997), and

the VGS systems present a unique location to search for surrounding low column density intergalactic gas.

Further evidence of gas accretion in void galaxies can be found in the literature. Individual studies of dwarf galaxies in voids suggest that they are uniquely unevolved, with low metallicities and high star formation rates (Corbin et al. 2005; Pustilnik et al. 2006). KK 246, a dwarf galaxy in the Local Void, has an extremely extended H I disk and evidence of gas at anomalous velocities compared to regular disk rotation (Chapter 3 of this thesis). NGC 6946 has been imaged in H I because of its unusual gas kinematics and signs of gas infall (Boomsma et al. 2008), and was selected for these characteristics independent of its location within the Local Void (Sharina et al. 1997). Individually, these examples are interesting, but taken together they convincingly show that voids are a uniquely promising place to search for evidence of ongoing gas accretion.

5.5.2 Void galaxy H I properties at fixed morphology, luminosity, and stellar mass

To statistically examine the integrated H I properties for our sample considering their biased morphology, luminosity and stellar mass distributions, we have constructed an environmentally constrained control galaxy sample by cross-matching galaxies in the five publicly available catalogs of the Aricebo Legacy Fast ALFA Survey (ALFALFA; Giovanelli et al. 2007; Saintonge et al. 2008; Kent et al. 2008; Martin et al. 2009; Stierwalt et al. 2009) with the Sloan Digital Sky Survey Data Release 7 (SDSS DR7; Abazajian et al. 2009). The ALFALFA catalog identifies H I detected galaxies with a signal-to-noise ratio greater than 6.5 sigma, as well as marginal detections between 4 and 6.5 sigma that have clear optical counterparts. The ALFA receiver's 3.5 arcminute beam allows sufficient resolution to uniquely determine a corresponding optical counterpart for almost all cataloged H I detections, though confusion of sources within the beam can be an issue for more distant targets. We have restricted this control sample to a redshift range of $0.007 < z < 0.024$ and a volume limited subset with $M_{H\,I} \geq 10^9$ $M_\odot$ to approximately match the H I sensitivity limits to the WSRT observations (Figure 5.14, see also Section 5.3). Following the cross-matching technique described in Toribio et al. (2011), we require that the optical counterpart centers need to agree in each catalog by less than 10 arcseconds, a typical minimum size for the optical disks of galaxies in that redshift range. We also require that the optical and H I

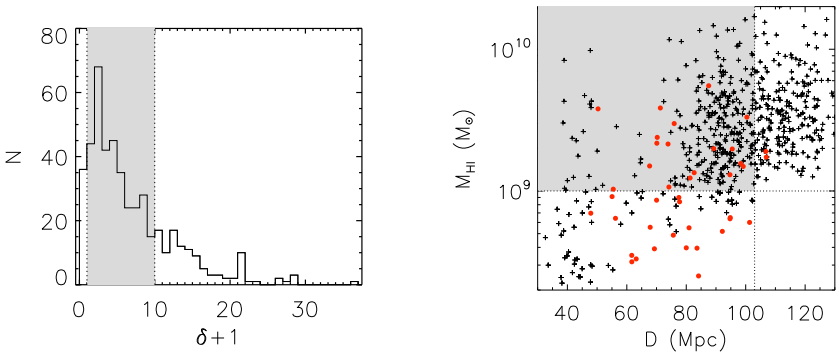

Figure 5.14: Properties of the galaxies cross-matched between the ALFALFA and SDSS DR7 catalogs. The 447 nearby galaxies span a representative range of environments, including both void and cluster galaxies (left). The Malmquist bias in the ALFALFA H I flux limit is apparent in the Spaenhauer diagram (right), and the VGS galaxies (circles) are detected at lower H I masses to greater distances compared to the ALFALFA galaxies (crosses). As a control sample, we construct a volume limited ($M_{H\,I} > 10^9$ $M_\odot$, $z < 0.024$) sample in average ($1 < \delta + 1 < 10$) environments (in grey) of 207 ALALFA galaxies.

redshift velocities agree by less than 300 km s^{-1}, though most source optical redshifts are within ∼30 km s^{-1} of the H I detection. We omit any targets flagged as suffering from confusion within the beam, and we further exclude 24 galaxies from this cross-matched catalog that are identified within the SDSS redshift survey to have close companions, within $2'$ and a velocity difference of ($W_{50}/2$ + 50 km s^{-1}). We recalculate the distances for the ALFALFA detections and adjust the H I masses based on the Hubble flow velocity, instead of the cataloged CMB velocity, to remove any bias when comparing with the VGS. Given the imposed lower limit on the redshift range this does not significantly affect our distance estimates. We identify 447 galaxies for this control sample, with 207 in the volume limited subsample. As expected, the bulk of the control sample galaxies are located at average densities, with a limited number in voids and clusters (Figure 5.14).

We find that late type ($r_{90}/r_{50} < 2.86$) void galaxies have approximately the same median H I mass to light ratios at fixed luminosity as compared to late type galaxies in the volume limited ALFALFA control sample (Figure 5.15, left). Here the void sample has been subjected to the same volume limited ($M_{H\,I} > 10^9$ $M_\odot$) restrictions to avoid a Malmquist bias. The slight systematic offset to lower values is approximately equal to the typical errors

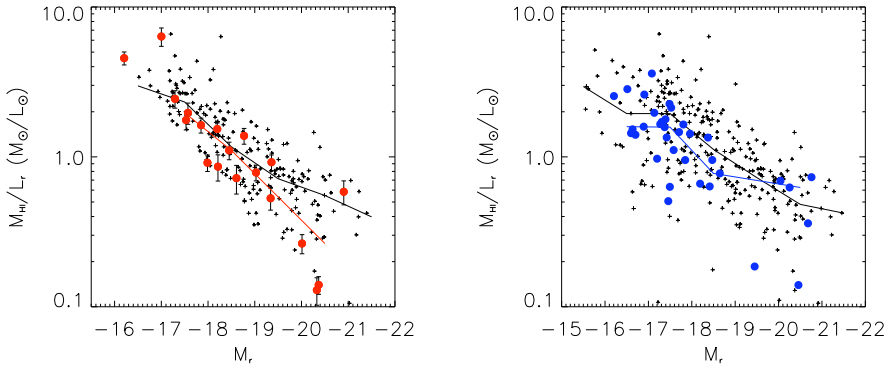

Figure 5.15: Left: H I mass to light ratio for volume limited subsets ($M_{H\,I} > 10^9\ M_\odot$) of late type galaxies in the VGS (circles) and ALFALFA control sample (crosses) in average ($1 < \delta + 1 < 10$) environments. Our void galaxies are slightly offset from the ALFALFA control sample. Right: H I mass to light ratio of all ALFALFA galaxies in average environments (crosses) compared with low density ($1 < \delta + 1 < 10$) environments (circles) as a function of r-band absolute magnitude. A systematic offset is much more apparent, suggesting the offset found for the VGS galaxies may be real. In all figures, errors on ALFALFA are omitted as they are typically smaller than the symbol. Lines show the median of each sample.

due to uncertainty in the H I mass, however the lack of high H I mass to light ratio galaxies in the VGS brighter than $M_r = -17$ is striking.

This effect is not seen when comparing with the WHISP and Ursa Major cluster galaxies (Figure 5.12), and so we consider whether the total H I masses may be affected by instrumental differences between the WSRT and Aricebo observations. Three galaxies in the VGS sample overlap with the ALFALFA control, and for these we find H I masses that agree within the quoted errors. Most convincingly, we observe a similar effect in H I mass to light ratio when comparing the low density ($\delta + 1 < 1$) subset of ALFALFA control galaxies with average density ALFALFA galaxies (Figure 5.15, right). For both the low density ALFALFA galaxies and the VGS, the galaxies in low density regions appear to have an H I mass to light ratio that is approximately 10-20% lower than that of galaxies in average density environments.

It is possible that galaxies in higher density environments are preferentially more contaminated by confusion within the ALFALFA beam, which would result in an overestimate of the total H I mass. At a redshift of $z = 0.024$ the $3.5'$ beam includes any emission

within a physical distance of ∼50 kpc, approximately the distance from the Milky Way to the Large Magellanic Cloud. Within the VGS sample, five of our targets could potentially suffer from confusion with their nearby companions, resulting in mass increases of up to a factor of two. Toribio et al. (2011) examined a sample of cross-matched SDSS and ALFALFA galaxies, and for a subsample of well resolved galaxies with known morphological type and optical diameter they calculated the expected H I mass following Haynes & Giovanelli (1984) and Solanes et al. (1996). They reported a negative H I deficiency of 20-30% which increases with redshift, suggesting that their H I masses may be overestimated, however they attribute this to the omission of H I deficient galaxies below the survey detection limits, the inclusion of more gas rich late type galaxies, as well as a difference in the methods used compared to previous work. We consider such a large contribution to the total H I mass by confusion unlikely, but possible. As we see an offset within the ALFALFA sample at different environments, this would require a strongly environmental effect, with gas-rich galaxies in low density regions less clustered. This is in contradiction with our own findings (see Section 5.5.4).

We also compare the normalized star formation of the VGS galaxies with the average density ALFALFA galaxies (Figure 5.16, top). We find good agreement between the SSFRs when comparing the volume limited VGS and average density ALFALFA samples, which we also find when comparing with a magnitude limited sample of SDSS galaxies (see Section 5.4.6). This suggests that star formation proceeds as expected within voids, independent of the large scale environment. However the SFE appears systematically higher (Figure 5.16, bottom), as was already suggested by our pilot study. Again, the ALFALFA H I masses are susceptible to contamination within the beam, which would have the effect of decreasing the ALFALFA SFEs, but this observed trend is intriguing if true.

5.5.3 Baryon content

In Figure 5.17 we show the I-band and baryonic Tully-Fisher relation for the void galaxy sample overplotted on the fit derived by McGaugh et al. (2000) and Geha et al. (2006). W_{20} values have been corrected for instrumental velocity broadening and inclination. Error bars reflect a 10% uncertainty in the inclination angle. In considering the I-band relation, we convert the SDSS *ugriz* bands to the Johnson Cousins I-band using the transformation equations of Jester et al. (2005), and find very good agreement with the general relation.

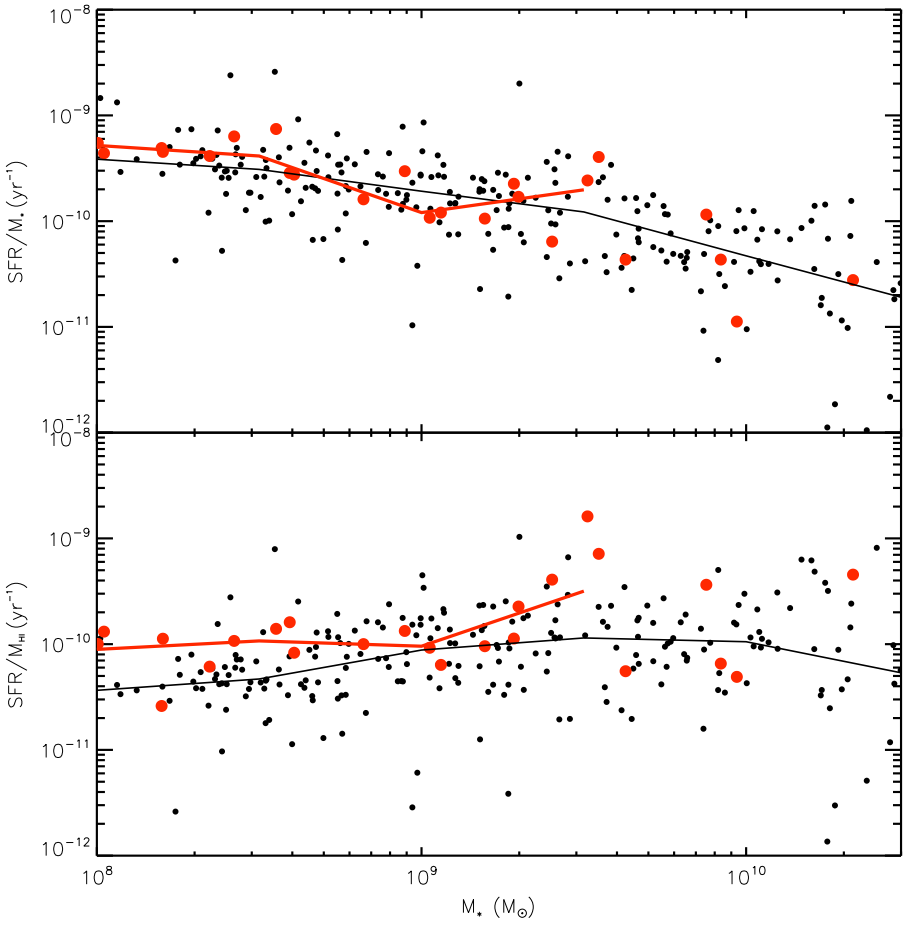

Figure 5.16: SFR normalized by stellar mass (top) and H I mass (bottom) as a function of stellar mass for the VGS (red) and the ALFALFA average density sample (black). The medians of both samples are overplotted (lines), revealing no strong trends in the specific star formation rate (top) but a systematically slightly higher star formation efficiency (bottom) for the void galaxies.

We calculate the total baryons by adding the stellar mass and 1.4 times the H I mass, to correct for the contribution from Helium and other metals. While the baryonic relation has been found to typically have less scatter and more reliably fit lower mass galaxies where there is a more significant gas fraction, we find close agreement with relations from the literature but a slight systematic scatter towards higher velocities or lower baryon masses.

This is particularly interesting as it appears most pronounced for the higher mass galaxies, where the Tully-Fisher relation is typically the most robust, while the low mass systems are generally consistent with average galaxies. All of the targeted void galaxies have in-

clination corrected velocity widths, $W_{20,it}$, of more than 40 km s^{-1}, the threshold below which baryon deficiency due to UV photoheating is predicted (Hoeft & Gottlöber 2010). Excluded from calculations of the baryon mass of these systems is the molecular gas mass, which is not generally considered to contribute significantly (Schombert et al. 1990; Leroy et al. 2005), however considering the possible increase in the efficiency of star formation in these galaxies perhaps this assumption does not hold. Molecular gas has been found to contribute significantly more to the baryonic gas fraction in galaxies at higher redshift, in an earlier phase of their evolution (Tacconi et al. 2010).

It is also possible we are over-estimating the rotational velocity in some of these systems, and in fact the agreement is much better when we consider only galaxies with flattened rotation curves (Figure 5.17, filled symbols). For those galaxies without a turnover observed in the rotation curve, turbulent motions in the disk or beam smearing of central bulge effects on the kinematics may result in overestimation of the rotational velocity width.

5.5.4 Emptiness of the voids and void galaxy clustering

Though void galaxies have very few nearby galaxies on the large ∼10 Mpc scale size of the void, they are not necessarily isolated on small ∼1 Mpc scales. Szomoru et al. (1996) found that the clustering of H I detected galaxies within 1 Mpc of galaxies in the void and the field is the same within a factor of two. Abbas & Sheth (2007) similarly observed that galaxies in the void centers are more clustered than galaxies in the void outskirts, which in turn are less clustered than in moderately overdense regions, and find that this arises naturally from the development of perturbations in a primordial Gaussian density field. In our survey, we are sensitive to H I rich neighboring galaxies, many of which are optically quite faint ($M_r > -14$). We detect galaxies up to $25'$ (roughly 600 kpc at the average distance of ∼85 Mpc) and 600 km s^{-1} away, however we find that the majority of galaxies are within 100 kpc and 100 km s^{-1}.

Because of the pencil beam shape and limited volume of space probed by our observations, calculating nearest neighbor statistics that include the H I detected companions is difficult. Instead, to compare the number of galaxy companions with typical small scale galaxy clustering we examine a volume of the SDSS from $0.001 < z < 0.0135$ containing redshift information for all galaxies brighter than $M_r < -16$. Within this sample we consider how many would have companions detectable given our observational constraints: sky

separations of 600 kpc and velocity differences of 600 km s^{-1}. Additionally, given that the observed VGS velocity separations are strongly biased towards smaller values, and noting a strong threshold in velocity separation at 200 km s^{-1} for the SDSS sample, we limit our comparison to close companions within 600 kpc and 200 km s^{-1}. Though a 200 km s^{-1} difference in Hubble flow velocity corresponds to a distance of nearly 3 Mpc, it is within the expected galaxy pairwise velocity dispersion in low density regions (Strauss et al. 1998). As we are comparing with an optically selected redshift survey, we note that the clustering of H I selected galaxies is observed to be weaker than for optically selected samples (Meyer et al. 2007). From a sample of 3,323 SDSS galaxies, we find that 11% have close neighbors observable by our survey, with 8% having one neighbor and 2% having two. For similar clustering in our sample of 55 galaxies, we expect to find about six galaxies with neighbors,

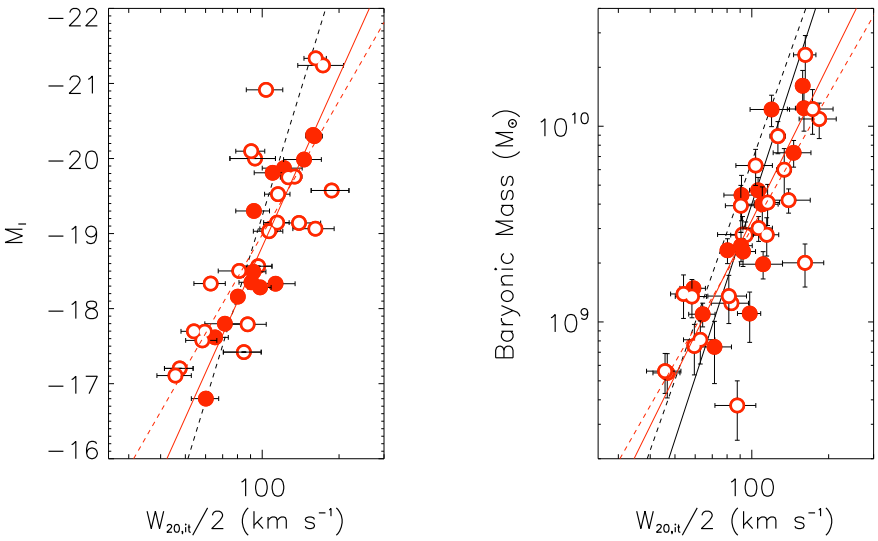

Figure 5.17: *I*-band (left) and baryonic (right) Tully-Fisher relations. Open points indicate those galaxies where we see no flattening of the curve, and may be underestimating the H I line width, $W_{20,it}$. The dashed black line is the observationally determined fit from Geha et al. (2006), and the solid black line is from McGaugh et al. (2000). The dashed red line is a fit to all the VGS, and the solid red line is fit to just those filled points where we see flattening of the rotation curve. While the sample is in good agreement with the *I*-band relation, it is diverges somewhat from the baryonic relation for high rotation velocities and high baryon masses.

four having one neighbor and one having two, and in fact we find eight that have neighbors with $M_r > -16$, and one with two neighbors. This startling agreement shows that even to relatively faint limits the small scale clustering of galaxies in voids is remarkably similar to average environments.

Aside from the detection of nearby neighbors, the wide bandwidth of the WSRT observations in our survey also serves as a blind search in H I for galaxies throughout the voids. There has been much debate on the distribution of galaxies in the void as predicted by CDM cosmology, which arguably predicts a large population of faint galaxies that fill the void (see Peebles 2001; Tinker & Conroy 2009), but has not been detected. We probe with the WSRT a total volume in voids of 485 Mpc^3 around the targeted void galaxies, and are sensitive to targets down to $\sim 10^8$ $M_\odot$. This is significantly smaller than the 1100 Mpc^3 probed by Szomoru et al. (1996) in the Boötes void, but an order of magnitude deeper in H I mass sensitivity. It is equivalent to the volume and sensitivity reached with H I Blind searches within the Pisces-Persius void, where no void galaxies are detected (Weinberg et al. 1991; Saintonge et al. 2008). Our sample is inherently biased towards finding at least one void galaxy with each observation, our chosen target, and the many companions we detect are strongly clustered around the target, even though the volume probed away from it is significantly larger. Only one detection, VGS_26a, is at a significant distance from the target and in the void outskirts, however with M_r = -21 it is not a representative of the missing void galaxy population (Peebles 2001).

5.5.5 Red and dead galaxies within the voids

With the VGS we sample a truncated stellar mass range, where all galaxies have less than 3×10^{10} $M_\odot$. This transition mass is observed to be the point where bulges and spheroids begin to dominate and SFRs decrease (Kauffmann et al. 2003b). Yet within the voids we do observe galaxies representative of the entire Hubble sequence, including three gas-poor early type galaxies (Figure 5.4). It is interesting to consider how these formed, and how they lost their gas. This small ($\sim$5%) fraction is suggestive of an extension of the morphology-density relation to the deepest underdensities of the voids, as was also found by Park et al. (2007). We note that in our sample of 60 galaxies none have radio AGNs, which has been suggested as a secular mechanism for halting star formation in void galaxies (Croton & Farrar 2008). Seven of the VGS galaxies could potentially be classified optically as AGNs, and of these

one appears to be an early type galaxy, forming an interesting population for further study.

5.6 Conclusion

We have carefully chosen a geometrically selected sample of 60 void galaxies from the SDSS to form a new Void Galaxy Survey, and imaged 55 of them in H I with the WSRT. We find that optically they are generally low luminosity, though not dwarf, blue disk galaxies. In H I they are gas rich with regular rotation, about half of which have strongly disturbed gas morphologies and kinematics. This is consistent with similar luminosity and optical morphology galaxies in average environments. Fourteen galaxies are not detected in H I, though six of these appear to have very similar small blue disks that are presumably gas rich with an H I mass below the detection limits. Only three of the VGS appear to be early type, none of which are detected in H I.

Compared with a sample of gas rich galaxies cross-matched between ALFALFA and SDSS, the VGS has star formation rates normalized by the stellar mass that is average for their stellar mass. We find no evidence for an increased H I mass to light ratio in low density regions, and in general find very few void galaxies with elevated H I mass to light ratios. At fixed morphology and luminosity the late type VGS galaxies have H I mass to light ratios consistent with the ALFALFA control sample, though there is some concern that the H I masses measured in ALFALFA are affected by confusion within the beam. Assuming instrumental differences in H I mass are negligible, the VGS galaxies are slightly more efficient at forming stars.

The small scale clustering of galaxies in voids is very similar to that in higher density regions, and all but one of the neighboring galaxies detected in H I in the voids appear to be companions of the targeted void galaxy, with most detected within 100 kpc and 100 km s^{-1}. Though we probe 485 Mpc^3 within the voids with H I sensitivity of $\sim 10^8$ $M_\odot$ we find no evidence of the missing void galaxy population.

Through the irregularities in the H I morphology and kinematics of these systems, void galaxies show many signs of ongoing interactions and gas accretion. VGS_12 in particular shows evidence of ongoing accretion by cold flows (Chapter 2 of this thesis). In general, void galaxies form a very interesting population of gas rich disk galaxies in which to study galaxy evolution.

APPENDIX

5.A Image catalog and discussion of individual systems

This Appendix presents an image atlas of the 60 galaxies comprising the Void Galaxy Survey, as well as an H I atlas presenting an overview of our observations of 55 of the VGS targets and the VGS companions detected in H I. These are followed by a brief discussion of some individually interesting galaxies in our sample.

5.A.1 Atlas of VGS targets

Figure 5.A-1 presents the *ugriz* combined color image from the SDSS catalog for each of the 60 VGS galaxies, with the VGS catalog name given above each image. All are scaled to the same physical size, such that each image shows approximately a 16 kpc by 16 kpc region of the sky at the distance of the target.

Figure 5.A-2 provides a H I atlas of the 41 void galaxies detected with the WSRT. On the left, H I contours from the total intensity map are overlaid on the SDSS *g*-band optical image. In the center, the intensity weighted velocity field is colored to emphasize any rotation in the gas, with contours to guide the eye. On the right, we present a position velocity slice that is aligned with the H I kinematic major axis. All images are created following the uniform reduction described in Section 5.3, and are shown with uniformly defined contours to aid comparison between the targets.

Figure 5.A-3 shows the H I radial surface density profiles for the 41 galaxies detected with the WSRT. The technique used to determine these profiles is described in Section 5.4.

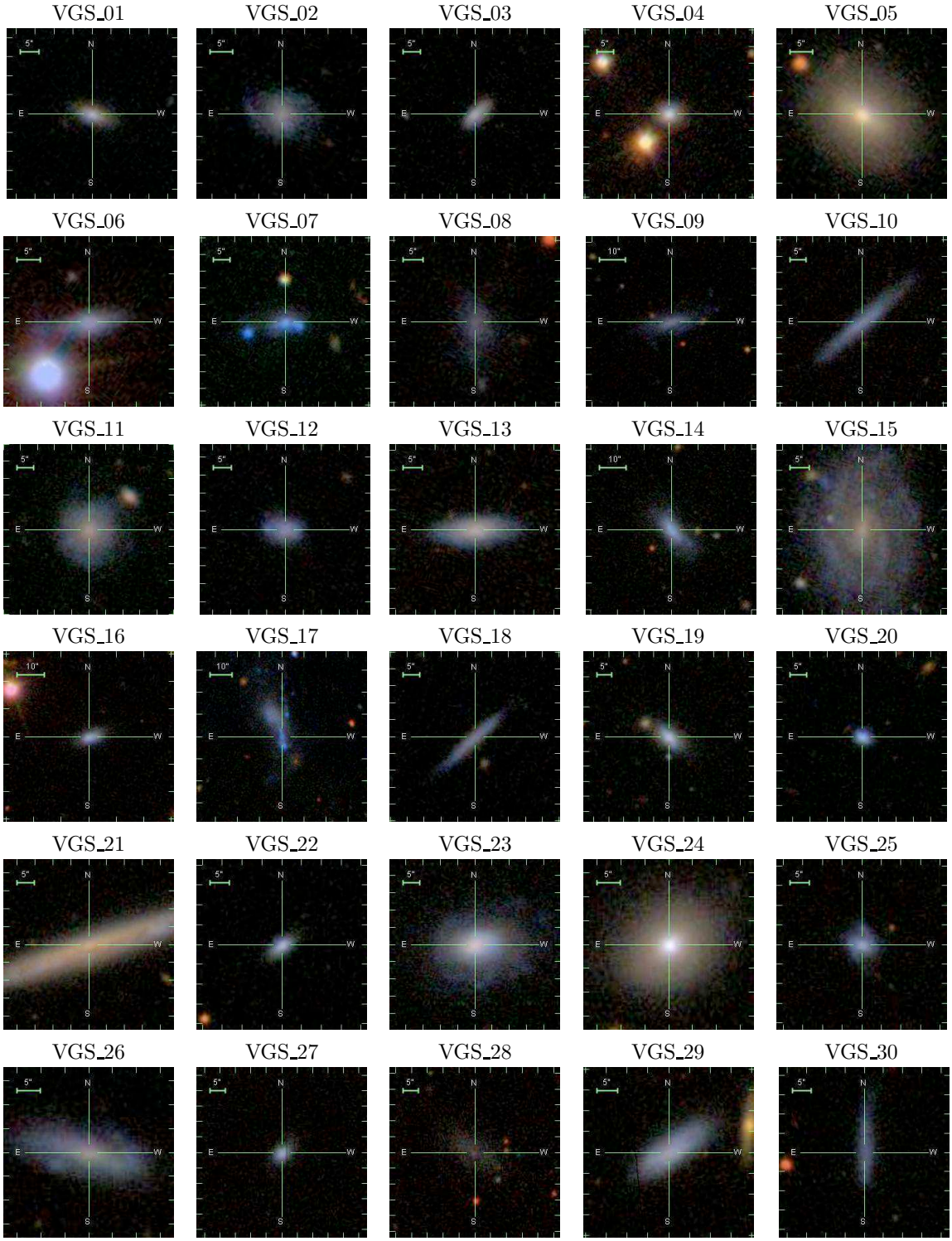
VGS_01
VGS_02
VGS_03
VGS_04
VGS_05
VGS_06
VGS_07
VGS_08
VGS_09
VGS_10
VGS_11
VGS_12
VGS_13
VGS_14
VGS_15
VGS_16
VGS_17
VGS_18
VGS_19
VGS_20
VGS_21
VGS_22
VGS_23
VGS_24
VGS_25
VGS_26
VGS_27
VGS_28
VGS_29
VGS_30

Figure 5.A-1

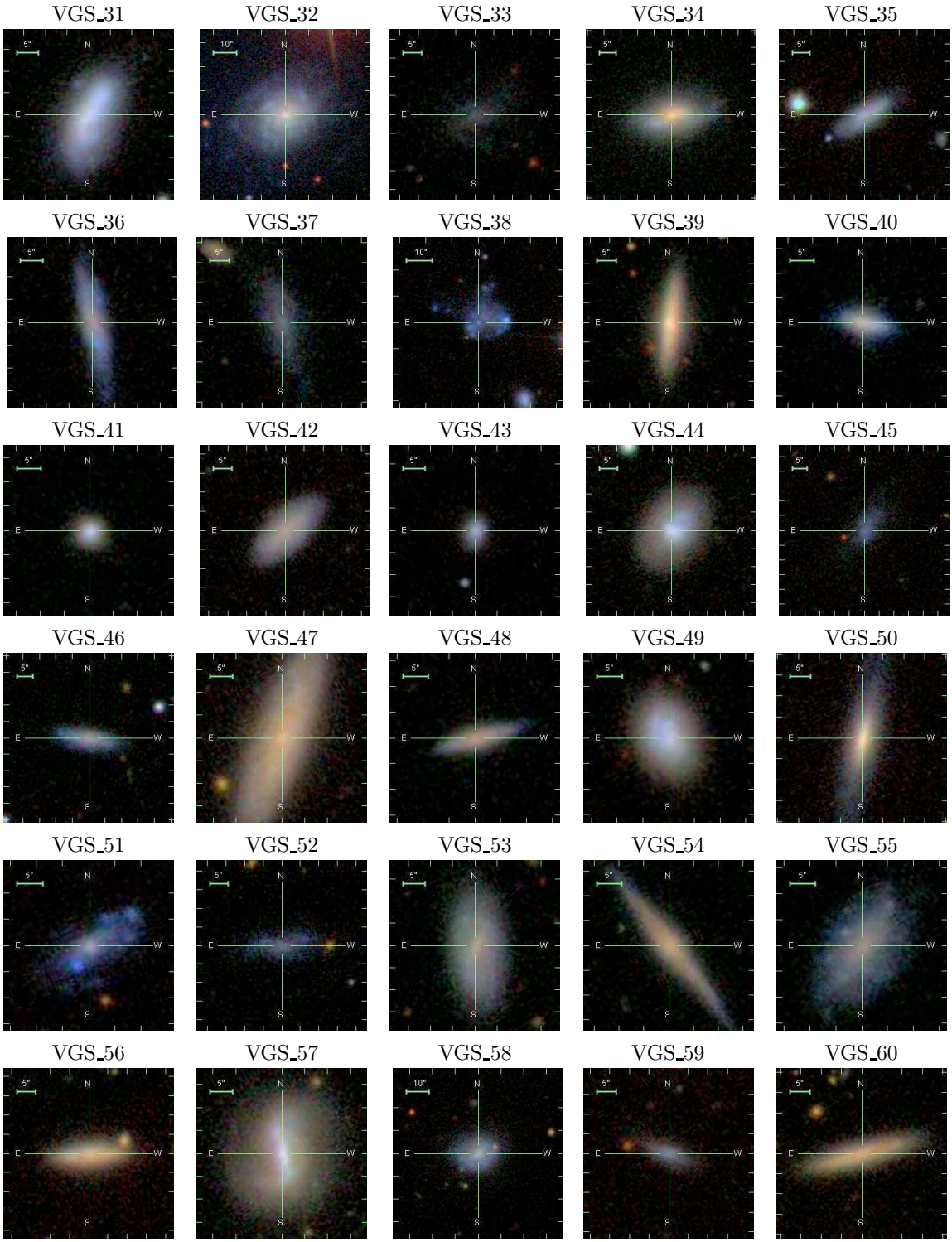

Figure 5.A-1: Our sample of void galaxies, scaled to the same physical size. Composite color images are taken from the online SDSS Finding Chart tool.

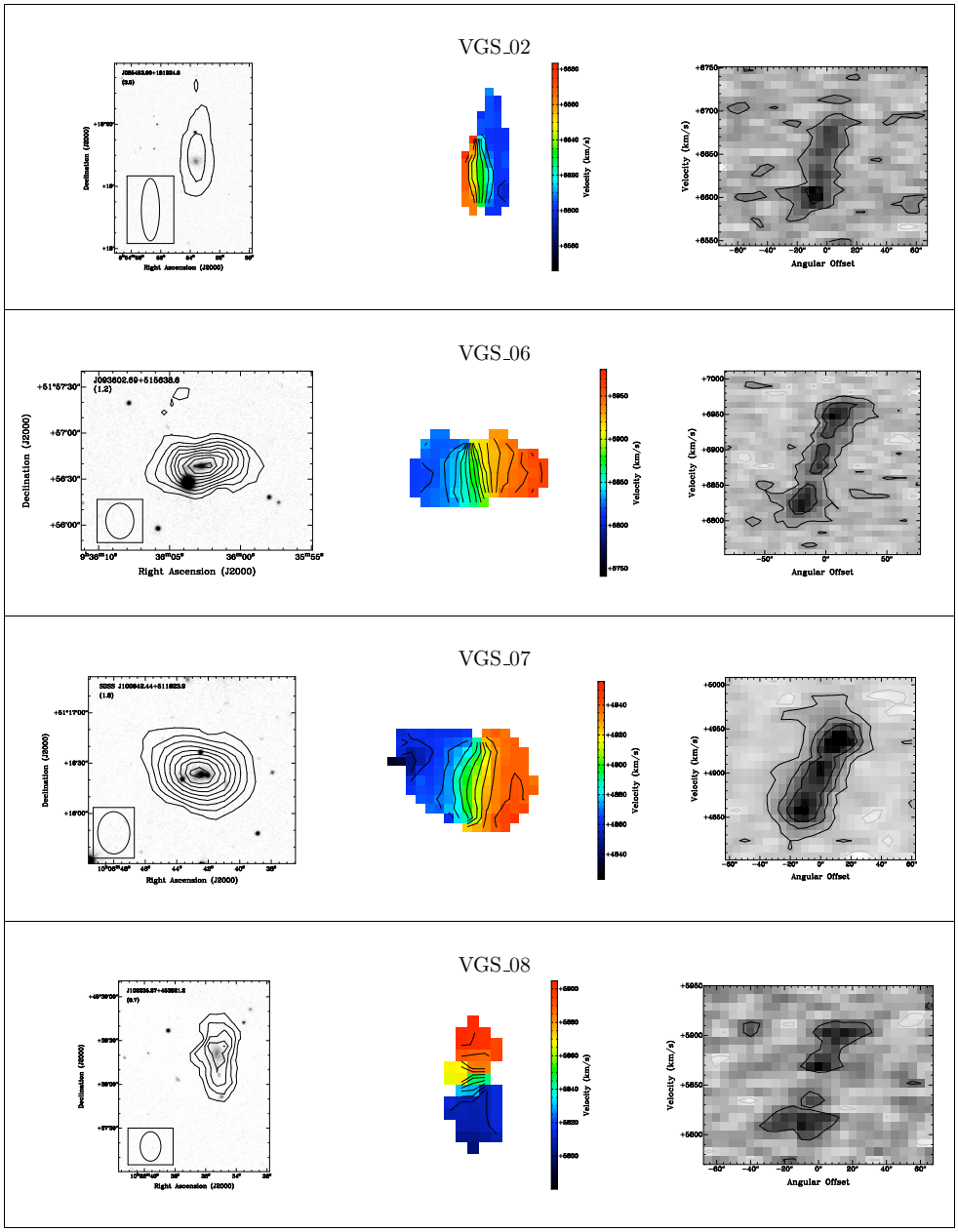
VGS_02
VGS_06
VGS_07
VGS_08
Declination (J2000)
Right Ascension (J2000)
Velocity (km/s)
Angular Offset

Figure 5.A-2

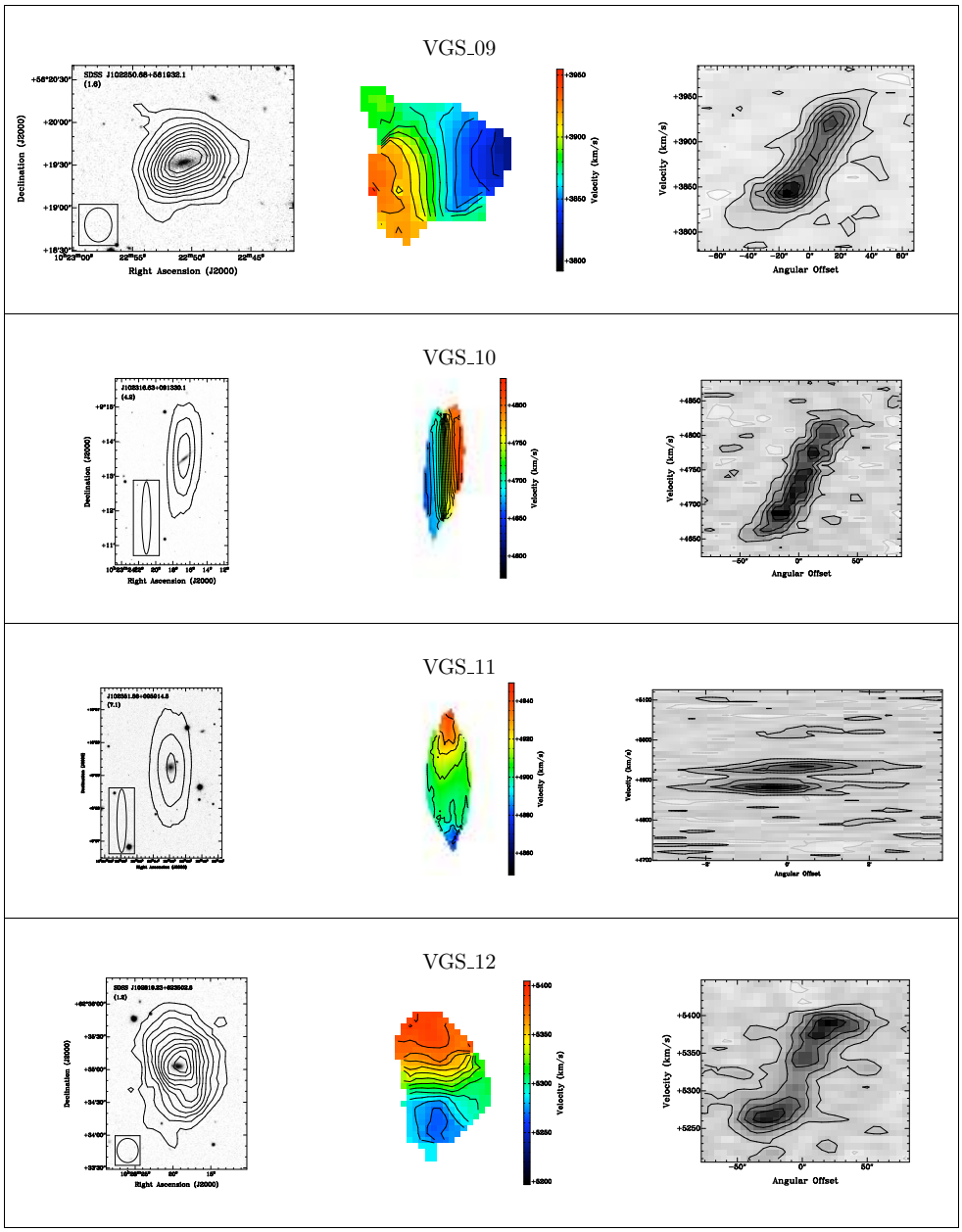
VGS_09
Declination (J2000)
Right Ascension (J2000)
Velocity (km/s)
Angular Offset
VGS_10
Declination (J2000)
Right Ascension (J2000)
Velocity (km/s)
Angular Offset
VGS_11
Velocity (km/s)
Angular Offset
VGS_12
Declination (J2000)
Right Ascension (J2000)
Velocity (km/s)
Angular Offset

Figure 5.A-2

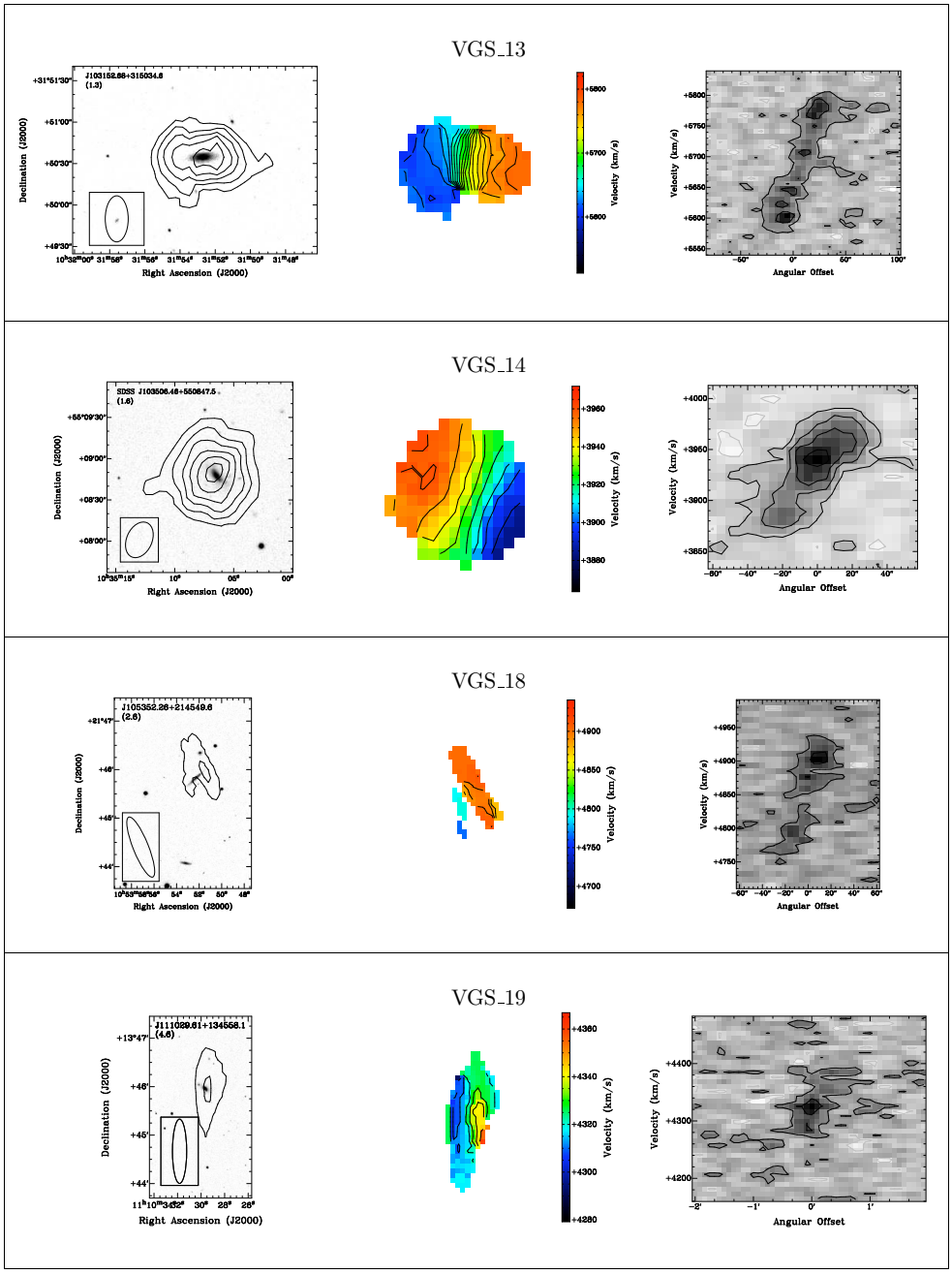
VGS_13
J103152.68+315034.6
(1.3)
Declination (J2000)
Right Ascension (J2000)
Velocity (km/s)
Angular Offset
VGS_14
SDSS J103506.46+550847.5
(1.6)
Declination (J2000)
Right Ascension (J2000)
Velocity (km/s)
Angular Offset
VGS_18
J105352.26+214549.6
(2.6)
Declination (J2000)
Right Ascension (J2000)
Velocity (km/s)
Angular Offset
VGS_19
J111029.61+134558.1
(4.6)
Declination (J2000)
Right Ascension (J2000)
Velocity (km/s)
Angular Offset

Figure 5.A-2

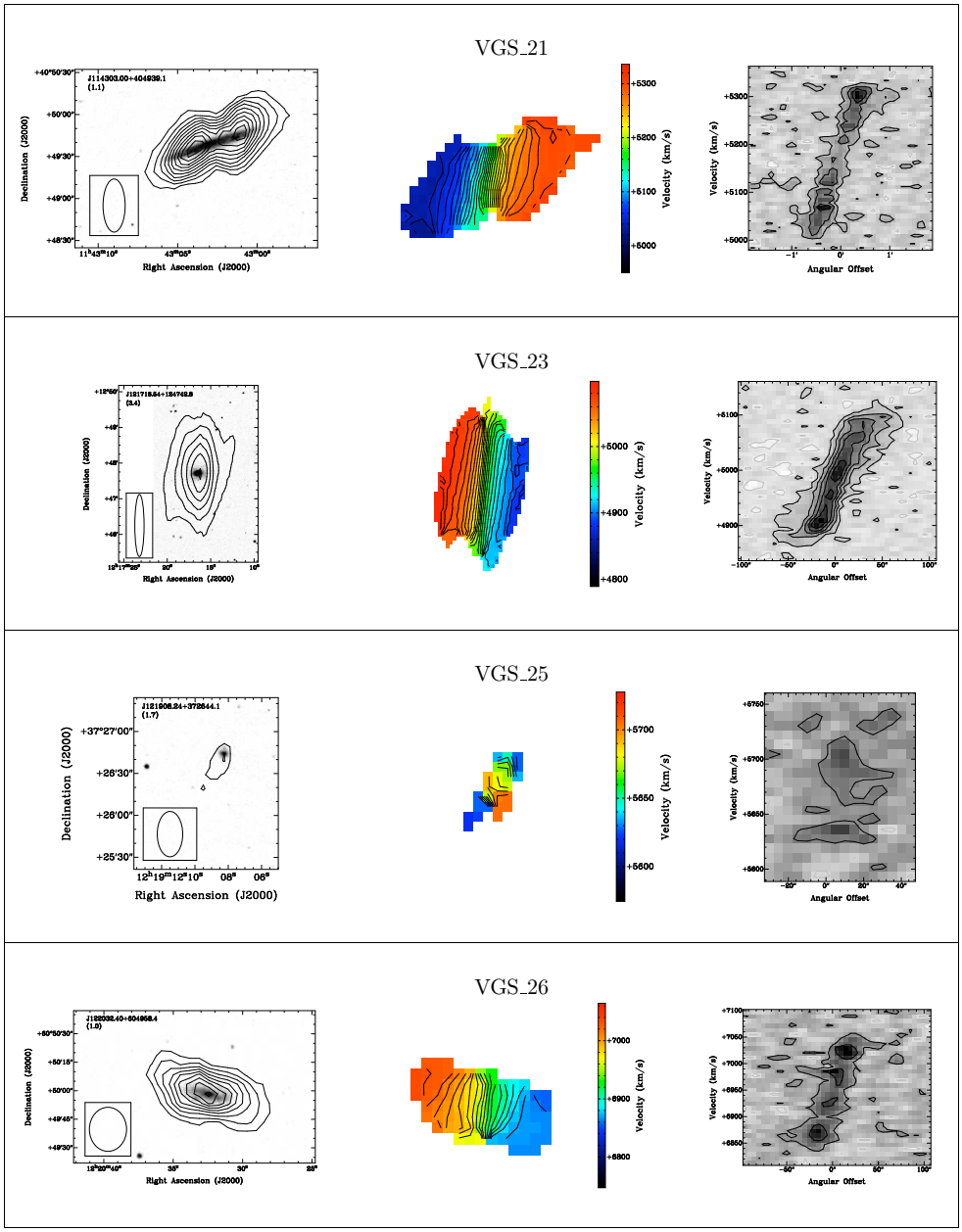
VGS_21
Declination (J2000)
Right Ascension (J2000)
Velocity (km/s)
Velocity (km/s)
Angular Offset
VGS_23
Declination (J2000)
Right Ascension (J2000)
Velocity (km/s)
Velocity (km/s)
Angular Offset
VGS_25
Declination (J2000)
Right Ascension (J2000)
Velocity (km/s)
Velocity (km/s)
Angular Offset
VGS_26
Declination (J2000)
Right Ascension (J2000)
Velocity (km/s)
Velocity (km/s)
Angular Offset

Figure 5.A-2

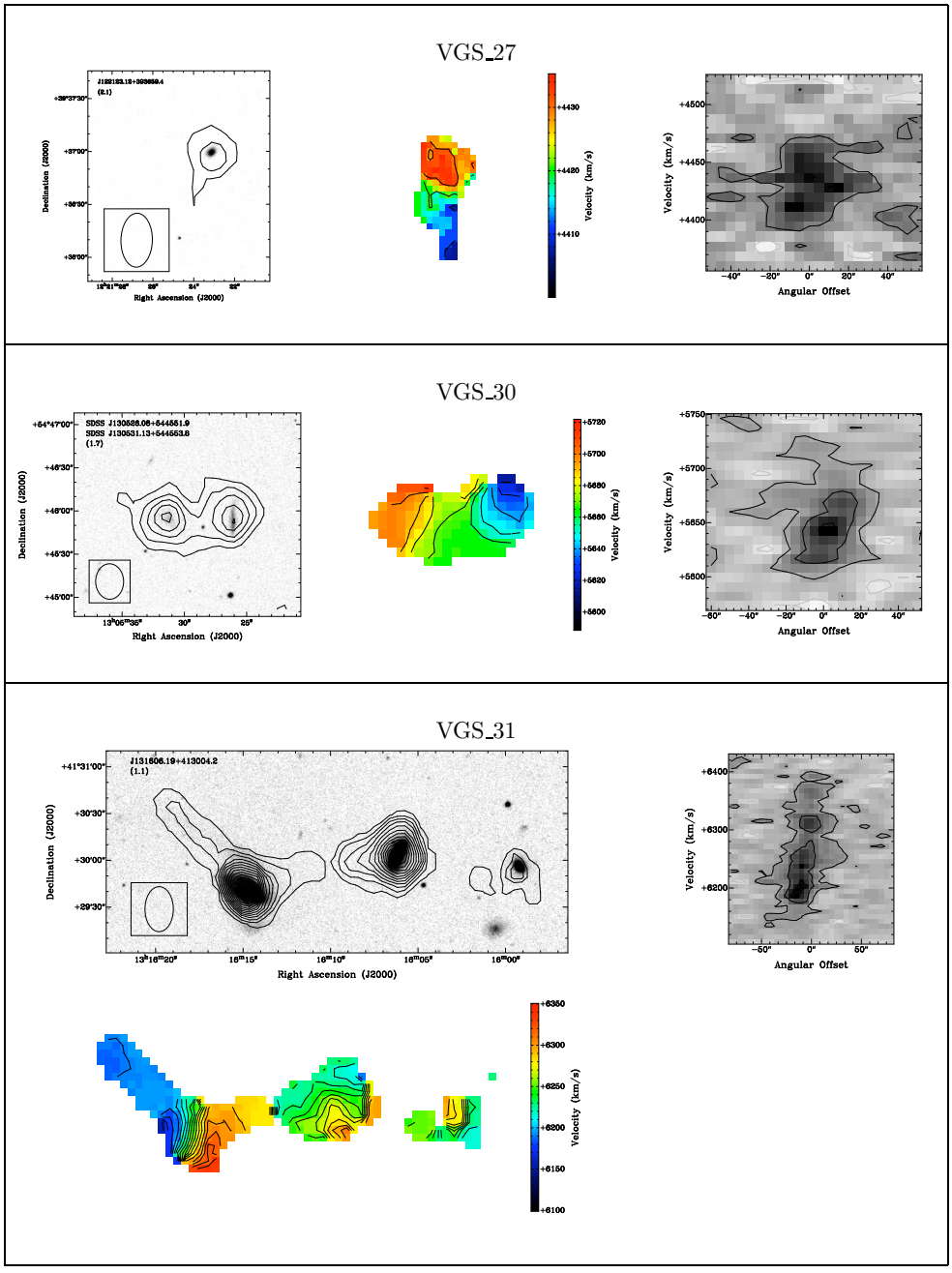
VGS_27
Declination (J2000)
Right Ascension (J2000)
Velocity (km/s)
Angular Offset
VGS_30
SDSS J130526.06+544551.9
SDSS J130531.13+544553.8
(1.7)
Declination (J2000)
Right Ascension (J2000)
Velocity (km/s)
Angular Offset
VGS_31
J131606.19+413004.2
(1.1)
Declination (J2000)
Right Ascension (J2000)
Velocity (km/s)
Angular Offset

Figure 5.A-2

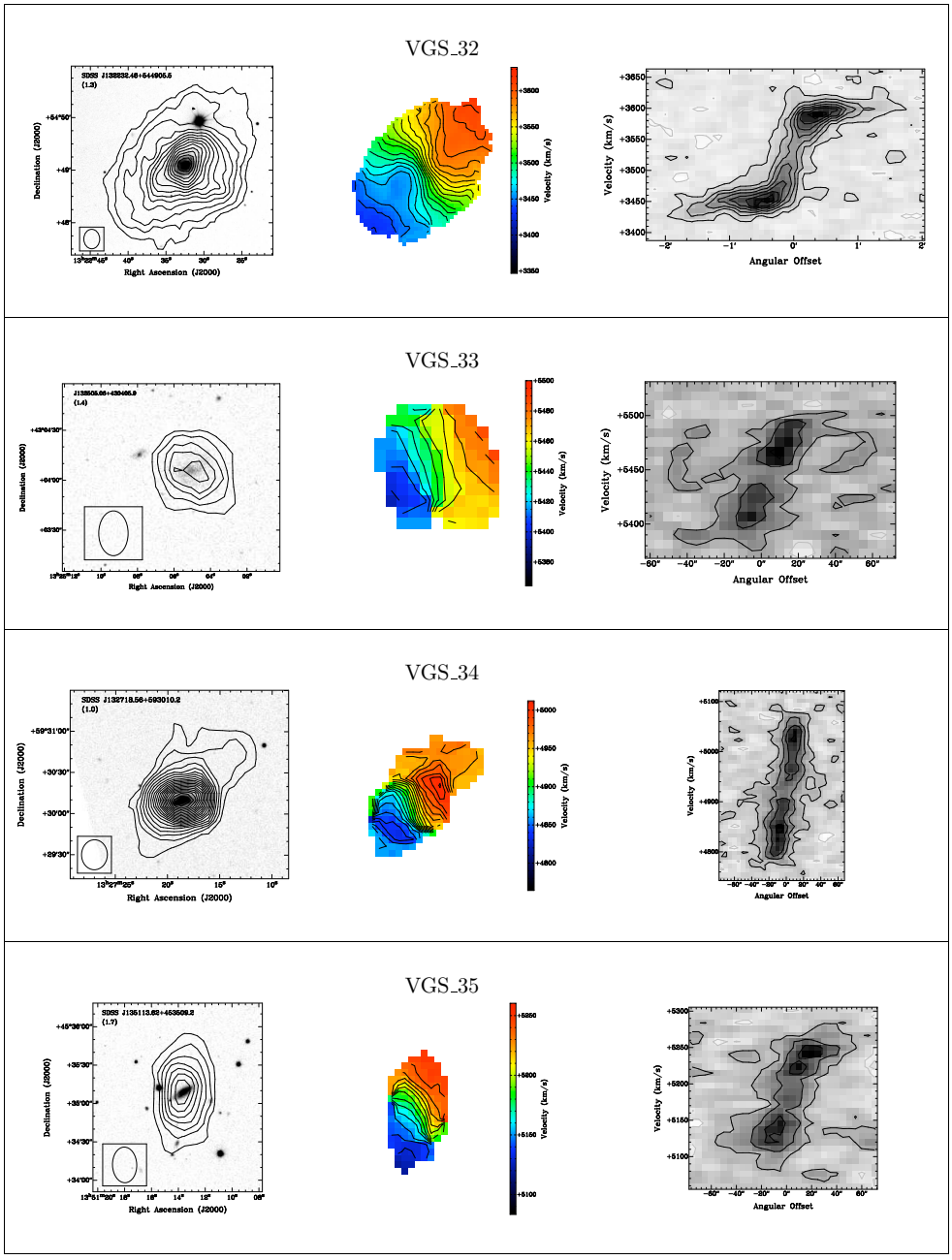
VGS_32
Declination (J2000)
Right Ascension (J2000)
Velocity (km/s)
Angular Offset
VGS_33
Declination (J2000)
Right Ascension (J2000)
Velocity (km/s)
Angular Offset
VGS_34
Declination (J2000)
Right Ascension (J2000)
Velocity (km/s)
Angular Offset
VGS_35
Declination (J2000)
Right Ascension (J2000)
Velocity (km/s)
Angular Offset

Figure 5.A-2

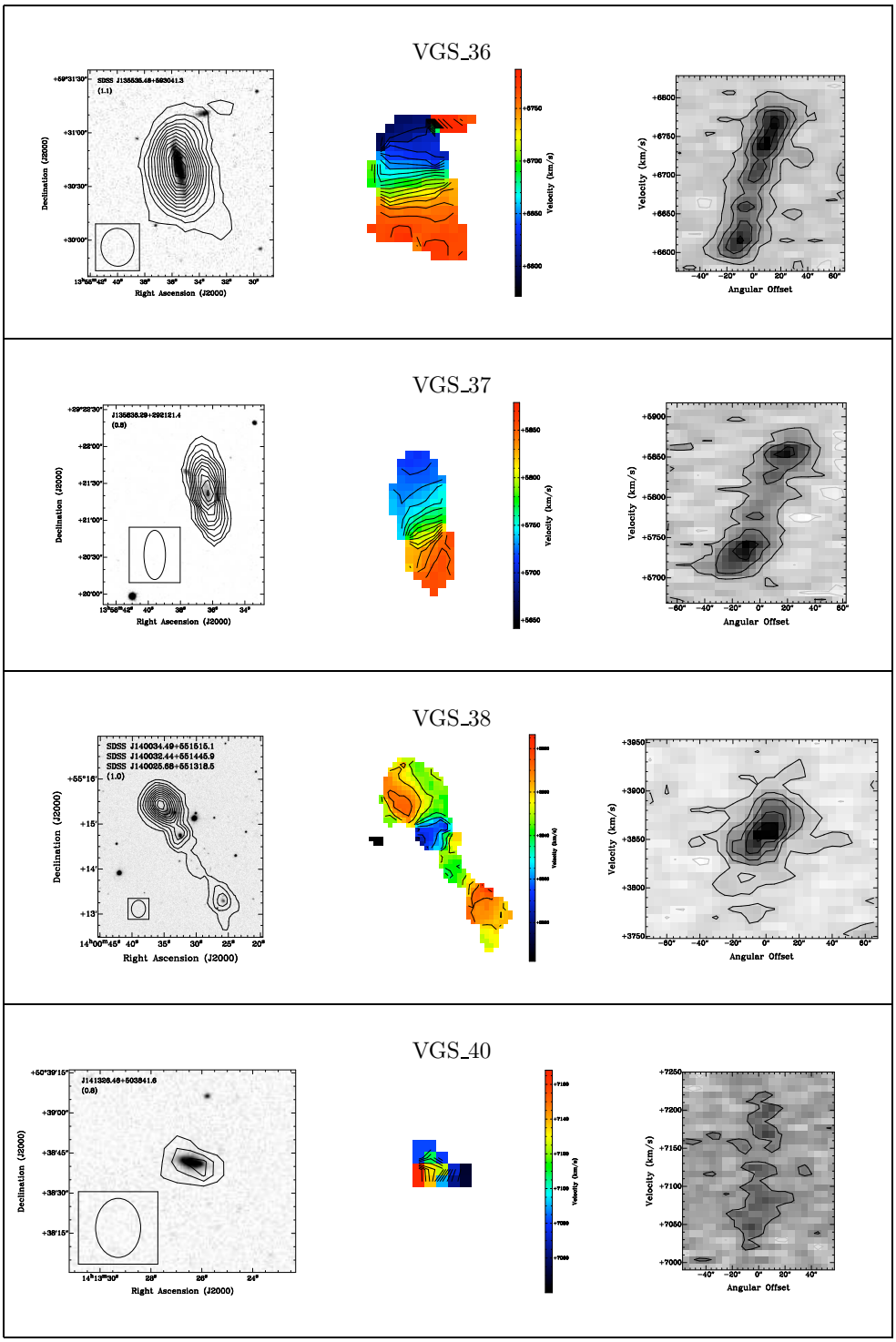
VGS_36
SDSS J135536.48+523041.3
(1.1)
Declination (J2000)
Right Ascension (J2000)
Velocity (km/s)
Angular Offset
VGS_37
J135536.29+292121.4
(0.8)
Declination (J2000)
Right Ascension (J2000)
Velocity (km/s)
Angular Offset
VGS_38
SDSS J140034.49+551515.1
SDSS J140032.44+551445.9
SDSS J140025.58+551318.5
(1.0)
Declination (J2000)
Right Ascension (J2000)
Velocity (km/s)
Angular Offset
VGS_40
J141338.46+503841.6
(0.8)
Declination (J2000)
Right Ascension (J2000)
Velocity (km/s)
Angular Offset

Figure 5.A-2

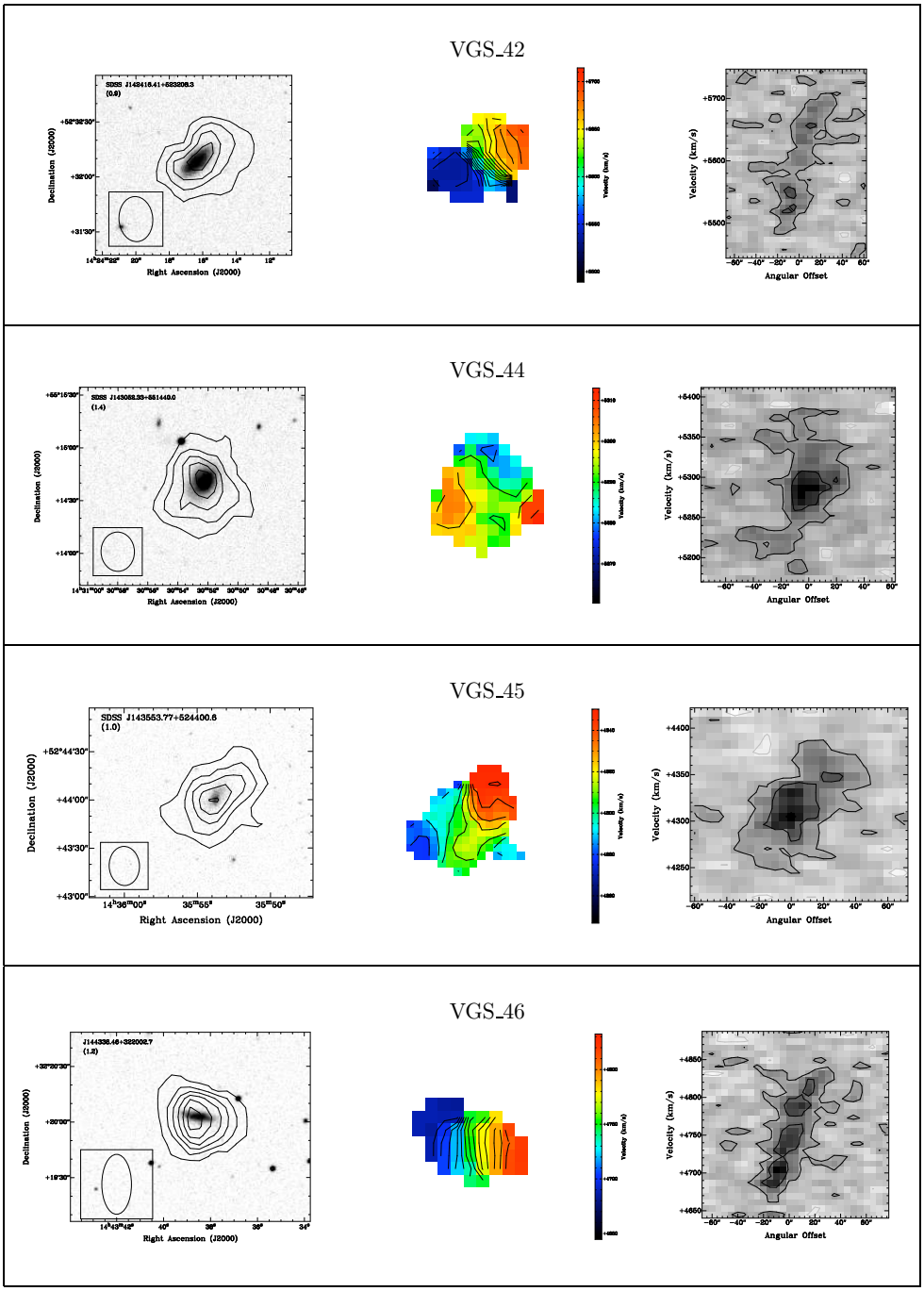
VGS_42
Declination (J2000)
Right Ascension (J2000)
Velocity (km/s)
Angular Offset
VGS_44
Declination (J2000)
Right Ascension (J2000)
Velocity (km/s)
Angular Offset
VGS_45
Declination (J2000)
Right Ascension (J2000)
Velocity (km/s)
Angular Offset
VGS_46
Declination (J2000)
Right Ascension (J2000)
Velocity (km/s)
Angular Offset

Figure 5.A-2

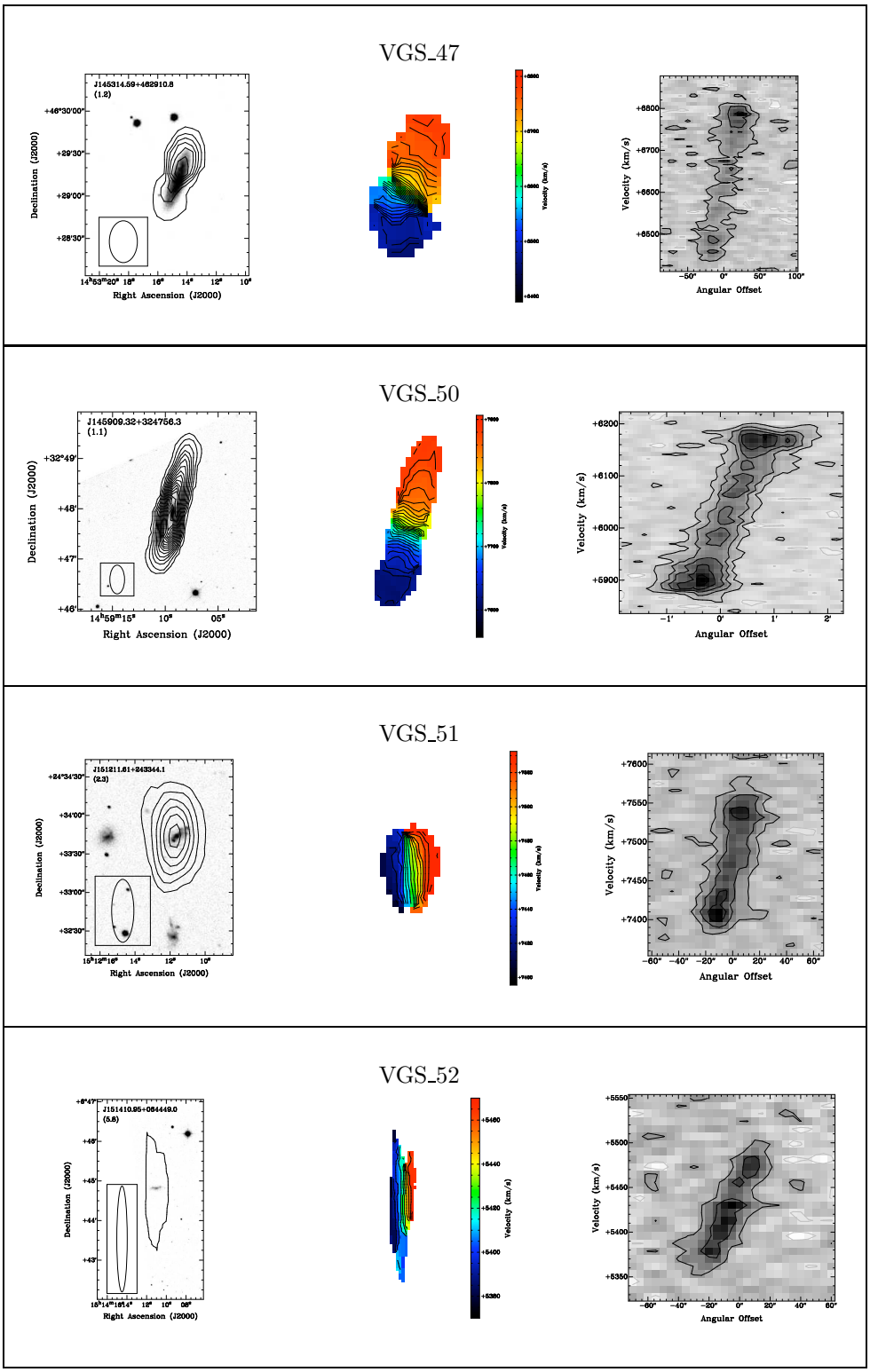
VGS_47
J145314.59+462910.8
(1.2)
Declination (J2000)
Right Ascension (J2000)
Velocity (km/s)
Angular Offset
VGS_50
J145909.32+324756.3
(1.1)
Declination (J2000)
Right Ascension (J2000)
Velocity (km/s)
Angular Offset
VGS_51
J151211.61+243344.1
(2.3)
Declination (J2000)
Right Ascension (J2000)
Velocity (km/s)
Angular Offset
VGS_52
J151410.95+084449.0
(5.8)
Declination (J2000)
Right Ascension (J2000)
Velocity (km/s)
Angular Offset

Figure 5.A-2

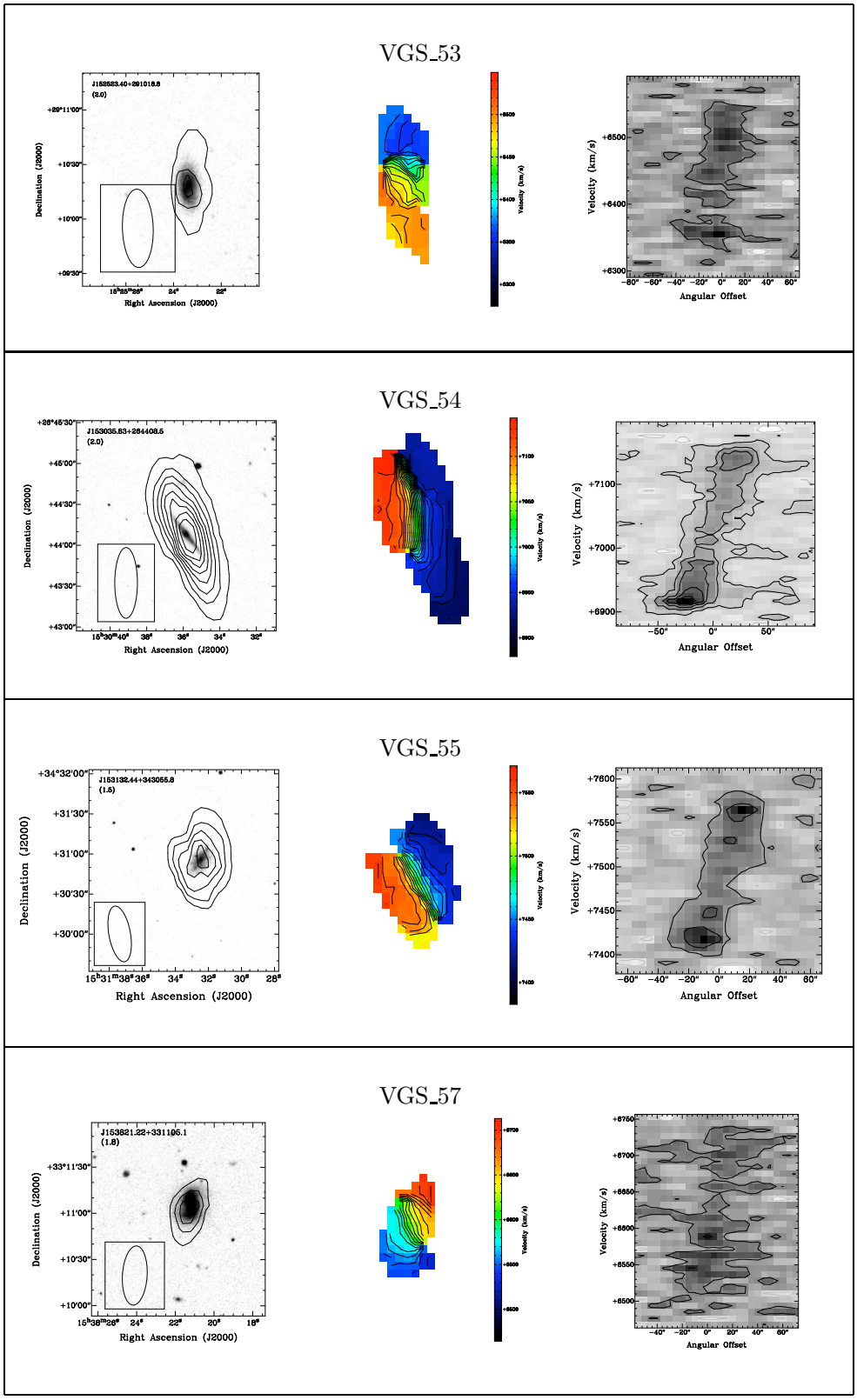
VGS_53
Declination (J2000)
Right Ascension (J2000)
Velocity (km/s)
Angular Offset
VGS_54
Declination (J2000)
Right Ascension (J2000)
Velocity (km/s)
Angular Offset
VGS_55
Declination (J2000)
Right Ascension (J2000)
Velocity (km/s)
Angular Offset
VGS_57
Declination (J2000)
Right Ascension (J2000)
Velocity (km/s)
Angular Offset

Figure 5.A-2

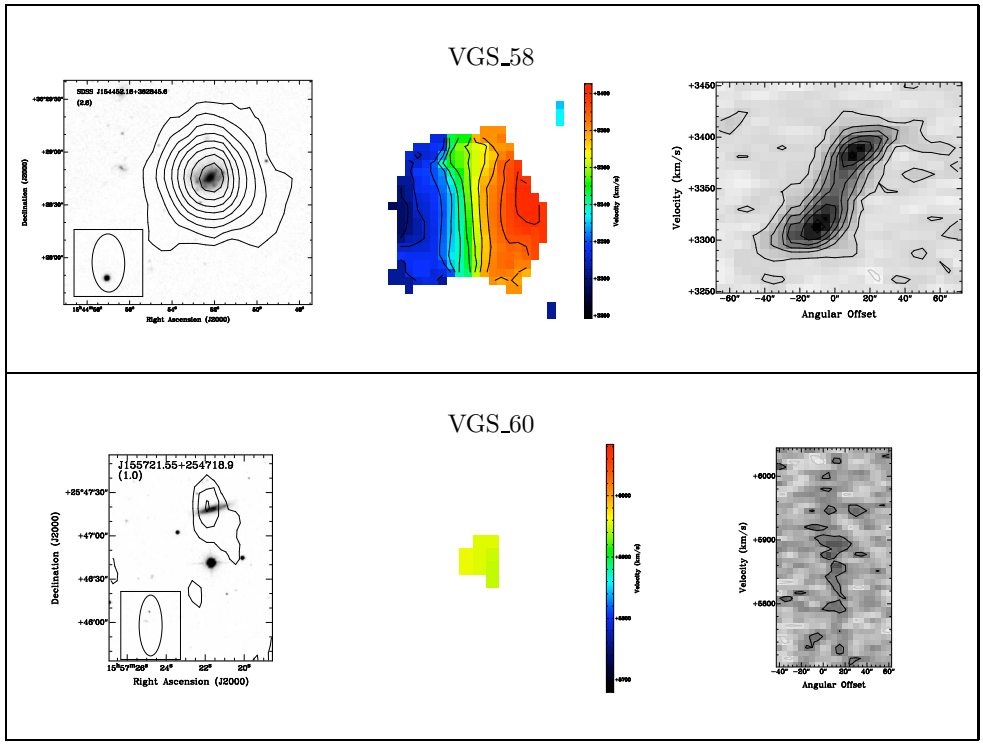

Figure 5.A-2: Targeted void galaxies. Contours in the total intensity maps (left) are at 5×10^{19} cm^{-2} plus increments of 10^{20} cm^{-2}. Confidence level (σ) of the lowest contour is given in the top left corner of each image. Lines in the velocity field images (center) indicate increments of 10 km s^{-1}. Position-Velocity diagrams (right) are along the kinematic major axis, contours are at increments of -1.5 (grey), 1.5 (black) + increments of 3σ .

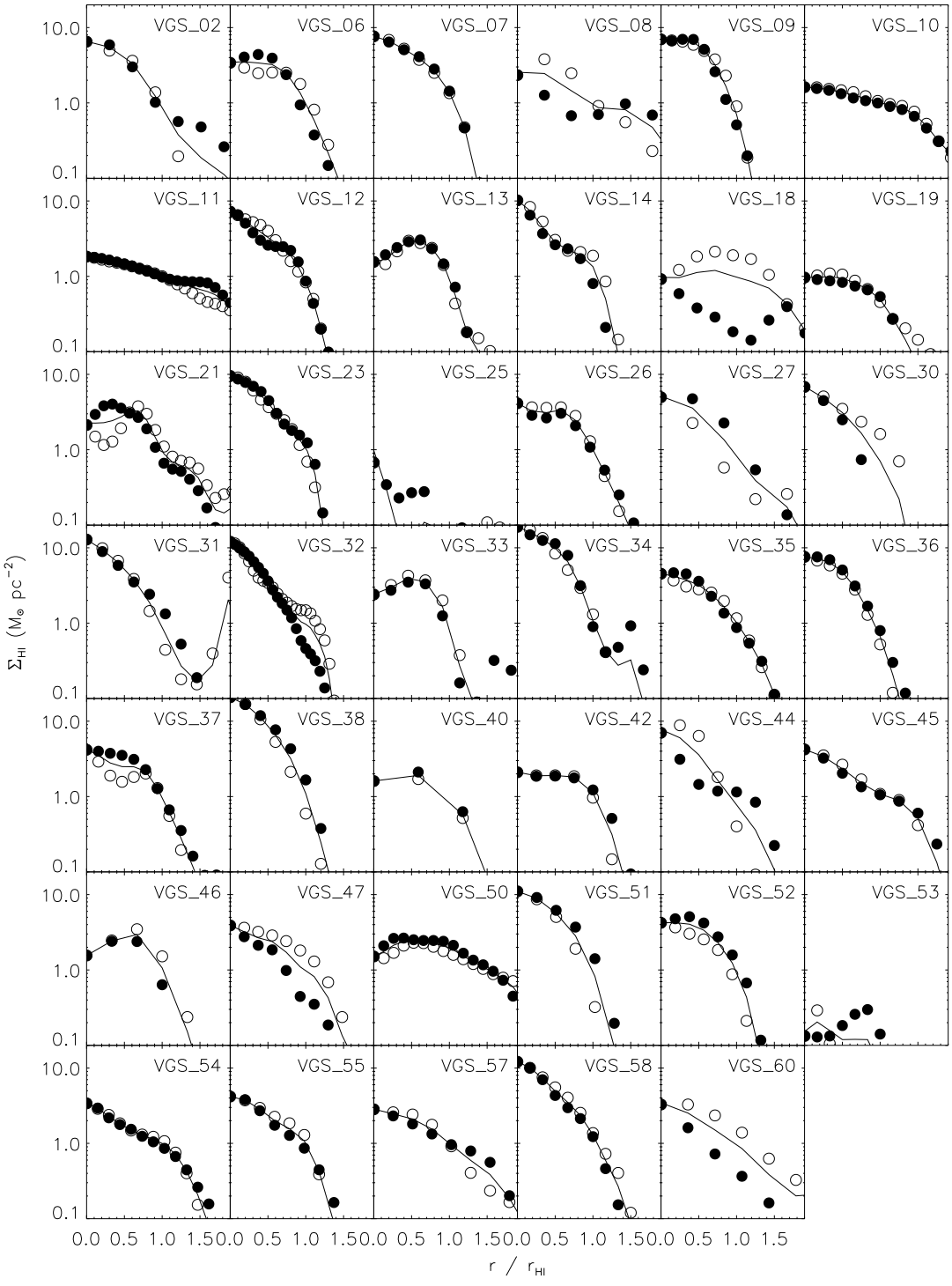

Figure 5.A-3: Radial surface density profiles for the east (open circles) and west (filled circles) sides of each disk, with the average overdrawn.

5.A.2 Atlas of VGS companions

In addition to the detection of 41 of the 55 VGS targets imaged with the WSRT, we detect in H I 18 neighboring galaxies within the void. Seven of these are shown in Figure 5.A-2 along with the target galaxies, and the remaining 11 are shown in Figure 5.A-4. As many of these targets are observed within the primary beam but removed from the beam center, the H I sensitivity is typically somewhat worse for these detections than for the primary targets. Thus we show here the H I contours for these detections with a lowest contour at 3σ, and indicate the corresponding column density in the upper right corner of each image.

5.A.3 Notes on individual systems

In addition to the very interesting objects previously described in our pilot study (Chapter 4 of this thesis), including interacting systems (VGS_30, VGS_34, VGS_38), misaligned gas disks (VGS_12, VGS_35), optically unusual morphologies (VGS_07) and undisturbed gas morphologies (VGS_32), we highlight here some additional interesting galaxies identified within the VGS.

VGS_05 is not detected in H I, and has an early type optical morphology. Red in color ($g-r \ = \ 0.76$), it does not present an entirely uniform elliptical morphology, with the light distribution in the center suggesting the presence of a disk or bar. It has the lowest specific star formation rate of the VGS.

VGS_24 is also not detected in H I, and has an optically very smooth, elliptical morphology but a slightly blue ($g - r \ = \ 0.55$) color.

VGS_25 has a small stellar disk and low H I mass, consistent with the small blue disk galaxies not detected that have very uniform optical properties (see Section 5.4.3). The H I mass detected in this galaxy is just above the stacked detection limit for the six other undetected targets described in Section 5.4.3, and we expect that this galaxy is analogous to those just below the limits.

VGS_31 is the second void galaxy in our sample to have two H I rich companions, with all three sharing a common envelope in H I. The first, VGS_38, was described in the pilot survey, and presents a very similar linear alignment of the three galaxies, suggesting filamentary structure within the void. The H I bridge connecting all galaxies in VGS_31 is more apparent in Figure 5.9, where we have imaged with natural weighting to increase our

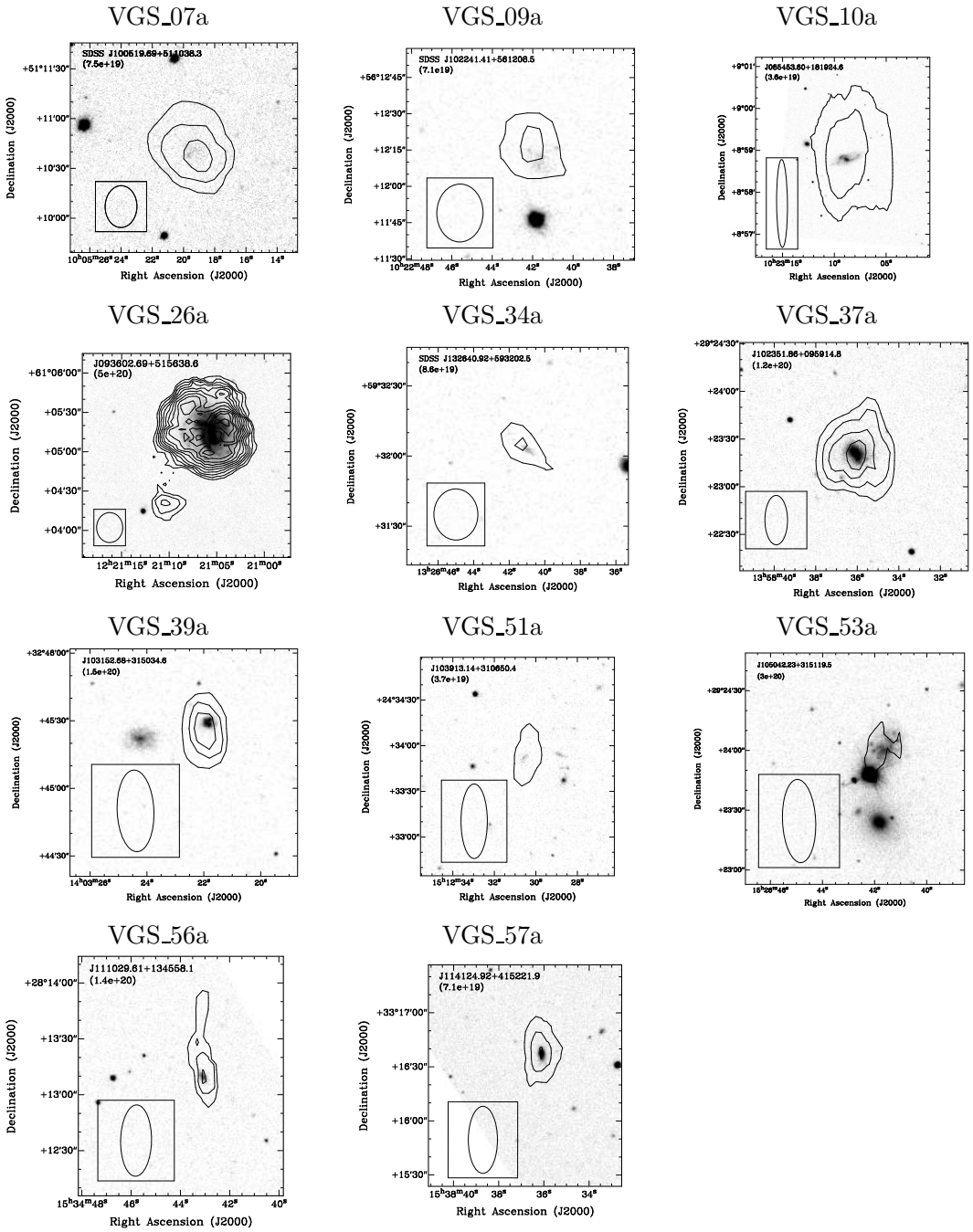

Figure 5.A-4: Companions. Note that VGS_30a, VGS_31a, VGS_31b, VGS_36a, VGS_38a, VGS_38b and VGS_54a are shown in Figure 5.A-2 along with the targeted void galaxy. Contours in the total intensity maps are at 3σ plus increments of 10^{20} cm^{-2}. Column density at the lowest contour, in atoms per cm^{-2}, is given in the top left corner of each image.

sensitivity. This system shows further signs of ongoing interactions in the left most galaxy, where a gas poor stellar ring is present just at the boundary of the H I disk. This interesting system is discussed in greater detail in Beygu et al. (in prep.).

VGS_47 has an undisturbed stellar disk but extremely lopsided H I morphology. This is not strongly reflected in the gas kinematics, though some evidence of warping may be seen.

VGS_50 is identified as having an extremely extended H I disk, with $r_{H\,I}/r_{90} \sim 5$, though it appears that the r_{90} optical radius includes only the brighter, redder inner disk and excludes the faint blue, more extended disk observed in the combined color image. With an edge-on gas disk and fairly regular kinematics with no indication of a warp, its 32 kpc physical extent is one of the largest in this sample. The H I surface density profile shows some evidence for a central hole in the gas distribution.

VGS_51 is located the deepest within the void, being at a density of less than a tenth the mean. Optically, it presents a disk morphology with many distinctive blue knots presumably related to areas of high star formation, and the galaxy as a whole does have a relatively high specific star formation rate. The HI distribution appears quite regular both morphologically and kinematically, though the gas disk may be slightly offset from the center of the stellar disk. This is difficult to judge as the optical disk center may be confused by the irregular morphology. It has a very faint (M_r = -14) dwarf companion at nearly coincident velocity and a sky separation of 133 kpc.

VGS_57 has the highest star formation efficiency of the VGS. It is one of the most luminous (M_r = -20.4) galaxies in our sample with one of the highest SFRs, almost 2 $M_\odot$ yr^{-1}. Optically, it appears to be a large, face-on strongly barred spiral, however the H I appears as a fairly concentrated disk with a significant warp at the position of the optical spiral arms. It has a smaller companion with a systemic velocity only $\sim$70 km s^{-1} different and a separation on the sky of 175 kpc.

Part III

Cosmological Constraints from Void Galaxies

Chapter 6

Simulated void galaxies in the standard cold dark matter model

The following text has been published in the Astrophysical Journal. The full reference for the published work is Kreckel, K., Joung, M. R., Cen, R. 2011, ApJ, 735, 132.

We analyze a $(120\ h^{-1}\ \mathrm{Mpc})^3$ adaptive mesh refinement hydrodynamic simulation that contains a higher-resolution $31 \times 31 \times 35h^{-3}$ Mpc subvolume centered on a $\sim$30 Mpc diameter void. Our detailed $\sim$1 kpc resolution allows us to identify 1300 galaxies within this void to a limiting halo mass of $\sim 10^{10}$ $\mathrm{M}_\odot$. Nearly 1000 galaxies are found to be in underdense regions, with 300 galaxies residing in regions less than half the mean density of the simulation volume. We construct mock observations of the stellar and gas properties of these systems, and reproduce the range of colors and luminosities observed in the SDSS for nearby ($z < 0.03$) galaxies. We find no trends with density for the most luminous ($\mathrm{M}_r < -18$) galaxies, however our dwarf void galaxies ($\mathrm{M}_r > -16$), though they are less reliably resolved, typically appear bluer, with higher rates of star formation and specific star formation and lower mean stellar ages than galaxies in average density environments. We find a significant population of low luminosity ($\mathrm{M}_r \sim -14$) dwarf galaxies that is preferentially located in low density regions and specifically in the void center. This population may help to reduce, but not remove, the discrepancy between the predicted and observed number of void galaxies.

6.1 Introduction

ΛCDM has proven fairly robust when compared with a wide range of existing observations (Lacey & Cole 1993; Cen et al. 1994; Zhang et al. 1995; Springel et al. 2005; Komatsu et al. 2011). Simulations can reproduce the galaxy clustering properties we observe in large redshift surveys, as well as the size of galaxy clusters. In addition, Λ cold dark matter (ΛCDM) predicts hierarchical growth as the dominant mechanism in galaxy evolution (Peebles 1969; White & Frenk 1991).

However, discrepancies with observation remain, particularly on individual galaxy scales. Theory predicts a centrally peaked mass distribution (cusp) should dominate the shape of the dark matter density profile (Navarro et al. 1996; but see Governato et al. 2010), while observations show that a wide range of halo sizes, from galaxy clusters to dwarf spheroidals, may instead have cored profiles (Tyson et al. 1998; Kleyna et al. 2003; Walker et al. 2009). Simulations have difficulty reproducing exponential, bulgeless disks, and observations within the Local Volume disagree with predictions of where we should find the largest disk galaxies (Peebles & Nusser 2010; Kormendy et al. 2010). The missing satellite problem describes from the overprediction of small dark matter halos clustering around the Milky Way Galaxy (Klypin et al. 1999; Moore et al. 1999; Simon & Geha 2007). CDM simulations result in the overprediction of the number of low-mass halos existing within voids (Peebles 2001). One key to solving these problems may come from the inclusion of sufficient physics to properly simulate the baryon content of galaxies, which does not dominate their mass but contributes significantly to small scale dynamics and observables, such as stars or gas.

Early cosmological simulations of voids were based on dark matter only, N-body simulations (e.g., Ryden & Turner 1984; White et al. 1987; Little & Weinberg 1994; Vogeley et al. 1994; Mathis & White 2002). These authors compared the dark matter distribution with the void statistics in large surveys such as the CfA redshift catalogs and the Las Campanas redshift survey, in terms of their sizes and abundances. Using semi-analytic prescriptions for galaxy formation on outputs from N-body simulations, Patiri et al. (2006b) studied the colors and specific star formation rates of void galaxies, finding that there are more blue galaxies in void but no systematic differences between void galaxies and the general galaxy population. Ceccarelli et al. (2006) used a similar method to study void dynamics and the effect of redshift distortions in void identification. The only cosmological hydrodynamic

simulations run to date focusing on voids are Viel et al. (2008), who analyzed the void statistics at $z \sim 2$, and Hoeft et al. (2006), who investigated the effect of the cosmological UV background on the formation of dwarf galaxies in voids.

We have selected a void region from within a full (120 h^{-1} Mpc)^3 cosmological simulation, and we examine with moderate resolution the dark matter, gas and stars of a large sample of galaxies located within and around this large void. We employ an adaptive mesh refinement (AMR) code to reproduce the gas physics on a scale of 1 kpc. Observationally, void galaxies are distinguishable from galaxies in average or overdense environments as they are typically less luminous, and at fixed luminosity are bluer, with higher rates of star formation and specific star formation (Rojas et al. 2004, 2005). This is not strongly reflected in their gas content, though they are generally gas-rich, as their total mass in H I is fairly typical for their luminosities (Szomoru et al. 1996, Chapters 4 & 5 of this thesis).

We compare the integrated properties of void galaxies from our simulation, described in Section 6.2, both with observed void galaxies and galaxies in higher density regions within this simulation. We present our results in Section 6.4 and our conclusions are summarized in Section 6.5.

6.2 Simulation Initial Conditions and Physical Processes

We perform cosmological simulations using the adaptive mesh refinement Eularian hydro code, Enzo (Bryan 1999; Norman & Bryan 1999; O'Shea et al. 2004), with a periodic box of size 120 h^{-1} Mpc comoving on a side and cosmological parameters taken from the WMAP5 ΛCDM results combined with measurements of Type Ia supernovae and Baryon Acoustic Oscillations in the galaxy distribution (Hinshaw et al. 2009) : $(\Omega_m, \Omega_\Lambda, \Omega_b, h, \sigma_8, n_s) = (0.279,$ 0.721, 0.0462, 0.701, 0.817, 0.960). We first run a low-resolution simulation with a uniform dark matter particle mass of 7.6×10^{10} M$_\odot$, 128^3 root grid cells, and only 4 levels of refinement from an initial redshift of $z = 99$ to 0. Based on the $z = 0$ output of this simulation, a large void region having a diameter of ∼30 h^{-1} Mpc was identified. (see also Cen (2010)). Tracing the dark matter particles back to the initial redshift of $z = 99$ showed that the void region expands with time in terms of comoving volume, as expected. To achieve high mass and spatial resolution, we then use the multimass initialization technique and employ three nested volumes with successive particle masses decreased by a factor of 8. Hence, the

innermost 31 $\times$ 31 $\times$ 35 h^{-3} Mpc^3 comoving volume, sufficiently large to contain the identified void volume at $z = 0$, has a dark matter particle mass of 1.5 $\times 10^8$ M$_\odot$. Within this innermost nested volume, hydrodynamic refinements were allowed beginning with a root grid cell size of 937 h^{-1} kpc and a maximum refinement level of $l_{\rm max} = 10$, resulting in a maximum resolution of 0.916 h^{-1} kpc at $z = 0$.

The simulation includes a metagalactic UV background (Haardt & Madau 1996), a diffuse form of photoelectric and photoionization heating (Abbott 1982; Joung & Mac Low 2006), and shielding of UV radiation by neutral hydrogen (Cen et al. 2005). They also include cooling due to molecular hydrogen (Abel et al. 1997) and metallicity-dependent radiative cooling (Cen et al. 1995) extended down to 10 K (Dalgarno & McCray 1972). Reionization of hydrogen and helium is included and is assumed to be completed by $z = 6$.

Inside the innermost nested volume where AMR is allowed, additional physical processes of star formation and feedback are implemented. Star particles are created in cells that satisfy a set of criteria for star formation proposed by Cen & Ostriker (1992), which requires that the gas within that cell be contracting, cooling rapidly and gravitationally unstable. Under these conditions, a stellar particle of mass $m_* = c_* m_{\rm gas} \Delta t / t_*$ is created to replace gas from that cell, and is tagged with its initial mass, creation time, and metallicity. Here, Δt is the time step, $t_* = \max(t_{\rm dyn}, 3 \times 10^6 {\rm yr})$, $t_{\rm dyn} = \sqrt{3\pi/(32 G \rho_{\rm tot})}$ is the dynamical time of the cell, $m_{\rm gas}$ is the baryonic gas mass in the cell, and $c_* = 0.03$ is the star formation efficiency. Star particles typically have an initial mass of $\sim 5 \times 10^6$ M$_\odot$. Star formation and supernovae feedback are modeled following Cen et al. (2005) with a supernovae efficiency of $e_{SN} = 10^{-5}$. Star particle masses decay slightly as feedback energy and ejected metals are distributed into the 27 local gas cells, weighted by the specific volume of each cell, and centered at the star particle in question. The temporal release of metal enriched gas and thermal energy at time t has the following form: $f(t, t_i, t_{\rm dyn}) \equiv (1/t_{\rm dyn})[(t - t_i)/t_{\rm dyn}] \exp[-(t - t_i)/t_{\rm dyn}]$, where t_i is the formation time of a given star particle. The metal enrichment inside galaxies and in the intergalactic medium (IGM) is followed self-consistently in a spatially resolved fashion (Cen et al. 2005). Recently, Cen (2010) used a simulation of the same system with a higher spatial resolution (by a factor of 2) to study the nature of damped Ly-α systems.

6.3 Mock Observations within the Simulation Volume

We identify virialized objects in our high-resolution simulations using the HOP algorithm (Eisenstein & Hut 1998) with the threshold parameter ($\delta_{\rm outer}$) of 125. For identifying galaxies, we used higher $\delta_{\rm outer}$ values of 10^3 and 10^4 to additionally find subhalos located within virialized objects. Galaxies are excluded that are outside of the central, high-resolution $\sim (30\ h^{-1}\ {\rm Mpc})^3$ region, or that contain any coarse dark matter particles more massive than the highest particle resolution achieved. We also exclude any dark matter halos with fewer than 100 particles within the virialized region to ensure sufficient resolution of the physical balance between pressure and self-gravity within the simulated galaxies. For this work, we have extracted the hydrodynamic data around every identified galaxy at a uniform resolution corresponding to level 8, or a physical scale of 3.66 h^{-1} kpc at $z = 0$, as it is sufficient for our examination of the integrated properties in these systems and significantly speeds our analysis.

The light distribution is computed from the star particles using the Galaxy Isochrone Synthesis Spectral Evolution Library (GISSEL) stellar synthesis code (Bruzual & Charlot 2003). We calculate the luminosities of the simulated galaxies in the five Sloan Digital Sky Survey (SDSS, Abazajian et al. 2009) bands (*ugriz*). Internal extinction corrections were applied by considering the mass column density of metals, Σ_Z, along the line of sight within the virial radius for a randomly chosen viewing direction along the simulation volume axes. Starting with the observational relation determined in the Milky Way at solar metallicity (Binney & Merrifield 1998),

$$A_V \ = \ \frac{N(H_{\rm tot})}{1.9 \ \times \ 10^{21} \ \ {\rm cm}^{-1}} \ mag, \tag{6.1}$$

we allow for some dependence on metallicity, and scale for the fraction of refractory elements, f_{Fe} (Vladilo 2004). Thus we find that

$$A_V \ = \ \frac{\Sigma_Z \ f_{\rm Fe}}{F \ m_p \ 4 \ \times \ 10^{19} \ \ {\rm cm}^{-2}} \ mag. \tag{6.2}$$

We choose a scaling factor, $F = 1.5$, to match our simulated extinction with the observational relation (Equation 6.1) for those simulated galaxies with solar metallicity. We also considered the observational dust to gas relation determined in the Large Magellanic Cloud, which has a much larger uncertainty, as compared to 1/3–1/2 solar metallicity simulated galaxies (Koornneef 1982). We find a best fit with a factor of $F \sim 3$, however a factor of

$F = 1.5$ is still in agreement to within the errors, which are quite large, and we adopt this value for the remainder of this paper. Extinctions for each star particle were then scaled to the central wavelength for each of the five SDSS bands following Calzetti et al. (2000). We define the integrated stellar parameters (i.e. mass, luminosity, star formation rate) of each simulated galaxy to be the sum of the properties of the star particles located within 15% of the virial radius of the galaxy at a given redshift.

The dark matter density field was determined by calculating the mean dark matter density for the entire simulation volume, gridding all dark matter particles to a 1 h^{-1} Mpc grid, then applying a 5 h^{-1} Mpc three-dimensional Gaussian smoothing filter. The smoothing length was chosen to agree with the galaxy correlation length observed in large redshift surveys (Jing et al. 1998; Park et al. 2007). We also note that our choice of smoothing length assigns a reasonable dark matter density contrast of $\delta\rho/\rho < -0.5$ to all galaxies where the distance to the third nearest neighbor is greater than 7 h^{-1} Mpc, which was the more restrictive void galaxy selection technique used by Rojas et al. (2004).

6.4 Results

Of a total of 1268 galaxies with high resolution hydrodynamic simulation, none are found at positions with a dark matter density contrast (see Section 6.3) of more than 1 as we include only filaments and walls bounding the void but no massive clusters. 950 galaxies are found at locations with $\delta\rho/\rho < 0$, from which we form a void sample (VS) of 648 galaxies with $-0.5 < \delta\rho/\rho < 0$, and 302 that are in regions with $\delta\rho/\rho < -0.5$ form a low-density void sample (LVS). There are also 318 galaxies that make up a non-void sample (NV) at roughly average densities ($0 < \delta\rho/\rho < 1$) on the void boundaries (Table 6.1, Figure 6.1). We make these divisions in part to facilitate direct comparison with observed void samples (Rojas et al. 2004, 2005). We can also define the distance, R, from the void center at [64, 71, 45] h^{-1} Mpc, as identified within the full 120 h^{-1} Mpc box, and find that only two galaxies resolved by the simulation are within 5.5 h^{-1} Mpc and no NV galaxies are within 18 h^{-1} Mpc. We use this to additionally define a void center sample (VC) of 176 galaxies within 18 h^{-1} Mpc. Simulated observations were made with a typical H I column density detection limit of 1×10^{19} cm^{-2}, and resulting integrated H I column density contours overlaid on simulated observations of the stellar luminosity (Figure 6.2).

Table 6.1: Categories defined for comparison between simulated galaxy populations.

Category	Description	Definition	Number of Galaxies
NV	non-void	$0 < \delta\rho/\rho < 1$	318
VS	moderate underdensity	$-0.5 < \delta\rho/\rho < 0$	648
LVS	lowest density	$\delta\rho/\rho < -0.5$	302
VC	void center	R $< 18h^{-1}$ Mpc	176

We apply a Kolmogorov-Smirnov test to determine if the luminosity distribution of these samples could be drawn from the same parent population. The probability that the LVS or VC samples are drawn from the same population as the NV sample is fairly low (P < 0.03), however there is a very strong probability (P $= 0.847791$) that the VS sample is drawn from the same population as the NV sample. This suggests that there is a sharp distinction between the galaxy populations in the deepest underdensities and those in more moderately underdense regions. This is most apparent in the large population of low luminosity galaxies found preferentially in the void center (see Section 6.4.5).

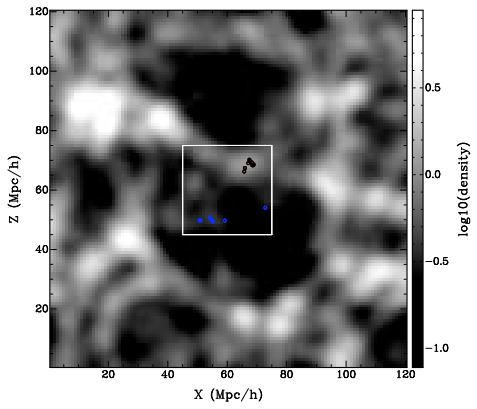

Figure 6.1: Slice of thickness 1 h^{-1} Mpc through the simulation volume smoothed dark matter density field. The high resolution region (white box) contains a large fraction of the large central void, and the positions of NV (black circles) galaxies trace the higher density regions while the LVS (blue circles) galaxies are located well within the void.

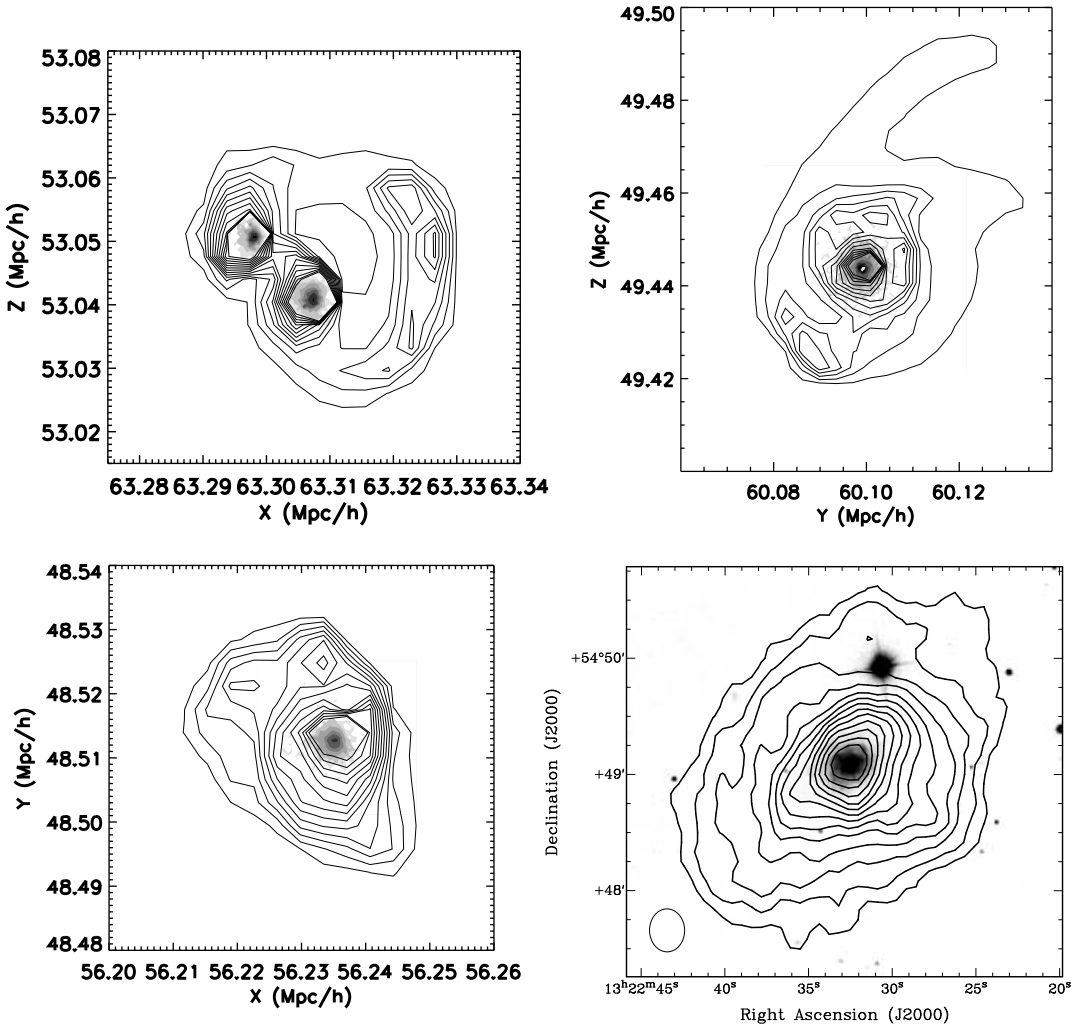

Figure 6.2: Simulated observations of LVS galaxies, with sample observed void galaxy (bottom right) for reference. Greyscale indicates g-band emission, contours show H I column densities of 5×10^{19} cm^{-2} plus increments of 10^{20} cm^{-2} with a maximum of 1.25×10^{21} cm^{-2}. The observed void galaxy VGS_32 (bottom right), described in Chapter 4 of this thesis, shows the H I beam shown in the lower left. The simulated and observed galaxies have roughly the same luminosity and H I extent, and in general the agreement is good. However, the simulated galaxies have significantly more low column density H I.

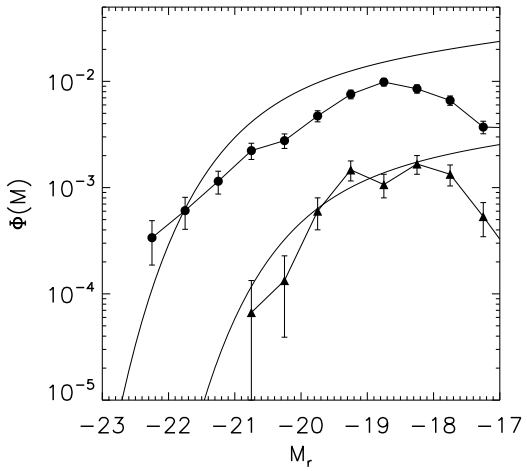

Figure 6.3: Luminosity function of simulated void and 'wall' galaxies. Following Hoyle et al. (2005), we split our sample into void galaxies with $\delta\rho/\rho < -0.4$ (triangles) and identify the remainder as 'wall' galaxies (circles), with the respective observationally determined Schechter function overplotted. The simulated void galaxies well reproduce observations, and we underpredict the function in the "wall" sample as we our simulation volume excludes higher density regions.

6.4.1 Luminosity Function

As the most luminous galaxies have been more robustly simulated throughout their merger history, we expect that this population will most closely match observations. Indeed, the observed void galaxy luminosity function is very well reproduced (Figure 6.3). Here we have divided our sample into two at $\delta\rho/\rho < -0.4$, following Hoyle et al. (2005), and contrast the lower density void galaxies with the higher density 'wall' galaxies. Our simulated void sample very closely matches their observationally determined Schechter function fit. Our 'wall' sample contains too few galaxies, however our volume excludes any significant high density regions and a significant number of galaxies contaminated by coarse particles. The turnover in both samples at $M_r = -18.5$ indicates the completeness limits in our simulated galaxy samples, and we expect that increased resolution would not significantly change our results for galaxies above this luminosity threshold.

6.4.2 Colors

Compared to observations, our simulated void galaxy colors appear consistent, however they do not differ greatly from the non-void galaxies. Table 6.2 compares the mean properties of our galaxy samples with the photometric study by Rojas et al. (2004), who construct a void galaxy sample of those galaxies with a third nearest neighbor distance greater than 7 h^{-1} Mpc and a wall sample of the remaining galaxies. Duplicating the magnitude limit ($-17.77 > M_r > -22.5$) for their distant galaxy sample, and subsequently dividing it into a bright ($M_r < -19.5$) and faint ($M_r > -19.5$) subsamples, we see no consistent trend with density in our galaxy colors, but a strong dependence on magnitude. In all magnitude limited samples, we note that the NV galaxies are too blue when compared to the Rojas et al. (2004, 2005) wall sample.

Table 6.2: Average color and star formation properties of our simulated galaxies as compared with the magnitude limited samples of Rojas et al. (2004) and Rojas et al. (2005).

Property	LVS	VS	NV	Rojas Void	Rojas wall
		$-17.77 > M_r > -22.5$			
g-r	0.586 ± 0.0144	0.600 ± 0.00930	0.589 ± 0.0133	0.615 ± 0.007	0.719 ± 0.002
SFR	0.988 ± 0.0838	1.80 ± 0.172	2.57 ± 0.394	0.734 ± 0.025	0.747 ± 0.007
S-SFR ($\times 10^{-11}$)	12.9 ± 1.17	15.0 ± 1.65	14.3 ± 1.80	3.744 ± 0.108	2.629 ± 0.034
		$-19.5 > M_r > -22.5$			
g-r	0.593 ± 0.0234	0.656 ± 0.0145	0.666 ± 0.0169	0.686 ± 0.009	0.765 ± 0.002
SFR	1.99 ± 0.318	4.30 ± 0.5309	6.54 ± 1.01	1.136 ± 0.063	0.920 ± 0.016
S-SFR ($\times 10^{-11}$)	8.31 ± 1.02	8.30 ± 0.753	12.1 ± 4.09	3.133 ± 0.169	2.137 ± 0.004
		$-17.77 > M_r > -19.5$			
g-r	0.585 ± 0.0169	0.579 ± 0.0113	0.550 ± 0.0171	0.567 ± 0.009	0.645 ± 0.003
SFR	0.770 ± 0.0606	0.838 ± 0.0544	0.618 ± 0.0548	0.508 ± 0.0237	0.530 ± 0.009
S-SFR ($\times 10^{-11}$)	13.9 ± 1.39	17.6 ± 2.25	15.3 ± 1.79	4.146 ± 0.137	3.349 ± 0.005

In addition, none of the samples exhibit bimodality of galaxy colors with a red sequence and blue cloud (Figure 6.4) such as is observed in both void and field galaxies (von Benda-Beckmann & Müller 2008). We compare the LVS with the geometrically selected Void Galaxy Survey (VGS, Chapter 5 of this thesis), and the NV with a magnitude-limited sample of SDSS galaxies selected at redshifts $0.1 < z < 0.3$. Both comparisons show general agreement between simulation colors and observations down to the observational limit $M_r \sim -16$. The choice of a lower scaling factor, F, in Equation 6.2 corresponds to more extinction and redder galaxies, however it affects void and non-void colors similarly, does

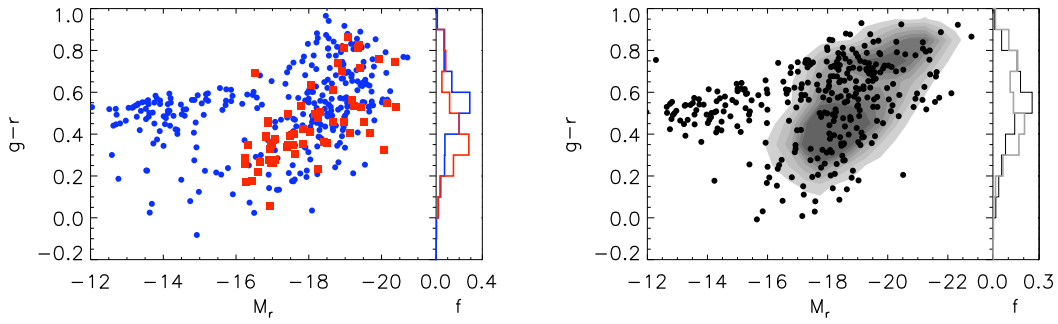

Figure 6.4: Color magnitude diagram. On the left, the LVS (blue circles) is in reasonable agreement with the observed VGS sample (red squares). On the right, the NV (black circles) roughly traces the SDSS distribution for galaxies at redshifts $0.1 < z < 0.3$. We see no bimodality in the colors of either simulated galaxy sample such as is observed in void and field galaxies (von Benda-Beckmann & Müller 2008).

not affect the bimodality, and produces an excess of low-luminosity red galaxies compared to the VGS. The lack of bimodality in color in the NV sample (Figure 6.5) suggests that the homogeneous distribution of galaxy colors is independent of density.

While the absolute value calculated for our galaxy colors may not be entirely reliable, we may still consider relative differences between the void and non-void samples. von Benda-Beckmann & Müller (2008) detect a slight blueward shift of the blue cloud galaxies that are deeper inside the void at fixed luminosity. Considering the mean color at fixed luminosity (Figure 6.5, left) we see no such shift at the high-end luminosities they were considering ($-19.2 > M_B > -20$). They have fit their color distribution with two Gaussians, which we cannot replicate as we see no bimodality, however dividing the sample at $u-r = 2.2$ (Strateva et al. 2001), we still find no trend with density (Figure 6.5, right). This result is consistent with Patiri et al. (2006b), who find that when selecting galaxies from the entire void region the void galaxy colors are indistinguishable from galaxies in typical environments. We do see indications of a blue shift at fainter magnitudes, $M_r > -18$. This is presumably due to the higher rates of star formation in galaxies at these densities, described below.

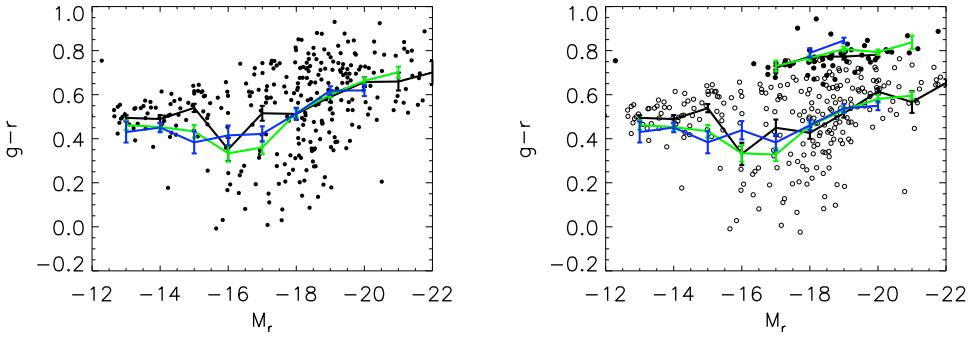

Figure 6.5: Color magnitude diagram for the NV. On the right, the sample has been split into red (filled circles) and blue (open circles) galaxies following the $u - r = 2.2$ cut identified by Strateva et al. (2001). In each, the mean for the NV galaxies is overplotted in black. Also shown is the mean for galaxies in the void outskirts (0.5 < delta < 1.0, in green) and the mean for galaxies in the deepest underdensities (delta < 0.5, blue). Among the dwarf galaxies, the void galaxies are somewhat bluer than the galaxies in average density environments.

6.4.3 H I Properties

The H I distribution typically forms a disk, however the ∼5 kpc resolution used for the extraction of the hydro variables is insufficient to attempt any analysis of the internal gas disk kinematics. The H I surface density profiles we find rise too steeply at the outskirts of the disks, often achieving fairly high column densities of $\sim 10^{21}$ cm^{-2} far outside the stellar disk (Figure 6.2, right) (cf Swaters et al. 2002). This inaccurate density profile persists even if we are careful to include in the integrated H I map only that H I that is above a detectable level (1×10^{19} cm^{-2}) for modern instruments. We believe our measured H I masses to be an upper limit based on two limitations with this simulation. First, the conversion of H I to H_2 through formation of H_2 on dust grains was not properly modeled even at this resolution. This should result in an overestimate of the H I mass in the highest density, central regions of the gas disk. Second, interstellar UV ionizing radiation by individual galaxies was neglected, which would have reduced H I in the outskirts of the disk, because it is likely that local ionizing radiation is larger than the meta-galactic background.

The resulting overestimate of the H I mass is apparent in comparing the H I mass to light ratio to observations (Figure 6.6, left). It shows the same decreasing trend with

increasing luminosity, however the overall value is about a factor of three too high compared with typical galaxies (Verheijen & Sancisi 2001; Swaters et al. 2002) or with void galaxies (Chapter 5 of this thesis). We note that there is a slight trend with density among our three density-selected samples (Figure 6.6, right), however when we examine the specifics of the trend, particularly for low luminosity and dwarf galaxies (Figure 6.7), it is not very pronounced and certainly much weaker than the trend observed for dwarf galaxies by Huchtmeier et al. (1997). We see no trend as a function of distance from the void center for our VC galaxies.

6.4.4 Star Formation and Stellar Properties

Although there is a no strong change in the star formation rate (SFR) at lower densities (Table 6.2), it is clear from Figure 6.8 that there is a strong dependence of SFR on luminosity. Thus we also consider the SFR scaled to the stellar mass (specific SFR, S-SFR), which is significantly increased for observed void galaxies, but unchanged within the error in the mean for our simulation (Table 6.2). We do, however, see significantly higher SFR and S-SFR for those lowest luminosity dwarf galaxies with $M_r > -16$ in underdense regions when compared to our NV galaxies (Figure 6.8 and Figure 6.9, left). The simulation does not reproduce the observed trend for increased SFR per H I mass at lower densities

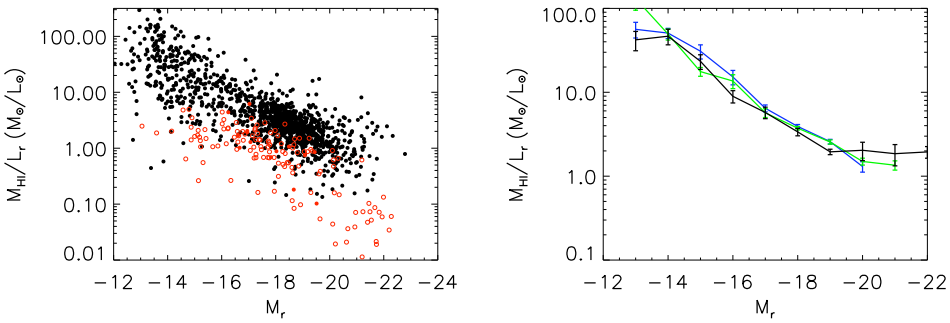

Figure 6.6: H I mass to r-band light ratio. On the left, all simulated galaxies (black) are roughly an order of magnitude too high compared to the observed relation (in red) from Verheijen & Sancisi (2001) and Swaters et al. (2002) (open circles) and Chapter 4 of this thesis (filled circles). On the right, the mean value for the LVS (blue), NV (black) and VS (green) shows a very slight trend with density within the simulated dwarf galaxies. .

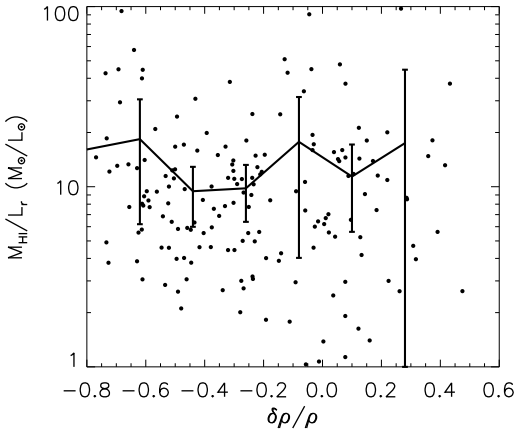

Figure 6.7: $M_{H\ I}/L_r$ vs density for all galaxies with $-15 > M_r > -17$, with the mean overplotted, reveals no clear trend with density.

(Chapter 4 of this thesis), and there is good agreement between densities for all but the faintest dwarf galaxies (Figure 6.9), however our H I masses are only upper limits and our sample is not complete for low mass galaxies.

We find no trend in the mass-metallicity relation with density (Figure 6.10), or with distance from the void center. This is likely because metal enrichment is mostly due to self-enrichment, and thus depends more on halo mass than large scale environment. We reproduce the observed increase in metallicity for more massive galaxies (Lequeux et al. 1979; Garnett & Shields 1987; Zaritsky et al. 1994). We also reproduce the general shape in the mass-metallicity relation as calculated using the gas-phase oxygen abundance measurement of SDSS galaxies (Tremonti et al. 2004), however their survey measures only the 3″ of the observed galaxies, ∼25% of the total light, in the central region where galaxy metallicity is typically higher (Searle 1971; Vilchez et al. 1988). This aperture bias may result in an overestimate of the total metal abundance by as much as a factor of 2, though it should not affect the general trend (Tremonti et al. 2004). In comparing with their measured oxygen abundance, 12 + log(O/H), we have normalized the Tremonti et al. (2004) relation to solar metallicity, $Z_\odot$, at 8.69 (Allende Prieto et al. 2001). Our measured values reasonably well reproduce the Milky Way, with $Z_\odot$ at $M_* = 5 \times 10^{10}$ $M_\odot$, and the LMC, with $Z_\odot/2$ at $M_* = 5 \times 10^9$ $M_\odot$.

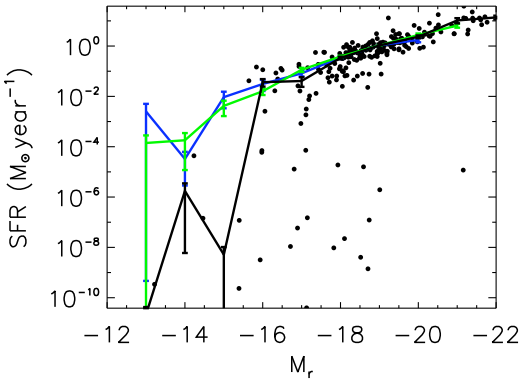

Figure 6.8: SFR for NV galaxies (in black), with the mean overplotted for the LVS (blue), NV (black) and VS (green). Only at the faintest luminosities is there any difference in the three samples.

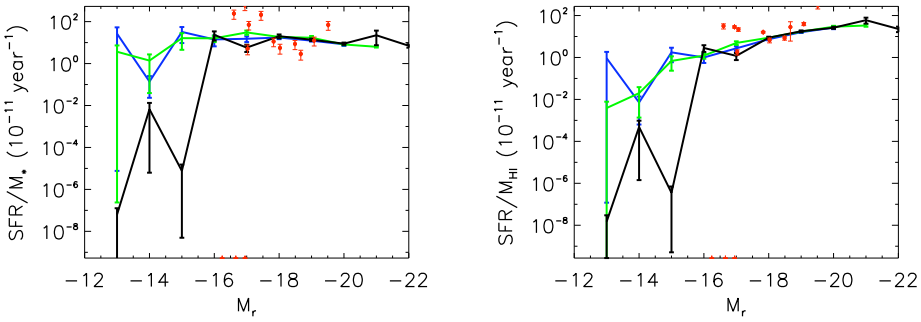

Figure 6.9: S-SFR (left) and SFR/H I mass (right). The LVS (blue) and VS (green) are somewhat higher than the NV (black) for the faintest galaxies, but consistent with each other and with the void galaxies described in Chapter 5 of this thesis (red circles). The rather large discrepancy between observed and simulated values in the SFR per H I mass are consistent with the large discrepancy in the H I masses (see Figure 6.6).

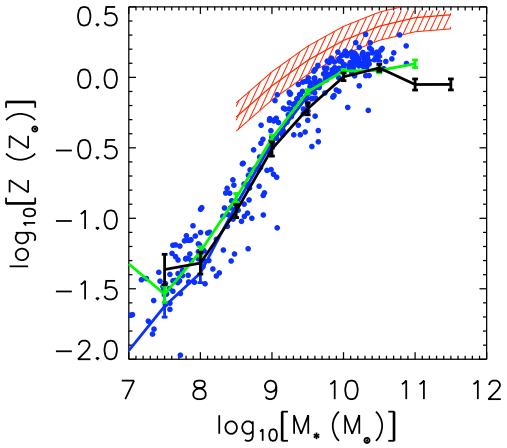

Figure 6.10: Mass weighted metallicity as a function of stellar mass for the LVS (blue) with the mean overplotted for LVS, NV (black) and VS (green). We reproduce the same trend as Tremonti et al. (2004) (red) for increasing metallicity with increasing stellar mass, but find no trend with density. The observed relation, normalized to $Z_{\odot}$ at 12 + log(O/H) = 8.69 (Allende Prieto et al. 2001) with 1σ error bars indicated by the shaded region, is somewhat higher as the measurements were done in the galaxy centers were metallicity is typically enhanced.

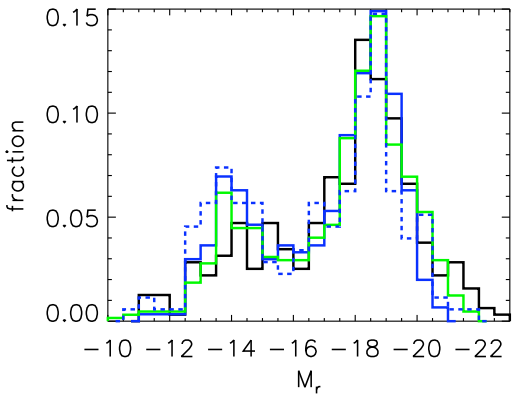

Figure 6.11: Fraction of galaxies with a given luminosity for the VC (blue dashed line), LVS (blue), NV (black) and VS (green). The excess of low luminosity galaxies is most apparent in the VC sample and relatively less dominant as a function of density , suggesting that this population is a result of the large scale underdensity.

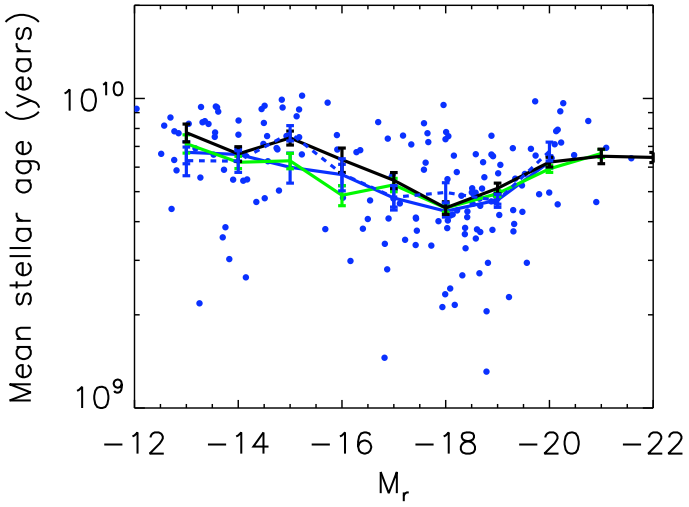

Figure 6.12: Mean stellar ages as a function of luminosity for the LVS (blue) with the mean overplotted for LVS (blue solid), VC (blue dashed), NV (black), and VS (green). The low luminosity void galaxies are somewhat younger than the non-void galaxies.

6.4.5 Excess of Low Luminosity Galaxies

One surprising discovery is the population of low luminosity galaxies apparent below the observational survey limit in the color-magnitude diagram (Figure 6.4). While these galaxies do inhabit the lowest mass dark matter halos, we believe that this excess is not a resolution effect as it persists into halos ∼3 times more massive than we can reliably resolve and has a strong trend with density. Figure 6.11 shows we have a slight excess of Mr ~ -14 galaxies for our NV, a noticeable excess for the VS, and a substantial excess for the LVS. In the VC this excess is particularly notable. This excess may be due in part to the youth of galaxies in the underdense regions (Figure 6.12), although at $M_r = -14$ the mean ages are about the same. We note that while these galaxies are sufficiently resolved at $z = 0$, the galaxies that formed them earlier in their merger history presumably were not, so their integrated properties are correspondingly less reliable than in more massive galaxies. For example, these galaxies are generally gas rich, with masses $\sim 10^9$ $M_\odot$, which may be due to decreased gas consumption at earlier times resulting from simulation resolution limits.

While complete volume limited samples of dwarf galaxies are not yet possible, comparison with observations show that our simulated dwarf galaxies are distinctly too red

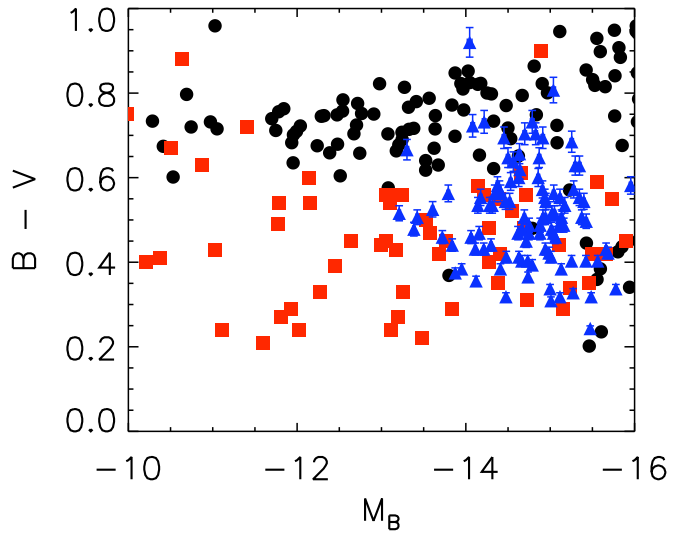

Figure 6.13: Comparison of simulated NV low-luminosity galaxy colors with observational samples of dwarf galaxies from the Local Volume (red squares, Makarova 1999; Makarova et al. 2002, 2009) and from the SDSS (blue triangles, Geha et al. 2006). Error bars reflect uncertanties in the color conversion from SDSS *ugzri* bands to Johnson-Cousins UBVRI bands. Simulated dwarf galaxies are distinctly redder than observed dwarf galaxies.

(Figure 6.13). Here we compare with dwarf galaxies within the Local Volume that have integrated B and V band observations (Makarova 1999; Makarova et al. 2002, 2009), and with dwarf galaxies identified within the SDSS redshift survey (Geha et al. 2006). We convert *ugzri* colors for the SDSS and simulated galaxy samples to Johnson-Cousins $UBVRI$ colors following the prescription of Jester et al. (2005). In Figure 6.4 (right), when comparing our NV galaxy colors with typical SDSS galaxies, the simulated low luminosity galaxy population appears almost as an extension of the red sequence while the observed dwarf galaxies (Figure 6.13) appear more continuous with the blue cloud. While the observational samples are not complete in any way, there is no bias for color in their selection and both samples should be sensitive to a redder dwarf galaxy population such as we simulate. This suggests that our simulated colors for the lowest mass galaxies, which contain very few star particles, are not realistic, presumably due to resolution effects earlier in their merger histories.

Despite the discrepancy in colors, the increased number of simulated dwarf galaxies in the lowest density regions may present a way to reduce the discrepancy between the number

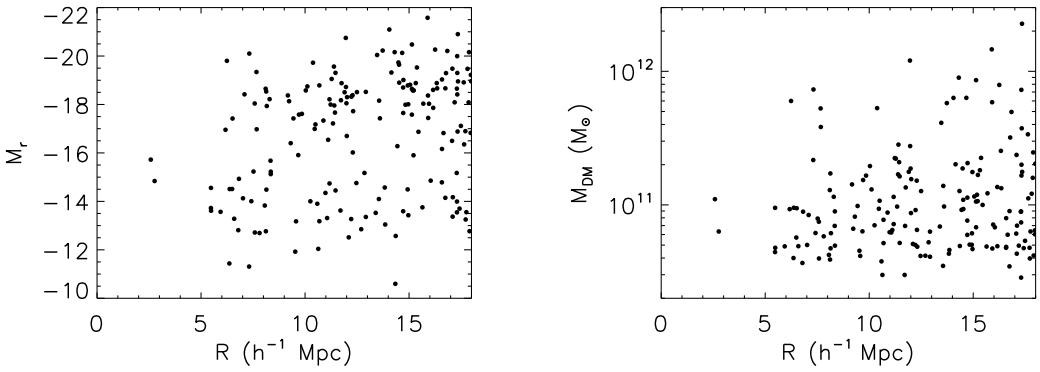

Figure 6.14: M_r (left) and M_{DM} as a function of distance from the void center. We see no trailing of low luminosity galaxies into the void, however the dark matter halos do seem to segregate by mass.

of dark matter halos predicted within voids and the number of galaxies observed (Peebles 2001). Tinker & Conroy (2009) suggested a sufficiently tailored halo occupation distribution could solve this problem, and predict that the maximum halo mass (and thus luminosity) will increase as a function of distance from the void center. We see no such relation for VC galaxy luminosities, though we do see a slight trend with dark matter halo mass but not nearly as steep a cutoff (Figure 6.14).

Comparing the number density of void galaxies in our simulation, which is likely a lower limit due to imperfect resolution, with the most sensitive observational surveys we still over-predict the number of void galaxies. If we consider observations of the Local Volume, where the galaxy sample within 8 Mpc of us is thought to be fairly complete to M_B = -12 (Tikhonov & Klypin 2009), and consider its overlap with the Local Void, which has a center 23 Mpc away from us and extends roughly 20 Mpc in radius (Tully et al. 2008), we find one void galaxy per 394 Mpc^3. In our simulation the luminosity limit is lower, but from our VC sample we expect a similar volume should yield about 6 galaxies. This is somewhat smaller than the factor of ten discrepancy found by Tikhonov & Klypin (2009), but still quite pronounced. It is still possible that these dwarf galaxies in the voids are low surface brightness and thus have been largely missed by existing surveys. Future simulations with increased stellar resolution may be able to constrain the surface brightness of these systems.

The one galaxy located in both the Local Volume and the Local Void, KK 246, has

M_B = -13.7, a color[1] of $B - R = 1$, and a significant H I mass (Chapter 3 of this thesis). Again it is too blue, but otherwise it is in good agreement with the expected properties of our low luminosity void galaxy population. All sky H I surveys are on the verge of reaching the sensitivity needed to detect these galaxies. HIPASS can detect galaxies with 10^8 $M_\odot$ to distances of ∼10 Mpc, just within the edge of the Local Void. ALFALFA reported no detections within the Pisces- Perseus foreground void with a detection limit of 10^8 $M_\odot$ (Saintonge et al. 2008), however considering the discrepancy between the H I masses of our simulated galaxies compared to observations, detailed examination of closer voids within 20 Mpc where we are sensitive to $\sim 10^7$ $M_\odot$ may be necessary.

6.5 Conclusion

We have run cosmological simulations using the adaptive mesh refinement Eulerian hydro code, Enzo, with a moderate resolution refined region $31 \times 31 \times 35h^{-3}$Mpc centered on a large $\sim 30\ h^{-1}$ Mpc diameter void. We have constructed mock observations of the integrated properties (color, star formation rate, gas content, etc.) in a sample of roughly 900 void galaxies, 300 in especially low density regions and 200 located well within the void center, and 300 additional galaxies in the surrounding average density filaments. The same realization of this simulation output at a higher resolution, as well as an additional simulation focused on a galaxy cluster, have found that the damped Lyman-alpha statistics are consistent with observations (Cen 2010).

These and other simulations run within the same framework with similar physical prescriptions have been broadly consistent with observations (e.g. Nagamine et al. 2006; Kim et al. 2009). Given the general difficulty in hydrodynamic simulations of reproducing observations (Mayer et al. 2008), we are able to accurately reproduce the range of galaxy luminosities and colors observed, but are unable to reproduce the observed bimodality in galaxy colors. At low luminosities ($M_r > -16$), where we are more affected by resolution effect from earlier in the galaxy merger history and beyond the scope of most observational studies, we see that void galaxies are bluer with higher SFR and S-SFR, but we see no trend for the brightest galaxies ($M_r < -18$).

The gas content of all our simulated galaxies is anomalously high, roughly 3 times

[1]The mean color for our simulated low luminosity galaxies with $M_B > -16$ is $B - R \sim 1.3$.

what is expected for their luminosity when compared with observations, and their radial extent too large, both of which we interpret as a result of limitations in the implementation of chemistry and radiative transfer in the simulations. Taking that into account, we do reproduce the trend for fainter galaxies to have relatively more H I for their luminosity, but find no trend with density or distance from the void center. We reproduce the general mass-metallicity trend observed in SDSS galaxies, and we see no trend with density.

We do not see the strong segregation of the most luminous galaxies to the void edges predicted by Tinker & Conroy (2009), however we do see that the most massive dark matter halos avoid the void center. We observe a significant population of low luminosity ($M_r \sim -14$) dwarf galaxies that is preferentially located in low density regions and specifically in the void center. This population is too faint to be detected in most large scale redshift surveys, however studies of the Local Void may soon become sensitive to this population, where we do observe a relatively lower median luminosity (Nasonova & Karachentsev 2011).

While omission of some physical effects, such as local sources of UV radiation from galaxies and AGN feedback, may ultimately affect the details of our resulting simulated observations, we emphasize the remarkable general agreement we find with observations without any tuning of the input parameters. As a matter of fact, the only adjustable parameter, aside from the unavoidable finite numerical resolution, is the feedback strength from supernovae that is essentially fixed by the theory of stellar interior and independent observations of supernovae. The supernova feedback parameter is essentially left unadjustable given the broad agreement between our simulations and observations of damped Lyman-alpha systems (Cen 2010) that depends sensitively on this parameter. Future work should examine whether or not some of the discrepancies with observations may be explained by inclusion of additional baryonic physics. Of the possible astrophysical processes, given the observational lack of connection between gas rich spiral galaxies and AGN activities, it would seem likely that AGN feedback is probably unimportant with respect to neutral gas in the vicinities of spiral galaxies. A detailed treatment of radiative transfer that includes both UV background and local UV sources will be examined in our future work. At this time, on the scales that we have examined, we are not compelled to suggest that any alteration of the current standard cold dark matter paradigm is required.

Part IV

Conclusions

Chapter 7

Concluding Remarks

Void galaxies represent a very interesting population of galaxies well suited for detailed study of gas accretion and galaxy growth within the large-scale cosmological context. In the proceeding chapters we have investigated the nature of void galaxies in the context of their H I gas morphology both in detail for individually interesting galaxies, as well as in a more statistical sense while considering void galaxies as a population. We also discussed both observed and simulated void galaxies, and compared the integrated stellar and gas properties of cutting-edge cosmological simulations with surprisingly encouraging results. Below we present an overview of our results and discuss continuing questions that remain to be addressed.

7.1 Summary of Results

In many respects void galaxies do not appear distinct from galaxies in average density environments. We find that the void galaxy population is systematically composed of low luminosity, late type, gas rich, star forming galaxies, but that their properties are not unusual at fixed luminosity and morphology. This is consistent with our simulation results, which show very little difference in galaxy properties for void and non-void galaxies. We also observe that the small scale clustering in voids is similar to that in average density environments, suggesting that evolution driven by interactions should proceed very similarly in voids.

However, observationally we do find some evidence that the gas content is different in void galaxies. We find very few void galaxies with elevated H I mass to light ratios. Given

that the star formation rate is not correspondingly decreased, it suggests that these galaxies are relatively more efficient at forming stars and may modulate star formation differently. Our study of void galaxies as a population also shows that void galaxies are dynamically very interesting, with many that are morphologically and kinematically disturbed in H I. As it is generally difficult observationally to distinguish if galaxy evolution is predominantly driven by mergers or by diffuse accretion, the well constrained environment and shorter merger history particular to void galaxies may make it possible to distinguish the effects of interaction from cosmological inflow. The polar disk galaxy discussed in Chapter 2 represents one of the most convincing cases for cosmological cold mode accretion. KK 246 also presents an unusual morphology and signs of anomalous gas kinematics that hint at ongoing gas accretion.

We find no observational evidence for a missing population of galaxies in the voids, consistent with previous work. Yet our cosmological hydrodynamic simulation, which improves upon previous dark matter only predictions by fully simulating the baryonic components of galaxies, shows that the discrepancy between theory and observations persists. Surprisingly, we predict a predominance of ultra-faint dwarf galaxies to be located specifically within the void center. This population is somewhat beyond current detection capabilities on large scales, but is largely ruled out by Local Volume observations.

We also observe two systems in our sample consisting of three galaxies linearly aligned within the void. These are tantalizingly suggestive of substructures forming within the voids, as is predicted from dark matter simulations. The H I bridge between galaxies in both these systems could be indicative of the collapse of pristine gas along these filaments. This claim is supported by a lack of stars in these extended, low column density gas features, although it is complicated by the quite disturbed stellar morphologies of the larger galaxies in these systems.

7.2 Future Work

Many of the systems selected for our survey of void galaxies reveal interesting features that merit followup studies with higher resolution H I imaging. Examining the relatively low resolution H I imaging of the galaxy disks, VGS_35 appears significantly misaligned and VGS_47 appears extremely lopsided, both signs of unusual gas accretion at play. The optical

morphology of VGS_07 is quite unusual, with a chain-like structure of bright knots of star formation along the disk, however the H I resolution is insufficient to trace the kinematic details of the gas around theses features to judge if they are being triggered by gas infall. We have acquired higher resolution H I data for the polar disk galaxy, and though our analysis is not yet complete, imaging reveals that the extended gas disk is morphologically extremely irregular and lumpy though kinematically relatively smooth.

A more detailed study of the stellar disks of our void galaxies could also help determine the accretion history of these systems. The optical observations used for this thesis come from the SDSS, which has fairly limited exposure times of about one minute. Deeper optical imaging might reveal faint tidal features that indicate a rich merger history. We have begun a program to acquire B and R band imaging for the full sample of 60 galaxies with integration times of one hour, allowing us to identify structures up to two magnitudes fainter than were previously visible (Beygu et al. in prep.). Measurements of the stellar kinematics would also allow us to identify any discrepancies between the motions of the stellar and gaseous disks.

The suggestive increase in star formation efficiency for these void galaxies makes them ideal for detailed examination of the star formation within the galaxy disks. We have completed imaging of the VGS in H α and the near-UV to measure more precisely the integrated star formation rates of these galaxies, and to compare the morphological distribution of star formation within the galaxy disks. This multi-wavelength approach also samples slightly different young stellar populations, and will allow us to constrain the star formation history. Should this study present interesting results for the void galaxy population as a whole, it could be instructive to pursue highly resolved studies of star formation in nearby void galaxies, such as KK 246. We are also interested in completing our examination of the gas content of void galaxies by observing the CO gas, thus directly constraining the total baryonic mass of these galaxies and forming a complete picture of the molecular star-forming component of the gas disks.

The interacting and aligned filamentary systems are very intriguing. Metallicity measurements of regions in the outskirts of these systems may provide the key to understanding the source of this gas. We can also examine the two filamentary systems, VGS_31 and VGS_38, in the context of the surrounding large scale structure to test whether their orientation agrees with predictions that low density filaments are aligned with the surrounding

large matter overdensities. In addition, the bridges between aligned structures and the regions extending linearly beyond them present interesting regions of the sky to pursue absorption line searches for void substructure, provided there are suitable background sources.

Our simulations predict a population of ultra-low luminosity dwarfs that reside specifically in the void centers. If these galaxies are gas rich, with H I masses typical for dwarf galaxies of $\sim 10^7$ $M_\odot$, they may be detectable with full sky H I surveys that are planned for the near future, like WALLABY and WNSHS, or in the large surveys undertaken by the SKA. Until then, the faint H I detected companions identified near our targeted void galaxies present a new population of dwarf galaxies within the voids that exist at the limit of the thresholds for galaxy formation, and represent a small sample of those faint galaxies that may comprise the true bulk of the void galaxy population.

Part V

Bibliography

Bibliography

Abazajian, K. N., et al. 2009, ApJS, 182, 543

Abbas, U., & Sheth, R. K. 2007, MNRAS, 378, 641

Abbott, D. C. 1982, ApJ, 263, 723

Abel, T., Anninos, P., Zhang, Y., & Norman, M. L. 1997, New A, 2, 181

Adelman-McCarthy, J., et al. 2008, ApJS, 175, 297

Allende Prieto, C., Lambert, D. L., & Asplund, M. 2001, ApJL, 556, L63

Aragón-Calvo, M. 2007, Morphology and Dynamics of the Cosmic Web (Ph.D. Thesis, University of Groningen)

Aragón-Calvo, M. A., Platen, E., van de Weygaert, R., & Szalay, A. S. 2010, ApJ, 723, 364

Aragon-Calvo, M. A., van de Weygaert, R., Araya-Melo, P. A., Platen, E., & Szalay, A. S. 2010, MNRAS, 404, L89

Aragón-Calvo, M. A., van de Weygaert, R., Jones, B. J. T., & van der Hulst, J. M. 2007, ApJL, 655, L5

Arnaboldi, M., Oosterloo, T., Combes, F., Freeman, K. C., & Koribalski, B. 1997, AJ, 113, 585

Arnaboldi, M., & Sparke, L. S. 1994, AJ, 107, 958

Baars, J. W. M., Genzel, R., Pauliny-Toth, I. I. K., & Witzel, A. 1977, A&A, 61, 99

Baldwin, J. A., Phillips, M. M., & Terlevich, R. 1981, PASP, 93, 5

Balogh, M. L., Baldry, I. K., Nichol, R., Miller, C., Bower, R., & Glazebrook, K. 2004, ApJL, 615, L101

Begum, A., Chengalur, J. N., & Karachentsev, I. D. 2005, A&A, 433, L1

Begum, A., Chengalur, J. N., Karachentsev, I. D., Sharina, M. E., & Kaisin, S. S. 2008, MNRAS, 386, 1667

Bernardeau, F., & van de Weygaert, R. 1996, MNRAS, 279, 693

Binney, J. 1977, ApJ, 215, 483

Binney, J., & Merrifield, M. 1998, Galactic astronomy (Princeton: Princeton University Press)

Biswas, R., Alizadeh, E., & Wandelt, B. D. 2010, Phys. Rev. D, 82, 023002

Blanton, M. R., Eisenstein, D., Hogg, D. W., Schlegel, D. J., & Brinkmann, J. 2005, ApJ, 629, 143

Bond, J. R., Kofman, L., & Pogosyan, D. 1996, Nature, 380, 603

Boomsma, R., Oosterloo, T. A., Fraternali, F., van der Hulst, J. M., & Sancisi, R. 2008, A&A, 490, 555

Bosma, A. 1981, AJ, 86, 1825

Bournaud, F., & Combes, F. 2003, A&A, 401, 817

Bournaud, F., Jog, C. J., & Combes, F. 2005, A&A, 437, 69

Bower, R. G., Benson, A. J., Malbon, R., Helly, J. C., Frenk, C. S., Baugh, C. M., Cole, S., & Lacey, C. G. 2006, MNRAS, 370, 645

Briggs, D. S. 1995, in Bulletin of the American Astronomical Society, Vol. 27, Bulletin of the American Astronomical Society, 1444–+

Brinchmann, J., Charlot, S., White, S. D. M., Tremonti, C., Kauffmann, G., Heckman, T., & Brinkmann, J. 2004, MNRAS, 351, 1151

Brocca, C., Bettoni, D., & Galletta, G. 1997, A&A, 326, 907

Brook, C. B., Governato, F., Quinn, T., Wadsley, J., Brooks, A. M., Willman, B., Stilp, A., & Jonsson, P. 2008, ApJ, 689, 678

Brunino, R., Trujillo, I., Pearce, F. R., & Thomas, P. A. 2007, MNRAS, 375, 184

Bruzual, G., & Charlot, S. 2003, MNRAS, 344, 1000

Bryan, G. L. 1999, Comput. Sci. Eng., Vol. 1, No. 2, p. 46 - 53, 1, 46

Bureau, M., Freeman, K. C., Pfitzner, D. W., & Meurer, G. R. 1999, AJ, 118, 2158

Calzetti, D., Armus, L., Bohlin, R. C., Kinney, A. L., Koornneef, J., & Storchi-Bergmann, T. 2000, ApJ, 533, 682

Carignan, C., & Purton, C. 1998, ApJ, 506, 125

Cautun, M. C., & van de Weygaert, R. 2011, ArXiv e-prints, arXiv:1105.0370

Ceccarelli, L., Padilla, N. D., Valotto, C., & Lambas, D. G. 2006, MNRAS, 373, 1440

Cen, R. 2010, ArXiv e-prints, arXiv:1010.5014

Cen, R., Kang, H., Ostriker, J. P., & Ryu, D. 1995, ApJ, 451, 436

Cen, R., Miralda-Escudé, J., Ostriker, J. P., & Rauch, M. 1994, ApJL, 437, L9

Cen, R., Nagamine, K., & Ostriker, J. P. 2005, ApJ, 635, 86

Cen, R., & Ostriker, J. P. 1992, ApJL, 399, L113

Colberg, J. M., Sheth, R. K., Diaferio, A., Gao, L., & Yoshida, N. 2005, MNRAS, 360, 216

Colberg, J. M., et al. 2008, MNRAS, 387, 933

Colless, M., et al. 2001, MNRAS, 328, 1039

Combes, F., & Arnaboldi, M. 1996, A&A, 305, 763

Corbin, M. R., Vacca, W. D., Hibbard, J. E., Somerville, R. S., & Windhorst, R. A. 2005, ApJL, 629, L89

Croton, D. J., & Farrar, G. R. 2008, MNRAS, 386, 2285

Dalgarno, A., & McCray, R. A. 1972, ARA&A, 10, 375

de Lapparent, V., Geller, M. J., & Huchra, J. P. 1986, ApJL, 302, L1

De Lucia, G., Springel, V., White, S. D. M., Croton, D., & Kauffmann, G. 2006, MNRAS, 366, 499

de Vaucouleurs, G. 1953, AJ, 58, 30

—. 1958, AJ, 63, 253

Dekel, A., & Birnboim, Y. 2006, MNRAS, 368, 2

Dekel, A., Birnboim, Y., Engel, G., Freundlich, J., Goerdt, T., Mumcuoglu, M., Neistein, E., Pichon, C., Teyssier, R., & Zinger, E. 2009, Nature, 457, 451

Delaunay, B. N. 1934, Bull. Acad. Sci. USSR (VII) Classe Sci. Mat., 793

Dobos, L., Budavari, T., Csabai, I., & Szalay, A. 2006, The Virtual Observatory in Action: New Science, New Technology, and Next Generation Facilities, 26th meeting of the IAU, Special Session 3, 17-18, Aug. 2006 in Prague, Czech Republic, SPS3, #76, 3

Doyle, M. T., et al. 2005, MNRAS, 361, 34

Dressler, A. 1980, ApJ, 236, 351

Dubinski, J., da Costa, L. N., Goldwirth, D. S., Lecar, M., & Piran, T. 1993, ApJ, 410, 458

Efstathiou, G., & Moody, S. J. 2001, MNRAS, 325, 1603

Einasto, J., Joeveer, M., & Saar, E. 1980, MNRAS, 193, 353

Einasto, J., Suhhonenko, I., Hütsi, G., Saar, E., Einasto, M., Liivamägi, L. J., Müller, V., Starobinsky, A. A., Tago, E., & Tempel, E. 2011, ArXiv e-prints, arXiv:1105.2464

Eisenstein, D. J., & Hut, P. 1998, ApJ, 498, 137

Espada, D., Verdes-Montenegro, L., Huchtmeier, W. K., Sulentic, J., Verley, S., Leon, S., & Sabater, J. 2011, A&A, 532, A117+

Fairall, A. P., ed. 1998, Large-scale structures in the universe

Fraternali, F., & Binney, J. J. 2008, MNRAS, 386, 935

Fraternali, F., van Moorsel, G., Sancisi, R., & Oosterloo, T. 2002, AJ, 123, 3124

Furlanetto, S. R., & Piran, T. 2006, MNRAS, 366, 467

Gao, L., Springel, V., & White, S. D. M. 2005, MNRAS, 363, L66

Garnett, D. R., & Shields, G. A. 1987, ApJ, 317, 82

Geha, M., Blanton, M. R., Masjedi, M., & West, A. A. 2006, ApJ, 653, 240

Gentile, G., Salucci, P., Klein, U., & Granato, G. L. 2007, MNRAS, 375, 199

Giovanelli, R., et al. 2007, AJ, 133, 2569

Goldberg, D. M., & Vogeley, M. S. 2004, ApJ, 605, 1

Goto, T., Yamauchi, C., Fujita, Y., Okamura, S., Sekiguchi, M., Smail, I., Bernardi, M., & Gomez, P. L. 2003, MNRAS, 346, 601

Gottlöber, S., Łokas, E. L., Klypin, A., & Hoffman, Y. 2003, MNRAS, 344, 715

Governato, F., Brook, C., Mayer, L., Brooks, A., Rhee, G., Wadsley, J., Jonsson, P., Willman, B., Stinson, G., Quinn, T., & Madau, P. 2010, Nature, 463, 203

Granett, B. R., Neyrinck, M. C., & Szapudi, I. 2008, ApJL, 683, L99

Gregory, S. A., & Thompson, L. A. 1978, ApJ, 222, 784

Grogin, N. A., & Geller, M. J. 1999, AJ, 118, 2561

—. 2000, AJ, 119, 32

Gwyn, S. D. J., & Hartwick, F. D. A. 2005, AJ, 130, 1337

Haardt, F., & Madau, P. 1996, ApJ, 461, 20

Hahn, O., Carollo, C. M., Porciani, C., & Dekel, A. 2007, MNRAS, 381, 41

Haynes, M. P., & Giovanelli, R. 1984, AJ, 89, 758

Hinshaw, G., Weiland, J. L., Hill, R. S., Odegard, N., Larson, D., Bennett, C. L., Dunkley, J., Gold, B., Greason, M. R., Jarosik, N., Komatsu, E., Nolta, M. R., Page, L., Spergel, D. N., Wollack, E., Halpern, M., Kogut, A., Limon, M., Meyer, S. S., Tucker, G. S., & Wright, E. L. 2009, ApJS, 180, 225

Hoeft, M., & Gottlöber, S. 2010, Advances in Astronomy, 2010

Hoeft, M., Yepes, G., Gottlöber, S., & Springel, V. 2006, MNRAS, 371, 401

Hopkins, A. M., Miller, C. J., Nichol, R. C., Connolly, A. J., Bernardi, M., Gómez, P. L., Goto, T., Tremonti, C. A., Brinkmann, J., Ivezić, Ž., & Lamb, D. Q. 2003, ApJ, 599, 971

Hoyle, F., Rojas, R. R., Vogeley, M. S., & Brinkmann, J. 2005, ApJ, 620, 618

Hoyle, F., & Vogeley, M. S. 2002, ApJ, 566, 641

—. 2004, ApJ, 607, 751

Huchra, J., Davis, M., Latham, D., & Tonry, J. 1983, ApJS, 52, 89

Huchra, J., et al. 2005, in Astronomical Society of the Pacific Conference Series, Vol. 329, Nearby Large-Scale Structures and the Zone of Avoidance, ed. A. P. Fairall & P. A. Woudt, 135–+

Huchtmeier, W. K., Hopp, U., & Kuhn, B. 1997, A&A, 319, 67

Hui, L., Nicolis, A., & Stubbs, C. W. 2009, Phys. Rev. D, 80, 104002

Iodice, E., Arnaboldi, M., De Lucia, G., Gallagher, III, J. S., Sparke, L. S., & Freeman, K. C. 2002, AJ, 123, 195

Iodice, E., Arnaboldi, M., Saglia, R. P., Sparke, L. S., Gerhard, O., Gallagher, J. S., Combes, F., Bournaud, F., Capaccioli, M., & Freeman, K. C. 2006, ApJ, 643, 200

Jester, S., Schneider, D. P., Richards, G. T., Green, R. F., Schmidt, M., Hall, P. B., Strauss, M. A., Vanden Berk, D. E., Stoughton, C., Gunn, J. E., Brinkmann, J., Kent, S. M., Smith, J. A., Tucker, D. L., & Yanny, B. 2005, AJ, 130, 873

Jing, Y. P., Mo, H. J., & Boerner, G. 1998, ApJ, 494, 1

Jones, D. H., et al. 2009, MNRAS, 399, 683

Joung, M. K. R., & Mac Low, M. 2006, ApJ, 653, 1266

Kaiser, N. 1987, MNRAS, 227, 1

Karachentsev, I. D., Dolphin, A., Tully, R. B., Sharina, M., Makarova, L., Makarov, D., Karachentseva, V., Sakai, S., & Shaya, E. J. 2006, AJ, 131, 1361

Karachentsev, I. D., Karachentseva, V. E., Huchtmeier, W. K., & Makarov, D. I. 2004, AJ, 127, 2031

Kauffmann, G., Heckman, T. M., Tremonti, C., Brinchmann, J., Charlot, S., White, S. D. M., Ridgway, S. E., Brinkmann, J., Fukugita, M., Hall, P. B., Ivezić, Ž., Richards, G. T., & Schneider, D. P. 2003a, MNRAS, 346, 1055

Kauffmann, G., Heckman, T. M., White, S. D. M., Charlot, S., Tremonti, C., Peng, E. W., Seibert, M., Brinkmann, J., Nichol, R. C., SubbaRao, M., & York, D. 2003b, MNRAS, 341, 54

Kauffmann, G., et al. 2003c, MNRAS, 341, 33

Kent, B. R., Giovanelli, R., Haynes, M. P., Martin, A. M., Saintonge, A., Stierwalt, S., Balonek, T. J., Brosch, N., & Koopmann, R. A. 2008, AJ, 136, 713

Kereš, D., Katz, N., Fardal, M., Davé, R., & Weinberg, D. H. 2009, MNRAS, 395, 160

Kereš, D., Katz, N., Weinberg, D. H., & Davé, R. 2005, MNRAS, 363, 2

Kewley, L. J., Heisler, C. A., Dopita, M. A., & Lumsden, S. 2001, ApJS, 132, 37

Khoury, J., & Weltman, A. 2004, Phys. Rev. D, 69, 044026

Kim, J.-h., Wise, J. H., & Abel, T. 2009, ApJL, 694, L123

Kirby, E. M., Jerjen, H., Ryder, S. D., & Driver, S. P. 2008, AJ, 136, 1866

Kirshner, R. P. 2002, The extravagant universe : exploding stars, dark energy and the accelerating cosmos (Princeton, N.J. : Princeton University Press)

Kirshner, R. P., Oemler, Jr., A., Schechter, P. L., & Shectman, S. A. 1981, ApJL, 248, L57

Kleyna, J. T., Wilkinson, M. I., Gilmore, G., & Evans, N. W. 2003, ApJL, 588, L21

Klypin, A., Kravtsov, A. V., Valenzuela, O., & Prada, F. 1999, ApJ, 522, 82

Klypin, A. A., & Shandarin, S. F. 1983, MNRAS, 204, 891

Komatsu, E., Smith, K. M., Dunkley, J., Bennett, C. L., Gold, B., Hinshaw, G., Jarosik, N., Larson, D., Nolta, M. R., Page, L., Spergel, D. N., Halpern, M., Hill, R. S., Kogut, A., Limon, M., Meyer, S. S., Odegard, N., Tucker, G. S., Weiland, J. L., Wollack, E., & Wright, E. L. 2011, ApJS, 192, 18

Koornneef, J. 1982, A&A, 107, 247

Kormendy, J., Drory, N., Bender, R., & Cornell, M. E. 2010, ApJ, 723, 54

Kreckel, K., Platen, E., Aragón-Calvo, M. A., van Gorkom, J. H., van de Weygaert, R., van der Hulst, J. M., Kovač, K., Yip, C., & Peebles, P. J. E. 2011, AJ, 141, 4

Kuhn, B., Hopp, U., & Elsaesser, H. 1997, A&A, 318, 405

Lacey, C., & Cole, S. 1993, MNRAS, 262, 627

Larson, R. B. 1972, Nature, 236, 21

Lauberts, A. 1982, ESO/Uppsala survey of the ESO(B) atlas (Garching: European Southern Observatory (ESO))

Lauberts, A., & Valentijn, E. A. 1989, The surface photometry catalogue of the ESO-Uppsala galaxies (Garching: European Southern Observatory)

Lavaux, G., & Wandelt, B. D. 2010, MNRAS, 403, 1392

Lee, J., & Park, D. 2009, ApJL, 696, L10

Lee, J. C., Salzer, J. J., Law, D. A., & Rosenberg, J. L. 2000, ApJ, 536, 606

Lequeux, J., Peimbert, M., Rayo, J. F., Serrano, A., & Torres-Peimbert, S. 1979, A&A, 80, 155

Leroy, A., Bolatto, A. D., Simon, J. D., & Blitz, L. 2005, ApJ, 625, 763

Little, B., & Weinberg, D. H. 1994, MNRAS, 267, 605

Lucy, L. B. 1974, AJ, 79, 745

Macciò, A. V., Moore, B., & Stadel, J. 2006, ApJL, 636, L25

Madau, P., Pozzetti, L., & Dickinson, M. 1998, ApJ, 498, 106

Makarova, L. 1999, A&AS, 139, 491

Makarova, L., Karachentsev, I., Rizzi, L., Tully, R. B., & Korotkova, G. 2009, MNRAS, 397, 1672

Makarova, L. N., Karachentsev, I. D., Grebel, E. K., & Barsunova, O. Y. 2002, A&A, 384, 72

Manning, C. V. 2002, ApJ, 574, 599

Martin, A. M., Giovanelli, R., Haynes, M. P., Saintonge, A., Hoffman, G. L., Kent, B. R., & Stierwalt, S. 2009, ApJS, 183, 214

Mathis, H., & White, S. D. M. 2002, MNRAS, 337, 1193

Mayer, L., Governato, F., & Kaufmann, T. 2008, Advanced Science Letters, 1, 7

McGaugh, S. S., Schombert, J. M., Bothun, G. D., & de Blok, W. J. G. 2000, ApJL, 533, L99

McGaugh, S. S., Schombert, J. M., de Blok, W. J. G., & Zagursky, M. J. 2010, ApJL, 708, L14

McLin, K. M., Stocke, J. T., Weymann, R. J., Penton, S. V., & Shull, J. M. 2002, ApJL, 574, L115

Meurer, G. R., Carignan, C., Beaulieu, S. F., & Freeman, K. C. 1996, AJ, 111, 1551

Meyer, M. J., Zwaan, M. A., Webster, R. L., Brown, M. J. I., & Staveley-Smith, L. 2007, ApJ, 654, 702

Meyer, M. J., et al. 2004, MNRAS, 350, 1195

Miller, C. J., Nichol, R. C., Gómez, P. L., Hopkins, A. M., & Bernardi, M. 2003, ApJ, 597, 142

Moore, B., Ghigna, S., Governato, F., Lake, G., Quinn, T., Stadel, J., & Tozzi, P. 1999, ApJL, 524, L19

Nagamine, K., Ostriker, J. P., Fukugita, M., & Cen, R. 2006, ApJ, 653, 881

Nasonova, O. G., & Karachentsev, I. D. 2011, Astrophysics, 54, 1

Navarro, J. F., Frenk, C. S., & White, S. D. M. 1996, ApJ, 462, 563

Norman, M. L., & Bryan, G. L. 1999, in Astrophysics and Space Science Library, Vol. 240, Numerical Astrophysics, ed. S. M. Miyama, K. Tomisaka, & T. Hanawa, 19–+

O'Shea, B. W., Bryan, G., Bordner, J., Norman, M. L., Abel, T., Harkness, R., & Kritsuk, A. 2004, ArXiv Astrophysics e-prints, arXiv:0403044

Pan, D. C., Vogeley, M. S., Hoyle, F., Choi, Y.-Y., & Park, C. 2011, ArXiv e-prints, arXiv:1103.4156

Park, C., Choi, Y.-Y., Vogeley, M. S., Gott, J. R. I., & Blanton, M. R. 2007, ApJ, 658, 898

Park, D., & Lee, J. 2007, Physical Review Letters, 98, 081301

—. 2009a, MNRAS, 400, 1105

—. 2009b, MNRAS, 397, 2163

Patiri, S. G., Betancort-Rijo, J. E., Prada, F., Klypin, A., & Gottlöber, S. 2006a, MNRAS, 369, 335

Patiri, S. G., Prada, F., Holtzman, J., Klypin, A., & Betancort-Rijo, J. 2006b, MNRAS, 372, 1710

Peebles, P. J. E. 1969, ApJ, 155, 393

—. 2001, ApJ, 557, 495

Peebles, P. J. E., & Nusser, A. 2010, Nature, 465, 565

Platen, E. 2009, A Void Perspective of the Cosmic Web (Ph.D. Thesis, University of Groningen)

Platen, E., van de Weygaert, R., Aragń-Calvo, M., Jones, B. J. T., & Vegter, G. 2010, MNRAS

Platen, E., van de Weygaert, R., & Jones, B. J. T. 2007, MNRAS, 380, 551

Popescu, C. C., Hopp, U., & Elsaesser, H. 1997, A&A, 325, 881

Postman, M., & Geller, M. J. 1984, ApJ, 281, 95

Praton, E. A., Melott, A. L., & McKee, M. Q. 1997, ApJL, 479, L15+

Prochaska, J. X., & Wolfe, A. M. 2009, ApJ, 696, 1543

Pustilnik, S. A., Engels, D., Kniazev, A. Y., Pramskij, A. G., Ugryumov, A. V., & Hagen, H. 2006, Astronomy Letters, 32, 228

Pustilnik, S. A., Martin, J.-M., Huchtmeier, W. K., Brosch, N., Lipovetsky, V. A., & Richter, G. M. 2002, A&A, 389, 405

Pustilnik, S. A., & Tepliakova, A. L. 2011, MNRAS, 415, 1188

Rees, M. J., & Ostriker, J. P. 1977, MNRAS, 179, 541

Regős, E., & Geller, M. J. 1991, ApJ, 377, 14

Richter, O.-G., & Sancisi, R. 1994, A&A, 290, L9

Rojas, R. R., Vogeley, M. S., Hoyle, F., & Brinkmann, J. 2004, ApJ, 617, 50

—. 2005, ApJ, 624, 571

Roškar, R., Debattista, V. P., Brooks, A. M., Quinn, T. R., Brook, C. B., Governato, F., Dalcanton, J. J., & Wadsley, J. 2010, MNRAS, 408, 783

Rubin, V. C. 1994, AJ, 108, 456

Rudnick, L., Brown, S., & Williams, L. R. 2007, ApJ, 671, 40

Ryden, B. S., & Turner, E. L. 1984, ApJL, 287, L59

Sackett, P. D., Rix, H.-W., Jarvis, B. J., & Freeman, K. C. 1994, ApJ, 436, 629

Sahni, V., Sathyaprakah, B. S., & Shandarin, S. F. 1994, ApJ, 431, 20

Saintonge, A., Giovanelli, R., Haynes, M. P., Hoffman, G. L., Kent, B. R., Martin, A. M., Stierwalt, S., & Brosch, N. 2008, AJ, 135, 588

Salim, S., et al. 2007, ApJS, 173, 267

Sancisi, R., Fraternali, F., Oosterloo, T., & van der Hulst, T. 2008, A&A Rev., 15, 189

Schaap, W. 2007, The Delaunay Tessellation Field Estimator (Ph.D. Thesis, University of Groningen)

Schaap, W. E., & van de Weygaert, R. 2000, A&A, 363, L29

Schechter, P. L., Sancisi, R., van Woerden, H., & Lynds, C. R. 1984, MNRAS, 208, 111

Schiminovich, D., Catinella, B., Kauffmann, G., Fabello, S., Wang, J., Hummels, C., Lemonias, J., Moran, S. M., Wu, R., Giovanelli, R., Haynes, M. P., Heckman, T. M., Basu-Zych, A. R., Blanton, M. R., Brinchmann, J., Budavári, T., Gonçalves, T., Johnson, B. D., Kennicutt, R. C., Madore, B. F., Martin, C. D., Rich, M. R., Tacconi, L. J., Thilker, D. A., Wild, V., & Wyder, T. K. 2010, MNRAS, 408, 919

Schlegel, D. J., Finkbeiner, D. P., & Davis, M. 1998, ApJ, 500, 525

Schombert, J. M., Bothun, G. D., Impey, C. D., & Mundy, L. G. 1990, AJ, 100, 1523

Schweizer, F., Whitmore, B. C., & Rubin, V. C. 1983, AJ, 88, 909

Searle, L. 1971, ApJ, 168, 327

Shandarin, S. F. 2009, Journal of Cosmology and Astro-Particle Physics, 2, 31

Shapley, H., & Ames, A. 1932, A survey of the external galaxies brighter than the thirteenth magnitude (Cambridge, Mass.: Astronomical Observatory of Harvard College)

Sharina, M. E., Karachentsev, I. D., & Tikhonov, N. A. 1997, Astronomy Letters, 23, 373

Shectman, S. A., Landy, S. D., Oemler, A., Tucker, D. L., Lin, H., Kirshner, R. P., & Schechter, P. L. 1996, ApJ, 470, 172

Shen, S., Mo, H. J., White, S. D. M., Blanton, M. R., Kauffmann, G., Voges, W., Brinkmann, J., & Csabai, I. 2003, MNRAS, 343, 978

Sheth, R. K., & van de Weygaert, R. 2004, MNRAS, 350, 517

Shimasaku, K., Fukugita, M., Doi, M., Hamabe, M., Ichikawa, T., Okamura, S., Sekiguchi, M., Yasuda, N., Brinkmann, J., Csabai, I., Ichikawa, S.-I., Ivezić, Z., Kunszt, P. Z., Schneider, D. P., Szokoly, G. P., Watanabe, M., & York, D. G. 2001, AJ, 122, 1238

Silk, J. 1977, ApJ, 211, 638

Simon, J. D., & Geha, M. 2007, ApJ, 670, 313

Simonson, G. F. 1982, PhD thesis, Yale University., New Haven, CT.

Skillman, E. D. 1987, NASA Conference Publication, 2466, 263

Smolčić, V., Schinnerer, E., Scodeggio, M., Franzetti, P., Aussel, H., Bondi, M., Brusa, M., Carilli, C. L., Capak, P., Charlot, S., Ciliegi, P., Ilbert, O., Ivezić, Ž., Jahnke, K., McCracken, H. J., Obrić, M., Salvato, M., Sanders, D. B., Scoville, N., Trump, J. R., Tremonti, C., Tasca, L., Walcher, C. J., & Zamorani, G. 2008, ApJS, 177, 14

Solanes, J. M., Giovanelli, R., & Haynes, M. P. 1996, ApJ, 461, 609

Sparke, L. S. 2004, in Astrophysics and Space Science Library, Vol. 312, High Velocity Clouds, ed. H. van Woerden, B. P. Wakker, U. J. Schwarz, & K. S. de Boer, 273–+

Springel, V., White, S. D. M., Jenkins, A., Frenk, C. S., Yoshida, N., Gao, L., Navarro, J., Thacker, R., Croton, D., Helly, J., Peacock, J. A., Cole, S., Thomas, P., Couchman, H., Evrard, A., Colberg, J., & Pearce, F. 2005, Nature, 435, 629

Steidel, C. C., Adelberger, K. L., Giavalisco, M., Dickinson, M., & Pettini, M. 1999, ApJ, 519, 1

Stierwalt, S., Haynes, M. P., Giovanelli, R., Kent, B. R., Martin, A. M., Saintonge, A., Karachentsev, I. D., & Karachentseva, V. E. 2009, AJ, 138, 338

Stocke, J. T., Danforth, C. W., Shull, J. M., Penton, S. V., & Giroux, M. L. 2007, ApJ, 671, 146

Strateva, I., Ivezić, Ž., Knapp, G. R., Narayanan, V. K., Strauss, M. A., Gunn, J. E., Lupton, R. H., Schlegel, D., Bahcall, N. A., Brinkmann, J., Brunner, R. J., Budavári, T., Csabai, I., Castander, F. J., Doi, M., Fukugita, M., Győry, Z., Hamabe, M., Hennessy, G., Ichikawa, T., Kunszt, P. Z., Lamb, D. Q., McKay, T. A., Okamura, S., Racusin, J., Sekiguchi, M., Schneider, D. P., Shimasaku, K., & York, D. 2001, AJ, 122, 1861

Strauss, M. A., Ostriker, J. P., & Cen, R. 1998, ApJ, 494, 20

Strauss, M. A., et al. 2002, AJ, 124, 1810

Swaters, R. A., van Albada, T. S., van der Hulst, J. M., & Sancisi, R. 2002, A&A, 390, 829

Szomoru, A., van Gorkom, J. H., Gregg, M. D., & Strauss, M. A. 1996, AJ, 111, 2150

Tacconi, L. J., Genzel, R., Neri, R., Cox, P., Cooper, M. C., Shapiro, K., Bolatto, A., Bouché, N., Bournaud, F., Burkert, A., Combes, F., Comerford, J., Davis, M., Schreiber, N. M. F., Garcia-Burillo, S., Gracia-Carpio, J., Lutz, D., Naab, T., Omont, A., Shapley, A., Sternberg, A., & Weiner, B. 2010, Nature, 463, 781

Tikhonov, A. V., & Karachentsev, I. D. 2006, ApJ, 653, 969

Tikhonov, A. V., & Klypin, A. 2009, MNRAS, 395, 1915

Tinker, J. L., & Conroy, C. 2009, ApJ, 691, 633

Toribio, M. C., Solanes, J. M., Giovanelli, R., Haynes, M. P., & Masters, K. L. 2011, ApJ, 732, 92

Trachternach, C., de Blok, W. J. G., McGaugh, S. S., van der Hulst, J. M., & Dettmar, R. 2009, A&A, 505, 577

Tremonti, C. A., Heckman, T. M., Kauffmann, G., Brinchmann, J., Charlot, S., White, S. D. M., Seibert, M., Peng, E. W., Schlegel, D. J., Uomoto, A., Fukugita, M., & Brinkmann, J. 2004, ApJ, 613, 898

Trujillo, I., Carretero, C., & Patiri, S. G. 2006, ApJL, 640, L111

Tully, R. B., Shaya, E. J., Karachentsev, I. D., Courtois, H. M., Kocevski, D. D., Rizzi, L., & Peel, A. 2008, ApJ, 676, 184

Tyson, J. A., Kochanski, G. P., & dell'Antonio, I. P. 1998, ApJL, 498, L107+

van de Weygaert, R., & Bond, J. R. 2008, in Lecture Notes in Physics, Berlin Springer Verlag, Vol. 740, A Pan-Chromatic View of Clusters of Galaxies and the Large-Scale Structure, ed. M. Plionis, O. López-Cruz, & D. Hughes, 335–+

van de Weygaert, R., & Platen, E. 2009, ArXiv e-prints, arXiv:0912.2997

van de Weygaert, R., & Schaap, W. 2009, in Lecture Notes in Physics, Berlin Springer Verlag, Vol. 665, Lecture Notes in Physics, Berlin Springer Verlag, ed. V. J. Martinez, E. Saar, E. M. Gonzales, & M. J. Pons-Borderia , 291–+

van de Weygaert, R., & van Kampen, E. 1993, MNRAS, 263, 481

van der Hulst, J. M., van Albada, T. S., & Sancisi, R. 2001, in Astronomical Society of the Pacific Conference Series, Vol. 240, Gas and Galaxy Evolution, ed. J. E. Hibbard, M. Rupen, & J. H. van Gorkom, 451–+

van Gorkom, J. H., Schechter, P. L., & Kristian, J. 1987, ApJ, 314, 457

van Woerden, H., Schwarz, U. J., Peletier, R. F., Wakker, B. P., & Kalberla, P. M. W. 1999, Nature, 400, 138

van Zee, L., Haynes, M. P., & Giovanelli, R. 1995, AJ, 109, 990

Verheijen, M. A. W., & Sancisi, R. 2001, A&A, 370, 765

Viel, M., Colberg, J. M., & Kim, T. 2008, MNRAS, 386, 1285

Vilchez, J. M., Pagel, B. E. J., Diaz, A. I., Terlevich, E., & Edmunds, M. G. 1988, MNRAS, 235, 633

Vladilo, G. 2004, A&A, 421, 479

Vogeley, M. S., Geller, M. J., Park, C., & Huchra, J. P. 1994, AJ, 108, 745

von Benda-Beckmann, A. M., & Müller, V. 2008, MNRAS, 384, 1189

Walker, M. G., Mateo, M., Olszewski, E. W., Peñarrubia, J., Wyn Evans, N., & Gilmore, G. 2009, ApJ, 704, 1274

Warmels, R. H. 1988, A&AS, 72, 427

Warren, B. E., Jerjen, H., & Koribalski, B. S. 2004, AJ, 128, 1152

Warren, M. S., Abazajian, K., Holz, D. E., & Teodoro, L. 2006, ApJ, 646, 881

Wegner, G., & Grogin, N. A. 2008, AJ, 136, 1

Weinberg, D. H., Szomoru, A., Guhathakurta, P., & van Gorkom, J. H. 1991, ApJL, 372, L13

White, S. D. M., & Frenk, C. S. 1991, ApJ, 379, 52

White, S. D. M., Frenk, C. S., Davis, M., & Efstathiou, G. 1987, ApJ, 313, 505

White, S. D. M., & Rees, M. J. 1978, MNRAS, 183, 341

Whitmore, B. C., Lucas, R. A., McElroy, D. B., Steiman-Cameron, T. Y., Sackett, P. D., & Olling, R. P. 1990, AJ, 100, 1489

Wong, O. I., et al. 2006, MNRAS, 371, 1855

York, D. G., et al. 2000, AJ, 120, 1579

Yun, M. S., Reddy, N. A., & Condon, J. J. 2001, ApJ, 554, 803

Zaritsky, D., Kennicutt, Jr., R. C., & Huchra, J. P. 1994, ApJ, 420, 87

Zel'Dovich, Y. B. 1970, A&A, 5, 84

Zhang, Y., Anninos, P., & Norman, M. L. 1995, ApJL, 453, L57+

Zitrin, A., Brosch, N., & Bilenko, B. 2009, MNRAS, 1177